إصدار خاص

لأبحاث المؤتمر الخامس للعلوم الهندسية والتقنية
«دور العلوم الهندسية في إحياء التنمية المكانية»
الـذي نظمــته كلية الهندسة جادو - جامعـة نالوت
فـي الفـترة مـن 20 إلــى 22 ديسـمـبر 2022م

الجزء الأول

JOURNAL OF
Sharwes

Annual Refereed Scientific Journal Issued by Nalut University

Special issue

For research papers displayed at the 5th Conference for engineering sciences and technology. organized by the faculty of engineering/Jado/ Nalut University From 20th To 22nd December 2022

VOL (1)

جامعة نالــوت

NALUT UNIVERSITY

مجلة شروس العلمية

الجزء الأول

جامعة نالوت

NALUT UNIVERSITY

مجـلة شروس

إن تقديم البحوث المنشورة أو تأخيرها في ترتيب الصفحات لا يعني المفاضلة بينها ولكن متطلبات التنسيق الفني هي التي تتحكم في هذا الترتيب. وإن البحوث المنشورة لا تعبر بالضرورة عن رأي المجلة أو الجامعة.

جامعة نالوت

NALUT UNIVERSITY

مجلة شروس

NALUT UNIVERSITY

جامعة نالوت

5th **E** **2022**
C **ST**

المؤتمر الخامس للعلوم الهندسية والتقنية
جامعة نالوت - كلية الهندسة جادو

المؤتمر الخامس للعلوم الهندسية والتقنية
5th Conference of Engineering Science and Technology
ⵜⴰⵚⴷⵡⴰⵚⵜ ⵜⵉⵙⴰⵎⵙⴰⵜ ⵏ ⵜⵓⵙⵙⵏⴰ ⵜⴰⵚⵏⴰⵏ ⴷ ⵜⵉⵙⵙⵏⴰ ⴳ ⵓⵙⵓⵜⵍⵉⵙ ⵜⴰⵜⵇⵏⵉⵜ

المقام في كلية الهندسة / جادو
في الفترة من 20 إلى 22 ديسمبر 2022م
تحت شعار:
«دور العلوم الهندسية في إحياء التنمية المكانية»

تنظيم

كلية الهندسة جادو
Faculty of Engineering - Jadu
ⵜⴰⵚⴷⵡⴰⵚⵜ ⵏ ⵜⵓⵎⴰⵙⵜ ⵉⴰⵎⵓⵚ

دولــة ليبيــا

وزارة التعليم العالي والبحث العلمي

جامعة نالوت

القرارات

قرار رئيس جامعة نالوت رقم (27) لسنة 1443 هجري الموافق 2022 ميلادي بشأن تشكيل لجنة و تحديد مهامها

رئيس الجامعة .... ☞

☞ بعد الاطلاع على الإعلان الدستوري وتعديلاته.

☞ وعلى القانـــــون رقـــــم (12) لسنـــــة 2010 ميـــــلادي بشـــــأن علاقـــات العمل ولائحتـــــه التنفيذيــة.

☞ وعلى قرار اللجنة الشعبية العامـة سابقا رقم (22) لسنة 2008 بشأن اعتماد الهيكل التنظيمي للجامعات ومؤسسات التعليم الـــعالـــي.

☞ وعلى قرار السيــــد مجلـــس الــــــوزراء رقم (606) لسنة 2017 بشأن تشكيل جامعـــــة نـــالوت.

☞ وعلى كتاب السيـــد /د عميد بلدية نالوت (إشاري د ن 4-140/1) بتاريخ 2017/8/17م بشـــأن ترشيـــح رئيس جامعـــة نـــالوت.

☞ وعلى قرار السيد وزير التعليم العالي رقم (1564) لسنة 2017م بشأن تشكيل لجنة لتقييم المرشحين لشغل قيادات مؤسسات التعليم العـــالي.

☞ على قرار الســــيد الـــوزير رقـــم (1378) لسنـــة 2018م بشـــأن تكليف رئيساً لجامعــة نـــالوت.

☞ بالإشارة إلى خطاب السيد/عميد كلية الهندسة المؤرخ في 2020/3/6م بشأن مقترح استضافة المؤتمر العلمي للعلوم الهندسية والتقنية بنسخته المشرفة.

☞ وعـــــلى كتــاب السيد وكيل الجامعة للشؤون العلمية رقم ج.ن.404 .1.3. المؤرخ في 2022/3/14م بشـــأن استصدار قرار للجنة المشرفة.

☞ وبمـــــا تقتضيـــه المصلحـــة العامـــة.

قـــــرر

مـادة ((1))

يتم بموجب أحكام هذا القرار استضافة المؤتمر العلمي للعلوم الهندسية والتقنية بنسخته الخامسة بكلية الهندسة جادو.

مـادة ((2))

يتم تشكيل لجان تحضيرية وعلمية للمؤتمر من السادة الــ نية أسمائهم:-

أولا :-

أ. د محمد مسعود قنان	رئيسا شرفيا للمؤتمر
أ. أمحمد على أبودينة	رئيسا للمـــــــؤتمر

ثانيا : اللجنة التحضيرية :-

أ. عيسى سليمـــــان لشهب	رئيســـــا
د.أبو القاسم عبد الفتاح الأخضــر	عضـــــواً
أ.عصـــام ابراهيـــم معموعـــة	عضـــــواً
أ. أيمن ساسي القطـــــوس	عضـــــواً
أ. فيصـل صـــــالح ورغ	عضـــــواً
أ. باديس خليفة غـــــزال	عضـــــواً
أ. ضو عمر الشيبـــــاني	عضـــــواً
أ. عماد مسعود دوحـــــة	عضـــــواً
أ. رياض سليمان جرنـــــاز	عضـــــواً
أ. أنور احمد ابو عصـــــارة	عضـــــواً

دولــة ليبيــا

وزارة التعليم العالي والبحث العلمي

جامعة نالوت

القرارات

عضواً		م. خليفة عياد كـــــــــاشور
عضواً		م. أيمن علي الحـــــــــارس
عضواً		صـــالح علــــي السحوبي
عضواً		أحمــــد سليمـــــان الأطرش
عضواً		شعبان أحمد المشـــــــائخ

ثالثا : اللجـنة العلميــة :

رئيســـــــاً		د. صـــالح سعيـــد العلـــوي
عضواً		أ.د المبروك منصور ابــو قديـــرة
عضواً		أ.د ميلـــود العجيـلي الغبـــار
عضواً		د. احمد سعيـــد كاجالـيك
عضواً		د. عـلي محمد ابو صلوعـة
عضواً		د. صالحين محـمد العـــود
عضواً		د. عـمر الحروشي سلطـــان
عضواً		د. صـــالح محمد مهنـــي
عضواً		د.عمر المبـــروك ابــوزيـد
عضواً		د. محمد ابــو بكر الرمـــاح
عضواً		د. بلعيد ساســـي ابــوزيد
عضواً		د. علـي محـــمد حقيـــق
عضواً		د. محـــمد قاســـم الزغبي
عضواً		د. خـــالد عمرو المعيـــوف
عضواً		أ. ابراهيـم محـــمد اجبودة
عضواً		أ. مـسعـــود احـمد البرشني
عضواً		أ. وليـــد خـــليفة حـــسن
عضواً		أ.حسنـــي المختـــار التواتـــي

مـادة ((3))

تتولى اللجان المشكلة في المادة الثانية القيام بالإشراف على جميع الأعمال المتعلقة بالمؤتمر العلمي للعلوم الهندسية والتقنية بنسخته الخامسة بكلية الهندسة.

مـادة ((4))

يعمل بهذا القرار من تاريخ صدوره وعلى الجهات المعنية تنفيذه.

د/ محمد مسعود قنان

رئيـــس جــامعة نالوت

صدر في نالوت

بتاريخ: 13/ شعبان/ 1443 موافق 16 /مارس/ 2022 ميلادي

"قواعـد النشـر في "مجلة شروس"

أولاً شروط النشر:

تنشر مجلة شروس الدراسات والبحوث الأصيلة في مجالات العلوم التطبيقية والإنسانية التي تتوفر فيها مقومات البحث العلمي من حيث أصالة الفكر ووضوح المنهجية، ودقة التوثيق، كما تنشر المجلة تقارير المؤتمرات والندوات ومراجعة الكتب، وملخصات الرسائل الجامعية في مختلف مجالات العلوم، على أن تتوفر فيها شروط البحث العلمي وخطواته المتعارف عليها عالميًا.

1ـ أصالة أفكار البحوث: يشترط في الدراسات والبحوث المقدمة للنشر ألا تكون قد نشرت في أية مجلة محلية، أو دولية، أو دورية علمية بجميع أشكالها الورقية، أو الالكترونية، أو المنقولة، أ والمنسوخة.

2ـ سلامة المنهج العلمي: يجب التقيد بأصول البحت العلمي وقواعده، من حيت أسلوب العرض والمصطلحات وتوثيق المصادر والمراجع، وذلك وفق القواعد المتعارف عليها في كتابة الدراسات والبحوث العلمية.

3ـ لغة الكتابة: يجب أن تكون لغة الدراسات والبحوث المقدمة للنشر هي العربية، أو الانجليزية، أو الأمازيغية المعيارية المراجعة من قبل متخصص في علم اللغة.

4ـ حقوق الملكية والنشر: تقاضى المجلة أجورا مقابل النشر فيها، ولا تدفع للباحث أية مكافأة مالية عن البحث الذي ينشر فيها. وبمجرد إشعار الباحث بقبول بحثه للنشر قبولا نهائيا، نتنقل حقوق النشر إلى المجلة، حيث لا يحق لأصحاب الأعمال المقدمة للمجلة نشرها في أية مجلة أخرى، وتحتفظ المجلة بحقها في نشر البحوث المقبولة وفقا لحالاتها الخاصة.

5ـ تخصص المجلة: تُعنى المجلة بالمراجعات العلمية والنقدية للدراسات والبحوث، وكذلك المراجعات وعروض الكتب ذات القيمة الفكرية والعلمية والثقافية، كما تنشر المجلة وثائق المؤتمرت والندوات العلمية ونتائجها الخاصة.

6ـ ما ينشر في المجلة يعبر عن وجهة نظر الباحث / الباحثين، ولا يعبر عن وجهة نظر المجلة، أو الجامعة.

ثانيا) طريقة النشر في مجلة شروس:

تخضع الأعمال المقدمة للنشر لعدد من الإجراءات

1ـ يوقع الباحث على نموذج "طلب النشر بالمجلة" متضمنًا تعهده بالمسؤولية الكاملة عن أي انتهاك، أو تجاوز لأخلاقيات البحث في حالة ثبوته، وإقراره بأن عمله لم ينشر البحث في أية مجلة أو دورية علمية أخرى، وظانه لن يقدم على نشره في أية واحدة منها في حالة قبوله.

2_ عدم التقدم بطلب سحب العمل بعد إبلاغ الباحث بوصول إنتاجه الفكري للمجلة ودفع سعر نشره.

3_ عدم اعتراض أي عضو من فريق البحث على أية قضية تخص الفريق الذي يعمل فيه.

4_ يتم إشعار الباحث عبر وسائل الاتصال المتوفرة في حينها بتاريخ استلام عمله العلمي، بحث، وإعلامه بالملاحظات إن وجدت، أو أن يتم الاعتذار عن متابعة إجراءات النشر في ضوء التحكيم الأولي

5_ دور البحث في النشر: يتم نشر العمل حسب تاريخ قبوله للنشر بغض النظر عن عدد المجلة، ويتم ذلك وفق اعتبارات فنية صرفه.

ثالثًا) قواعد الكتابة:

يجب أن أخذ بعين الاعتبار الاشتراطات التالية عند إعداد البحث للنشر في المجلة:

1_ أن لا يزيد عدد صفحات البحث عن عشرين صفحة، بما في ذلك ملاحقه، ولإيفل عن عشر صفحات.

2_ أن لا تزيد كلمات العنوان عن عشرين كلمة بما في ذلك العنوان الرئيسي والثانوي

3_ ان لا تزيد الكلمات المفتاحية عن 7 ولا تقل عن 5 كلمات، ولا يقل

4_ ان لا يزيد عدد كلمات الملخص باللغة العربية عن 250 كلمة وباللغة الإنجليزية عن 300 كلمة.

5_ يقدم البحث مكتوبًا باللغة العربية أو الإنجليزية ومطبوعاً على الكمبيوتر باستخدام برنامج ميكروسوفت وورد (Microsoft–Word) (1.15) وبخط Simplified Arabic حجم 14 للبحث باللغة العربية، وبخط Times New Roman بحجم 12 للبحث باللغة الإنجليزية، وحجم خط الهوامش السفلية 11 ، على ورق A4 على وجه واحد من ثلاث نسخ ورقية ونسخة إلكترونية على نسخ ورقية ونسخة إلكترونية على "CD" قرص مدمج.

6_ يكتب كامل البحث باللون الأسود بما في ذلك الجداول والأشكال

7_ يجب أن تظهر في الصفحة الأولى من البحث البيانات التالية:

- عنوان البحث

- اسم الباحث أو الباحثون

- العنوان الرئيسي لجهة العمل

- أرقام الهواتف المحمولة والبريد الإلكتروني للباحث.

8_ لضمان السرية والشفافية يجب عدم ذكر اسم الباحث/ الباحثين / الباحثات في المتن، أو استغلال أية إشارة تكشف هويته، أو هوياتهم / هوياتهن.

9_ إذا استعمل الباحث برمجيات أو أدوات قياس من اختبارات واستبانات أو غيرها من أدوات البحث، فعليه أن يقدم نسخة كاملة من الأداة التي استعملها إذا لم ترد في متن البحث، أو لم ترفق بملاحقه، وأن يشير إلى الإجراءات القانونية التي تسمح له باستعمالها في بحثه. وأن يحدد للمستفيدين من البحث الآلية التي يمكن اتباعها للحصول على البرمجية أو الأداة في كتابة المراجع أو الإشارة إليها داخل البحث.

10_ تستعمل طريقة IEEE 10.

11_ عند تقديم البحت كاملا يجب أن يحتوي على: الملخص، المقدمة، بما ذلك مشكلة البحث، أهدافه، طريقة البحث، النتائج، المناقشة، الاستنتاج، المراجع.

إننا نروم من وراء توظيف مصطلح (مخلص) توضيح مكونات هذا العمل باقتضاب: ضرورة توفر اسم الباحث (ة) في مستهل البحث، درجته العلمية، تاريخ إنجاز البحث المعوَّل على نشره في أحد الأعداد القادمة للمجلة، عدد الصفحات، اسم الكلية، التخصص، تلخيص الموضوع في فقرة، أو فقرتين مركَّزتيْنِ لا تتجاوزان (250)، أو (300) كلمة باللغتين العربية والانجليزية، وذلك حسب الجدول التالي:

اسم الكلية :	التخصص :	تاريخ إنجاز البحث : ....
اسم الباحث (ة) :	الدرجة العلمية :	عدد صفحاته : ....
عنوان البحث :		
الملخص : يجب التطرق بإيجاز وتركيز إلى مجال البحث ، أو حقله المعرفي المتخصص ، مشكلته ، أسباب اختياره ، أهدافه ، فرضياته .		

12_ يلتزم الباحث (ة) بكتابة عمله المقدم للنشر، مقسما إلى أبواب رئيسة، كما هو مبين أسفله، وفى حالة مخالفة ذلك يرفض العمل المقدم للنشر.

1_ نموذج العلوم الإنسانية:

يجب أن يضم: الملخص، المقدمة، الهدف، الأهمية، الحدود، مشكلة البحث، الدراسات السابقة، الفرضيات، منهجية البحث، تقسيم البحث/ المبحث الأول...المطلب الأول.... الخ، المبحث الثاني...المطلب الأول.... الخ. المناقشة والاستنتاج، المصادر والمراجع.

2ـ نموذج العلوم التطبيقية:

يحتوي على: الملخص، المقدمة، الدراسات السابقة، الفرضيات، منهجية البحث، خلفيته /
تصميمه / موقعه / مجتمع البحث، العينة / أدوات الدراسة /تحليل البيانات احصائيا، النتائج،
المناقشة، الاستنتاج، التوصيات، المصادر والمراجع.

ملاحظة: الأبواب المبينة أعلاه تحتوي على عناوين فرعية وثانوية.

ـ يجب الالتزام بترتيب أبواب البحث، كما تترجم ذلك طريقة النشر في المجلة. 4.

أهداف المؤتمر:

- التركيز على التطورات الجديدة في المجالات التقنية وعرض دورها الرئيسي في التنمية
  الوطنية.

- تبادل الأفكار والخبرات بين الأكاديميين والتقنيين في المجالات الهندسية. العمل بين
  الأطر الهندسية المختلفة في تصميم وتنفيذ المشاريع. دور الكليات الهندسية والمعاهد
  التقنية في المساهمة الفعالة في تطوير البحث العلمي والربط بينهما وبين المؤسسات
  ذات العلاقة.

محاور المؤتمر:

المحاور

1.الهندسة النفطية والكيميائية

– حفر آبار النفط وهندسة المكامن.

– هندسة وتقنية البوليمر.

– كرير النفط وعمليات الغاز.

– العمليات الكيميائية والبتروكيماوية وتطويرها.

– تقنية محطات الإنتاج المبكر.

2. الهندسة الكهربائية والحاسوب

– نمذجة أنظمة الطاقة.

– محطات القوى الانتاج والتوزيع.

– أنظمة الاتصالات.

- معالجة الاشارة والصورة.

- تقنيات أنظمة التحكم والروبوت والأنظمة الذكية.

- شبكات الحاسب.. وتأمينها.

3. الهندسة المدنية والعمارة

- تقنيات الخرسانة ومواد البناء.

- هندسة المواصلات والمساحة.

- الهندسة الانشائية ودراسات التربة.

- هندسة البيئة والموارد المائية.

- العمارة والتخطيط الحضري والتراث العمراني.

- التطبيقات الهندسية واستخداماتها في التصميم العمراني والإنشائي.

4. تقنية المعلومات

- علوم الحاسب والخوارزميات.

- تقنية الوسائط المتعددة.

- أنظمة قواعد البيانات.

- الحوكمة والتجارة الإلكترونية.

- هندسة البرمجيات والحسابات السحابية.

5 الهندسة الميكانيكية والصناعية

- نمذجة وتصميم العمليات.

- أنظمة التكييف والتبريد وإنتاج الطاقة.

- عمليات الانتاج وتقنيات اللحام والمعالجة الحرارية.

- تقنيات النانو في العمليات الصناعية.

- علوم المواد.

6. الهندسة الجيولوجية والجيوفيزيائية

- هندسة استكشاف الخامات.

- التقييم الاقتصادي للخامات

- هندسة استكشاف النفط والغاز.

- دراسة الصخور.

- تطبيقات الهندسة الجيوفيزيائية.

- تقنيات الاستشعار عن بعد واستخدامها في عمليات الاستكشاف.

7. **الإدارة الهندسية والبيئية:**

- إدارة المشاريع الهندسية.

- استدامة الموارد البيئية الطبيعية.

- التغيرات المناخية وآثارها البيئية.

- دراسة وإدارة المخلفات والمخاطر البيئية.

- أنظمة إدارة الجودة.

8. **استراتيجيات وتقنيات الطاقات المتجددة**

- دراسة مصادر الطاقات المتجددة وتطبيقاتها.

- تصميم وتحليل وصيانة نظم الطاقة المتجددة.

- تقنيات نظم التخزين والتحكم بالطاقة المتجددة.

- تصميم وتركيب وتحليل تقنيات الشبكة الذكية.

- الاستراتيجيات ذات العلاقة باستخدام الطاقة المتجددة.

- تقنيات التحويل الحراري والكهروضوئي.

توصيات المؤتمر الخامس للعلوم الهندسية والتقنية

بسم الله الرحمن الرحيم

انعقد مؤتمر العلوم الهندسية والتقنية في نسخته الخامسة في الفترة ما بين 20 الى 22 ديسمبر 2022م والذي نظمته كلية الهندسة جادو بجامعة نالوت وقد شارك في المؤتمر نخبة من الباحثين والأساتذة من جميع مناطق ليبيا وقد خلص المؤتمر الي عدة توصيات.

أولا: يشدد الحاضرون على ضرورة تجدد مثل هذه اللقاءات العلمية لتبادل الآراء والأفكار والمعلومات.

ثانيا: يدعو المؤتمر الى ضرورة الربط بين مؤسسات التعليم العالي والمراكز البحثية لتبادل الخبرات والتعاون في مجال المختبرات وانشاء قاعدة بيانات للمعامل في الجامعات الليبية والمراكز البحثية.

ثالثا: ضرورة العمل على نقل الإنتاج المعرفي من مؤسسات التعليم العالي الى سوق العمل وإيجاد فرص للخرجين وجلب التحويل اللازم للبحث العلمي.

رابعا: ضرورة ابرام اتفاقيات تعاون بين الجامعات المحلية والعربية والدولية وتفعيل الاتفاقيات السابقة من اجل التطور والبحث والاشراف المتبادل على طلاب الدراسات العليا.

خامسا: يدعو المؤتمر الى استحداث جمعيات مختصة في مجالات لم يتم الاهتمام بها في السابق مثل جمعية الهيدروجين الأخضر.

وأخيرا بأذن الله سيكون تنظيم النسخة السادسة لهذا المؤتمر بكلية الهندسة القرة بوللي بجامعة المرقب.

والسلام عليكم ورحمة الله وبركاته

د/ صالح سعيد العلوي
رئيس اللجنة العلمية للمؤتمر

جامعة نالوت

NALUT UNIVERSITY

الفهرس

الهندسة الجيولوجية

Facies analysis of the Kurrush Formation, Gharian area Jabel Nafusah

Emhemed Alfandi [1*], Mohamed Ali Alrabi [2] ,
[1] alfandi73@ yahoo. com, [2] mrabeib2006@yahoo.com.
[1] Department of Geology, College of Science, Sabrahath University, Libya
[2,] Department of geology, College of Science, Zawia University, Libya
*Corresponding author email: emhemed.alfandi@sabu.edu.ly

Abstract

This paper presents the facies and depositional environment of the early Mesozoic Kurrush Formation. The Early Mesozoic records of northern Gowdwana were influenced by sea level-changes during the opening of the Neotethys Ocean. These records are clearly noted in the north-western parts of Libya, which were located on the tectonically active subsiding margin during rifting, and subsequently the opening of the Neotethys Ocean basin. These records include the Triassic sedimentary facies of the so-called Kurrush Formation in the Gharian area in Jafarah / Nafusah region. Field work in the area, and petrographic studies in the area have indicated that the Formation consists of red micaceous sandstone, mudstone, and siltstone facies overlained   mainly by carbonate rocks of Al Aziza Formation. These facies might have been deposited in transitional environment , possibly of delta plane. This study is intended to investe the possible influence of the tectonic activity on the depositional environment of the Kurrush Formation in the area.

Keywords: Sandstone Formation, Early Mesozoic Transitional environment, Nafusah region Libya.

1   .Introduction

The Kurrush Formation previously known as Ras Hamia Formation[1], Boutoniere and Currusc Formation [2,3,4], is the oldest Mesozoic rocks exposed in Nafusah/ Jafarah area. Although these has been controversy among these authors about having the rocks of this formation, their studies seem to describe same rock of the upper Kurrush Formation cropping out at or near small domes in Gharian and Wadi Ghan area.

according to[2,3,1,4], the Kurrush Formation consists mainly of red and brown, fine grained, micaceous sandstone with yellow to green clay and pale red to brown micaceous sandstone with minor calcarous inter beds at the top. subsurface studies by [4] on the Kurrush Formation at well A1-38 indicates that the Formation consists of 581 meter of gray, fine to coarse grained varicolored shale and sub ordinate dolomite. Most of the above mentioned studies on the upper unit of the Kurrush Formation in the Gharian area was delta with the lithological and stratigraphical description in the field, and have net attempted to utility these delta to study depositional processes that from theses rocks. This study is intended to use surface

and cahrotary data in interpretation of the depositional environment and tectonic setting of the upper Kurrush Formation.

2   .Location of study area and Exposure of Kurrush Formation.

The Kurrush Formation is the oldest Mesozoic rocks crops mostly in the Gharian area. it was previously known as Ras Hamia Formation [4]. The Kurrush Formation is exposed in four place in Gharian are, where all exposures are at ,or nearby centres of small domes (Fig.1). Two exposures are just north of Gharian town, willies on the other two just to the east of wadi Ghan   Fig.1 [5]. The Kurrush Formation in subsurface oil   well (A1-380 has been described by [4], who pointed that this Formation is underlined by Al Guidr Formation (well A1-38,). According to [4], the Kurrush Formation in this well consists of 581m of grey fine grained, and varicolored shale and subordinate dolomitie, while in its base tend to be constitutes   of white to grey occasionally dolomitic limestone (myophozia beds).
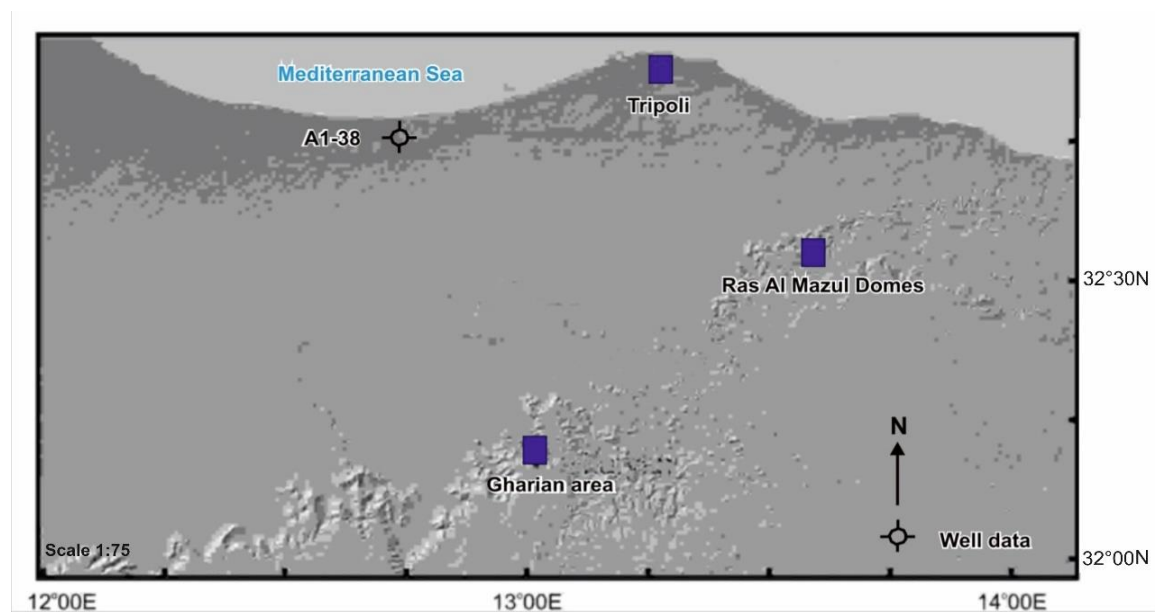
Figure 1. *DEM map showing 1) the location of the Gharian area and the Ras Mazul dome region and 2) the subsurface Al-38 oil well loction for the Kurrush Formation*

3   Field description

Exposures from three localities are used to describe the main sedimentary characteristics of the Kurrush Formation. These characteristics are summarized in Table 1.

3.1   South of the Wadi Abu Shaybah

This section is exposed in the area south of the Wadi Abu Shaybah located approximately 2.5 km to north of Gharian town. It shows the contact with the overlying Al Aziza Formation. Here, the Kurrush Formation is characterised by

facies (F-YS).F-YS is dominated by pale yellowish orange (10YR 8/6) fine-grained sandstones with minor dolomitic beds. This facies is capped by dolomitic limestone facies of the Al Aziza Formation. The maximum measured thickness of the yellow sandstone facies (F-YS) is *ca*. 0.90 m. The sandstones are massive, lack sedimentary structures and are lacking fossils and bioturbation structures.

3.2   North of the Wadi Abu Shaybah

This section is exposed along the north side of the Wadi Abu Shaybah . The main characteristics of the section are illustrated in field photographs (Fig. 2.A and Fig. 2. E) and a graphic log (Fig. 2. F). The log was recorded from the northern side of the Wadi Abu Shaybah and is characterised by reddish micaceous sandstone facies (F-SR). The maximum measured thickness of facies (F-SR) is *ca*. 1.10 m. The facies comprises moderate red coloured (10R 4/6), very fine to fine grained sandstone that displays symmetrical ripples. These have an average wavelength of 1 cm and crest height < 1 cm (Fig. 2.E). Some of the cross laminations have a north westerly palaeo flow direction (Fig. 2.F), although limited palaeocurrent analyses (n = 5) were conducted due to the poor quality of the sedimentary structures. Fossils and bioturbation were not observed in this facies.

3.3   West of the Wadi Abu Shaybah

This outcrop is exposed in the northwest of the study area along the Abu Rashada road , located approximately 1.5 km south of Kaf Kalaya The main characteristics of the section are illustrated in some field photographs (Fig. 2. C and Fig. 2. D). This section is affected by Tertiary basaltic volcanism. The outcrop is dominated by light brown (5YR 5/6) fine-grained sandstones with minor clay lenses. The maximum measured thickness of light brown sandstone (F-LS) is *ca*. 1.20 m (Fig. 2. C). This consists of fine grained sandstone and green silty claystone that displays fine parallel lamination. The average thickness of the parallel laminations is approximately 1 mm (Fig. 2. D)

3.4   Ras Lefa section

This outcrop is exposed in the Jafarah Plain at the Ras Lefa section, located approximately 21 km to north of Gharian town. The maximum measured thickness of facies (F-MS) is *ca* (Fig.2. B). 0.6 m.The section shows the contact between the Al Aziza and Kurrush Formations. The Kurrush Formation is characterised by facies (F-MS). F-MS is dominated by pale yellowish orange (10YR 8/6) mud and siltstone. This facies is capped by dolomitic limestone facies of the Al Aziza Formation. Fossils and bioturbation were not observed in this facies. Petrographic analysis reveals that the sandstone comprises quartz and mica grains that are angular to sub angular in shape with moderate sorting (Fig. 3). Quartz makes up approximately 92% of the grains. The quartz occurs as both mono-crystalline and polycrystalline forms (Fig. 3), but most of sandstone samples are dominated by polycrystalline quartz. Mica (muscovite) is also present and represents about 5% of total components. Feldspars are very rare (< 1% e.g. Sample K002 in Fig. 3). Rock fragments are also present and represent about 2% of total components. Furthermore, proportions (5-10%) of clay matrix were observed in the studied samples (Fig. 3).

Table 1 *Summary characteristics of the Kurrush Formation in the Gharian area.*

Lithology	Description				
	Thickness (maximum)	Grain size (Wentworth scale)	Colour (Munsell colour chart)	Sedimentary structures	Fossils
Redish sandstone (F-SR)	1.10 m	Very fine sand	10R 4/6 Moderate reddish brown	Symmetrically rippled	None
Yellow sandstone (F-YS)	0.90 m	Very fine sand	10YR 8/6 Pale yellowish orange	None	None
Lightbrown sandstone (F-LS)	1.20 m	Fine sand	5YR 5/6 Light brown	Cross-laminated	None
Paleyellowish orange (10yr 8/6) mudstone	0.6 m	Mud	10YR 8/6 Pale yellowish orange	None	None
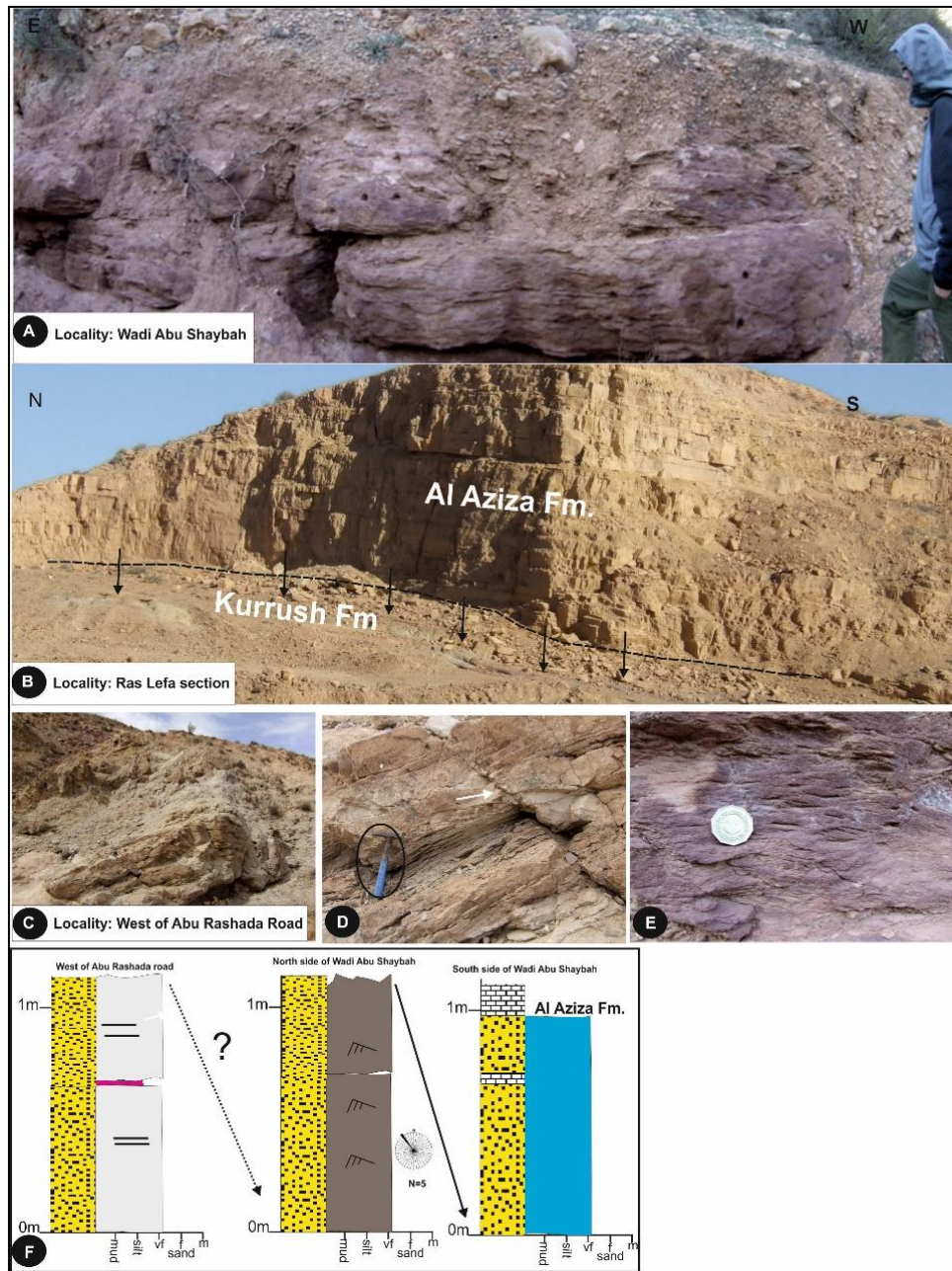
Figure 2 *A: General view of Reddish sandstone (F-SR) exposed in Wadi Abu Shaybah, person's height = 1.82 m.B: View of the Ras Lefa section showing the Kurrush Formation with the overlying Al Aziza Formation. C: General view of light brown sandstone (F-LS) exposed in west of Abu Rashada road..D: Parallel lamination exposed in the Kurrush Formation (west of Abu Rashada road.). Hammer circled for scale. Fault has NW trend (white arrow). E: View of symmetrical ripples in the Kurrush Formation (coin = 2.5 cm diameter) F: Sedimentary logs from the north and south of Wadi Abu Shaybah and west of Abu Rashada locations.*
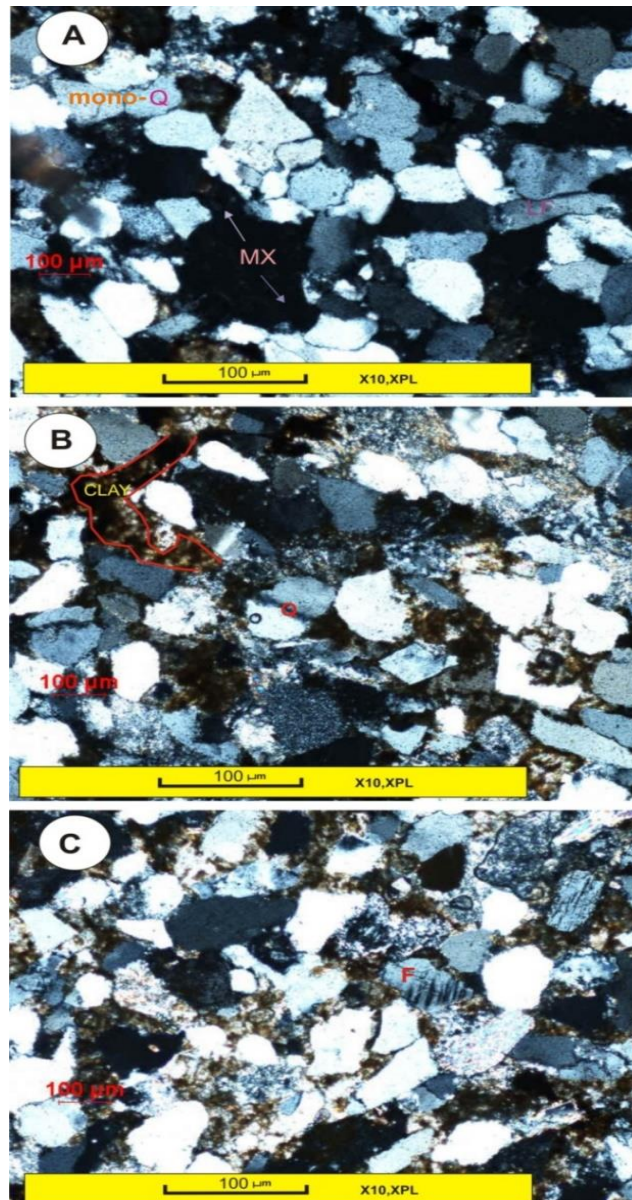
Figure 3. *Thin sections of the Kurrush Formation from west of the Abu Rashada road. A: Microphotograph of sample K001 taken under crossed polars illustrate moderate sorted. B and C: Microphotographs for sample K002 and K003 taken under crossed polars, illustrating clay and feldspar crystal at the right top of the view (C)*

4. Interpretation

4.1 Depositional environment

The textural characteristics observed in the southern part of Kurrush Formation show an overall fine-grain size indicative of a relatively low energy environment [6,7]. The occurrence of minor dolomitic beds within these sediments could suggest a shallow marine shelf setting. However, the lack of sedimentary structures makes palaeogeographic reconstruction difficult. The oil well data from the Jafarah basin which includes the presence of the *Myophoria* bivalve [4] provides clearer evidence for a marine setting [8]. The mud facies of the Kurrush Formation from the Jafarah

Plain is interpreted as a flood plain environment. Deposition of mud usually occurs under low energy conditions with low flow velocity. However, the sedimentological characteristics of the red sandstone in the Wadi Abu Shaybah indicate deposition within a continental environment. Textural characteristics show an overall fine grain size reflecting low energy depositional environment. Evidence from thin sections further supports a continental environment for Northern Wadi Abu Shaybah and West of Abu Rashada road, which the sediment possibly derived locally from quartzites or quartz rich metamorphic rocks. The presence of small-scale symmetrical ripples is typical of elements of shallow water waves [9] . However, it is not possible to be more precise about whether the environment is continental (e.g. lacustrine) or marine (e.g. tidal etc.). Siltstones often relate to fluvial environments with over bank flooding or low energy parts of a deltaic system [10,11,12] . Furthermore, delta plain settings often include low energy environments such as tidal flats and swamps. The upper part of the Kurrush Formation contact with Al Aziza Formation is transitional from marine clastics to marine carbonates. Therefore, the Kurrush is probably deposited in a marginal continental environment, possibly a delta plain setting, with facies changes possibly reflecting localised sea level oscillations. In the Jafarah Basin sub-surface record (A1-38) a marine incursion is indicated by the presence of dolomitic limestone and the bivalve Myophoria [4,12,13]. The upper part of the Kurrush Formation outcrops in the Gharian area of Jabel Nafusah regain where it is represented by micaceous red sandstones. Textural characteristics show an overall fine grain size reflecting low energy depositional environment.   Evidence for continental environments is based on 1) grain size; 2) colour; 3) palaeocurrent trend and the absence of fossils. Figure. 2 shows that the Kurrush Formation is dominantly marine environment in the Jafarah Plain and becomes marginal marine in the Gharian area.

4   Conclusions

The sedimentary facies and depositional systems were analysed to provide palaeoenvironmental and palaeogeographic reconstruction for the study area. For the purpose of this study, the Kurrush Formation is not described using fully developed facies analysis and this is due to poor exposure of facies. The Kurrush is probably deposited in continental to nearshore environments

 A number of important conclusions can be drawn from this study:

1) During the lower Triassic the Gharian area is a very low continental margin setting.

2) The sedimentary facies and depositional systems were analysed to provide palaeoenvironmental and palaeogeographic reconstruction for the study area. A shallow shelf sea (Neotethys) existed to the north and allows a major regressive event, with development of: The Kurrush Formation (marginal continental environment possibly delta plain).

References

[1]   CHRISTIE, W. 1966. *Geology of the Gharian area, Tripolitania,Libya, Ministry of Industry*, Geo.Sec, Bulletin, No.5.

[2] DESIO, A., RANCHETTI, C. R. & INVERNIZI, G. 1960. Sulla Strtigrafia del Trias in Tripolitania e nel sud-Tunisino, Rev. *lTAL-pALEONTAL. Stratigr,,* Vol .66**,** 273-322.

[3] MAGNIER, , P. 1963. Etude stratigraphique dans le Gebel Nefousa et le Gebel Garian (Tripolitaine, Libya). *Bulletine-Societe Geologique de,* 5**,** 89-94.

[4] HAMMUDA, O. S., SBETA, A. M. & ELIAGOUBI, B. A. 1985. *Stratigraphic nomenclature of the Northwestern offshore of Libya* The Earth Society of Libya, 166 pp.

[5] TAWADROS, , T. 2001. *Geology of Egypt and Libya.* , Balkema, Rotterdam, 461p.

[6] ALLEN. J, R., L 1965. A review of the origin and characteristics of recent alluvial sediments. *Sedimentary Geology,* 5, 89-191

[7] COLLINSON, J., MOUNTNEY, N. & THOMPSON, D. 2006. *Sedimentary structures*, T.

[8] hird edition, Terra Publishing. 292 pp.

[9] GAO, , Y., SHI, G. R. & PENG, Y. 2009. A new bivalve fauna from the Permian-Triassic boundary section of southwestern China. *Alchering* 33**,** 33-47.

[10] HARMS, , J. C., SOUTHARD, J. B., SPEARING, D. R. & WALKER, R. G. 1975. *Depositional environments as interpreted from primary sedimentary structures and stratification sequences*, Soc. Econ. Palaont, 161.

[11] SELLEY, R. C. 1976. *An introduction to sedimentology*, A cademic Press Inc. (London) Ltd, 408 pp.

[12] HEWARD, A. P. 1978. Alluvial fan sequence and megasequence modeles: with examples from Westphalian D - Stephanian B coalfields, northern Spain. *In:* MIALL, A. D. E. (ed.) *Fluvial sedimentology.* Canadian Society of Petrolum Geologists, Memoir, 5, 669-702.

[13] WALKER, , R. G. 1992. Facies, facies models and modern stratigraphic concepts. *In:* IN WALKER, R. G. & JAMES, N. P. (eds.) *Facies model, Respons to Sea level change.* Geological Association, 1-14.

[14] SWIER, , P. H. & GASHGESH, T. M. 2000. Concession 9 and surround the bio-chaono-and lithostratigraphy and hydrocaron prospectivity of the northwest Ghadames basin and Jafarah Plain. 52 p p.

Biostratigraphy of Ghanema Section (Lower Miocene Al Khums Formation)

Ali.M.Al Naddari (1)   Amar.M.Gammudi (2)

(1.2) alialendari2020@gmail.com

Abstract

Ghanema section have been Logging and nine rock samples have been collected with a total thickness about 15m of carbonate, these samples processed used normal technique in order to obtain microfossil ostracoda to be used in delimit age of the Ghanema section We obtained twenty eight genera and species. Twenty four of them previously recorded from North Africa and Middle East four Genus left in open nomenclature such as *Quadracythere* sp, *Costa* sp, *Semicytherura* sp and *Uroleberis* sp. The fauna assemblages in the study section indicate lower Miocene Age (Burdigalian) by the presence of diagnostic fossil (*Aurila soummamensis*) which is widely distributed in Egypt, Algeria and Libya.

Key Words: Miocene, Ostracoda, Ghanema and Al Khums Formation

Purpose of study

The aims of this study to delimit age of Ghanemah section using microfossil (ostracodas).

Location of the study section

The study section located North west Libya west of Al khums city approximitly30 with coordinate Km Away. Lat.32 33 00 N and long 13 30 15 00 E, see Figure .1
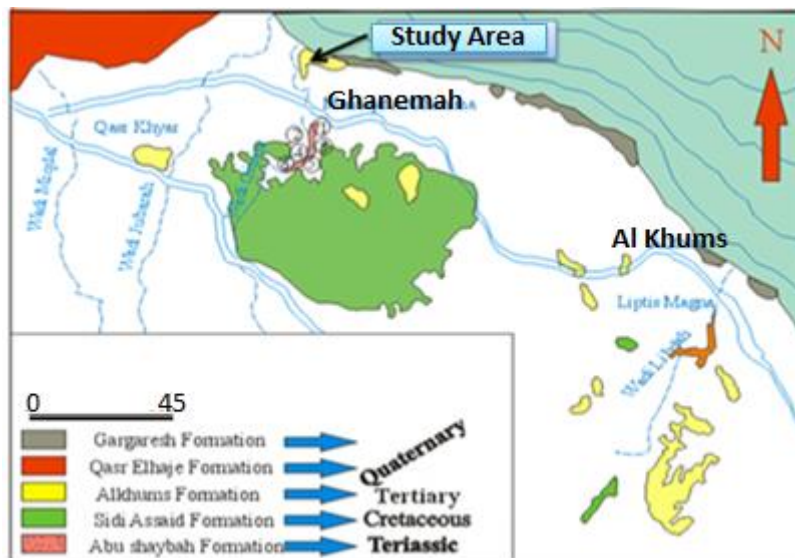
Fig 1. Location of the study Area Al Khums province , Ghanema village modified after (Mann,1975)

Introduction

The Miocene sediments outcrops al mostly along   the coastline from Alkhums to Cyrenaica nominated by different names. also exposed in the Marada Oasis with thickness 85-150m and comprise upper part AR- Rahlah lithological mainly carbonate while lower part called Garat Jahanam lithologically mainly sandstone with some Leges of carbonate ,these are usually disconformably overlies varies Oligocene rocks while in the subsurface overlies Oligocene (Dibia Formation) . The Miocene sediment widely distributed in Sirt Basin and Cyrenaica platform with small areas of Al Khums to Misratah city this sediment usually parallel coastline. The thickest sediment located in the Sirt Basin Around 853m in the subsurface (Wright and Benfield ,1980), lithologically composed of shale, clastic and carbonate with total Thickness. The Miocene in Cyrenaica platform Called by Al Ragma formation (Desio 1928). Lithological Composed mainly carbonat with thickness about 65 (Pietersz,1968).this Formation ucconformable some older rocks such as Eocene and Oligocene of Derna Limestone..

Al Khums Formation (MIOCENE)

This rock unit was first described by Floridia, (1939). Mann, (1975) established the Al Khums Formation for the Middle Miocene carbonet- clay marl sequence. In the studied section, this formation overlies unconformable . The Late Cretaceous Sidi as Sid Formation (Ain Tobi Member). Salem and Spreng, (1980) locally subdivided Al Khums Formation in Al Khums area into two informal members, from base to top: 1- An Naggazah Member and 2- Ras Al Mannubiyah Member, the An Naggazah Member recognized in this study.

1 - An Naggazah Member:

First introduced informally by Salem and Spreng, (1980) to define the lower part of Al Khums Formation in Al Khums area, NW Libya. It overlies unconformable the Late Cretaceous Sidi As Sid Formation (Ain Tobi Member) in the Ghanema section.
The lower part of this member characterized by polymictic conglomerates (clasts are composed predominantly of carbonate with chert in sandy carbonate matrix), also contains pebbly to coarse sandstones grading upwards into medium to fine grained, poorly sorted calcareous sandstones, fossiliferous with gastropodes and pelecypods shell fragments. The sandstone is forming, porous to hard, sandy, algal reefal limestone highly fossiliferous with corals, coralline algae, oyster bivalves, echinoide gastropods and pelecypods, (Hamad, 2013).

2 - Ras Al Mannubiyah Member:

This rock unit was first described by Salem and Spreng,(1980) to define the upper part of Al Khums Formation in Al Khums area, in the eastern side of Ras Al Mannubiyah village, about 8 km west – southeast of Al Khums, NW Libya.This member not exposed in the Ghanema section,This member overlies conformably An Naggazah Member and underlies unconformably the Quaternary clastic

sediments.This member composed of highly fossiliferous algal reefal limestone separated by white cream - coloured chalky limestone bed. algal reefal limestone, highly fossiliferous with coralline red algae, gastropods and other bivalved shell fragments, The environment of deposition variety from neritic to littoral and lagoonal(Hamad,2013).

Lithological section of Ghanemah

The total measured thickness about 18 meter mostly from Al Nagazah member, the top 3meter belong to Quaternary sediments covered top section study make unconformable surface. We collected nine samples begins from upper part Sid As side Formation upward the position of sample marked in the lithological log from S1-S9, see figure(2). The samples(1,2) were located in upper part Sid As Sid Formation   contact between Sidi AS Sid Formation the lithology was dolomite very hard, while the sample (3) consist of limestone with slightly sand ,the sample (4) contains sand limestone friable to hard, while sample (5) sandstone grey to white , the sample (6) consist of sandy limestone very hard, the sample (7) contains sandstone moderately hard , while sample (8) consist of sandstone with crystal quartz moderately hard , the sample (9) consist shell fragments moderately hard, while the Quaternary deposits which overlain the Al Nagazh member consist of conglomerate of gravel –boulder size moderately hard with shell fragments.

Age	Formation	Thickness(m)	Sample No	Lithology	Lithology Description
Quaternary					Conglomerates of gravel-boulder size ,rounded , Whitish,moderatly hard ,chalky with shell fragments
Miocene	Al Khums F.M (Al Naggazah Mem)	15	S9		Shell fragments with chalky-grey to whitish- moderately hard
			S8		Sandstone with crystal quartz –grey to whitish- moderately hard
			S7		Sandstone ,grey - white, moderately hard
		10	S6		Sandy limestone, light brown, brown, very hard
			S5		Sandstone, grey - white , calcareous
			S4		Sandy limestone - yellow, friable-hard ,com sands
		5	S3		limestone, yellow, calcareous and slightly sand
Cretaceous	Sidi AS Sid		S2		Dolomite –Grey to browinsh- vugs crystal -hard
			S1		Dolomite ,grey- browinsh ,white, hard ,vuggy

Fig.2 Stratigraphic column of the Al Khums Formation in the study area and location samples in the section

Dolomite   Chalky Limestone   Quaternary Deposits   Unconformity surface   S Sample position
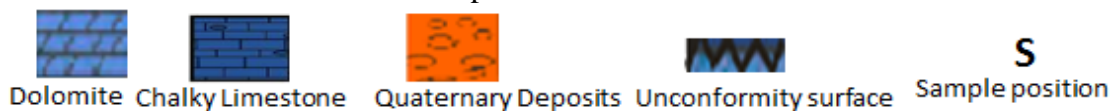
Biozone of the Al Khums Formation Ghanema Section:-
Previous Biozone study using ostracodas
Many Biozone find out around Mediterranean such as Carbonnel (1969) on the Aquitaian Tortonian of the Rhone basin in France , Sissingh (1972) on the Late Cenozoic of the south Aegean Islands , and Gammudi(1990) study subsurface of the Marada Formation and he recognize four Biozone from Aquitnian to upper Regarding the age of Al Khums Formation, assigned this rock unit as Miocene. Middle Miocene (Langhian). But on the contrary, Innocenti and Pertusai, (1984) and El Waer (1991) assigned it as Late Miocene (Tortonian to Early Messinian) on the basis of the ostracod content, Mann, (1975) recorded species and Genera ostracoda indicating a Langhian –Tortonian age. In the present study, ostracoda species recorded from the Ghanema section indicate the age Based on the following index species *Aurila soummamensi*s which is considered index fossil for Burdigalian age, *Carinovalva Carinata* which is reported by Gammudi and Keen,(1993) as Langhain –

Serravalian age while *Ruggieria tetraptera tetraptera* Tortonian age. In this study one Biostratigraphic zone was Propsed *Aurila soummamensi*s (Burdigalian). We cannot depends *Carinovalva Carinata, Ruggieria tetraptera tetraptera* due to not well preserved species (corroded) and partially distorted and rare species so that I will consider as reworked species.i.e not in Situ. see Table (1) present study

Miocene	Series	Stage	Biozone	Al Khums formation Present study	Sirt Basin,Libya Gammudi,1996	Turkey Gokcen,1985
	Early	Burdigalian		*Aurila soummamensis*	*Aurila soummamensis*	*Aurila soummamensis*
		Aquitanian		/	*Pokornyella deforms minor*	/

Table.1 Correlation chart showing *Aurila soummamensis* Biozone in different Location

Mag=174x   **Mag=200x**
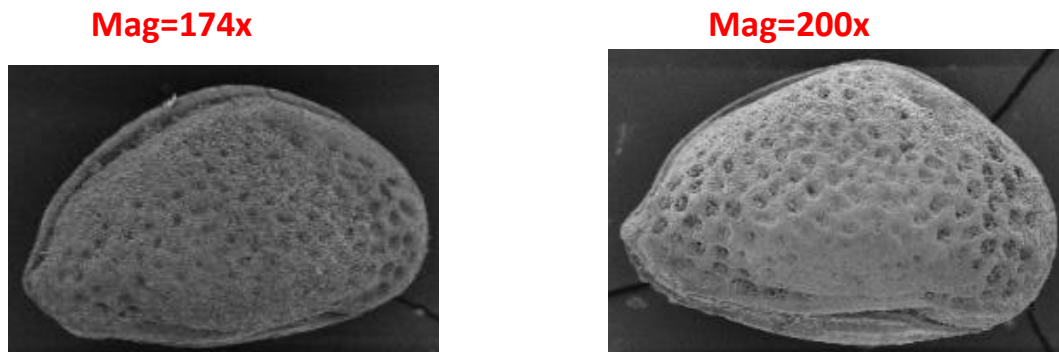
Material: Two carapaces
Horizon: Al Khums Formation, sample no.4, 7 at Ghanema studied section

Dimensions of figured specimen (in µm)

	Length	Height	L/H
Left carapace Male	630	385	1.63
Right carapace Female	546	464	1.17

Conclusion:

Microfossils (ostracodas) very important tool in oil companies exploration , they used to Age dating of rock sediments as well as Paleoenvironments and Paleogeography because of their worldwide distribution   and can survive into different kinds of environments from fresh water – hyper saline water . In this study we recorded twenty eight species; these are previously   recorded along Medetraian region and Middle East. The authors proposed one Biozone on the first appearance index fossil (*Aurilla soummamensis*) which indicate Miocene Age (Burdigalin).

References:

[1]   Carbonnel, G., (1969). Les ostracodas du Miocene Rhodanien. Systematique, 469.biostratigraphique, ecologique, paleobiologie.Docum.Lab .Geol, Fac.Sci. Lyon, 32-

[2]   Desio, A., 1928. Risultati Scientifici della Missione alla Oasi di Giarabub. Fasc. I. La morfologia*. R. SOCG. eol. Ital*., 1-82.

[3]   El Waear,A., (1991).Miocene Ostracoda from Al Khums Formation north western Libya .the Geology of the Libya (eds.M.J Salem ,O.S.Hammuda and B.A. Eliagoubi) .Elsevier, Amsterdam.1457-147.

[4]   Floridia, G.B., (1939). Osservazioni sul Miocene del dintorni di Horns. Boll Soc, GeoL. ItaL.58. 245-260.

[5]   Gammudi, A.M., (1990). Biostratigraphy and Ostracoda fauna of the Miocene Marada Formation of Eastern Sirt Basin ,Libya .M.S.C. Thesis , University, Glasgow, 118.

[6]   Gammudi, A.M. and Keen, M.C., (1993).Ostracoda from the Miocene Marada Formation of Libya .J.Micropalaeontol .394-415.

[7]   Gammudi, A.M.,(1996).The ostracodas fauna of the Miocene Marada formation exposed in the eastern Sirt Basin, (eds M.J.Salem and M.T.Busrewil) Elsevier, Amsterdam .392-417.

[8]   Gokcen, N., (1985). Les Ostracodes burdigaliens de La region de Kale-Yenisehir(Denizli) sud-ouest de 1'Anatolie (Turquie). The Burdigalian ostracods from the area S. W. Anatolia (Turkey). - Rev. micropaldont., 28, 1, 41-57.

[9]   Hamad, M.M., (2013), Biostratigraphy and paleoecology of the Miocene sequence along the stretch of Qabilt ash Shurfah to Wadi Zaqlum sections, Sirte Basin, Libya. Australian Journal of Basic and Applied Sciences, 7(10): 513-531, 2013 ISSN 1991-8178.

[10]   Innocenti, F and Pertusati, P., (1984). Geological map of Libya, 1;250,000. Sheet A1 AQAYLAH (NH34-5), Explanatory Booklet. Industrial Research Centre .Tripoli. Libya. 105.

[11]   Mann, K., (1975a). Geological Map of Libya, Explanatory Booklet, Sheet Al khums, NI 33-14 Industrial Research Centre,Tripoli.

[12]   Pietersz,C.R.1968. proposed nomenclature for rock units in Northern Cyrenaica.*petrol explor.Soc.libya,10th Ann field Conf.,*1968.in Geology And Archelogy of Northern Cyrenaica (Ed.F.T.Barr),pp.125-130,Tripoli.

[13]   Salem, M.J. and Spreng, A.C., (1980). Middle Miocene stratigraphy, Al Khums area, northwestern Libya. Second Symposium on the Geology of Libya.1 (eds. M.J. Salem and M.T. Busrewil), Academic Press, London. 97-116..

[14]   Sissingh, W., (1972). Late Cenozoic Ostracod of the south Aegean Island Arc. Utrecht . Micropaleont. Bull., 6, l-187.

الهندسة الكهربائية

Fifth Conference on Engineering Sciences and Technology (CEST-2022) 20-22 December 2022/ Libya

Comparative Performance Analysis for Transient and Steady State Response of DC Motor with One and Two Degree of Freedom Phase Lag-Lead Compensators using Frequency Response Technique

Comparative Performance Analysis for Transient and Steady State Response of DC Motor with One and Two Degree of Freedom Phase Lag-Lead Compensators using Frequency Response Technique

Dr. Ahmad Mohamad El-fallah Ismail

dr.ahmad_ismail_alrabty@yahoo.com

Department of Electricity and Electronics, College of Engineering, University of Gharian, Libya

ABSTRACT

This paper introduces design of different compensators and their output response for speed control of Direct Current (DC) motor with One and Two Degree of Freedom. DC motors are used in many industrial and commercial applications require higher performance, reliability, variable speed, easier controlling stability, accuracy, speed and position control of motor is required. In this paper in order to simulate the approach a MATLAB/SIMULINK model having one and two degree of freedom phase lead, phase lag and phase lead-lag compensators are constructed to control the modeled Direct Current (DC) motor for enhancement of static & dynamic response. In addition to that, the effect of adding two degree of freedom compensators on the transient and steady state response of the system is studied.

Keywords: DC Motor, Phase Lead Compensator, Phase Lag Compensator, Phase Lag-Lead, MATLAB/Simulink etc.

I. INTRODUCTION

DC motor has been popular in the industry control area for a long time because they have good characteristics that is high starting torque characteristics, high response performance and easier to be linear control. These motors are commonly used to provide rotary (or linear) motion to a variety of electromechanical devices and servo systems. DC motor has been widely used in industry even though its maintenance costs are higher than the induction motor. DC motor has good control response, wide speed control range and it is widely used in systems which need high control requirements, such as rolling mill, double-hulled tanker, high precision digital tools, etc. There are several well-known methods to control DC motors such as Compensation Technique and Controller Method. Despite a lot of researches and the huge number of different solutions proposed. The purpose of developing a control system is to enable stable and reliable control. Once the control system has been specified and the type of control has been decided, then the design and analysis are done. There are three major objectives of system analysis and design: producing the desired transient response, reducing steady-state error, and achieving stability. The

Fifth Conference on Engineering Sciences and Technology (CEST-2022) 20-22 December 2022/ Libya

Comparative Performance Analysis for Transient and Steady State Response of DC Motor with One and Two Degree of Freedom Phase Lag-Lead Compensators using Frequency Response Technique

control system has overall response that is transient response and steady state response is analyzed and to evaluate the performance of the optimal model of DC motor time response analysis and frequency response analysis are obtained [1]. The purpose of this paper is to comparative performance analysis for Transient and Steady State Response of DC Motor with One and Two Degree of Freedom Phase Lag-Lead Compensators using Frequency Response Technique (Bode Plot) for improving the transient and steady state response is presented. In addition to that, the effect of adding two degree of freedom compensators on the Transient and Steady State Response of the system is studied. In the frequency-response approach, the transient-response performance is specified in an indirect manner. The frequency domain specifications can be conveniently met in the Bode diagram approach. Therefore the open loop has been designed by the frequency-response method, the closed loop poles and zeros can be determined. The transient-response characteristics must be checked to see whether the designed system satisfies the requirements in the time domain. If it does not, then the compensator must be modified and the analysis repeated until a satisfactory result is obtained. Design in the frequency domain is simple and straightforward. The frequency-response plot indicates clearly the manner in which the system should be modified. In order to obtain the desired performance of the system, compensating networks are used. It is a fundamental building block in classical control theory. There are two general types of compensators: Lead compensators, and lag Compensators. If the two types are combined, a special lag-lead Compensator system can be gotten. Compensators influence disciplines as varied as robotics, satellite control, automobile diagnostics, and laser frequency stabilization. They are an important building block in analog control systems, and can also be used in digital control [2]. This paper is organized as follows. Mathematical Modeling of the DC Motor is given in Sec. II. Design Procedure of Compensators using Frequency Response Method (Bode Plot) is given in Sec. III. Analysis of Simulation Results is given in Sec. IV. Conclusion is demonstrated in Sec. V.

II. MATHEMATICAL MODELING OF THE DC MOTOR

The mathematical model of the DC motor is fundamental for the corresponding performance analysis and control system design.   Fig. 1 shows a DC motor [3].

Fifth Conference on Engineering Sciences and Technology (CEST-2022) 20-22 December 2022/ Libya

Comparative Performance Analysis for Transient and Steady State Response of DC Motor with One and Two Degree of Freedom Phase Lag-Lead Compensators using Frequency Response Technique
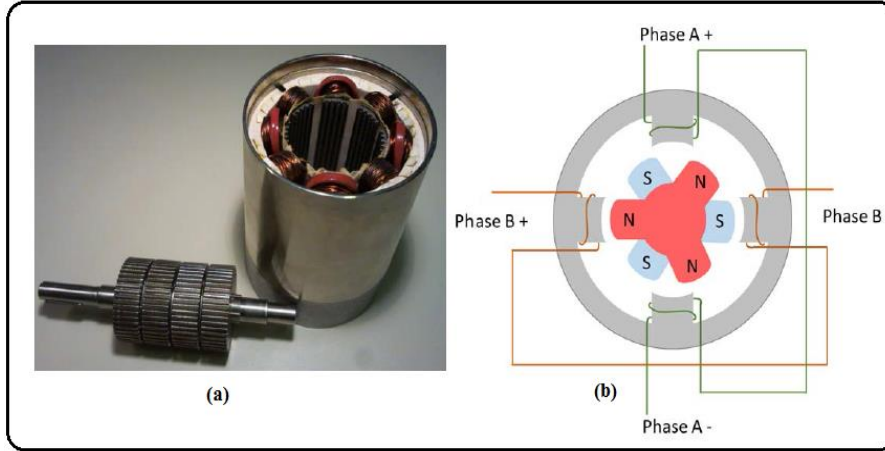
Figure 1: DC Motor (a) separated rotor and stator and (b) with three teeth [3].

The DC motor model could be divided into two sub-models, an electrical and a mechanical model. They are presented as follow:

A. The Electrical model of The DC motor

DC motor could be modeled as an RL circuit plus a back electromotive force (emf) in Fig. 2. According to [3] the differential equations of phase *a* and phase *b* are given by equation (1) and (2), respectively,

$$L_a \frac{di_{a(t)}}{dt} = -R_a i_a(t) - e_a(t) + v_a(t) \qquad (1)$$

$$L_b \frac{di_{b(t)}}{dt} = -R_b i_b(t) - e_b(t) + v_b(t) \qquad (2)$$

Where

R_a and R_b : → are the phase resistances

L_a and L_b : → are the phase inductances

i_a and i_b : → are the phase currents

v_a and v_b : → are the terminal voltages

And the back emf voltages are described by:

$$e_a(t) = -K_m \omega_m \sin(\rho \theta_m) \qquad (3)$$
$$e_b(t) = K_m \omega_m \cos(\rho \theta_m) \qquad (4)$$

Where

Km : → is the motor constant.

p : → is the number of motor pole pairs (teeth).

ω_m: →is the rotor (mechanical) angular speed [rad/s].

θ_m : → is the rotor (mechanical) angular position [rad].

In equation (1) and (2), the phase resistances and inductances are assumed to be equal, $R_a = R_b = R$ [ohm], $L_a = L_b = L$ [H]. Moreover, $v_a(t)$ and $v_b(t)$ are the terminal voltages [V], $e_a(t) = e_b(t)$ are the back emf [V].

Fifth Conference on Engineering Sciences and Technology (CEST-2022) 20-22 December 2022/ Libya

Comparative Performance Analysis for Transient and Steady State Response of DC Motor with One and Two Degree of Freedom Phase Lag-Lead Compensators using Frequency Response Technique
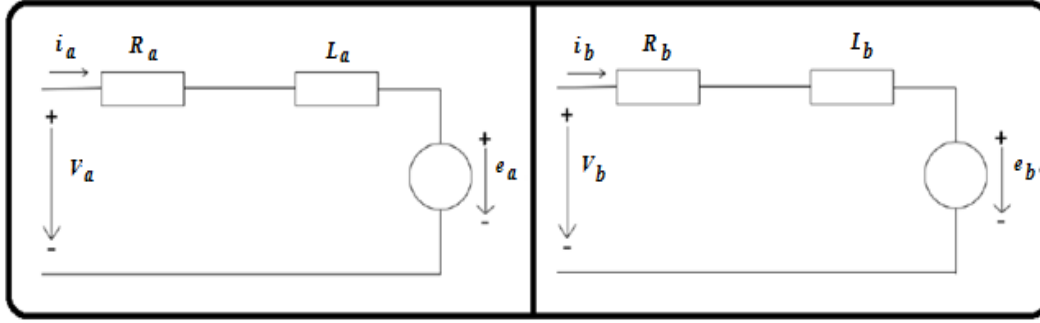
Figure 2: The equivalent circuits DC motor.

B. The Mechanical model of DC motor

The shaft of the DC motor, which represents the mechanical part of the system, is modeled as a rigid body subjected to different torques as shown in Fig. 3 [9].
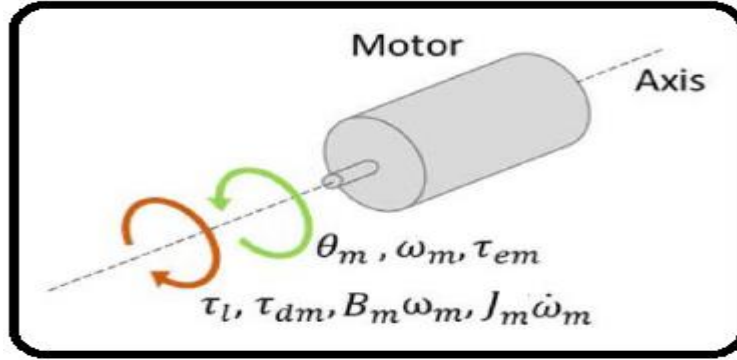
Figure 3: The mechanical sub-system of the DC motor [9].

The differential equation of the mechanical sub-system is given by equation (5),

$$J_m \frac{d\omega_m}{dt} = \tau_{em} - B_m\omega_m - \tau_{dm} - \tau_l \qquad (5)$$

And

$$\tau_{em} = K_m(-i_a \sin(\rho\theta_m) + i_b \cos(\rho\theta_m)) \qquad (6)$$
$$\tau_{dm} = T_{dm}\sin(2\rho\theta_m + \emptyset) \qquad (7)$$

Where

τ_{em} : →is the motor's electromagnetic torque or the generated torque [*N.m*]

J_m : → is the motor moment of inertia [*kg.m²*]

B_m: → is the motor viscous friction coefficient [*kg/s.m*]

T_{dm}: → is the detent torque amplitude applied [*N.m*]

$\emptyset$: → is a phase shift related to τ_{dm}

τ_l: →is the external or applied load torque [*N.m*]

With the following relation:

$$\theta_e = \rho\theta_m \qquad (8)$$

Where

θ_e: →is the electrical rotor position

III. DESIGN PROCEDURE OF COMPENSATORS USING FREQUENCY RESPONSE METHOD.

A.   Frequency Response Approach (Bode Plot)

A compensator is added to a system to improve its steady state as well as dynamic response. Nyquist plot is difficult to modify after introducing compensator. Instead, Bode plot is used since two important design criteria, phase margin and gain crossover frequency are visible from the Bode plot along with gain margin. In Bode plot, low frequency asymptote of the magnitude curve is indicative of one of the error constant *[Kp], [Kv], [Ka]* depending on the system types. In Bode Plot, specifications on the transient response can be translated into phase margin [*P.M*], gain margin[*G.M*], gain crossover frequency, bandwidth etc. Design using Bode plot is simple and straight forward and reconstruction of Bode plot is not a difficult task.

B.   Phase Lead Compensator Design using Bode Plot

The phase lead compensator is used to improve stability margin and increases system bandwidth thus improving the spread of the response [4-6]. The transfer function of the phase lead compensation network is

$$G_{Lead}(s) = K\left(\frac{1 + sT}{1 + \alpha sT}\right) = K_c \alpha \left(\frac{1 + sT}{1 + \alpha sT}\right) \quad (9)$$

Where

$\alpha : \rightarrow$ is an attenuation factor hence lead compensator is always used with an amplifier

[*1/α*], [$0 < \alpha < 1$].

$T : \rightarrow$ is the time constant, [$T > 0$].

Procedures for Design of Phase Lead Compensator using Frequency Response Techniques (Bode plot) are as follows:

1- Determine the phase lead compensator gain   [*K=K_c α*] satisfying the given error constant (according to steady state error requirement).

2- Draw the Bode plot for the uncompensated system *Gp(s)* after introducing [*K=K_c α*] in the system, which means [*KGp(s)*], and compute the gain crossover frequency [ω_g] and the phase margin [*P.M*].

 3- Determine the amount of phase lead angle to be contributed by the phase lead compensating network by using the formula

$$\phi_m = \phi_d - \phi_u - \epsilon \qquad (10)$$

Fifth Conference on Engineering Sciences and Technology (CEST-2022) 20-22 December 2022/ Libya

Comparative Performance Analysis for Transient and Steady State Response of DC Motor with One and Two Degree of Freedom Phase Lag-Lead Compensators using Frequency Response Technique

Where

Φ_m : → is the maximum phase lead angle of the phase lead compensator

Φ_d : → is the desired phase margin [phase margin specified or necessary phase margin required to be added]

Φ_u : → is the phase margin [*P.M*] of uncompensated system [*KGp(s)*]

ϵ :→ is the additional phase lead angle to compensate for shift in gain crossover frequency [ω_g] (margin of safety from 5^0 to 15^0 or (*+10% ~ 15%*)]

4-Calculate or obtain [α] from the required [Φ_m] by using the equation

$$\alpha = \frac{1 - \sin(\phi_m)}{1 + \sin(\phi_m)} \qquad (11)$$

5- From the Bode plot, determine the frequency at which the magnitude of the uncompensated system [*KGp(s)*] is [$-20 \log_{10}(1/\sqrt{\alpha})$]. This frequency is the new gain crossover frequency [$\omega_{g_{new}}$] where the maximum phase lead angle [Φ_m] should occure

$$K|G_P(j\omega_{g_{new}})| = -20 \log_{10}\left(\frac{1}{\sqrt{\alpha}}\right) \qquad (12)$$

6- Make

$$\omega_m = \omega_{g_{new}} \qquad (13)$$

7- Calculate [T] from the Relation

$$\omega_m = \frac{1}{T\sqrt{\alpha}} \qquad \Rightarrow \qquad T = \frac{1}{\omega_m\sqrt{\alpha}} \qquad (14)$$

8- Find the transfer function of phase lead compensator [$G_{lead}(s)$]

$$G_{Lead}(s) = K\left(\frac{1 + sT}{1 + \alpha sT}\right) = K_c\alpha\left(\frac{1 + sT}{1 + \alpha sT}\right) \qquad (15)$$

9- Determine the open-loop transfer function of compensated system

$$G(s) = G_{Lead}(s)G_P(s) = K_c\alpha\left(\frac{1 + sT}{1 + \alpha sT}\right)G_P(s) \qquad (16)$$

10- Draw the Bode plot of the compensated system and verify if the design satisfies the specifications. If the phase margin of the compensated system [*G(s)*] is less than the required phase margin then repeat steps[*3 to 10*] by taking [ϵ] as [5^0] more than the previous design.

C.   Phase lag compensator design using Bode Plot

The essential feature of a Phase lag compensator is to provide an increased low frequency gain, thus decreasing the steady state error, without changing the transient response significantly [7]. For frequency response design, it is convenient to use the following transfer function of the phase lag compensator

$$G_{Lag}(s) = K\left(\frac{1 + sT}{1 + s\beta T}\right) = K_c\beta\left(\frac{1 + sT}{1 + s\beta T}\right) \qquad (17)$$

Fifth Conference on Engineering Sciences and Technology (CEST-2022) 20-22 December 2022/ Libya

Comparative Performance Analysis for Transient and Steady State Response of DC Motor with One and Two Degree of Freedom Phase Lag-Lead Compensators using Frequency Response Technique

Where

T and β : → are respectively the time constant and DC gain, $[T > 0]$, $[\beta > 1]$.

Procedures for Design of Phase Lag Compensator using Frequency Response Techniques (Bode plot) are as follows:

1- Determine the phase Lag compensator gain $[K=K_c \; \alpha]$ satisfying the given error constant (according to steady state error requirement).

2- From the Bode plot, determine the phase margin of the uncompensated system

$$\phi_u = \phi_s - \epsilon \qquad (18)$$

Where

Φ_s : → Specified or desired phase margin of the uncompensated system

ϵ: → Margin of safety [In *general 5^0 to 15^0*]

Φ_u:→ The phase margin [*P.M*] of uncompensated system [*KGp(s)*]

Since the [*P.M*] is achieved only by selecting [*K_c*]. It might be deviated from this value when the other parameters are also designed. Thus a safety margin is putted.

3- Determine the frequency corresponding to the specified or required phase margin [Φ_s] plus safety margin [ϵ], which means [$\Phi_u=\Phi_{s \; +} \; \epsilon$] from the phase curve. This frequency is new gain crossover frequency [$\omega_{g_{new}}$]

$$P.M = \phi_u = 180^0 + \angle K_c G_P(j\omega_{g_{new}}) \quad (19)$$

Where

$\omega_{g_{new}}$: → New gain crossover frequency [rad/sec].

$K_c G_P(j\omega_{g_{new}})$: → The transfer function of the uncompensated system with new gain crossover frequency.

4- The magnitude curve is brought down to [*0 db*] at the new gain crossover frequency [$\omega_{g_{new}}$] where the phase margin is satisfied, the phase Lag network must provide the amount of attenuation equal to the value of magnitude curve at [$\omega_{g_{new}}$].

$$K_c|G_P(j\omega_{g_{new}})| = 1 \quad or \quad -K_c\beta|G_P(j\omega_{g_{new}})| = -20\log_{10}(\beta) \qquad (20)$$

5- Calculate or obtain [β] by using the equation

Fifth Conference on Engineering Sciences and Technology (CEST-2022) 20-22 December 2022/ Libya

Comparative Performance Analysis for Transient and Steady State Response of DC Motor with One and Two Degree of Freedom Phase Lag-Lead Compensators using Frequency Response Technique

$$K = K_c\beta \Rightarrow \beta = \frac{K}{K_c} \quad or \quad \beta = 10^{\frac{|G_P(j\omega_{gnew})|}{20}} \qquad (21)$$

6- Calculate [T] from the Relation, the only parameter left to be designed is [T]

$$\frac{1}{T} = \frac{\omega_{gnew}}{10} \Rightarrow T = \frac{10}{\omega_{gnew}} \qquad (22)$$

Usually the upper corner frequency [$1/T$] is placed at a frequency about one decade below the new gain crossover frequency [ω_{gnew}]

7- Find the transfer function of phase Lag compensator [$G_{lag}(s)$]

$$G_{Lag}(s) = K\left(\frac{1+sT}{1+s\beta T}\right) = K_c\beta\left(\frac{1+sT}{1+s\beta T}\right) \quad (23)$$

8- Determine the open-loop transfer function of compensated system

$$G(s) = G_{Lag}(s)G_P(s) = K_c\beta\left(\frac{1+sT}{1+s\beta T}\right)G_P(s) \quad (24)$$

9- Draw the Bode plot of the compensated system and investigate to see if the required phase margin is met or not, if not adjust the value of [β] and [T].

D.   Phase lag-lead compensator design using Bode Plot

Lag-Lead compensator is an electrical network which produces phase lag at one frequency region and phase lead at other frequency region. It is a combination of both the lag and the lead compensators. When a single phase Lead or phase Lag compensator cannot guarantee the specified design criteria, a phase Lag-Lead compensator is used. The speed of response and steady state error can be simultaneously improved if both phase Lead and Phase Lag compensation networks are used. Therefore, phase lag-lead compensator is employed where fast   time response as well as better steady state accuracy is desired [8-12]. The transfer function of the phase lead compensation network is

$$G_{Lag-Lead}(s) = K\left(\frac{1+sT_1}{1+s\beta T_1}\right)\left(\frac{1+sT_2}{1+\alpha sT_2}\right) \qquad (25)$$

Where

$$[\beta > 1], \quad and \quad [0 < \alpha < 1]$$

Procedures for Design of Phase Lag-Lead Compensator using Frequency Response Techniques (Bode plot) are as follows:

1- Determine the phase Lag-lead compensator gain [K] satisfying the given error constant (according to steady state error requirement).

 2- Draw the Bode plot for the uncompensated system $Gp(s)$ after introducing [K] in the system, which means [$KGp(s)$], and compute the gain crossover frequency [ω_g] and the phase margin [$P.M=\Phi_u$].

Fifth Conference on Engineering Sciences and Technology (CEST-2022) 20-22 December 2022/ Libya

Comparative Performance Analysis for Transient and Steady State Response of DC Motor with One and Two Degree of Freedom Phase Lag-Lead Compensators using Frequency Response Technique

3- Determine the amount of phase Lead angle to be contributed by the phase Lead compensating network by using the formula

$$\phi_m = \phi_d - \phi_u - \epsilon \qquad (26)$$

Where

$\Phi_m :$ → is the maximum phase lead angle of the phase lead compensator

$\Phi_d :$ → is the desired phase margin [phase margin specified or necessary phase margin

required to be added]

$\Phi_u :$ → is the phase margin [$P.M$] of uncompensated system [$KGp(s)$]

$\epsilon:$ → is the additional phase lead angle to compensate for shift in gain crossover

frequency [ω_g] (margin of safety from 5^0 to 15^0 or $(+10\% \sim 15\%)$]

4- Calculate or obtain [α] from the required [Φ_m] by using the equation

$$\alpha = \frac{1 - \sin(\phi_m)}{1 + \sin(\phi_m)} \qquad (27)$$

5- From the Bode plot, determine the frequency at which the magnitude of the uncompensated system [$KGp(s)$] is [$-20\log_{10}(1/\sqrt{\alpha})$]. This frequency is the new gain crossover frequency [$\omega_{g_{new}}$] where the maximum phase lead angle [Φ_m] should occurs

$$K|G_P(j\omega_{g_{new}})| = -20\log_{10}\left(\frac{1}{\sqrt{\alpha}}\right) \qquad (28)$$

6- Make

$$\omega_m = \omega_{g_{new}} \qquad (29)$$

7- Calculate [T_2] from the Relation

$$\omega_m = \frac{1}{T_2\sqrt{\alpha}} \quad \implies \quad T_2 = \frac{1}{\omega_m\sqrt{\alpha}} \quad (30)$$

8- Determine the parameter [β] from the relation

$$-20\log_{10}|KG_{Lag}(j\omega_{g_{new}})G_P(j\omega_{g_{new}})| = -20\log_{10}(\beta) \qquad (31)$$

9- Calculate [T_1] from the Relation

The only parameter left to be designed is [T_1]

$$\frac{1}{T_1} = \frac{\omega_{g_{new}}}{10} \implies T_1 = \frac{10}{\omega_{g_{new}}} \qquad (32)$$

[$1/T_1$] Should be placed much below the new gain crossover frequency [$\omega_{g_{new}}$] to retain the desired value [$P.M$]

10- Find the transfer function of phase Lag-lead compensator [$G_{Lag-lead}(s)$]

$$G_{Lag-Lead}(s) = K\left(\frac{1+sT_1}{1+s\beta T_1}\right)\left(\frac{1+sT_2}{1+\alpha sT_2}\right) \qquad (33)$$

11- Determine the open-loop transfer function of compensated system

$$G(s) = G_{Lag-Lead}(s)G_P(s) = K\left(\frac{1+sT_1}{1+s\beta T_1}\right)\left(\frac{1+sT_2}{1+\alpha sT_2}\right)G_P(s) \quad (34)$$

Fifth Conference on Engineering Sciences and Technology (CEST-2022) 20-22 December 2022/ Libya

Comparative Performance Analysis for Transient and Steady State Response of DC Motor with One and Two Degree of Freedom Phase Lag-Lead Compensators using Frequency Response Technique

12- Draw the Bode plot of the compensated system [*G(s)*] and verify if the specifications are satisfied or not [13].

IV. ANALYSIS OF SIMULATION RESULTS.

The modeling of the DC motor with different types of one and two degree of freedom compensators has been derived. in addition to that, simulation and performance analysis of the DC motor with and without compensators (one and two degree of freedom phase lead compensator, phase lag compensator, and phase lag-lead compensator) have been implemented and investigated by using MATLAB/SIMULINK software.

A.   Design Requirements of the control system

The goal of control engineering design is to obtain the configuration, specifications, and identification of the key parameters of a proposed system to meet an actual need. The design process is arranged into three groups [14-15]:

- Establishment of goals and variables to be controlled, and definition of specifications (metrics) against which to measure performance.
- System definition and modeling.
- Control system design and integrated system simulation and analysis.

The reference input is simulated by unit step input, then the actual output response of the DC motor should have the design requirements for the System in terms of time response specifications as shown on Table 1 and the design requirements for the System in terms of frequency response specifications as shown on Table 2.

Table 1: *Design requirements of the system in terms of the Time respons (Transient and steady state response)*

Time Domain Specifications	Design requirements of the system
Settling Time (t_s)	< 0.5 sec or < 500 ms
Maximum Overshoot (M_p)	< 5%
Peak Time (t_p)	< 0.15 sec or < 150 ms
Rise Time (t_r)	< 0.1 sec or <100 ms
Delay Time (t_d)	< 0.05 sec or <50 ms
Damping ratio (ζ)	$0.65 < \zeta < 0.75$
Steady state error (e_{ss})	< 0.02 or 2%

Table 2: *Design requirements of the system in terms of the Frequency response*

Frequency Domain Specifications	Design requirements of the system
Phase Margin (P.M)	Positive and , at least $\geq 60^{0}$
Gain Margin (G.M)	Positive and large, at least $\geq$ 10 (dB)
Bandwidth (ω_b)	Large as can possible
Resonant Peak (M_r)	Small as can possible

Fifth Conference on Engineering Sciences and Technology (CEST-2022) 20-22 December 2022/ Libya

Comparative Performance Analysis for Transient and Steady State Response of DC Motor with One and Two Degree of Freedom Phase Lag-Lead Compensators using Frequency Response Technique

	[$1 \leq M_r \leq 1.4$] or [0 dB $\leq M_r \leq 3$ dB]
Resonant Frequency (ω_r)	Large as can possible
Cut-off Frequency (ω_c)	Large as can possible
Gain crossover Frequency (ω_{gc})	It must be $\omega_{gc} < \omega_{pc}$ (Hz)
Phase crossover Frequency(ω_{pc})	It must be $\omega_{gc} < \omega_{pc}$ (Hz)

B. Simulation and analysis of the DC motor with One and Two Degree of Freedom Phase Lead Compensator using Bode plot

The block diagram of the DC motor with one degree of freedom phase Lead compensator is shown in Fig. 4.

Figure 4: The block diagram of the DC motor with One Degree of Freedom phase Lead compensator

Where

$K_t :$ ➔ is the tachometer constant
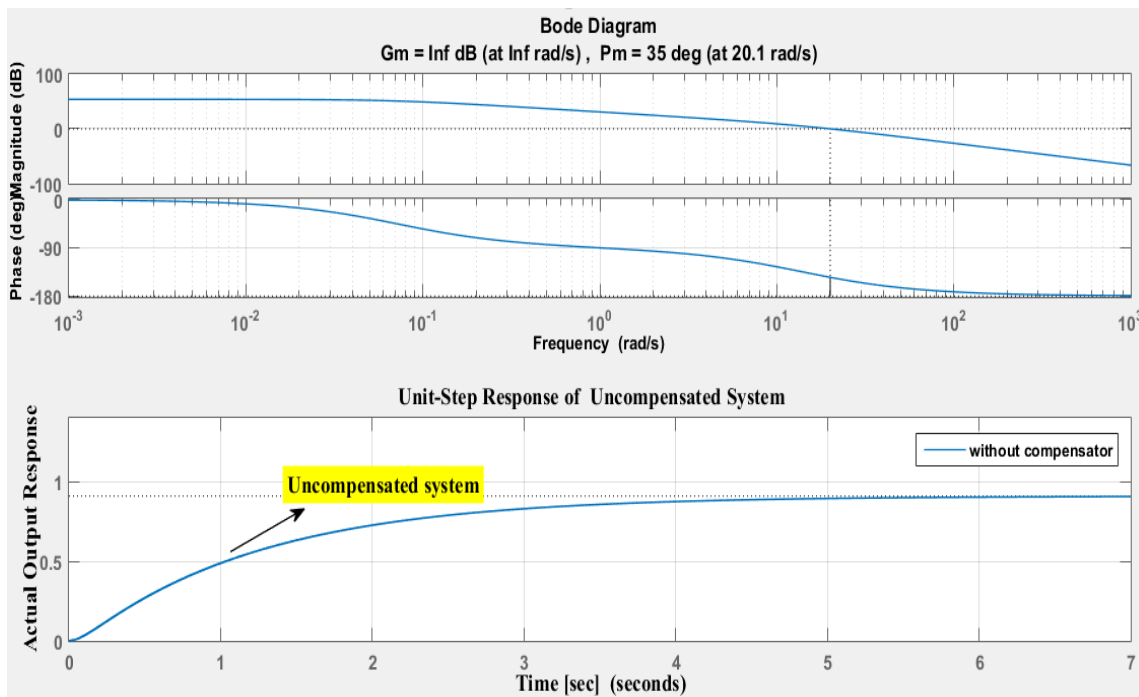
Figure 5: Simulation of the DC motor by unit step response and Bode plot

Fifth Conference on Engineering Sciences and Technology (CEST-2022) 20-22 December 2022/ Libya

Comparative Performance Analysis for Transient and Steady State Response of DC Motor with One and Two Degree of Freedom Phase Lag-Lead Compensators using Frequency Response Technique

without Phase Lead Compensator

Figure 6: Simulation of the DC motor by unit step response and Bode plot with One Degree of Freedom phase lead compensator

The block diagram of the DC motor with Two Degree of Freedom phase Lead compensator is shown in Fig. 7

Figure 7: The block diagram of the DC motor with Two Degree of Freedom phase Lead compensator

Fifth Conference on Engineering Sciences and Technology (CEST-2022) 20-22 December 2022/ Libya

Comparative Performance Analysis for Transient and Steady State Response of DC Motor with One and Two Degree of Freedom Phase Lag-Lead Compensators using Frequency Response Technique

Figure 8: Simulation of DC motor by unit step response and Bode plot with Two Degree of Freedom phase lead compensator

From the Fig. 5 , Fig. 6 and Fig. 8, it is noted that, actual output response of the DC motor with one and two degree of freedom phase lead compensator (compensated system) is better than actual output response of the DC motor without phase lead compensator (Uncompensated system), but still some of design requirements of the systems are not satisfied. Therefore, the another type of compensator is needed to get all design requirements of the system.

C. Simulation and analysis of the DC motor with One and Two Degree of Freedom Phase Lag Compensator using Bode plot

The block diagram of the DC motor with One Degree of Freedom phase Lag compensator is shown in Fig. 9.
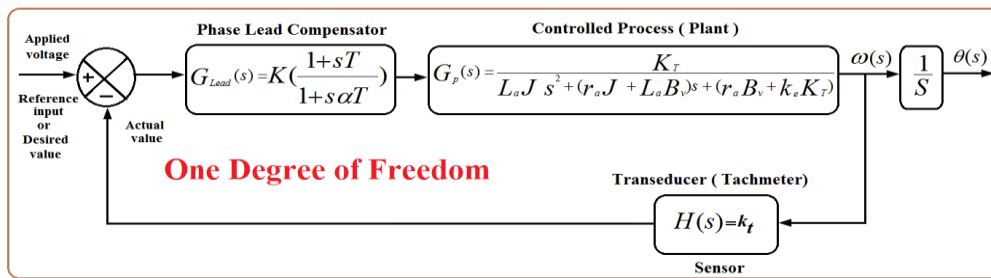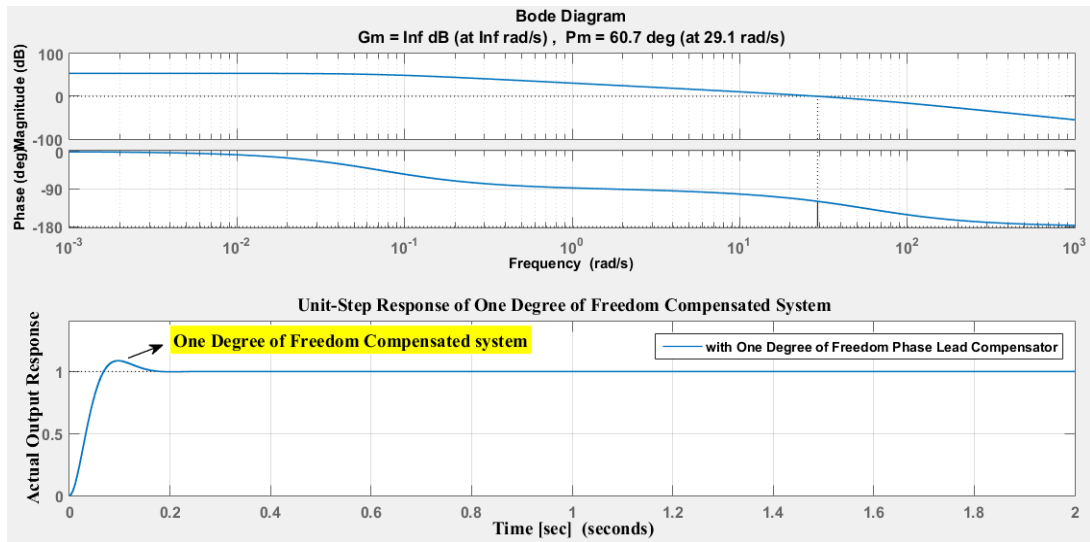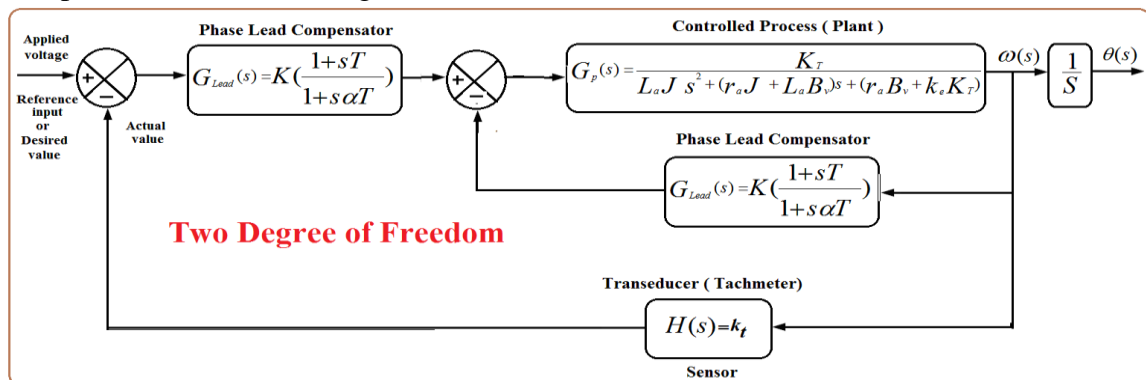

Figure 9: The block diagram of the DC motor with One Degree of Freedom phase Lag compensator

Fifth Conference on Engineering Sciences and Technology (CEST-2022) 20-22 December 2022/ Libya

Comparative Performance Analysis for Transient and Steady State Response of DC Motor with One and Two Degree of Freedom Phase Lag-Lead Compensators using Frequency Response Technique

Figure 10: Simulation of the DC motor with One Degree of Freedom phase lag compensator in addition to Bode plot

The block diagram of the DC motor with Two Degree of Freedom phase Lag compensator is shown in Fig. 11.

Figure 11: The block diagram of the DC motor with Two Degree of Freedom phase Lag compensator
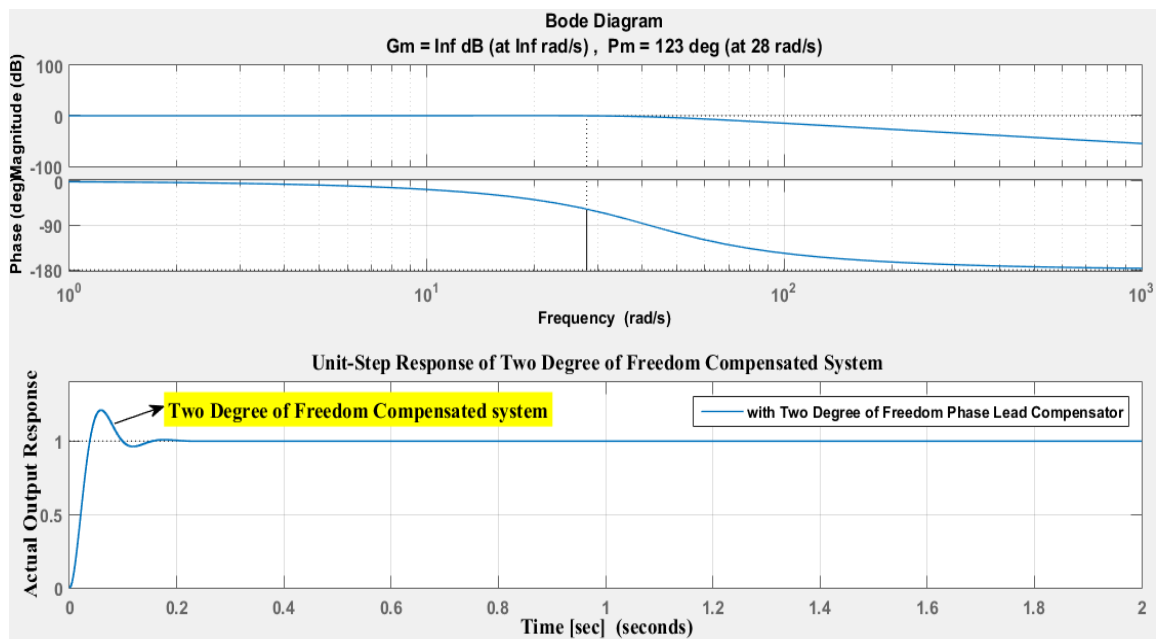
Fifth Conference on Engineering Sciences and Technology (CEST-2022) 20-22 December 2022/ Libya

Comparative Performance Analysis for Transient and Steady State Response of DC Motor with One and Two Degree of Freedom Phase Lag-Lead Compensators using Frequency Response Technique

Figure 12 Simulation of the DC motor with Two Degree of Freedom
phase lag compensator in addition to Bode plot

From the Fig. 10 and Fig. 12, it is noted that that, actual output response of the DC motor with One and Two Degree of Freedom phase lag compensator (Compensated system) is better than actual output response of the DC motor without phase lag compensator (Uncompensated system), but still some of design requirements of the systems are not satisfied and fulfilled. Therefore, the another type of compensator is needed to get all design requirements of the system.

D. Simulation and analysis of the DC motor with One and Two Degree of Freedom Phase Lag-Lead Compensator using Bode plot

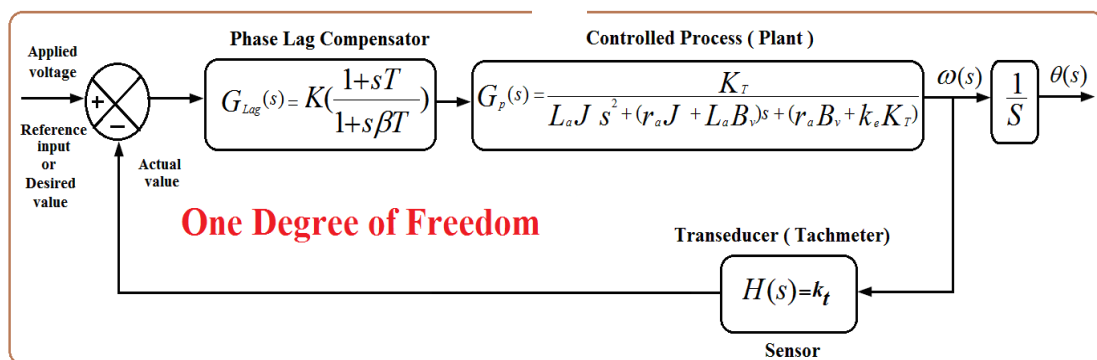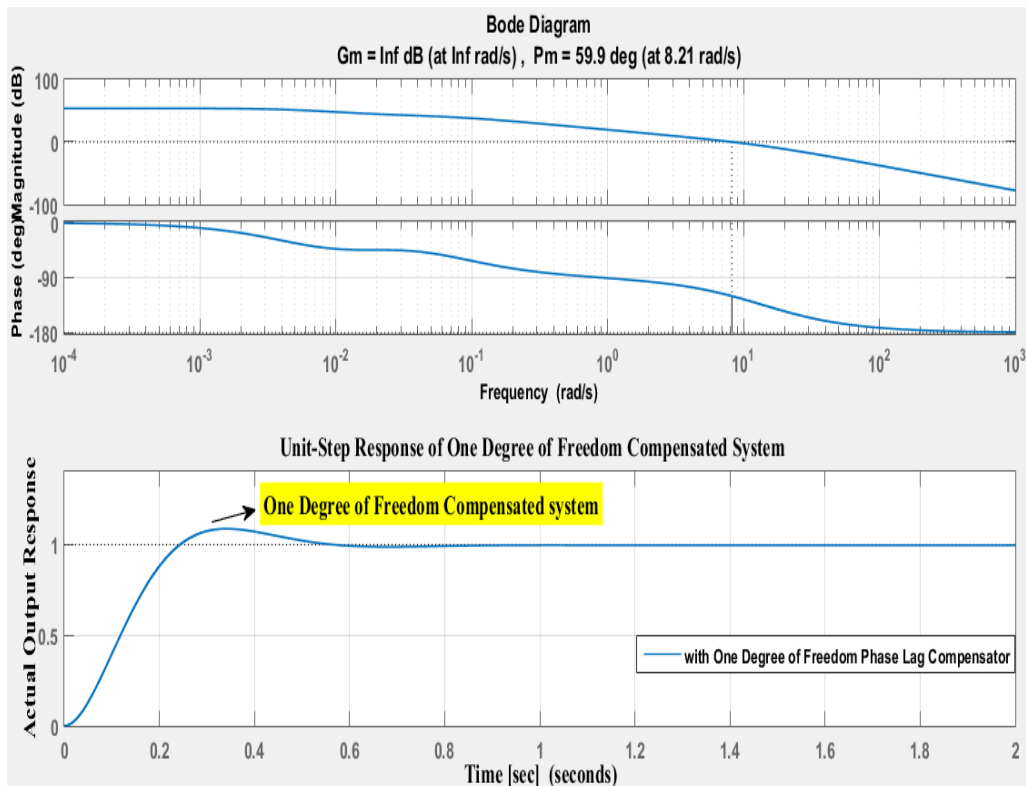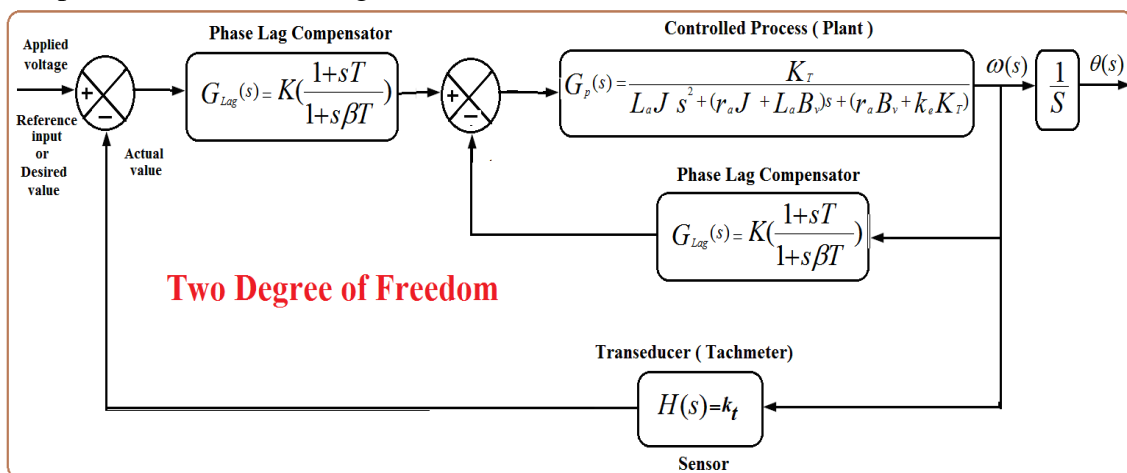The block diagram of the DC motor with one degree of freedom phase Lag-Lead compensator is shown in Fig. 13.

Figure 13: The block diagram of the DC motor with One degree of freedom phase Lag-Lead compensator

Fifth Conference on Engineering Sciences and Technology (CEST-2022) 20-22 December 2022/ Libya

Comparative Performance Analysis for Transient and Steady State Response of DC Motor with One and Two Degree of Freedom Phase Lag-Lead Compensators using Frequency Response Technique

Figure 14: Simulation of the DC motor with one degree of freedom phase Lag-Lead compensator in addition to Bode plot

The block diagram of the DC motor with two degree of freedom phase Lag-Lead compensator is shown in Fig. 15.

Figure 15: The block diagram of the DC motor with two degree of freedom phase Lag-Lead compensator

Fifth Conference on Engineering Sciences and Technology (CEST-2022) 20-22 December 2022/ Libya

Comparative Performance Analysis for Transient and Steady State Response of DC Motor with One and Two Degree of Freedom Phase Lag-Lead Compensators using Frequency Response Technique
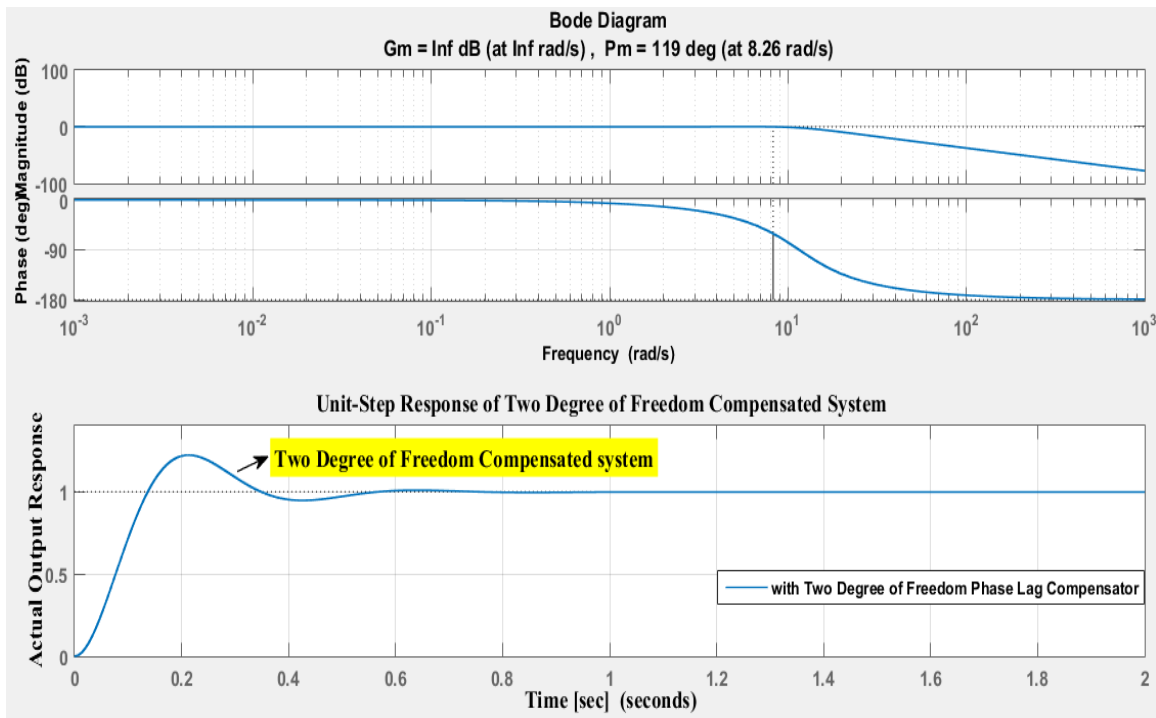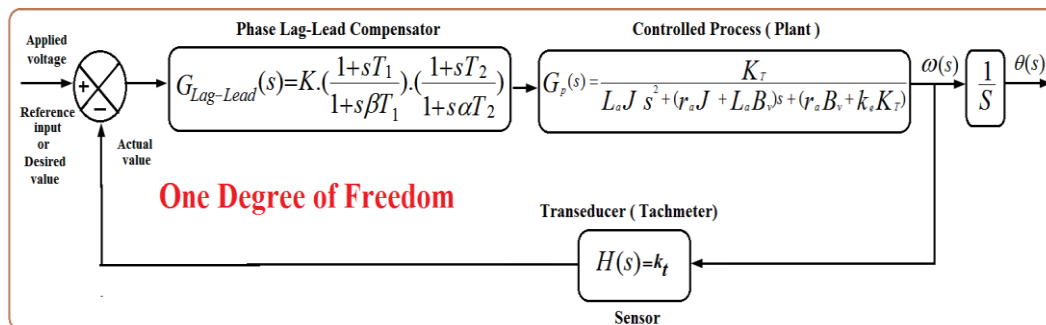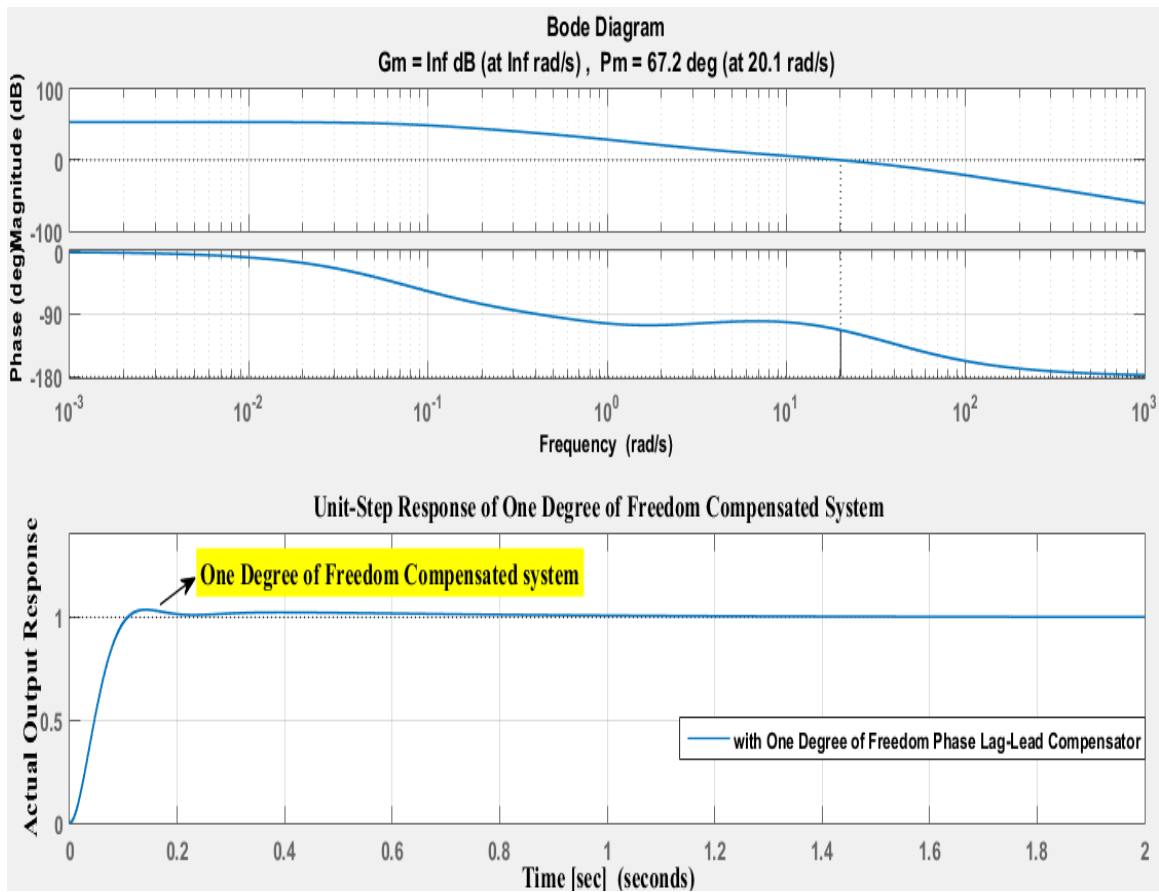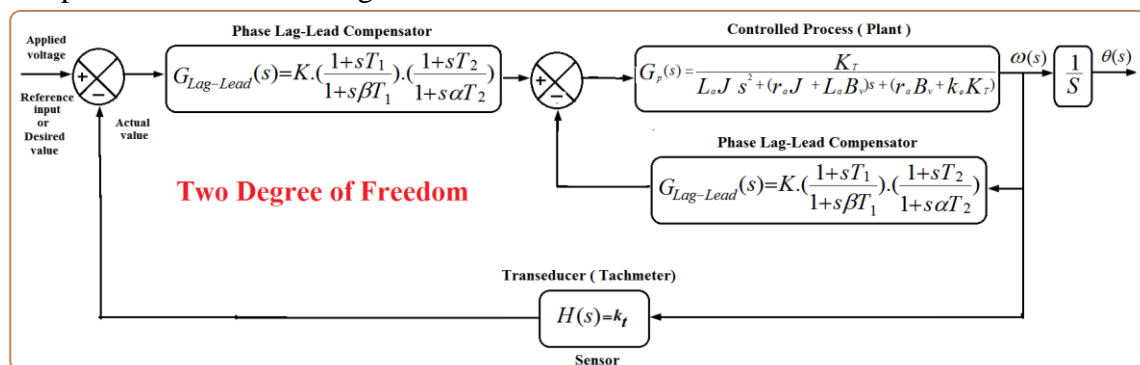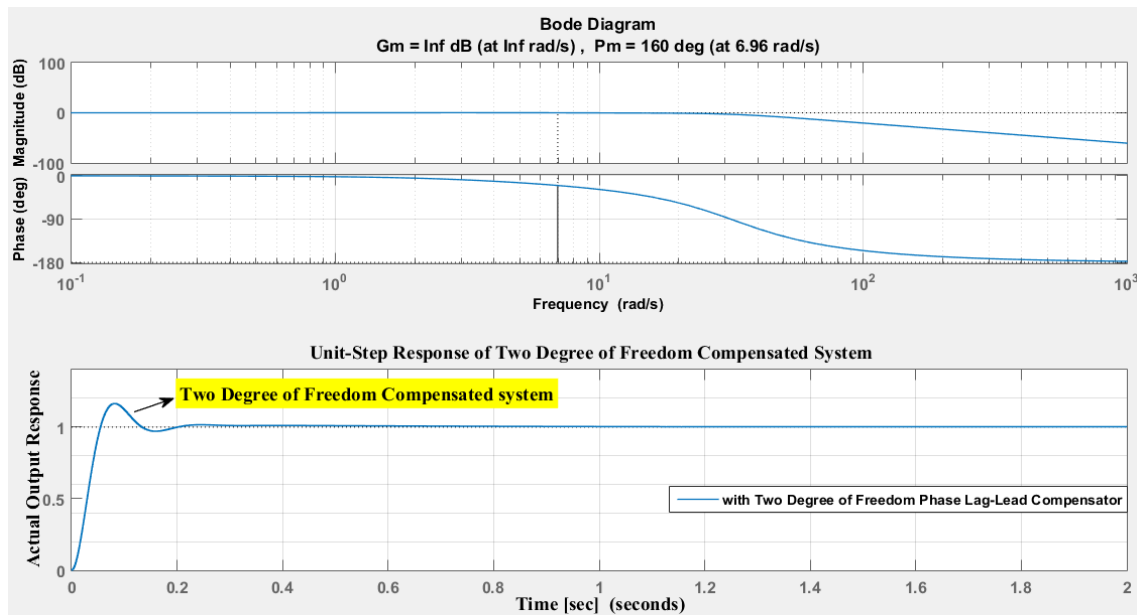
Figure 16: Simulation of the DC motor with two degree of freedom phase Lag-Lead compensator in addition to Bode plot

From the Fig. 14 and Fig. 16, it is noted that that, actual output response of the DC motor with one and two degree of freedom phase lag-lead compensator (Compensated system) is better than actual output response of the DC motor without compensator (Uncompensated system), and also all design requirements of the systems are satisfied and fulfilled) with one degree of freedom phase lag-lead compensator unlike two degree of freedom phase lag-lead compensator where some of design requirements of the systems are not satisfied and fulfilled. On the other side, two degree of freedom phase lag-lead compensator is better than one degree of freedom phase lag-lead compensator in some of design requirements of the system. but, one degree of freedom phase lag-lead compensator is chosen to drive the DC motor, because all the design requirements of the system are satisfied and fulfilled.

E.   Comparison All the simulation results with design requirements of the system

In order to verify the effect of the one and two degree of freedom phase lag-lead compensator in terms of time response specifications (Damping ratio (ξ), Settling Time (ts), Maximum Overshoot (%Mp), Steady-State Error (ess), Peak Time (tp), Delay Time(td) and Rise Time (tr)), and in terms of Frequency response specifications (Phase Margin (P.M), Gain Margin (G.M), Bandwidth (ωb), Resonant Peak (Mr), Resonant Frequency (ωr), Cut-off Frequency (ωc), Gain crossover Frequency (ωgc) and Phase crossover Frequency(ωpc)), one and two degree of freedom phase lag and phase lead compensators have been compared with one and two degree of freedom phase lag-lead compensators. In addition to that, one degree of

freedom phase lag-lead compensator is compared with two degree of freedom phase lag-lead compensator in terms of time response specifications and frequency response specifications.

Figure 17: Simulation of the DC motor with One Degree of Freedom Phase Lead, Lag and Lag-Lead compensator in addition to Bode plot

Table 3: *A comparison of the simulation results of the DC motor with One Degree Of Freedom*
phase lag, lead and lag-lead compensators in terms of time response specifications

Time Domain Specifications	Desired Results of the System	Strategy of Control		
		One Degree Of Freedom		
		Phase Lead Compensator	Phase Lag Compensator	Phase Lag-Lead Compensator
Settling Time (t_s)	< 0.5 sec	0.1564 Sec	0.5560 sec	0.545 sec
Maximum Overshoot (M_p)	< 5 %	8.4927 %	8.5210%	3.4276 %
Peak Time (t_p)	< 0.15 sec	0.097 Sec	0.3420 sec	0.141 sec
Rise Time (t_r)	< 0.1 sec	0.0456 Sec	0.1631 sec	0.0691 sec
Delay Time (t_d)	< 0.05 sec	0.0326 sec	0.118 sec	0.0462 sec
Steady state error (e_{ss})	$\leq$ 0.02	0.0020367	0.0047966	0.002
Damping ratio (ζ)	$(0.6 \leq \zeta \leq 0.8)$	0.61745	0.61693	0.73179

Fifth Conference on Engineering Sciences and Technology (CEST-2022) 20-22 December 2022/ Libya

Comparative Performance Analysis for Transient and Steady State Response of DC Motor with One and Two Degree of Freedom Phase Lag-Lead Compensators using Frequency Response Technique

Table 4: *A comparison of the simulation results of the DC motor with One Degree Of Freedom phase lag, lead and lag-lead compensators in terms of Frequency response specifications*

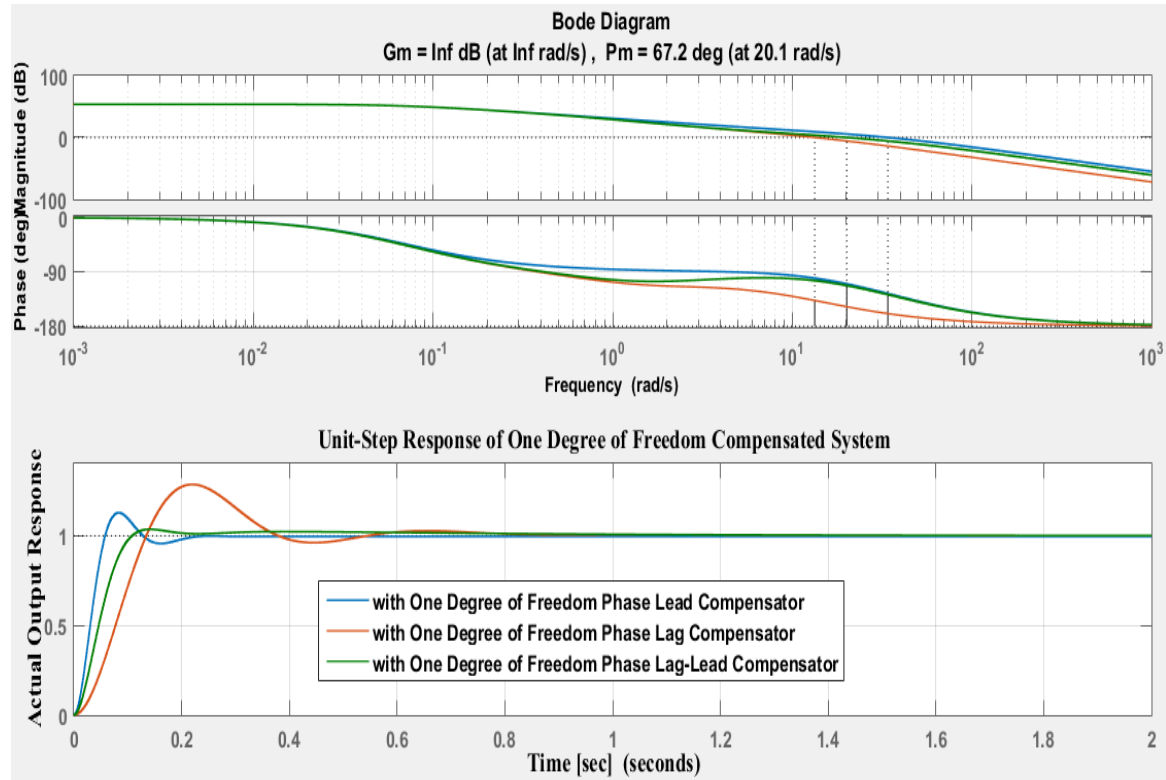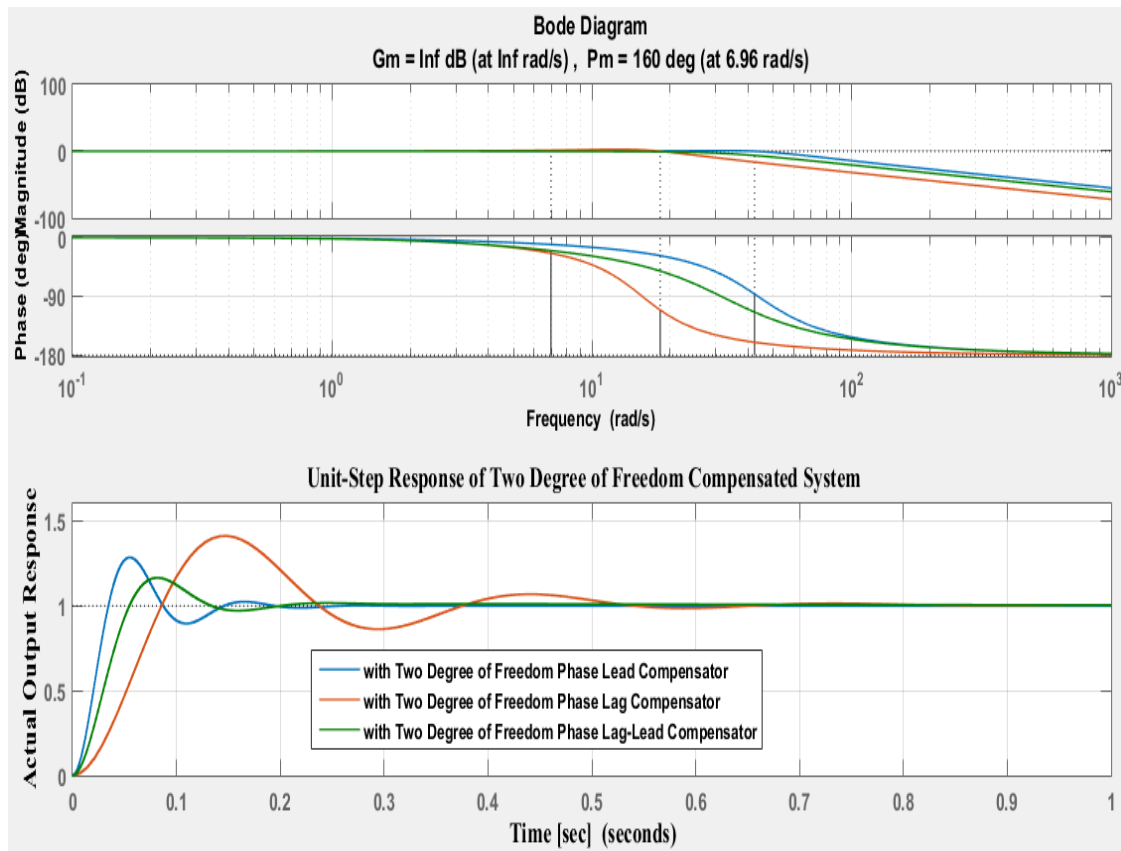| Frequency Domain Specifications	Desired Results of the System	Strategy of Control		
		One Degree Of Freedom		
		Phase Lead Compensator	Phase Lag Compensator	Phase Lag-Lead Compensator
Phase Margin (P.M)	Positive and , at least $\geq 60^0$	60.69^0	59.89^0	67.1699^0
Gain Margin (G.M)	Positive and large, at least ≥ 10 (dB)	Inf dB	Inf dB	Inf dB
Bandwidth (ω_b)	Large as can possible	46.5959 Hz	13.1257 Hz	30.9210 Hz
Resonant Peak (M_r)	Small as can possible $[1 \leq M_r \leq 1.4]$ or $[0 \text{ dB} \leq M_r \leq 3 \text{ dB}]$	1.0295	1.0298	$M_r=1$, if ($\zeta > 0.707$) ($\zeta=0.73179$)
Resonant Frequency (ω_r)	Large as can possible	20.1881 Hz	5.6985 Hz	ω_r is real only if ($\zeta < 0.707$) but ($\zeta=0.73179$)
Cut-off Frequency (ω_c)	Large as can possible	46.5959 Hz	13.1257 Hz	30.9210 Hz
Gain crossover Frequency (ω_{gc})	It must be $\omega_{gc} < \omega_{pc}$ (Hz)	29.1452 Hz	8.2090 Hz	20.1170 Hz
Phase crossover Frequency(ω_{pc})	It must be $\omega_{gc} < \omega_{pc}$ (Hz)	Inf Hz	Inf Hz	Inf Hz

Figure 18: Simulation of the DC motor with One Degree of Freedom Phase Lead, Lag and Lag-Lead compensator in addition to Bode plot

Table 5: *A comparison of the simulation results of the DC motor with Two Degree Of Freedom phase lag, lead and lag-lead compensators in terms of time response specifications*

Time Domain Specifications	Desired Results of the System	Strategy of Control		
		Two Degree Of Freedom		
		Phase Lead Compensator	Phase Lag Compensator	Phase Lag-Lead Compensator
Settling Time (t_s)	< 0.5 sec	0.1387 Sec	0.518 sec	0.178 sec
Maximum Overshoot (M_p)	< 5 %	20.9919 %	22.1626 %	16.3384 %
Peak Time (t_p)	< 0.15 sec	0.059 Sec	0.213 sec	0.082 sec
Rise Time (t_r)	< 0.1 sec	0.0258 Sec	0.0928 sec	0.0371 sec
Delay Time (t_d)	$<$ 0.05 sec	0.038608 Sec	0.13128 sec	0.15245 sec
Steady state error (e_{ss})	$\leq$ 0.02	0.0010194	0.0024012	0.0010194
Damping ratio (ζ)	$(0.6 \leq \zeta \leq 0.8)$	0.44499	0.43245	0.49956

Table 6: *A comparison of the simulation results of the DC motor with Two Degree Of Freedom phase lag, lead and lag-lead compensators in terms of Frequency response specifications*

Frequency Domain Specifications	Desired Results of the System	Strategy of Control		
		Two Degree Of Freedom		
		Phase Lead Compensator	Phase Lag Compensator	Phase Lag-Lead Compensator
Phase Margin (P.M)	Positive and , at least $\geq 60^0$	123.1635^0	119.4368^0	159.8746^0
Gain Margin (G.M)	Positive and large, at least ≥ 10 (dB)	Inf dB	Inf dB	Inf dB
Bandwidth (ω_b)	Large as can possible	45.2216 Hz	13.3348 Hz	11.2658 Hz
Resonant Peak (M_r)	Small as can possible $[\ 1 \leq M_r \leq 1.4\ ]$ or $[\ 0\ dB \leq M_r \leq 3\ dB\ ]$ $M_r=1$, if ($\zeta > 0.707$)	1.2547	1.2823	1.1554
Resonant Frequency (ω_r)	Large as can possible ω_r is real only if($\zeta < 0.707$)	26.3996 Hz	7.8512 Hz	6.2657 Hz
Cut-off Frequency (ω_c)	Large as can possible	45.2216 Hz	13.3348 Hz	11.2658 Hz
Gain crossover Frequency (ω_{gc})	It must be $\omega_{gc} < \omega_{pc}$ (Hz)	28.0024 Hz	8.2646 Hz	6.9627 Hz
Phase crossover Frequency(ω_{pc})	It must be $\omega_{pc} > \omega_{gc}$ (Hz)	Inf	Inf Hz	Inf Hz

Fifth Conference on Engineering Sciences and Technology (CEST-2022) 20-22 December 2022/ Libya

Comparative Performance Analysis for Transient and Steady State Response of DC Motor with One and Two Degree of Freedom Phase Lag-Lead Compensators using Frequency Response Technique
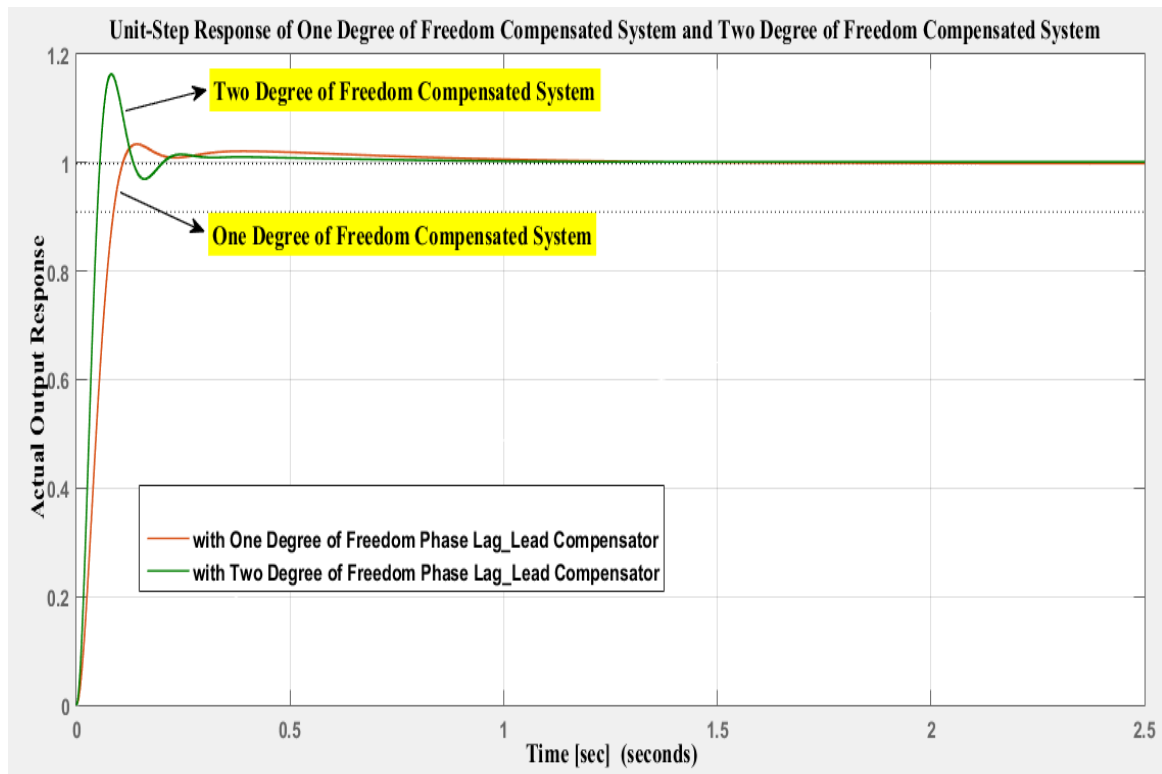
Figure 19: Simulation of the DC motor with One and Two Degree of Freedom Phase Lead, Lag and Lag-Lead compensator

Table 7: *A comparison of the simulation results of the DC motor with One and Two Degree Of Freedom phase lag, lead and lag-lead compensators in terms of time response specifications*

Time Domain Specifications	Desired Results of the System	Strategy of Control	
		One Degree Of Freedom	Two Degree Of Freedom
		Phase Lag-Lead Compensator	Phase Lag-Lead Compensator
Settling Time (t_s)	< 0.5 sec	0.545 sec	0.178 sec
Maximum Overshoot (M_p)	< 5 %	3.4276 %	16.3384 %
Peak Time (t_p)	< 0.15 sec	0.141 sec	0.082 sec
Rise Time (t_r)	< 0.1 sec	0.0691 sec	0.0371 sec
Delay Time (t_d)	< 0.05 sec	0.0462 sec	0.15245 sec
Steady state error (e_{ss})	≤ 0.02	0.002	0.0010194
Damping ratio (ζ)	(0. 6≤ ζ ≤ 0.8)	0.73179	0.49956

The main objective of controllers is to minimize the error signal or in other words the minimization of performance criteria (Integral Absolute Error (IAE), Integral Time Absolute Error (ITAE), Integral Square Error (ISE), Integral Time-

weighted Squared Error (ITSE)). A set of performance indicators may be used as a design tool aimed to evaluate tuning methods results. The simulation   results are shown on Table (8).

Table 8: *Comparison for all performance indices parameters of the DC motor with One and Two Degree of Freedom Phase Lag-Lead Compensator*

Strategy of Control	Performance Criteria			
	IAE $IAE=\int\limits_{0}^{t}\lvert e(t)\rvert\ dt$	ITAE $ITAE=\int\limits_{0}^{t}t\lvert e(t)\rvert\ dt$	ISE $ISE=\int\limits_{0}^{t}(e(t))^2 dt$	ITSE $ITSE=\int\limits_{0}^{t}t\bigl(e(t)\bigr)^2 dt$
One Degree of Freedom Phase Lag-Lead Compensator	0.0239828778	0.0599571945	0.0001150357	0.0002875892
Two Degree of Freedom Phase Lag-Lead Compensator	0.00509684	0.0127420999	0.0000051956	0.0000129889

V. Conclusion

The actual output response of the DC motor is controlled by means of the three different compensators: One and Two Degree of Freedom Phase lead compensator, phase lag compensator and phase lag-lead compensator for enhancement the stability and accuracy. In addition to that, the effect of adding two degree of freedom compensators on the transient and steady state response of the system is studied. In this paper, with reference to the results of the computer simulation by using (MATLAB & SIMULINK) software, the performance characteristics of One and Two Degree of Freedom Phase lead compensator, phase lag compensator and phase lag-lead compensator are compared in terms of the time response (transient and steady state response) specifications: Delay Time (td), Rise Time (tr), Peak Time (tp), Maximum Overshoot (Mp), Settling Time (ts) and Steady state error (ess), and in terms of the frequency response specifications : Phase Margin (P.M), Gain Margin (G.M), Bandwidth (ωb), Resonant Peak (Mr), Resonant Frequency (ωr), Cut-off Frequency (ωc), Gain crossover Frequency (ωgc) and Phase crossover Frequency (ωpc). The simulation results illustrate that one degree of freedom phase lag-lead compensator performs better than other one degree of freedom compensators proposed in this paper and has verified all design requirements of the system. In addition to that, one degree of freedom phase lag-lead compensator

performs better than two degree of freedom phase lag-lead compensator in some design requirements of the system where two degree of freedom phase lag-lead compensator performs better than one degree of freedom phase lag-lead compensator in some design requirements of the system, but one degree of freedom phase lag-lead compensator is chosen to drive the DC motor, because all the design requirements of the system are satisfied and fulfilled unlike two degree of freedom phase lag-lead compensator where   some design requirements of the system are not satisfied and fulfilled.

REFERENCES

[1] Someshwar Dutt Pathak and V.K. Tripathi "A Comparative Study of DC Motor for Optimal Performance Using LAG Compensator and PID Controller Implemented by MATLAB" International Journal of Advanced Research in Computer and Communication Engineering Vol. 5, Issue 5, May 2016. DOI 10.17148/IJARCCE.2016.5566.

 [2] Abhilash D. Karmankar1, Poonam R. Hatti2, Yogita R. Ashtekar3, Dinesh L. Mute4 "Design of Compensators for Speed Control of DC Motor by using Bode Plot Techniques" International Research Journal of Engineering and Technology (IRJET), E-ISSN: 2395 -0056 , Volume: 03 Issue: 01 | Jan-2016.

[3] Ruilope R. P., "Modelling and Control of Stepper Motors For High Accuracy Positioning System Used in Radioactive Environments", Thesis, Politechnical University of Madrid, 2014.

[4]- Lakshmi C. R. , Supriya Shigwan, Ronita Pawn and Shruti Gite. "Design of Compensators for Speed Control of DC Motor Using Frequency- Response Techniques" . International Journal of Electrical Electronics & Computer Science Engineering Volume 5, Issue 5 (October, 2018). E-ISSN : 2348-2273. P-ISSN : 2454-1222.

[5] Jayasuriya, S."Frequency Domain Design for Robust Performance Under Parametric, Unstructured, or Maxed Uncertainties," ASMEJ. Dynamic System, Measurement, and Control,115 (1993), pp.439-51.

[6]   Xu JianXin, "New Lead Compensator Designs for Control Education and Engineering", Proceedings of the 27th Chinese Control Conference, July 16-18, 2008.

Fifth Conference on Engineering Sciences and Technology (CEST-2022) 20-22 December 2022/ Libya

Comparative Performance Analysis for Transient and Steady State Response of DC Motor with One and Two Degree of Freedom Phase Lag-Lead Compensators using Frequency Response Technique

[7] Abhilash D. Karmankar, Poonam R. Hatti, Yogita R. Ashtekar and Dinesh L. Mute" Design of Compensators for Speed Control of DC Motor by using Bode Plot Techniques" International Research Journal of Engineering and Technology (IRJET), Volume: 03 Issue: 01 | Jan-2016. e-ISSN: 2395 -0056, p-ISSN: 2395-0072.

[8] Huey Yang Horng, "Lead-Lag Compensator Design Based on Genetic Algorithms", IEEE 2012 Conference on Technologies and applications of Artificial Intelligence.

[9] J. Nancy Namratha and K. Bhaskara Rao, "Lag-Lead Compensator Design for Higher Order Discrete systems using Model Formulation Employing ABC Algorithm", Proceedings of 7th International Conference on Intelligent Systems and Control (ISCO-2013).

[10] Evans, W.R, "The Use Of Zero And Pole For Frequency Response Or Transient Response", ASMF. Trans, 76(1954), pp 1135- 44.

[11] Ogata. K, "Designing Linear Control Systemwith MATLAB". Upper Saddle River, NJ: Prentice Hall, 1994.

[12] D. Antunes, W. Geelen, and W. Heemels, "Frequency-domain analysis of real-time and networked control systems with stochastic delays and drops," in European Control Conference (ECC), July 2015, pp. 934–940.

[13] Ali Ashor Moftah Billhag Ismail, and Ahmad Mohamad El-fallah , "Designing a Phase Lead, Phase Lag and Phase Lag-Lead Compensators using Frequency Response Technique for Performance Evaluation of the Hybrid Stepper Motor" http://www.libyanuniv.edu.ly/, 2021/10.

[14] B. Kuo, Automatic Control Systems, Prentice-Hall, Englewood, Cliffs. NJ, 1995.

[15] N. S. Nise, Control Systems Engineering (3rd Edition), John Wiley and Sons Inc., New York, 2000.

Cough Sound Based COVID-19 Detection System Using Machine Learning Algorithms

Basmah A. Abdulhamid[1]*, Khamis F. Alarabi Aljribi[2]

[1]babd.almrimi@gmail.com , [2]kf.aljribi@bwu.edu.ly
[1]Computer deprtment, Faculty of Electronic Technology, Baniwalid, Libya
[2]Computer deprtment, Baniwalid University, Baniwalid, Libya
*Corresponding author email: babd.almrimi@gmail.com

Abstract

Due to the nature of the COVID-19 pandemic, the need for early detection is essential for a rapid recovery and limiting the spread of the virus. Ordinary and traditional methods of diagnosing COVID-19 depend on contact which is susceptible to transmission of the virus, as any misuse of traditional methods can lead to the spreading of the epidemic, increasing its severity and may lead to death. However, since the better methods and techniques are always required for diagnosis, this study is aimed at presenting a contactless approach to distinguish COVID-19 infection from other similar symptoms infections based on the cough sound. COVID-19 detection system has been implemented by using machine learning techniques; the Mel Frequency Cepstral Coefficients (MFCC) algorithm for extracting features from audio signals and Multilayer Perceptron Neural Network (MLP) for classification. The system has been implemented by using a sample of data downloaded from online provided COUGHVID dataset. The model has considerably shown a high performance as it achieved 96%, 92%, and 100% for average accuracy, sensitivity and specificity respectively.

Keywords— COVID-19, Cough Sound, MFCC, MLP, speech recognition

I. INTRODUCTION

At the end of 2019, a new virus emerged in China, spread rapidly and affected the whole world. The virus has caused a huge crisis worldwide as it leads to severe infections and eventually death in humans. Three months later, the World Health Organization (WHO) has announced that the virus outbreak has occurred[1]. The disease which is commonly known as covid-19 has converted into a global pandemic affecting all people's lifestyles. The disease is highly contagious, so it spreads rapidly. Since the time when the covid-19 epidemic has begun, health care teams around the world have been working to follow up on it in terms of diagnosis and knowledge to suggest appropriate solutions[2]. In addition to the fact that most researchers and interested people set out in their scientific career through programs and studies, the aim of which is to discover the disease in early time. Therefore, this topic has been interested for researcher and study based on the need of understanding the covid-19 problem for finding appropriate solutions as soon as possible. It is worth mentioning that, although the pandemic level has notably decreased in the

beginning of the current year 2022, the international website "worldmeter.com" indicates that the daily new infected cases are still considerably high [3] as depicted by Fig. **1**.
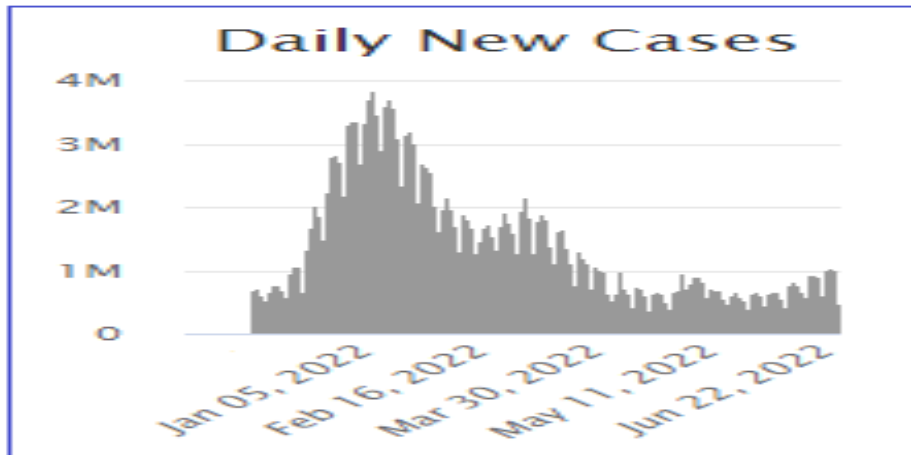

Fig. 1: Daily new cases of COVID-19 in the world in 2022.

However, fever, cough and feeling tired are the most common symptoms of covid-19, in addition to shortness of breath, headache, and loss of sense of smell and taste, as these symptoms appear after a period ranging from two to fourteen days of infection with the virus[4]. Cough is one of the early recognizable symptoms of covid-19[5]. In fact, coughing is a sound, so it can be represented as a sound signal and thus can be investigated to help detecting the virus[4]. This study proposes an approach for detecting covid-19 based on cough sound analysis. That is, the system is designed to distinguish the cough of infected patients by covid-19 from the cough of those who are not infected with the virus.

The techniques of audio signal processing and machine learning algorithms are commonly used within the systems of voice recognition, speech synthesis, and speech/speaker recognition[4]. Therefore, they have been suggested to be applied on the cough sound signals for the purpose of infected patient detection. Generally, Speech recognition system consists of three stages; preprocessing, feature extraction, and classification as depicted in Fig. **2**.
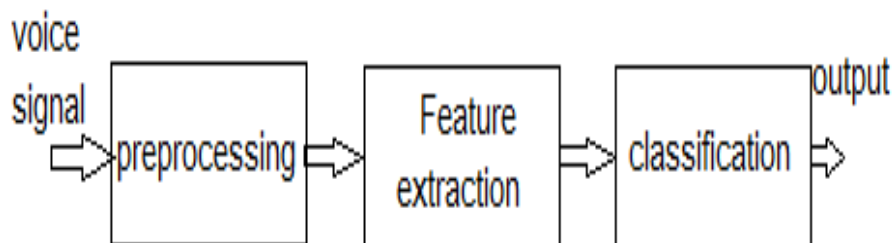

Fig. 2: General Speech recognition system

In voice and speech recognition systems, The Mel Frequency Cepstral Coefficients (MFCC) algorithm has shown a high performance for extracting features from sound signals[6], while Multi-Layer Perceptron (MLP) Neural Networks have been found as an effective method for classification[7]. Therefore, MFCC and MLP algorithms have been suggested to be used in this work for feature extraction and classification respectively.

II. RELATED WORK

The spread of covid-19 as an epidemic around the world pushes the researchers to show their interests and studies by discovering the disease at an early stage, and then they made their efforts to suggest advanced methods and techniques for discovering and diagnosing covid-19 based on the sound of coughing as it is one of the Early recognizable symptoms of covid-19. This section presents the relevant work that has been done for covid-19 detection based on cough sound.

In March 2021 K. Kumar et.al. in [8] reviewed the literature on COVID-19 diagnosis from respiratory sound data. They focused in their study mainly on how SARS-CoV-2 is spread and in-depth analysis of the diagnosis of COVID-19 from human respiratory sounds such as coughing, vocalization and breathing by analyzing respiratory sound parameters.

Paper [9] presented a study on COVID-19 Cough Analysis Using Automatic Speech Recognition System, in which they discussed cough changes in infected people based on a hidden Markov model (HMM) classification and analysis Speech recognition based on the formulation of cough sounds by exploiting spectrum technology. They have implemented an HMM-based cough recognition system with 5 HMM states, 8 Gaussian mixture distributions (GMMs) and 13 dimensions of Cepstral Fundamental Frequency Mel coefficients (MFCC) with 39 dimensions of the total feature vector. The overall accuracy of the cough recognition system was 93.33% for healthy coughs and 86.66% for COVID-19 cough sounds.

Tena et al. in [10] conducted a study for automated detection of COVID‑19 based on cough sounds. The have proposed an automated system for extracting features from time-frequency domain by using machine learning algorithms where they have used autoencoder and recursive features elimination (RFE) for features extraction and selection while they have used support vector machine (SVM) for classification. They have reported that their proposed model achieves a high performance with an average accuracy of 90%.

The paper [11] presented a study on identifying COVID-19 by using spectral analysis of cough recordings based on machine learning algorithms. They have used dataset of 16 individuals with suspected MERS-CoV infection with a particular patient demographic. In study, cough of patients infected by

COVID-19 could be distinguished from other coughs by applying effective feature extraction and classification techniques. The power spectrum density (PSD) was selected based on the Short Time Fourier transform (STFT) and Mel Frequency Cepstral coefficients (MFCC) as an effective feature extraction method and Support Vector Machine (SVM) algorithm for classification with accuracy of 95.86 and sensitivity of 91.7%.

Muzhir Shaban Al-Ani et al. in [4] presented a study on how to diagnose corona virus through patients' coughs. Accordingly, real samples were taken from people infected with the Corona virus and others who suffer from some respiratory diseases. The discrete wavelet transform is the adopted method to realize the detection process by approximation and analysis of the details of the coefficients. The obtained results show the acceptable detection accuracy of the studied samples.

In [2] researchers presented a study on detecting COVID-19 from non-COVID-19 patients by classifying just only a single cough sound. The study was able to distinguish the COVID-19 patients from the common cold or influenza patients by analyzing the sound of coughing via smart phones. A total of 328 cough sounds of four different types including COVID-19, asthma, bronchitis and healthy subjects were recorded from 150 people. The authors have used the MFCCs method for feature extraction stage and they have got average accuracy of 92.85%

III. COVID-19 DTECTION SYSTEM

This section describes an approach by using machine learning algorithms for designing a COVID-19 detection system based on patient coughing sound. The system has been adopted from speech recognition system[12] which illustrated by Fig. **2**. Patient cough is a sound signal that can be digitally acquired and recorded and generally it has the same characteristics of speech signal such as frequency and amplitude ranges [13]. Therefore, coughing signal features can be extracted with the same speech features extraction algorithms and then can be classified by common classifiers of speech.

A. Data set

Coughing sound data have been downloaded from publicly-available dataset called COUGHVID which has been collected by VIRUFY, the international non-profit organization and has been supported by several universities. The dataset were mainly collected for the purpose of building an international dataset of coughing sounds that can be used for detecting patterns of respiratory diseases, especially COVID-19. COUGHVID data is very accurate as it has been collected at a hospital and controlled by physicians. Data has also been labeled as positive COVID-19, negative COVID-19, along with other clinical information and metadata [14]. 4238 instances of the coughing sound data have

been collected from 152 participants to be used in research. Among them, there are 80 participants were diagnosed with positive COVID-19. Data were divided into four participant groups; 65 positive COVID-19 for training, 15 positive for testing, 57 negative for training, and 15 negative for testing.

B. Data preprocessing

Coughing is a sound, so it can be recorded and represented as a sound signal and it is usually recorded in digital forms contaminated with environmental noises. Therefore, to obtain a noise-free signal, a filter is utilized for selecting only the desired frequencies and for removing noise frequencies and recordings that do not contain a cough signal, i.e. silent segments as depicted by Fig. 3 . Another issue worth mention is that data have been originally recorded at frequency sample 48000Hz and have been downsampled to 4.8 KHz.
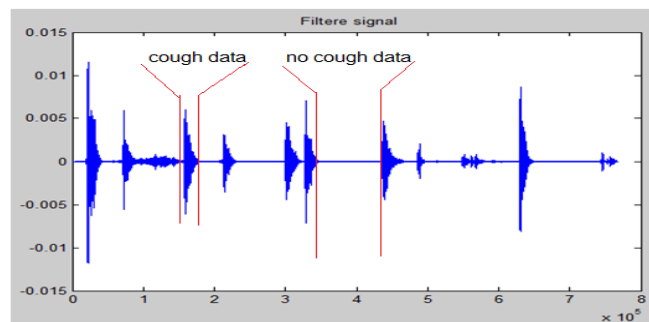

Fig. 3: cough signal including silent periods

C. Feature extraction

The second stage of recognition system is the feature extraction. There are several algorithms have been used for extracting features from signals. Mel Frequency Cepstral Coefficients (MFCC) in particular is frequently used with sound and voice signals. Therefore it has been suggested to be used in this work as it has shown high potential for extracting features from sound or voice signals. MFCC has been designed to perform the following steps as illustrated by Fig. **4**.

1- Frame blocking and windowing: coughing signal is a quasi-stationary signal. For best performance, cough signals have been analyzed in short time segments. 20 ms overlapped Hamming window technique has been applied for signal segmentation and thereby each segment has been analyzed as a stationary signal.

2- Fast Fourier transform: Discrete Fourier Transform (DFT) has been applied on each framing window to transform it from time domain into frequency domain in form of magnitude spectrum.

3- Mel-spectrum: The transformed signal for each segment is filtered by band-pass mel-frequency bank filter for computing the Mel-Spectrum. The mel scale utilizes the characteristics of human ears where it

follows the linear frequency spacing below 1 kHz, and a logarithmic spacing above that[7].

4- Discrete Cosine Transform (DCT): DCT is applied to the transformed mel-frequency coefficients after representing it on a log scale to produce a set of cepstral coefficients. The system can be affective by extracting only the lower coefficients. Commonly, MFCC uses 13 cepstral coefficients but the zeroth coefficient is usually ignored
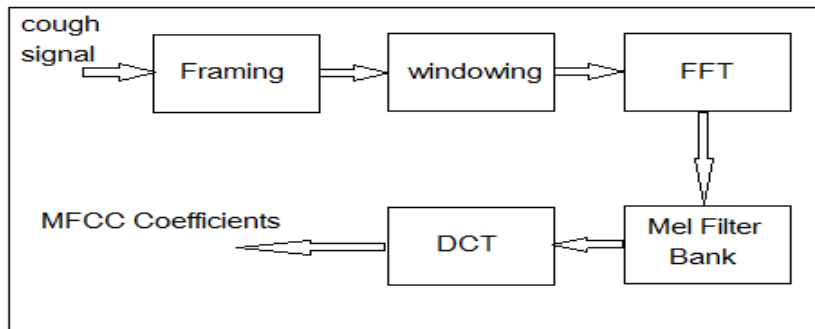

Fig. 4: Mel Frequency Cepstral Coefficients components.

D. Coughing signal classification

Machine learning algorithms are frequently used for classifying voice and speech signals. Thus, a type of Artificial Neural Network; the Multi-Layer Perceptron (MLP) has been suggested to be used for classifying the patients cough sound in the proposed COVID-19 detection system. The used MLP classifier has a 12-neuron input layer, 20-neuron hidden layer, and one single-neuron output layer. It designed with 'tan-sigmoid' and 'purelin' activation functions for hidden and output layers respectively. The best training performance of MPL was 0.023 at epoch 9993. The results of the experiment are presented and discussed in details in the next section.

IV. RESULTS AND DISCUSSION

The output of the MLP classifier is a value ranged from -1 to +1 where the negative value indicates the negative infection of COVID-19 while the positive value indicates the positive infection of the virus. As a classifier, MLP has been given a set of instances from 122 patients for training and a set of instances from other 30 patients for testing. The 80 subjects who were diagnosed positively with COVID-19 infection have been divided into two groups; 65 for the training group and 15 of the test group. In the same manner, the rest subjects who were diagnosed negatively with COVID-19 have been divided into 57 for training group and 15 of the test group as presented by Table 1.

TABLE 1: DATA SAMPLE OF TRAINING AND TEST

Sample	Negative	Positive
Training (122)	1701 instances from 57 subjects	1560 instances from 65 subjects
Test (30)	390 instances from 15 subjects	587 instances from 15 subjects
Total (152)	2091 instances	2142 instances

System performance can be measured by the ability of classifying each instance whether it is correctly or wrongly classified. *Figure 5* presents the results of classifying the positive status of 2 subjects from the same pool of data that were used in the training phase.
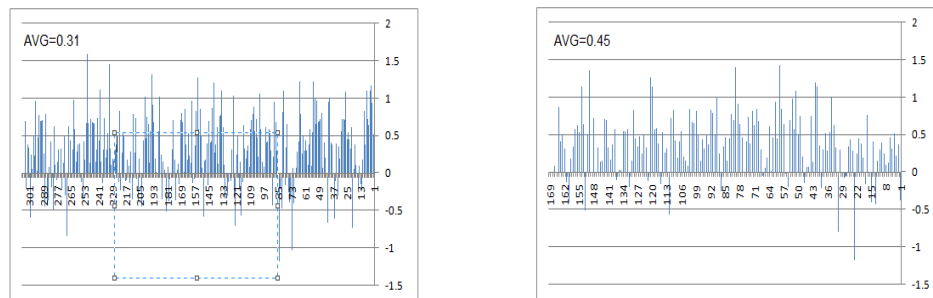

Figure 5: Classification result of positively infected subjects; S1 at left and S2 at right

Figure 6 presents the results of classifying the negative status of 2 subjects from the same pool of data that were used in the training phase.
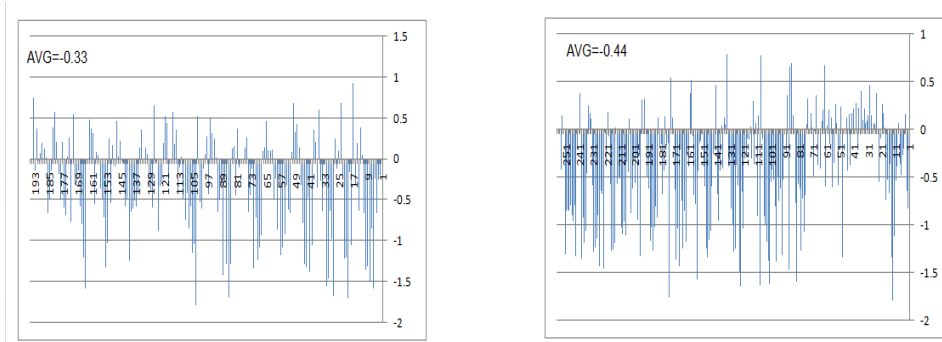
Figure 6: Classification result of negatively infected subjects; S1 at left and S2 at right

The final result of the subject classification can be calculated by taking the average of all instances for that subject. As it can be seen from the Figure 5, S1and S2 have been classified as positively infected with averages of +0.31 and +0.45 respectively, while it can be seen from Figure 6 that S1 and S2 from uninfected group have been classified as negatively infected with averages of -0.33 and -0.44 respectively.

The system performance is actually depends on the ability of the system on classifying data from outside training pool, which known as validation data. 977 instances from 15 infected and 15 uninfected subjects have been used for validation test. Figure 7 presents the classification results of 2 uninfected subjects while Figure 8 represents the classification results of 2 infected subjects.
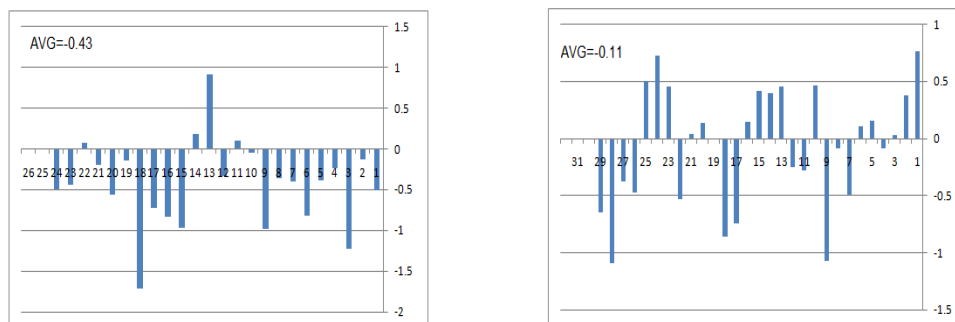

Figure 7: Classification result of negatively infected subjects; #S60 at left and #S61 at right
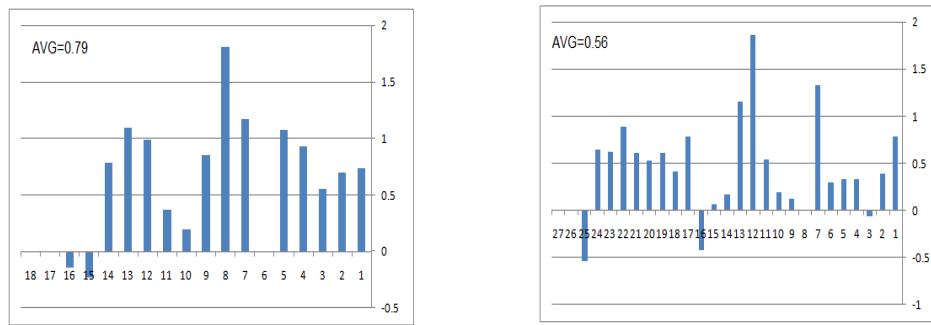
Figure 8: Classification result of positively infected subjects; #S70 at left and #S71 at right

Classification results of all 30 subjects of validation data are represented by Table 2: **Classification results of all 30 subjects of validation data with their averages (Avg.)** . The system was able to correctly classify positively infected data with accuracy of 100%, while it was able to correctly classify negatively infected data with accuracy of 93%.

Table 2: Classification results of all 30 subjects of validation data with their averages (Avg.)

S.#	Status	Predicted	Avg.	Subject number	status	predicted	Avg.
S66	POS	POS	0.20	S58	NEG	NEG	-0.04
S67	POS	POS	0.54	S59	NEG	POS	0.31
S68	POS	POS	0.22	S60	NEG	NEG	-0.43
S69	POS	POS	0.35	S61	NEG	NEG	-0.11
S70	POS	POS	0.79	S62	NEG	NEG	-0.19
S71	POS	POS	0.56	S63	NEG	NEG	-0.02
S72	POS	POS	0.43	S64	NEG	NEG	-0.01
S73	POS	POS	0.57	S65	NEG	NEG	-0.12
S74	POS	POS	1.02	S66	NEG	NEG	-0.39
S75	POS	POS	0.45	S67	NEG	NEG	-0.13
S76	POS	POS	0.54	S68	NEG	NEG	-0.22
S77	POS	POS	0.45	S69	NEG	NEG	-0.03
S78	POS	POS	0.66	S70	NEG	NEG	-0.12
S79	POS	POS	0.50	S71	NEG	NEG	-0.19
S80	POS	POS	0.40	S72	NEG	NEG	-0.13

The evaluation of the system performance can be carried out through the following parameters:

The accuracy: the Ratio of the correctly classified samples to the total number of samples and it can be calculated from the equation 1.

$$Accuracy = \frac{TP + TN}{TP + TN + FP + FN} \qquad (1)$$

Sensitivity: the system ability to correctly classify the positively infected cough signal as positive from the total positive samples and it can be calculated from the equation 2.

$$Sensitifity = \frac{TP}{TP + FN} \qquad (2)$$

Specificity: is the proportion of correctly classified negatively infected samples in relation to the total number of negatives and it can be calculated from the equation 3.

$$Specificity = \frac{TN}{TN + FP} \qquad (3)$$

where P= Positive, N = Negative, TP = True Positive, FP =False Positive, TN = True Negative, and FN = False Negative. The accuracy, sensitivity, and specificity are illustrated by Table 3.

TABLE 3: THE SYSTEM ACCURACY, SENSITIVITY, AND SPECIFICITY

Parameters	Evaluation
Accuracy	97 %
Sensitivity	94%
Specificity	100%

Figure 9 shows our model's performance compared to other related work reviewed in this paper. The model average accuracy is the key of comparison. Even though, some work presents the accuracy of performance as well as the sensitivity, specificity, and F1 scoring. Some work shows also detailed accuracy such as [9], where the paper presents the accuracy of model for classifying positive cough as 93.33% while its accuracy for classifying negative accuracy was 86. For such models we have averaged the accuracy of both types.
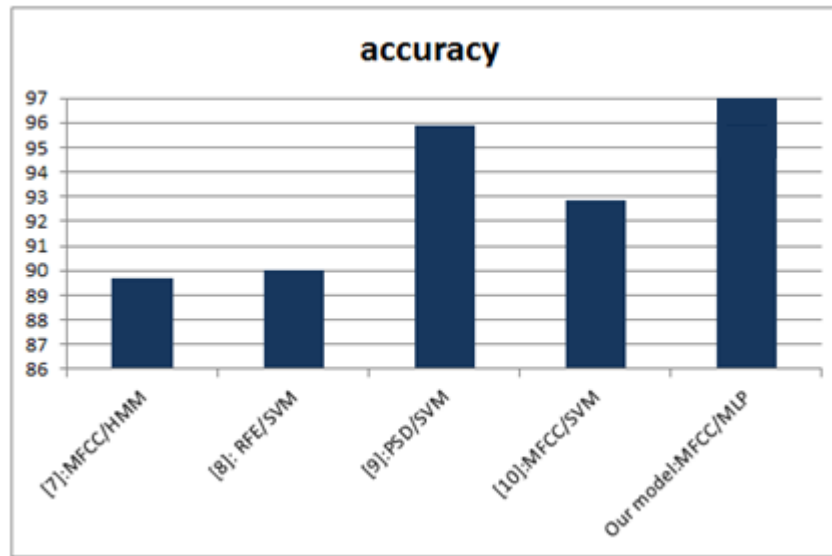
Figure 9: A comparison of our model to related work

V. CONCLUSION

This paper proposes a system for detecting and diagnosing people who are infected by covid-19 from those who are not based on cough sound analysis. Data of 152 (4238 instances) participants have been downloaded from online available COUGHVID dataset and have been used for the system design and test. The system manipulates the cough as a sound signal; thereby it has been built upon the idea of voice recognition system. It uses MFCC for extracting features from cough signal and uses MPL neural network to classify the signal to infected or non-infected. The system has shown a high performance with accuracy of 100% and 93% for detecting positive and negative cases of patients respectively.

REFERENCES

[1] W. H. O. WHO, "Mental health and psychosocial considerations during the COVID-19 outbreak," Mar. 13, 2020. [Online]. Available: https://apps.who.int/iris/rest/bitstreams/1272383/retrieve.

[2] M. Melek, "Diagnosis of COVID-19 and non-COVID-19 patients by classifying only a single cough sound," *Neural Comput. Appl.*, vol. 33, no. 24, pp. 17621–17632, Dec. 2021, doi: 10.1007/s00521-021-06346-3.

[3] "COVID-19 CORONAVIRUS PANDEMIC." [Online]. Available: https://www.worldometers.info/coronavirus/.

[4] M. S. Al-Ani, T. S. Mohammed, A. I. Sultan, H. I. Sultan, K. M. A. Alheeti, and K. M. Aljebory, "Detection and Diagnostic Approach of COVID-19 Based on Cough Sound Analysis," *J. Comput. Sci.*, vol. 17, no. 6, pp. 580–597, Jun. 2021, doi: 10.3844/jcssp.2021.580.597.

[5] J. R. Larsen, M. R. Martin, J. D. Martin, P. Kuhn, and J. B. Hicks, "Modeling the Onset of Symptoms of COVID-19," *Front. Public Health*, vol. 8, p. 473, 2020, doi: 10.3389/fpubh.2020.00473.

[6] J. Martinez, H. Perez, E. Escamilla, and M. M. Suzuki, "Speaker recognition using Mel frequency Cepstral Coefficients (MFCC) and Vector quantization (VQ) techniques," in *CONIELECOMP 2012, 22nd International Conference on Electrical Communications and Computers*, Cholula, Puebla, Mexico, Feb. 2012, pp. 248–251. doi: 10.1109/CONIELECOMP.2012.6189918.

[7] K. Alarabi Aljribi, "A Comparative Analysis of Frequency Bands in EEG Based Emotion Recognition System," in *The 7th International Conference on Engineering & MIS 2021*, Almaty Kazakhstan, Oct. 2021, pp. 1–7. doi: 10.1145/3492547.3492618.

[8] K. K. Lella, A. Pja, and Department of Computer Applications, NIT Tiruchirappalli, Tamil Nadu, India-620015, "A literature review on COVID-19 disease diagnosis from respiratory sound data," *AIMS Bioeng.*, vol. 8, no. 2, pp. 140–153, 2021, doi: 10.3934/bioeng.2021013.

[9] O. Zealouk, H. Satori, M. Hamidi, N. Laaidi, A. Salek, and K. Satori, "Analysis of COVID-19 Resulting Cough Using Formants and Automatic Speech Recognition System," *J. Voice*, p. S0892199721001879, Jun. 2021, doi: 10.1016/j.jvoice.2021.05.015.

[10] A. Tena, F. Clarià, and F. Solsona, "Automated detection of COVID-19 cough," *Biomed. Signal Process. Control*, vol. 71, p. 103175, Jan. 2022, doi: 10.1016/j.bspc.2021.103175.

[11] N. Melek Manshouri, "Identifying COVID-19 by using spectral analysis of cough recordings: a distinctive classification study," *Cogn. Neurodyn.*, vol. 16, no. 1, pp. 239–253, Feb. 2022, doi: 10.1007/s11571-021-09695-w.

[12] V. Tiwari, "MFCC and its applications in speaker recognition.," 2010.

[13] Y. Amrulloh, U. Abeyratne, V. Swarnkar, and R. Triasih, "Cough Sound Analysis for Pneumonia and Asthma Classification in Pediatric Population," in *2015 6th International Conference on Intelligent Systems, Modelling and Simulation*, Kuala Lumpur, Malaysia, Feb. 2015, pp. 127–131. doi: 10.1109/ISMS.2015.41.

[14] L. Orlandic, T. Teijeiro, and D. Atienza, "The COUGHVID crowdsourcing dataset, a corpus for the study of large-scale cough analysis algorithms," *Sci. Data*, vol. 8, no. 1, p. 156, Dec. 2021, doi: 10.1038/s41597-021-00937-4.

دراسة تأثير تشتت نمط الاستقطاب والفقد المعتمد على الاستقطاب على بارامترات الأداء في أنظمة اتصالات الالياف البصرية

سعاد محمد ابوزريبة، سمية محمد الطرشي، سعاد ابوالقاسم مجاور

قسم الفيزياء-كلية العلوم – جامعة مصراتة

suadabu@yahoo.com (218918108138)

الملخص

في هذا البحث تم دراسة تأثير الفقد الاستقطابي للإشارات الداخلة في انظمة اتصالات الالياف البصرية على كفاءة الاشارات الخارجة عن طريق نموذج حاملات الموجة المار عبر الالياف البصرية وحيدة النمط مع اعتبار التشتت الحاصل في الموجات المارة خلال الليف البصري الناجم عن التشتت اللوني و تشتت نمط الاستقطاب للموجات المارة خلال الليف البصري وفق القوانين الفيزيائية لفيزياء الألياف البصرية التي تعمل على اظهار الإشارة الخارجة من نظام الاتصالات الألياف البصرية بكفاءة معينة وذلك من خلال دراستنا لتأثير الفقد الاستقطابي (PDL) على معدل الخطأ النبضي (BER) في أنظمة الألياف البصرية. زيادة على ذلك تمت دراسة تأثير الفقد الاستقطابي على حساب معدل الخطأ النبضي (BER) للإشارات الخارجة و وجد انه بزيادة الفقد الاستقطابي (PDL) وزيادة تشتت نمط الاستقطاب (PMD) يزداد معدل الخطأ النبضي (BER), ويكون أفضل قيمة (BER) عندما يكون (PDL=0dB و PMD=2ps) , كما تمت دراسة تأثير الفقد الاستقطابي على عامل الجودة (Q–Factor) و وجدنا بزيادة الفقد الاستقطابي (PDL) وزيادة تشتت نمط الاستقطاب (PMD) يقل عامل الجودة (Q–Factor), إضافة الى ذلك تمت دراسة تأثير الفقد الاستقطابي على نسبة الإشارة الى للتشويش المستقبلة في اجهزة الاستقبال (OSNR) أوضحت الدراسة انه بزيادة الفقد الاستقطابي (PDL) وزيادة تشتت نمط الاستقطاب (PMD) يقل نسبة الإشارة البصرية للتشويش (OSNR) . أوضحت الدراسة ان أفضل قيمة (Q–Factor) ومعدل الخطأ النبضي و كذلك نسبة الإشارة البصرية للتشويش عندما يكون PDL=0dB وPMD=2ps. أجريت كافة الحسابات في هذا البحث باستخدام برنامج الماتلاب.

الكلمات المفتاحية: الالياف البصرية ، تشتت نمط الاستقطاب ، الفقد المعتمد على الاستقطاب، معدل الخطأ النبضي، عامل الجودة.

مقدمة

مع التطور الهائل والقفزة النوعية العالية في مجال تقنيات المعلوماتية، والاتصالات، ومع التزايد السكاني الكبير الذي يفرض حاجةً على التواصل بين الأفراد، مما يسبب ضغطاً على نظم الاتصالات العامة، فقد أصبحت الحاجة ملحة إلى تطوير شبكات نقل ذات عرض حزمة أكبر بحيث تستطيع نقل المعلومات بسرعة أكبر، وزمن أقل، مما مهد السبيل للحاجة إلى خدمات شبكة ذات عرض حزمة ذات أعلى [1].

عند إرسال الإشارات ضمن قناة اتصال فإنها تعاني بعض التشوهات نتيجة للتشويش الناتج عن تراكب الضجيج (التشويش) عليها إضافة إلى تأثير ممانعة بعض أنواع خطوط النقل على جودة ونوعية الإشارات المرسلة غيرها وبالتالي صعوبة كشف تلك الإشارات بشكلها الحقيقي في قسم الاستقبال نتيجة المؤثرات الموجودة في قناة الاتصال [2]. بعد مسافة الإرسال تعاني الاشارة البصرية أثناء انتشارها ضمن الألياف من عدة عوامل فقد طاقية، تنتج عن عيوب الدليل الموجي وامتصاص المادة المكونة لليف والاستطارة ومعوقات أخرى منها التشتت اللوني (CD) وتشتت نمط الاستقطاب (PMD) والفقد الاستقطابي (PDL) لهذا تستخدم المضخمات البصرية من أجل تعويض هذا الفقد حيث تضيف المضخمات تشويش وتؤثر على نسبة الإشارة البصرية للتشويش (OSNR). لذلك من المهم من وجود مقاييس لتقييم جودة النظام ومن أهم هذه المقاييس معدل الخطأ النبضي (BER) وعامل الجودة (Q-Factor) ونسبة الإشارة البصرية للتشويش (OSNR) تعد هذه المقاييس من أهم العوامل التي تحدد كفاءة النظام المتمثلة في معدل البتات ومسافة الإرسال [3].

في سنة 1995 قامجيسين N.Gisin وزملائه بدراسة مشكلة تعيين الاحصائي لـ N من عناصر ذات الفقد الاستقطابي (PDL) المتصلة بواسطة الألياف البصرية المتسلسلة, وقد تمت مناقشة كل من التوهين والفقد الاستقطابي (PDL) وتم اقتراح تعريفات أساسية واشتقاق صيغ كل من القيمة المتوسطة والانحرافات المعيارية [4].في سنة 2002 قام أنطونيو ميكوزي Antonio Mecozzi وزملائه بدراسة إحصائيات الفقد الاستقطابي (PDL) في الأنظمة البصرية. ووضحوا أن توزيع PDL هو توزيع ماكسويل عندما يتم التعبير عنه بالديسيبل, وقارنوا النتائج التحليلية مع المحاكاة العددية, حيث تمت ملاحظة وجود اتفاق ممتاز بينهما [5].

سنة 2007 قام ليانغ تشن Liang Chen وزملائه بتقديم تقييم تحليلي جديد لاحتمالية الخطأ الناتج عن الاستقطاب للأنظمة البصرية التي تتكون من PMD وPDL.   باستخدام نموذج مبسط يحتوي على قطع الألياف PMD وPDL, ومضخم الضوضاء ASE, مع المصفى البصري والمصفى الكهربي, حيث تمت دراسة تأثيرين مرتبطين بالاستقطاب وهما الفقد الاستقطابي وتشتت نمط الاستقطاب, أي اقتران بين اتجاه متجهي PMD وPDL وقد تم استنتاج ان التداخل الناجم عن الاستقطاب يعتمد تأثيره على معدل الخطأ في البتات بشدة على قيمة PDL [6].

في سنة 2010 قام فرحان حسن Farhan Hussain وزملائه بدراسة تأثير الفقد الاستقطابي على نظام اتصال الألياف البصرية عالي السرعة, ولقد وجد أنه في وجود PDL فإن BER وQ–factor في المستقبل يخضعان لتقلبات مما يتسبب في عدم استقرار النظام وتظهر النتائج أنه يرجع بشكل أساسي إلى تذبذب نسبة الإشارة الضوئية إلى الضوضاء الموازية (OSNR) وقيمة معامل الجودة عموما Q–factor الامر الذي يؤثر على معدل الخطأ في البتات (BER) [7].

سنة 2010 قام مكسيم كوشنيروف Maxim Kuschnerov وزملائه بتقييم أداء الأنظمة البصرية المتعددة الاستقطاب في وجود الفقد الاستقطابي (PDL) للمستقبلات الخطية والاحتمالية القصوى والضوضاء المجمعة في المستقبل، وناقشوا طرق انقاص قيمة الفقد الاستقطابي (PDL)[8]. في سنة 2015 قام كل من انجري ليوYangzi Liu وزملائه بتصميم محاكي للفقد الاستقطابي مع وحدات تحكم الاستقطاب التي تعمل بالكمبيوتر والنمط الأحادي, واثبتت هذه الدراسة أن الفقد الاستقطابي PDL يتبع توزيع ماكسويل عندما يتم التعبير عنه بالديسيبل ووضع وحدات تحكم الاستقطاب في أماكن مختلفة في رابط المحاكي, وقد تم أيضًا استنتاج ان مواضع مكونات PDL لها تأثير كبير على احصائيات PDL في نظام الاتصال بطول ثابت نظرًا لأن عدد مكونات الاستقطاب المعنية وطول الاتصال يبقى ثابتًا, اضافة الى انه كلما كان عدد الالياف الواصلة أطول كلما كان أصغر متوسط قيم PDL أصغر [9]. في سنة 2019 قدم كل من براين كيربي Brian T. Kirby وزملائه نموذجًا نظريًا يصف كيف يؤثر عاملي حجم واتجاه الفقد الاستقطابي (PDL) على جودة النظام وميزوا نظريًا كيف يمكن تطبيق PDL في

قناة ليفية واحدة على النحو الأمثل من أجل تعويض الفقد الناتج عن (PDL) وقدموا نتائج تجريبية تتحقق من الوضع النظري [10]. في سنة 2020 قام جهانجيز علم JahangirAlam وزملائه باقتراح مخطط لتقنيات التعديل المختلفة لتحسين معدل الخطأ النبضي (BER) في اتصالات الألياف البصرية. تم اختبار النظام المطور على أنظمة الألياف البصرية التي تعمل بتعديل العودة إلى الصفر (NRZ) بمعدلات إرسال تصل 10Gbps, أظهرت المحاكاة العددية تحسناً ملحوظًا في نظام (BER) بعد تحسين عملية المعالجة المقترحة على الإشارات الكهربائية المكتشفة عند أطوال موجية مركزية في منطقة 1310nm [11].في هذا البحث ستتم دراسة تأثير الفقد الاستقطابي للإشارات الداخلة في انظمة اتصالات الالياف البصرية على كفاءة الاشارات الخارجة عن طريق نموذج حاملات الموجة المار عبر الالياف البصرية وحيدة النمط مع اعتبار التشتت الحاصل في الموجات المارة خلال الليف البصري الناجم عن التشتت اللوني و تشتت نمط الاستقطاب للموجات المارة خلال الليف البصري وفق القوانين الفيزيائية لفيزياء الألياف البصرية التي تعمل على اظهار الإشارة الخارجة من نظام الاتصالات الألياف البصرية بكفاءة معينة وذلك من خلال دراستنا لتأثير الفقد الاستقطابي (PDL) على معدل الخطأ النبضي (BER) في أنظمة الألياف البصرية. كفاءة الاشارات المستقبلة ستقاس عن طريق حساب معدل الخطأ النبضي (BER), وعامل الجودة (Factor−Q), ونسبة الإشارة الى للتشويش المستقبلة في اجهزة الاستقبال (OSNR).

الدراسة الرياضية التحليلية

عندما تسافر الإشارة داخل الليف البصري في أنظمة اتصالات الألياف البصرية فأنها تعاني من خسائر مختلفة، تسبب هذه الخسائر صعوبة ضبط الإشارة عند المستقبل، وبالتالي عند نقل الإشارة إلى مسافات طويلة في الليف من ضروري دعم الإشارة داخل الليف البصري [12]. لذلك تستخدم المضخمات لاستقبال وتضخيم الإشارة المرسلة إلى شدتها الأصلية ومن ثم يتم تمريرها إلى الألياف الرئيسية [13].

التشويش (الضوضاء) هو إشارات غير مفيدة تجمع مع الإشارة مسببة تغييرًا غير مرغوب فيه مما يؤدي إلى قلة مردودها وسوء أدائها وتخفيض جودتها، الامر الذي يتسبب في حدوث أخطاء في نظام الاتصال، ويقيم أداء نظام الاتصال بمعرفة نسبة الإشارة البصرية إلى التشويش

(الضوضاء)، لا يمكن أن يحدث التضخيم البصري من دون توليد انبعاث تلقائي مضخم(ASE) (Amplified Spontaneous Emission)،هذا التشويش (الضوضاء) الناتجة عن مضخم الانبعاث التلقائي تعبر من أهم العيوب التي تحد من قدرة النظام [14]:

(1)

$$P_{ASE} = 2hV.\Delta V.n_{sp}(G-1)$$

حيثP_{ASE} هي قوة ASE (الضوضاء) في عرض النطاق الترددي البصري ΔV, h تابت بلانك،v التردد البصري، n_{sp} معامل الانبعاث التلقائي،G كسب المضخم البصري، تضاف هذه المساهمات بشكل تراكمي على طول السلسلة المضخم، وتؤدي إلى زيادة إشارة الضوضاء التلقائية عند المستقبل، وهو الحد الأساسي للتشويش في نظام إرسال المضخم بصرياً [15].

يمكن تمييز ضعف الإشارة التلقائية من حيث نسبة الإشارة البصرية إلى نسبة التشويش Optical Signal to Noise Ratio (OSNR) كما هو موضح في المعادلة (2) ويتم تعريفها على أنها نسبة قدرة قناة الإشارة إلى قدرة ASE في عرض نطاق بصري محدد [16]:

$$OSNR = \frac{P_{out}}{2hV.\Delta V.n_{sp}(G-1)}$$ (2)

البتات المستلمة عندما يعرف عدد الأخطاء يمكن تحديد BER على النحو التالي [4]:

$$BER = \frac{Number\ of\ error}{Numer\ of\ transmitted\ bits}$$ (3)

الدالة المولدة للعزوم (Moment Generating Function Method) (MGF): هي واحدة من أكثر دوال التوزيع أهمية لأنها يستخدم لتقييم أهم باراميتر أداء متوسط معدلالخطأ(BER) لأنظمة الاتصالات الرقمية، يمكن استخدام MGF للحصول على متوسط معدل(BER) بمختلف صيغ التعديل لذلك [17‘18].

تعد نسبة الإشارة البصرية للتشويش (OSNR) أحد المعلمات الرئيسية التي تحدد المدى الذي يمكن أن ينتقل إليه طول الموجة قبل التجديد. تعمل (OSNR) كمؤشر معياري لتقييم أداء الأنظمة الإرسال البصرية، تحتاج شبكات الاتصال إلى العمل فوق حد (OSNR) الخاص بها لضمان تشغيل فوق حد (OSNR) الخاص بها لضمان التشغيل الخالي من الأخطاء [19,16]. توجد علاقة مباشرة بين نسبة الإشارة البصرية للتشويش (OSNR) ومعدل الخطأ النبضي (BER) حيث (BER) هي القيمة النهائية لقياس جودة الإرسال. لحساب (BER) للألياف

أحادية النمط هي [20] , ولكي يكون نظام ذو كفاءة عالية يجب أن يكون معدل الخطأ النبضي (BER) منخفض ونسبة الإشارة البصرية للتشويش (OSNR) عالي [21].

معدل الخطأ النبضي (BER) للنظام قد يكون في بعض منخفضًا جدًا بحيث لا يمكن قياسه خلال فترة زمنية معقولة، فمن المفيد اعتماد قياس عامل الجودة (Q-Factor) كطريقة غير مباشرة لقياس معدل الخطأ في البتات (BER), حيث أن عامل الجودة (Q-Factor) هي معلمة بلا أبعاد تستخدم على نطاق واسع لقياس أداء أنظمة اتصالات البصرية [11].

يمكن كتابة عامل الجودة (Q-Factor) على أنه:

(4)

$$Q = \frac{\mu_1 - \mu_0}{\sigma_1 + \sigma_0}$$

حيث أن μ_1 و μ_0 متوسط log 0, log1, و σ_1, σ_0 هي الانحرافات المعيارية المقابلة.

تعطى العلاقة الرياضية بين عامل الجودة (Q-Factor) و (BER) بالمعادلة التالية [22]:

$$BER = \frac{1}{2} \, erfc\left(\frac{Q}{\sqrt{2}}\right) \qquad (5)$$

نموذج النظام تحت الدراسة

في الشكل (1) يظهر نموذج الليف البصري تحت الدراسة بحيث يتم تقسيمه إلى أجزاء صغيرة، سيتم التركيز على مقطع واحد طوله (L)، والذي يمثل الليف البصري المقسم إلى أجزاء عددها (N).
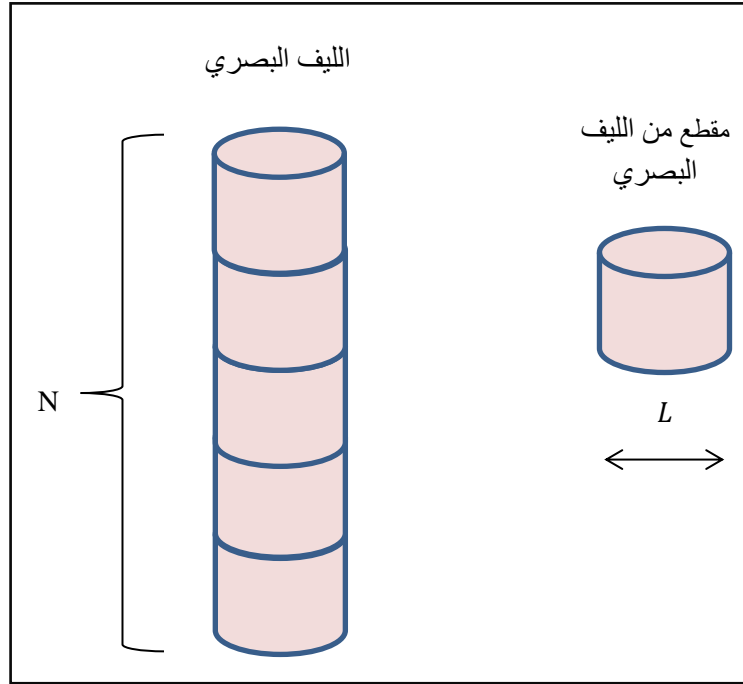
شكل (1) الليف البصري تحت الدراسة

التطور السريع في الاتصالات والرغبة الملحة للوصول إلى سرعات فائقة يجعلنا نلجأ إلى أنظمة اتصالات ذات نطاق عريض [23]، تعتبر الألياف البصرية الوسط المناسب والمستخدم لنقل المعلومات من نقطة إلى نقطة وذلك بتحميلها على أمواج ضوئية، ولضمان نقل تلك المعلومات واستقبالها بأفضل جودة ممكنة يتطلب مكونات نظام تؤدي وظيفتها لتحقيق نقل بيانات بجودة وسرعة عالية [24].

الشكل (2) يوضح مخطط النظام المدروس حيث تدخل الإشارة $\vec{s}_{input}(t)$ الى محور الإشارة في العملية المسماة عملية التحوير Modulation و تمر بعدة مراحل ليتم استقبالها في الشكل النهائي عند دائرة القرار Decision Circuit .
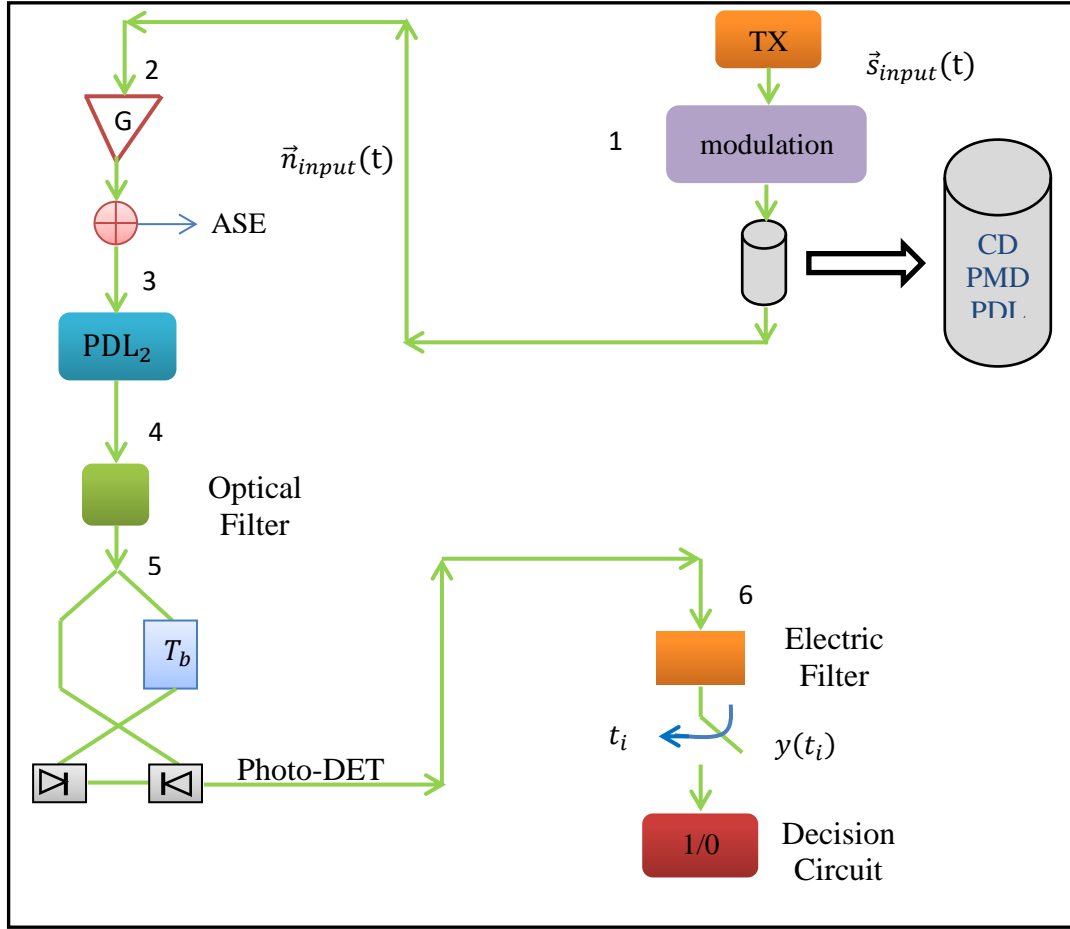
شكل (2) نموذج النظام تحت الدراسة

الدراسة النظرية

المرحلة الأولى : في هذه المرحلة نلاحظ أن الإشارة البصرية $\vec{s}_{input}(t)$ بدأت في الدخول في نظام الليف البصري بحيث يتم تعديلها بأحدي صيغ التعديل المستخدمة ومن ثم تمر على مصدر التشتت اللوني (CD)ثم تمر بمصدر تشتت نمط الاستقطاب (PMD) لتمر بعدها خلال مصدر الفقد الاستقطابي (PDL_1) وذلك بعد أن عبرت المسار (1) [17].

يمكن كتابة الإشارة الداخلة للنظام على صورة متسلسلة فورييه كالتالي:

$$\vec{s}_{in}(t) = s_{in}(t)|\vec{p}_s> = \sum_{l=-\infty}^{\infty} (s_{in})_l e^{j\omega_l t} |\vec{p}_s> \qquad (6)$$

حيث $|\vec{p}_s>$ يمثل متجه الوحدة و $\left(\omega_l = \frac{2\pi l}{NT_b}\right)$ يمثل التردد الزاوي، بحيث l طول قطعة الليف البصري، N يمثل عدد النبضات، T_bيمثل الفترة الزمنية لكل بت (نبضة). يمكن كذلك تمثيل مصادر الفقد في الإشارة البصرية المارة خلال الليف البصري من خلال المعادلات التالية:

- التشتت اللوني (CD): يمثل بالعلاقة التالية [17]:

$$H_{CD}(f) = e^{-2j\pi^2 \beta_2 f^2 L} \tag{7}$$

حيث $\beta_2 = -\lambda^2 D(\lambda)/(2\pi c)$, بحيث يكون $D(\lambda)$ بارامتر التشتت اللوني (CD) لليف البصري في الطول الموجي λ، f تردد الموجة.

- تشتت نمط الاستقطاب (PMD): في مجال التردد، يتم إعطاء مصفوفة جونز (T_{PMD})لتشتت نمط الاستقطاب (PMD)من الدرجة الأولى بواسطة العلاقة

$$T_{PMD}(\omega_l) = \exp(-j\omega_l \vec{\tau} \cdot \vec{\sigma}/2) \tag{8}$$

حيث $(\vec{\sigma})$ يمثل التدوين القياسي لمصفوفات باولي التي تحقق العلاقة $\vec{\sigma} \times \vec{\sigma} = 2j\vec{\sigma}$, $\vec{\tau}$يمثل متجه ستوكس حقيقي ثلاثي الأبعاد. في هذا العمل، قيمته (DGD) واتجاهه $\vec{\tau}_0$ (= $\vec{\tau}/\tau$) يفترض أن يكون غير معتمد على التردد. المصفوفة بالمعادلة (8) لها اثنين من المتجهات الذاتية $|\vec{\tau}_0 >$ و $|\vec{\tau}_\perp >$ في فضاء جونز ثنائي البعد، تشير إلى اتجاهات البطيئة ($|\vec{\tau}_0 >$) والسريعة ($|\vec{\tau}_\perp >$) للحالة الرئيسية للاستقطاب (PSP) مع عناصر المصفوفة:

حيث $|\vec{\tau}_0 >$ يمثل متجه جونز المتوافق معمتجه ستوكس $\vec{\tau}_0$. للحصول على إشارة الدخل المقدمة في المعادلة (6)، نقدم مصفوفة تشتت نمط الاستقطاب (PMD) لجونز المعطاة في المعادلة (8)بحيث أن متجه تشتت نمط الاستقطاب (PMD) $(\vec{\tau})$ يشير في الاتجاه البطيء، والذي يكون متفق عليه عادة.

- الفقد الاستقطابي (PDL): بالنسبة لمصفوفة جونز (T_{PDL}) للفقد الاستقطابي (PDL) فإنه يتم إعطاءها بواسطة العلاقة [17]:

$$T_{PDL_1} = \exp(-\alpha/2) \exp(\vec{\alpha} \cdot \vec{\sigma}/2) \tag{9}$$

حيث تربط هذه المصفوفة بين دخل وخرج الفقد الاستقطابي (PDL_1)، ويكون لها متجهين ذاتيين متعامدين وهما $|\vec{\alpha}_0 >)$ و$|\vec{\alpha}_\perp >)$ في فضاء جونز ثنائي البعد.

عندما تسافر الإشارة في أنظمة اتصالات الألياف البصرية يحدث تهوين لهذه الإشارة مما يسبب ضعف في جودة المعلومات عند استقبالها في المستقبل، لهذا وجب استخدام مضخمات بصرية

لتضخيم الإشارة حيث يتم ادخالها في أماكن محددة لتعزيز الإشارات البصرية، يتيح هذا التعزيز إرسال الإشارات بنجاح من خلال طول الكابل المتبقي[17]. بالتالي في هذه المرحلة تدخل الإشارة البصرية إلى المضخم البصري ذو الكسب البصري G بعد مرورها عبر المسار (2) حيث تتم عملية التضخيم لهذه الإشارة الداخلة. من جهة أخرى، فإن التضخيم البصري يسبب في الانبعاث التلقائي المضخم، تشويش الناتج من المضخم البصري يدعى تشويش الانبعاث التلقائي المضخم (ASE) يضعف النظام ويقلل من جودته ويؤثر بشكل سلبي على نسبة الإشارة إلى التشويش (OSNR) [17].

بعد خروج الإشارة المضخمة من المضخم البصري عند المسار (3) نجد أن ضوضاء الانبعاث التلقائي المضخمة (ASE) قد أضيفت إلى الإشارة على هيئة ضوضاء جاوس $\vec{n}_{input}(t)$ (بافتراض أن القوة المدخلة للنظام منخفضة بما فيه الكفاية، مما يجعل تأثير التشويش غير الخطي الناجم عن ضوضاء الانبعاث التلقائي المضخمة(ASE) مهملة. يمكن أن تحلل الضوضاء الناتجة عن ضوضاء الانبعاث التلقائي المضخمة($\vec{n}_{input}(t)$) (ASE) في الشكل السابق في متجهين جونز المتعامدين (أي $|\vec{e}_x >$ و $|\vec{e}_y >$)، كما يمكن كتابتها على صورة فورييه باستخدام مفكوك (Karhunen–Lo`eve) على الصورة التالية:

$$\vec{n}_{input}(t) = n_x(t)|\vec{e}_x > + n_y(t)|\vec{e}_y >$$

$$= \sum_{l=-\infty}^{\infty} \left[(N_{in})_{x,m}|\vec{e}_x > + (N_{in})_{y,m}|\vec{e}_y > \right] e^{-j\frac{2\pi m(t-t_i+T_0)}{T_0}} \qquad (10)$$

في المعادلة (10)، نفترض أن الفترة الزمنية الكلية لاستجابة النبضة داخل المرشحات (المصفيات) البصرية (عرض النطاق الترددي لها B_o) والمرشحات الكهربائية (عرض النطاق الترددي لها B_r) تكون على الصورة $\left(T_0 = \mu(\frac{1}{B_o} + \frac{1}{B_r}) \right)$, حيث يمثل μ معامل تسوية عديم الأبعاد يجب أن يحسب لكل فترة زمنية. تدخل الإشارة البصرية بعد ذلك إلى مصدر آخر للفقد الاستقطابي (PDL_2) بالتالي فإن الإشارة تكون مشوهة بشكل إضافي. الجدير بالذكر أنه يمكن دراسة تأثير ضوضاء الانبعاث التلقائي المضخمة (ASE) على النظام البصري السابق من خلال المقارنة لحالتين خاصتين، وهما:

1- النظام ذو ضوضاء (ASE) المستقطب جزئيًا (على افتراض(PDL_2)تكون غير مهملة).

2– النظام ذو ضوضاء (ASE)غير المستقطب (بافتراض أن(PDL$_2$)تكون مهملة).

المرحلة الثانية: تعبر الإشارة البصرية المسار (4) لتدخل للمصفى البصري ليتم تصفيتها بصريًا، وعلى افتراض أن المرشح البصري ليس له أي تأثير على استقطاب الإشارة حيث أن تأثير الفقد الاستقطابي (PDL)المحتمل للمرشح البصري على الإشارة والضوضاء يمكن أن يكون تضمينه في الفقد الاستقطابي(PDL$_2$)الذي تم إهماله في هذه الدراسة.

بعد مرور الإشارة البصرية للمسار (5) يتم استقبالها للكشف عنها بصيغة التضمين المناسبة، ومن ثم تعبر المسار (6).

تمر الإشارة البصرية خلال المسار (6) لتدخل إلى المصفى الكهربي،حيث يتم تحويل الضوء الخارج من الطرف البعيد لوسط النقل مرة أخرى إلى إشارة كهربائية بواسطة المصفى الكهربي والذي يتم وضعه عند مدخل جهاز الاستقبال لتكون الإشارة البصرية على الصورة الكهربائية عند زمن t_i. يتم بعد ذلك تضخيم هذه الإشارة الكهربائية قبل فك التشفير أو إزالة التضمين من أجل الحصول على المعلومات المرسلة الأصلية.

يعطى التيار الكهربي الناتج عن هذه المرحلة بالعلاقة:

$$y(t_i) = \frac{1}{2}[\vec{s}^o(t_i + T_b) + \vec{n}^o(t_i + T_b)] \cdot [\vec{s}^o(t_i) + \vec{n}^o(t_i)]^* + c.c. \quad (11)$$

حيثt_i يمثل زمن العينة $(t_i = t_0 + T_b , i = 0, ... , N - 1)$, c.c., أو $[...]^*$ يمثل المرافق المركب للإشارة،$\vec{s}^o(t_i)$ الاشارة الداخلة،$\vec{n}^o(t_i)$ الضوضاء الناتجة عن الانبعاث التلقائي المضخمة (عند خرج المصفى البصري).مساهمة الضوضاء في التيار الكهربي $((t_i))$ ناتج عن الضوضاء الداخلة خلال الفترة الزمنية$(t_i - T_o, t_i)$, حيث يتألف هذا التيار من ثلاثة أجزاء في النظام البصري بحيث يمكن كتابته بالعلاقة التالية:

$$y(t) = y_{ss}(t) + y_{nn}(t) + y_{ns}(t) \qquad\qquad (12)$$

حيث: $y_{ss}(t)$ تمثل تفاعل الإشارة – الإشارة المساهم في تيار المستقبل.

$y_{nn}(t)$ تمثل تفاعل الضوضاء – الضوضاء المساهم في تيار المستقبل.

$y_{ns}(t)$ تمثل تفاعل الإشارة – الضوضاء المساهم في تيار المستقبل.

تتم دراسة هذه الأجزاء الثلاثة للتيار الناتج كالتالي:

تفاعل الإشارة – الإشارة لنموذج قطعة (PMDوPDL):

يمكن تمثيل الإشارة المدخلة المعطاة في المعادلة (12) بواسطة رموز ديراك عن طريق المعادلة:

$$|\vec{s}_{in}(t_i)\rangle = \left[(S_{in})_{-L}e^{-j\frac{2\pi L t_i}{NT_b}}, \ldots, (S_{in})_L e^{j\frac{2\pi L t_i}{NT_b}}\right]^T |\vec{p}_s\rangle \qquad (13)$$

بمساعدة علاقات الاكتمال $|\vec{k}_0\rangle\langle\vec{k}_0| + |\vec{k}_\perp\rangle\langle\vec{k}_\perp| = 1 (\vec{k} = \vec{\tau}, \vec{\alpha})$ في فضاء جونز ثنائي البعد، نجد أن:

$$T_{PMD} = e^{-j\frac{\omega_l\tau}{2}}|\vec{\tau}_0\rangle\langle\vec{\tau}_0| + e^{j\frac{\omega_l\tau}{2}}|\vec{\tau}_\perp\rangle\langle\vec{\tau}_\perp| \qquad (14)$$

$$T_{PDL1} = (|\vec{\alpha}_0\rangle\langle\vec{\alpha}_0| + |\vec{\alpha}_\perp\rangle\langle\vec{\alpha}_\perp|)T_{PDL1}(|\vec{\alpha}_0\rangle\langle\vec{\alpha}_0| + |\vec{\alpha}_\perp\rangle\langle\vec{\alpha}_\perp|)$$

$$T_{PDL1} = |\vec{\alpha}_0\rangle\langle\vec{\alpha}_0| + e^{-\alpha}|\vec{\alpha}_\perp\rangle\langle\vec{\alpha}_\perp| \qquad (15)$$

وهو ما يعني عنصر مصفوفة الاستقطاب $(\vec{\tau}, \vec{\alpha})_{l,l/}$ تكون نحو استقطاب الدخل $|\vec{p}_s\rangle$ في اتجاهين متعامدين وهما:

$$P(\vec{\tau}, \vec{\alpha})_{l,l/}|\vec{p}_s\rangle = (P_{\alpha_0})_{l,l/}|\vec{p}_s\rangle + (P_{\alpha_\perp})_{l,l/}|\vec{p}_s\rangle \qquad (16)$$

بحيث أن:

$$(P_{\alpha_0})_{ll/}|\vec{p}_s\rangle = \delta_{l,l'}|\vec{\alpha}_0\rangle\left[\langle\vec{\alpha}_0|\vec{\tau}_0\rangle\langle\vec{\tau}_0|\vec{p}_s\rangle e^{\frac{-j\omega_l\tau}{2}} + \langle\vec{\alpha}_0|\vec{\tau}_\perp\rangle\langle\vec{\tau}_\perp|\vec{p}_s\rangle e^{\frac{j\omega_l\tau}{2}}\right]$$

$$\equiv \delta_{l,l'}c_{l\alpha_0}|\vec{\alpha}_0\rangle \qquad (17)$$

$$(P_{\alpha_\perp})_{ll/}|\vec{p}_s\rangle = \delta_{l,l'}e^{-\alpha}|\vec{\alpha}_\perp\rangle$$

$$\rangle\left[\langle\vec{\alpha}_\perp|\vec{\tau}_0\rangle\langle\vec{\tau}_0|\vec{p}_s\rangle e^{\frac{-j\omega_l\tau}{2}} + \langle\vec{\alpha}_\perp|\vec{\tau}_\perp\rangle\langle\vec{\tau}_\perp|\vec{p}_s\rangle e^{\frac{j\omega_l\tau}{2}}\right]$$

$$\equiv \delta_{l,l'}c_{l\alpha_\perp}|\vec{\alpha}_\perp\rangle \qquad (18)$$

حيث يمكن تمثيل الإشارة الموضحة في المعادلة (18) بالعلاقة:

$$|\vec{s}^0(t_i)\rangle = O^s\left[(P_{\alpha_0} + P_{\alpha_\perp})|\vec{p}_s\rangle\right]\phi_{CD}|s_{in}(t_i)\rangle$$

$$= \left[(P_{\alpha_0} + P_{\alpha_\perp})|\vec{p}_s\rangle\right]|s^0(t_i)\rangle \qquad (19)$$

لأن كل من المصفوفات الثلاثية الأبعاد $(2L + 1)$ في المعادلة (18) تكون قطرية، يمكن تخفيفها مع أي من المصفوفات الأخرى في المعادلة (18). يمكن الحصول بسهولة على تفاعل الإشارة – الإشارة المساهم في تيار المتلقي $y_{ss}(t)$

تفاعل تشويش (ضوضاء) – تشويش (ضوضاء) لنموذج قطعة(PMDوPDL):

إن معالجة ضوضاء الانبعاث التلقائي المضخمة (ASE) المدخلة عند المسار (3) في الشكل السابق لا يمكن معالجتها أو اعتبارها على أنها جزئيين أحدهما المقدار والآخر اتجاه. ومع ذلك، يمكننا أن تتحلل إلى عنصرين متعامد، بمعنى:

$$|\vec{N}_{in} > = |N_{in}^{\alpha_0} > \otimes |\vec{\alpha}_0 > + |N_{in}^{\alpha_\perp} > \otimes |\vec{\alpha}_\perp > \qquad (20)$$

وبشكل مشابه، يمكن كتابة التشويش المقابل عند المسار (4) في الشكل السابق بالصيغة:

حيث $U^\dagger$ هي المصفوفة الهرميتية لـ U, والتي تُستخدم لترتيب قطرية تفاعل الضوضاء – الضوضاء $(O^n)^\dagger \Re^{nn}(T_b)O^n$. وبالتالي فإن التيار المصفى الناجم عن تفاعل الضوضاء – الضوضاء يعطى بالعلاقة:

تفاعل الإشارة – تشويش (ضوضاء) لنموذج قطعة(PMDوPDL):

بنفس النسق بالنسبة لتفاعل الإشارة والضوضاء، فإن المجال المحول $|\vec{b}\ (t_i) >$ يعطى بالصيغة:

$$|\vec{b}^D(t_i) > = B^D[P(\vec{\tau}, \vec{\alpha})|\vec{p}_s >]|s^0(t_i) >= B^D[P_{\alpha_0}|\vec{p}_s >]|s^0(t_i)$$
$$> + B^D[P_{\alpha_\perp}|\vec{p}_s >]|s^0(t_i) >$$

$$|\vec{b}^D(t_i) > \equiv \tilde{b}_{\alpha_0}^D \otimes |\vec{\alpha}_0 > + \tilde{b}_{\alpha_\perp}^D \otimes |\vec{\alpha}_\perp > \qquad (21)$$

حيث $|b^D(t_i) >$ تمثل مجال الانتقال، وتعطى على الصورة:

$$|b^D(t_i) > = U^\dagger(O^n)^\dagger R_{ns}^n|s^o(t_i) >= B^D|s^0(t_i) > \qquad (22)$$

بالتالي فإن التيار المصفى كهربائيًا والناتج من تفاعل الإشارة والضوضاء يعطى بالعلاقة:

$$y_{ns}(t_i) = \langle \vec{Z}|\vec{b}^D(t_i)\rangle + c.c.$$
$$= \langle Z_{\alpha_0}|\tilde{b}_{\alpha_0}^D(t_i)\rangle + \langle Z_{\alpha_\perp}|\tilde{b}_{\alpha_\perp}^D(t_i)\rangle + c.c. \qquad (23)$$

استنتاج معدل الخطأ النبضي (BER) باستخدام دالة توليد العزوم (MGF):

بناءً على التيار الناتج$y(t)$يمكن الحصول على دالة توليد العزوم (MGF) عن طريق حساب المتوسط على الضوضاء عندالمسار (3) في الشكل السابق وذلك باستخدام الصيغة التالية:

$$\langle e^{s(c^2+2ca)}\rangle = \int \frac{dc}{\sqrt{2\pi\sigma^2}} e^{-\frac{c^2}{2\sigma^2}} e^{s(c^2+2ca)} = [1-2\sigma^2 s]^{\frac{1}{2}} e^{\frac{2\sigma^2 s^2 a^2}{1-2\sigma^2 s}} \qquad (24)$$

بالتالي يمكن كتابة دالة توليد العزوم(MGF) للتيار $y(t)$ الذي تمت تصفيته على الصورة:

$$\psi_{t_i}(s) = \langle e^{s[y(t)]} \rangle = e^{sy_{ss}(t)} \prod_{m=1}^{2M+1} \frac{e^{\frac{s^2 2\sigma^2 |\tilde{b}_m^D(t_i)|^2}{1-s\beta_m}}}{(1-s\beta_m)^2} \qquad (25)$$

⟨...⟩ يمثل المتوسط على المتغيرات العشوائية , $y(t)$ يتألف من ثلاثة أجزاء في النظام البصري كما هو موضح في المعادلة (12). بالتالي يمكن كتابة الدلة المولدة للنظام على الصورة:

$$\psi_{t_i}(s) = \langle e^{s[y_{ss}(t)+y_{nn}(t)+y_{ns}(t)]} \rangle$$

$$= e^{sy_{ss}(t)} \prod_{m=1}^{2M+1} \frac{e^{\frac{s^2 2\sigma^2 |\tilde{b}_m^D(t_i)|^2}{1-s\beta_m}}}{(1-s\beta_m)^2} \qquad (26)$$

في هذا العمل، الرمز ⟨.⟩ يُشير إلى متوسط الضوضاء، و⟨.|.⟩ الرمز يشير إلى المنتج الداخلي الهرميتي. بالنسبة لدالة توليد العزوم (MGF)، يمكن الحصول على معدل الخطأ النبضي (BER) والذي يعتبر بارامتر الأداء الأساسي لنظام الاتصالات البصرية باستخدام العلاقة التالية:

$$BER_{y_{th}} = \frac{\pm 1}{2\pi j} \int_{C_\pm} \frac{\psi_{t_i}(s)}{s} e^{-sy_{th}} ds \qquad (27)$$

حيث y_{th} تمثل عتبة الكشف $BER_{y_{th}}$) يمثل معدل الخطأ في البتات عند عتبة الكشف)، بحيث تؤخذ حدود التكامل + و C_+ عندما يكون $y_{ss} > y_{th}$, بينما تؤخذ حدود التكامل − و C_- عندما يكون $y_{ss} > y_{th}$. بالتعويض عن دالة توليد العزوم (MGF) في المعادلة الأخيرة نتحصل على:

$$BER_{y_{th}} = \frac{\pm 1}{2\pi j} \int_{C_\pm} ds \frac{e^{-(y_{th}-y_{ss})s}}{s} \prod_{m=1}^{2M+1} \frac{e^{\frac{s^2 2\sigma^2 |\tilde{b}_m^D(t_i)|^2}{1-s\beta_m}}}{(1-s\beta_m)^2} \qquad (28)$$

متوسط معدلات الخطأ النبضي (BERs) على جميع البتات خلال الفترة $t_i = t_0 + kT_b$ تعطى بالعلاقة [10]:

$$BER = \sum_{i=0}^{N-1} BER_{y_{th}}(t_i)/N \qquad (29)$$

النتائج

أولا: دراسة تأثير تشتت نمط الاستقطاب (PMD) على بارامترات الأداء

في هذه المرحلة تم دراسة تأثير نمط الاستقطاب (PMD) على بارامترات الأداء المتمثلة في عامل الجودة (Q-Factor) ومعدل الخطأ النبضي (BER) ونسبة الإشارة البصرية للتشويش (OSNR) حيث تم الحصول على قيم عامل الجودة (Q-Factor) ومعدل الخطأ النبضي (BER) ونسبة الإشارة للتشويش (OSNR) على المراحل التالية:

1- دراسة تأثير تشتت نمط الاستقطاب (PMD) على عامل الجودة (Q-Factor)
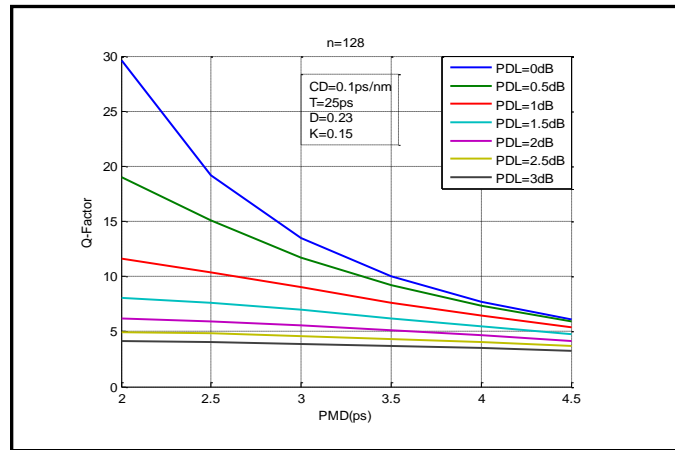
شكل(3) العلاقة بين تشتت نمط الاستقطاب (PMD) وعامل الجودة (Q-Factor) مع تغير الفقد الاستقطابي (PDL)

نلاحظ من خلال الشكل (3) أعلاه أنه كل ما زاد تشتت نمط الاستقطاب (PMD) والفقد الاستقطابي (PDL) قل عامل الجودة (Q-Factor), في المنحنى الأزرق كان الاضمحلال كبير, عندما كان (0 = PDL) وكان (0.5Ps = PMD) كانت أكبر قيمة لعامل الجودة (Q-Factor) ومع زيادة PMD و PDL النقصان في عامل الجودة يكون طفيف والاضمحلال يكون صغير وهذا بسبب التفاعل بين PMD و PDL.

2- تأثير تشتت نمط الاستقطاب (PMD) على معدل الخطأ النبضي (BER)
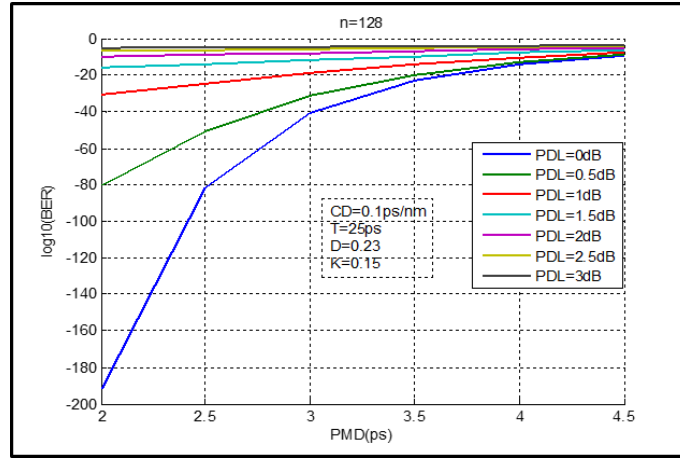
شكل (4) العلاقة بين تشتت نمط الاستقطاب (PMD) ومعدل الخطأ النبضي (BER) $\log_{10}$ مع تغير الفقد الاستقطابي (PDL)

نلاحظ من الشكل (4) أعلاه أنه يزداد معدل الخطأ النبضي (BER) بزيادة الفقد الاستقطابي (PDL) وتشتت نمط الاستقطاب (PMD) أفضل قيمة لمعدل الخطأ النبضي (BER) عند (0.5dB = PDL و PMD =2Ps)، مع زيادة PMD وPDL يقل الاضمحلال وذلك بسبب التفاعل بين PMDوPDL .

3- دراسة تأثير تشتت نمط الاستقطاب (PMD) على نسبة الإشارة البصرية للتشويش (OSNR)

نلاحظ من الشكل (5) أنه بزيادة تشتت نمط الاستقطاب (PMD) وزيادة الفقد الاستقطابي (PDL) يقل نسبة الإشارة البصرية للتشويش (OSNR), أفضل قيمة ل (OSNR) عندما كان (PDL=0dB و PMD=2ps).
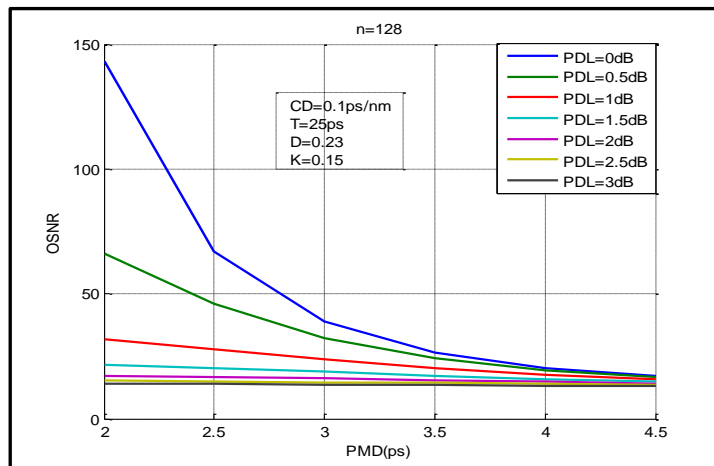
شكل (5) العلاقة بين تشتت نمط الاستقطاب (PMD) ونسبة الاشارة البصرية للتشويش (OSNR) مع تغير الفقد الاستقطابي (PDL)

ثانيا : تأثير الفقد الاستقطابي (PDL)على بارامترات الأداء

في هذه المرحلة تم دراسة تأثير الفقد الاستقطابي (PDL) على بارامترات الأداء المتمثلة في عامل الجودة (Q-Factor) ومعدل الخطأ النبضي (BER) ونسبة الإشارة للتشويش (OSNR), حيث تم الحصول على قيم عامل الجودة (Q-Factor) ومعدل الخطأ النبضي (BER) ونسبة الإشارة للتشويش (OSNR) حسب النموذج الرياضي المدروس باستخدام برنامج الماتلاب .

1-تأثير الفقد الاستقطابي (PDL)على عامل الجودة (Q-Factor)

نلاحظ من الشكل (6) أنه بزيادة الفقد الاستقطابي (PDL) وزيادة تشتت نمط الاستقطاب (PMD) يقل عامل الجودة (Q-Factor), ويكون أفضل قيمة (Q-Factor) عندما يكون (PDL=0dB) و PMD=2ps كما هو مبين في المنحنى الأزرق حيث كلما زاد كل من (PDL) و (PMD) يقل (Q-Factor) بشكل الكبير الأمر الذي يؤدي إلى إضعاف النظام ويقلل من كفاءته وجودة الإشارة المنتقلة عبر الليف.
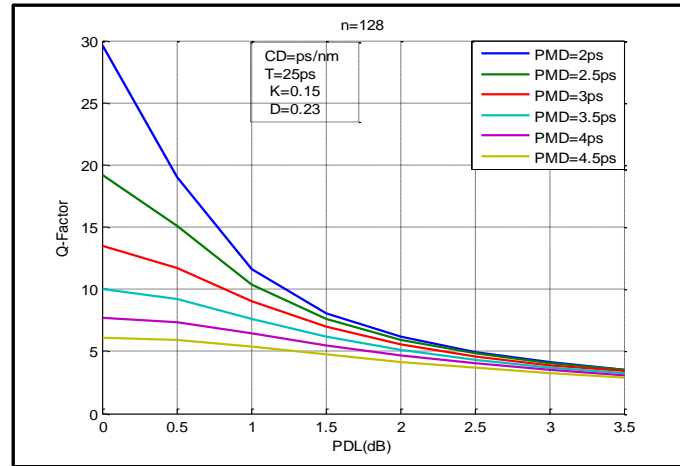
شكل (6) العلاقة بين الفقد الاستقطابي (PDL) وعامل الجودة (Q-Factor) مع تغير تشتت نمط الاستقطاب (PMD)

2- تأثير الفقد الاستقطابي (PDL)على معدل الخطأ النبضي (BER)
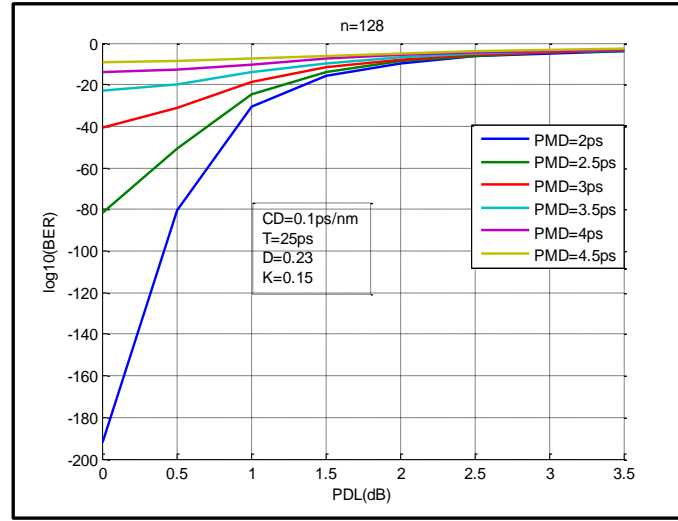
شكل (7) العلاقة بين الفقد الاستقطابي (PDL) معدل الخطأ النبضي $\log_{10}(BER)$ مع تغير تشتت نمط الاستقطاب (PMD)

نلاحظ من الشكل (7) أنه بزيادة الفقد الاستقطابي (PDL) وزيادة تشتت نمط الاستقطاب (PMD) يزداد معدل الخطأ النبضي (BER), ويكون أفضل قيمة (BER) عندما يكون (PDL=0dB و PMD=2ps) كما هو مبين في المنحنى الأزرق حيث كلما زاد كل من (PDL) و (PMD) يزيد (BER) بشكل الكبير الأمر الذي يؤدي إلى إضعاف النظام ويقلل من كفاءته وجودة الإشارة المنتقلة عبر الليف.

3- تأثير الفقد الاستقطابي (PDL) على قوة الاشارة البصرية بالنسبة للتشويش (OSNR)

من الشكل (8) يتضح أنه بزيادة الفقد الاستقطابي (PDL) وزيادة تشتت نمط الاستقطاب (PMD) يقل نسبة الإشارة البصرية للتشويش (OSNR), ويكون أفضل قيمة لـ (OSNR) عندما يكون (PDL=0dB وPMD=2ps) كما هو مبين في المنحنى الأزرق حيث كلما زاد كل من (PDL) و (PMD) يقل (OSNR) بشكل الكبير الأمر الذي يؤدي إلى إضعاف النظام ويقلل من كفاءته وجودة الإشارة المنتقلة عبر الليف.
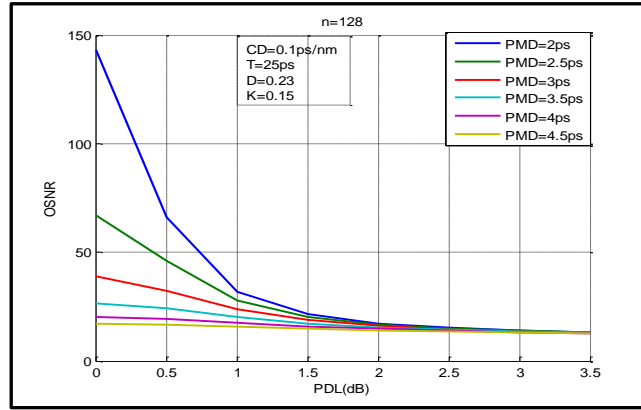
شكل (8) العلاقة بين الفقد الاستقطابي (PDL) ونسبة الإشارة البصرية للتشويش (OSNR) مع تغير تشتت نمط الاستقطاب (PMD)

الخلاصة

باستخدام الدراسة الرياضية التحليلية و برنامج الماتلاب لفهم الأسس العلمية لتأثير الفقد الاستقطابي على أنظمة اتصالات الالياف البصرية , تمت دراسة تأثير الفقد الاستقطابي على حساب معدل الخطأ النبضي (BER) للإشارات الخارجة من أنظمة اتصالات الالياف البصرية , و وجد انه بزيادة الفقد الاستقطابي (PDL) وزيادة تشتت نمط الاستقطاب (PMD) يزداد معدل الخطأ النبضي (BER), ويكون أفضل قيمة (BER) عندما يكون (PDL=0dB) و (PMD=2ps) , كما تمت دراسة تأثير الفقد الاستقطابي على عامل الجودة (Factor-Q) و وجدنا بزيادة الفقد الاستقطابي (PDL) وزيادة تشتت نمط الاستقطاب (PMD) يقل عامل الجودة (Q-Factor), إضافة الى ذلك تمت دراسة تأثير الفقد الاستقطابي على نسبة الإشارة الى للتشويش المستقبلة في اجهزة الاستقبال (OSNR) أوضحت الدراسة انه بزيادة الفقد الاستقطابي (PDL) وزيادة تشتت نمط الاستقطاب (PMD) يقل نسبة الإشارة البصرية للتشويش (OSNR) . أوضحت الدراسة ان أفضل قيمة (Q-Factor) ومعدل الخطأ النبضي وكذلك نسبة الإشارة البصرية للتشويش عندما يكون PDL=0dB وPMD=2ps.

References   المراجع

1- Shahada al Mwssa, Moieen Yonees, Weal Hassan sakr, "DMT Modulation is the Best Option for Digital Subscriber Line VDSL", Journal for Studies Scientific Research-Engineering Sciences Series Vol.28, No.2, 2006.

2- Rouba Daoud, "Studying and Analyzing the modulators and Demodulators of PCM", Tishreen University Journal for Studies Scientific Research-Engineering Sciences Series Vol.40, No 4, 2018.

3- Sudhir Babu, K.v Sambasiva Rao, " Evaluation of BER for AWGN, Rayleigh and Rician Fading Channels under Various Modulation Schemes", International Journal of Computer Applications" Vol. 26 ,No.9,July 2011.

4- N.Gisin, "The statistics of polarization-dependent loss" Opt,Commun, vol.144,pp.399-405,1995.

5- A.Mecozzi and M.shtaif, "The statistics of polarization-dependent loss in optical communication systems", IEEE Photon. Techonol. Lett, vol.14, 2002.

6- Zhongxi Zhang, Liang Chen, Xiaoyi Bao "Accurate BER evaluation for lumped DPSK and OOK systems with PMD and PDL" OPTICS EXPRESS Vol. 15, No. 15, 2007.

7- Farhan Hussain and M.S.Islam "Limitation Imposed by Polarization-Dependent Loss on a Fiber Optic Communication System", Engineering and Technology International Journal of Electronics and Communication Engineering, Vol:4, No:8, 2010.

8- Maxim Kuschnerov, Mohamed Chouayakh, Kittipong Piyawanno, Bernhard Spinnler, Mohammad S. Alfiad, Antonio Napoli, and Berthold Lankl, "On the Performance of Coherent Systems in the Presence of Polarization-Dependent Loss for Linear and Maximum Likelihood Receivers" IEEE PHOTONICS TECHNOLOGY LETTERS, VOL. 22, NO. 12, JUNE 15, 2010.

9- Yangzi Liu, Peter Shepherd and Duncan Allsopp, "Polarization Dependent Loss Emulator Built with Computer-driven Polarization Controllers and Single Mode Fibre", In Proceedings of the 6th International Conference on Optical Communication Systems (OPTICS-2015), pages 42-47.

10- Brian T. Kirby, Daniel E. Jones, and Michael Brodsky, "Effect of Polarization Dependent Loss on the Quality of Transmitted Polarization Entanglement", J. OF LIGHTWAVE TECHNOLOGY, VOL. 37, NO. 1, 2019.

11- Jahangir Alam S. M., M. Rabiul Alam. Hu Guoqing, Zakirul Mehrab, "Improvement of Bit Error Rate in Fiber Optic Communications", International Journal of Future Computer and Communication,Vol.3,No.4, August 2014.

12- M.A O thaman ,M,M,Ismail "erbium doped fiber amplifier (EDFA) for C – band optical communication system, JETIJENS 2012.

13- span katiyar, "Optical Communications", frist edition, New Delhi,2010.

14- A.Cem COKRAK ,Ahmet ALTUNCU" Gain and noise performance of erbium doped fiber amplifier, "J. OF ELECTRONIC ENGINEERING,2004.

15- Silvano Donati, Guido Giuliani, "Noise in an Optical Amplifier:Formulation of a New Semiclassical Model",IEEE J.OF QUANTUM ELECTRONICS, VOL.33,NO.9,1997.

16- Rajdi AGALLIU, Michal LUCKI, "BENEFITS AND LIMITS OF MODULATION FORMATS FOR OPTICAL COMMUNICATIONS", OPTICS AND OPTOECTRONICS,VOL.12, No. 2,2014.

17- Farhan Hussain and M.S.Islam "Limitation Imposed by Polarization-Dependent Loss on a Fiber Optic Communication System", Engineering and Technology International Journal of Electronics and Communication Engineering, Vol:4, No:8, 2010.

18- Zhongxi Zhang, Liang Chen, Xiaoy Bao, "Moment-generating function method used to accurately evaluate the impact of linearized optical noise amplified by EDFAs", arxiv:1207.3362v2 [physics. optics]18Jun 2013.

19- T. S. Khatavker, D.S.Bormane, "OSNR CHALLENGE IN DWDMLINK ",INTERNATIONAL JOURNAL OF ELECTRONICS AND COMMUNICATION ENGINEERING AND TECHNOLOGY(IJECT),Vol. 5, No.2, (2014).

20- Stamatios V. Kartalopoulos, "FREE SPACE OPTICAL NETWORKS for Ultra- Broad Band Services",Johan and Sons, Inc., Hobken,2011.

21- Mohamed Elbawab, Mohamed Abaza and Moustafa H. Aly,"Relay Selection Schemes for FSO Communications over Turbulent Channels", 2018.

22- EDWARD COLLETT, "POLARIZED LIGHT IN FIBER OPTICS", Library of Congress Cataloging-in-Publication Date 2003.

23- Abdelkerim Amari, Octavia A. Dobre, Ramachandran Venkatesan, O.S.Sunish Kumar, Phihippe Ciblat, and Yves Jaouen" A survey on fiber nonlinearity compensation for 400 Gbps and beyond optical communication systems", 2017.

Mitigation of DDoS Attack in SDN Technology Using Load Balancing Policy

H. Alshrif[*], B. Ghariba[2]

[1] hmalshrif@elmergib.edu.ly, [2] bmghariba@elmergib.edu.ly

[1] Department of Electrical and Computer engineering, College of Engineering, Elmergib University, Libya

[2] Department of Electrical and Computer engineering, College of Engineering, Elmergib University, Libya

1 ABSTRACT

Software Defined networking (SDN) is a new network technology that has been introduced to address the common issues in traditional networking. It provides central control by decoupling the control plane from network nodes and placing it in the controller. This allows the programmers to manage the entire network from one side. security issues, however, are challenging in this technology. There are many security issues in SDN networks, but Distributed Denial of Service (DDoS) is one of the biggest threats to SDN technology. This paper focuses on creating load balancing policy that can exploit the unutilized paths and use them for rerouting the packets in datacentres, we demonstrate how DDoS attack can exhaust the SDN network and provides the proper approach to deal with this attack in a short time. This method can be considered the first step to prevent the severe impact of attacks and alarm the system to block the attack ports.

Keywords: DDoS attack, SDN security, Load balancing.

2 Introduction

Software Defined Network (SDN) technology is a new networking architecture which is designed to allow programmers to manage the entire network from one side as well as to tackle some security issues that have increased in the last decade [1]. SDN was designed by decoupling the control plane from network devices such as routers and switches etc., and place it in a centralized controller; this controller is responsible for managing and configuring the whole network. Thus, applying new security policies and mechanisms would be much easier compared traditional networks. Therefore, designing new protocols and functions will be easy and powerful in order to enhance network security mechanism [2].

Security issues however, are considered an essential concern due to the increasing number of attacks which typically have harmful consequences, from stealing data to making the network collapse. These attacks include Denial of service (DoS), Distributed Denial of service (DDoS), Spoofing etc. they can cause tremendous

losses for companies and organizations. The security issues of the SDN model can be categorized depending on the SDN layer affected, i.e. Application layer, Application-Controller Interface, Control layer and Controller-Data Interface threats [3]. This paper will focus on the Control layer threats, and how they can be mitigated. This layer is the brain of the SDN architecture that manages the entire network, and if it fails, then the network will collapse. For this reason, intruders focus on attacks against the controller to cause severe damage such as system failure or crashes. The distributed denial of service attack is one of the biggest threats not only in traditional networks but also in SDN technology, and it mainly occurs at the network layer or application layer of the compromised system [4]. When the attack is launched to the network it causes bottleneck problems and overwhelms the CPU resources. Therefore, understanding the characteristics of the incoming data can be considered as a first step in detecting attacks. There is also another approach to deal with DDoS which is the load balancing policy. This policy can be implemented in the controller which is then responsible for managing the traffic within the network [5].

3   Related Works

The security threats of SDN are common to traditional networking, but in SDN network (centralized controller), the impact of attacks such as DDOS could be worse than that directed against a single router [6]. Attacking network devices, such as Routers and Switches, cannot be done in an SDN network as they only have a data plane, as the control plane is taken from these devices and placed in the SDN controller. However, SDN networks are not fully secured, there are some issues with detecting abnormal traffics and identifying whether the intrusion has a severe impact or not. Fast intrusion detection is also vital to react immediately, especially when DDOS takes place in the network. The early detection method based on Entropy (randomness of incoming packets) can classify the type of attacks using a fixed window widths which are 50 packets for DDOS attacks and 500 for slow DOS attacks [7]. Although the effectiveness of this method is exceptional, using a small window size can cause confusion to differentiate between normal and malicious traffic. There is also another approach to deal with DDOS which is the load balancing policy, this policy can be implemented in the controller which is responsible for managing the traffic within the network [8]. Basically, it reroutes the traffic and balances it between the links that can be used to get to the destination. Thus, during the attack, this policy will reduce the impact of exhausting the network with loads by balancing it between nodes and links; it can be considered a first step to deal with DDOS attacks.

4   Materials and Methods

4.1   SDN controller

OpenFlow controller is considered a strategic point or a brain in Software-defined network [9]. It simply manages the network and handles all communications between applications and network devices (such as Routers, Switches, etc.) to effectively modify the flow to meet changing needs by using a communication protocol called OpenFlow. There are many types of SDN controller such as Floodlight, Ryu, Nox, and Pox. Each one has its own advantages and programming language. Ryu controller has been used in this paper due to its advantages as it is an open source, supports OpenStack and is well-tested. It is also written in python and supports various protocols for managing network devices such as OpenFlow 1.0, 1.2, 1.3, 1.4, 1.5, and Nicira Extensions [10]. Ryu controller can be used remotely to manage the network topology in Mininet by using its IP as follows [10]:

```
$ sudo mn --controller=remote,ip=[controller IP],port=[controller listening  port]
```

4.2   System design and requirements

The SDN network of Open V Switches, hosts, links, and controllers has been created virtually by using a network emulator called Mininet. It supports research, prototyping, testing, and any task that could benefit from having a complete experimental network that can be deployed on real hardware for performance evaluation [11]. Mininet provides a very good alternative to physical SDN networks for development, testing, and evaluation. The network that has been created by this program simulates a datacenter called a fat tree network as is shown in figure 1; it consists of two types of switches, Core switches, and Edge switches. Edge switches are connected to the servers; three servers in each Edge switch, whereas Core switches are connected to all Edge switches to maintain availability. Two other servers were added by Mininet, the first one is a testing server which is used to test the behavior of the network as it is like an attempt to access the network by normal users, and ping packets will be used to simulate this matter, from which we will gather some information such as the response time between the testing server and the datacenter server, and the number of dropped packets. The other servers (Zombies) were added for launching controlled attacks (DDoS) using an IPERF (Internet Performance Working Group) tool which is a commonly used network testing tool that can create TCP and UDP packets and measure the throughput of a network between two nodes.It allows the user to set various parameters that can be used for testing a network, or alternatively for

optimizing or tuning a network [12].
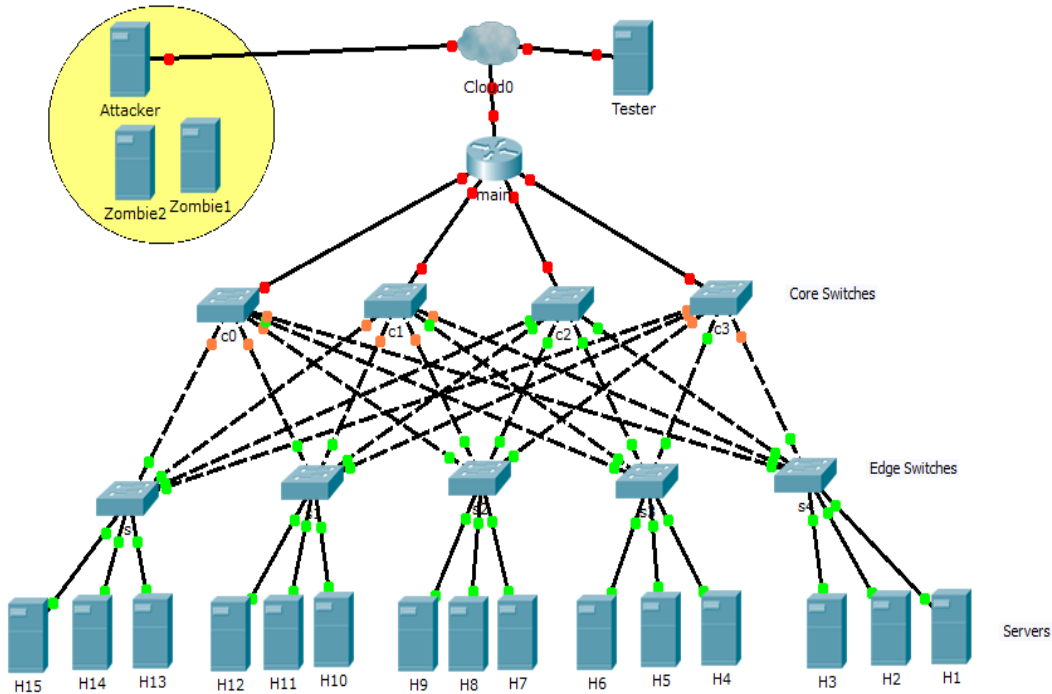
Figure 1. Fat tree topology of Datacenter with zombie's area

5   Theory and Calculation
5.1   Static policy
In the static policy, the SDN controller pushes the open flow table to the open V switches depending on the best route between each server. So the switches will assign each port a priority value and the MAC address of a server. Then the switches can identify where to forward the packets by using previous values as long as the network remains fixed (unchanged). However, if there are new devices connected to the network or the target of the incoming packet is not located in the routing table. Then the switch will send it to the controller which will update the routing table of the switch by sending back the proper route for that packet.

5.2   Load balancing policy
Load balancing policy distributes traffic intelligently between links in the network, it is adaptive, which continuously keeps making changes to the OpenFlow table of SDN switches. Using this policy in the controller allow us to find the best route at a specific time and send the update information to all

switches. Under high load flow, this policy will determine the unutilized switches and change the OpenFlow tables depending on that traffic. Figure 2 shows load balancing policy updating flow table diagram.
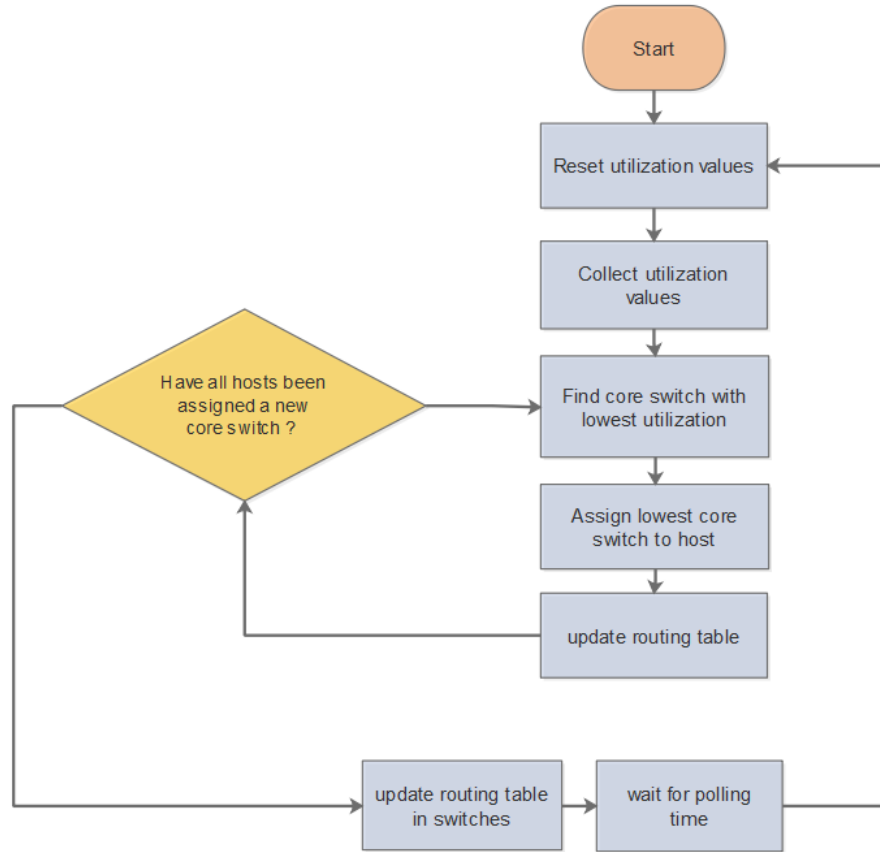
Figure 2 : Load balancing policy flow diagram

Evaluating these policies depend on two factors, time latency and throughput. These factors are considered the most crucial characteristics that measure the performance of a network. Latency is defined as the total time taken for a complete message to arrive at the destination. Networks with a longer delay have high latency, while those with fast response times have low latency. The second factor is throughput which is defined as the number of messages successfully transmitted per unit of time as in the equation below [13]:

$$Throughput = \frac{T}{D} \qquad (1)$$

Where T is the amount of the transferred data and D is the time duration (specific period of time).

6   Results and Discussion

The network topology that has been conducted in this paper is fat tree topology with one external server for testing and zombies for launching DDoS attacks. Table 1 shows experiments that has been conducted with low, medium and high load traffic flow against server 2 and 5.

Table 1: *Requirements of DDoS experiment*

Requirements	Experiment1	Experiment2
Datacenters links	Bandwidth = 5MB, queue_size = 1000, and delay = 1ms.	Bandwidth = 5MB, queue_size = 1000, and delay = 1ms.
Main switch links	Bandwidth = 10MB, queue_size = 1000, and delay = 3ms.	Bandwidth = 10MB, queue_size = 1000, and delay = 3ms.
Attack Loads	two levels of traffic flow are used, low (1MB), medium (2MB).	level of traffic flow are used, high load (10MB).
Victim	Server 2 and server 5 are the targets	Server 2 and server 5 are the targets

6.1   low and medium load evaluation

The graphs in Figure 3 below show how both policies, static and load balancing, manage the traffic flow of the network under low and medium loads. Experiments 1 and 2 show no noticeable change of average time response either in static or load balancing policies. The reason for that is that the network characteristics (especially Bandwidth) can accommodate the traffic flow without dropping any packets.
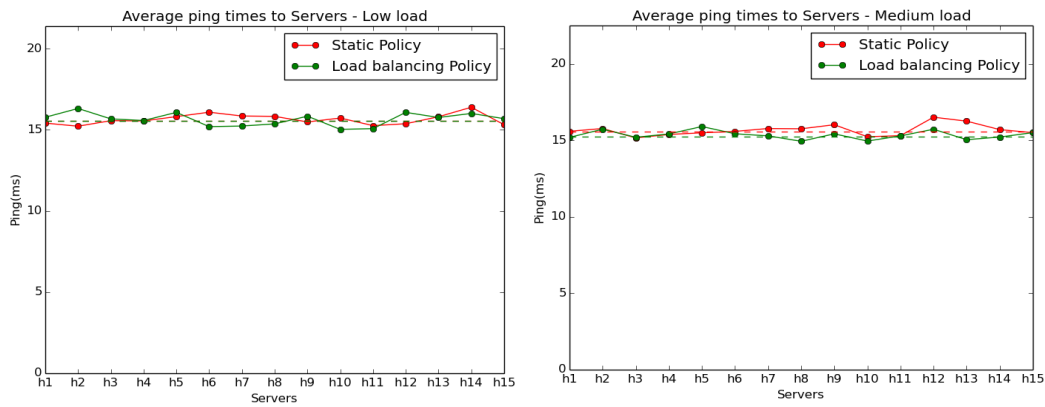
Figure 3: Average ping times to servers under low and medium loads

From the figure above, the ping response time is nearly the same in both policies, but in terms of power resources, load balancing policy consumes power and time to calculate the unutilized path continuously, unlike the static policy that uses a fixed routing table to forward packets to the destination.

6.2   high load evaluation

zombies servers have been used to attack two servers at the same time in order to exhaust the network or even to fail it. The targets were h2 and h5, and the load was different from the first experiment (high load 10MB), the dropped packets in static policy were extremely high and we can say that the network crashed under this policy, whereas the response time to servers under load balancing policy was incredibly short compared to the static policy.
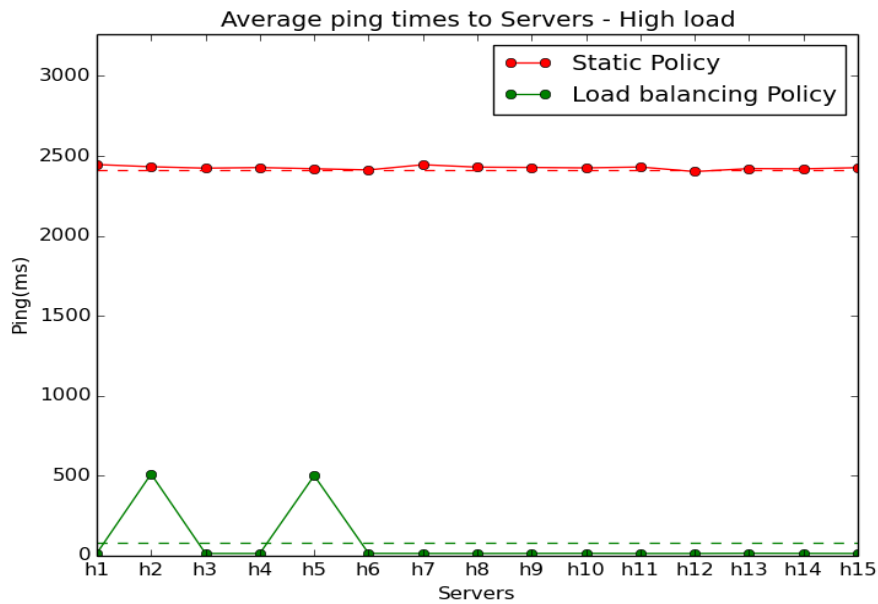
Figure 4 : Average ping times to servers

As is clear in figure 4, the average response times of servers under load balancing policy have an acceptable efficiency compared to static policy; moreover, the targets that have been attacked by zombies show an adequate improvement by utilizing the unusable paths, even the dropped packets in load balancing policy are almost nothing (only 11%) , while in static policy, around 70% of ping packets are dropped. The following Table 2 shows the comparison of both policies in terms of dropped packets, successful pings and ratio of dropped packets.

Table 2: *Ratio of dropped packets under high load attack*

Controller's policy	Dropped packets	Successful pings	Ratio of dropped packets	Servers that dropped pings
Static	219	81	73%	All server, but server 2 and 5 are unreachable.
Load Balancing	33	267	11%	Server 2,5

The throughput in static policy is approximately 17.408 B/s whereas in load balancing policy is 143.104 B/s which indicates the noticeable adaptation of load balancing policy to cope with high traffic flow by utilizing all the network links to avoid network failure.

Generally, We can say that rerouting the network traffic between links provides an incredible improvement in network behaviour which indeed assists the network to cope with DDoS attack, and reduces the impact of this attack to give the network administrator enough time to block vulnerabilities in the SDN system.

7   Conclusions

SDN networks have been investigated in terms of security, and there was an adequate study of policy approaches that prevent or even mitigate DDoS attacks. From the results we found how load balancing policy mitigate the severe impact of DDoS attack by rerouting the traffic between links in the centres. However, static policy caused SDN architecture failure. Furthermore, load balancing policy in high loads attacks against many servers coped with the change and showed a high efficiency in preventing bottlenecks and maintaining availability. Alarming the system is recommended to inform network administrator which server was under attack.

References

[1]   Kirkpatrik, K. , "Software-Defined Networking", *Communication of the ACM*, vol. 56, no. 9, pp. 16-19. 2013.

[2]   Shin, Seungwon, Lei Xu, Sungmin Hong, and Guofei Gu. "Enhancing network security through software defined networking (SDN)." In *2016 25th international conference on computer communication and networks (ICCCN)*, pp. 1-9. IEEE, 2016.

[3]   Scott-Hayward, Sandra, Sriram Natarajan, and Sakir Sezer. "A survey of security in software defined networks." *IEEE Communications Surveys & Tutorials* 18, no. 1 (2015): 623-654.

[4]   Barki, Lohit, Amrit Shidling, Nisharani Meti, D. G. Narayan, and Mohammed Moin Mulla. "Detection of distributed denial of service attacks in software defined networks." In *2016 International Conference on Advances in Computing, Communications and Informatics (ICACCI)*, pp. 2576-2581. IEEE, 2016.

[5]   Belyaev, Mikhail, and Svetlana Gaivoronski. "Towards load balancing in SDN-networks during DDoS-attacks." In *2014 international science and technology conference (modern networking technologies)(MoNeTeC)*, pp. 1-6. IEEE, 2014.

[6]   Hu, Zhiyuan, Mingwen Wang, Xueqiang Yan, Yueming Yin, and Zhigang Luo. "A comprehensive security architecture for SDN." In 2015 18th International Conference on Intelligence in Next Generation Networks, pp. 30-37. IEEE, 2015.

[7]   Oshima, Shunsuke, Takuo Nakashima, and Toshinori Sueyoshi. "Early DoS/DDoS detection method using short-term statistics." In 2010 International Conference on Complex, Intelligent and Software Intensive Systems, pp. 168-173. IEEE, 2010.

[8]   Belyaev, Mikhail, and Svetlana Gaivoronski. "Towards load balancing in SDN-networks during DDoS-attacks." In 2014 international science and technology conference (modern networking technologies)(MoNeTeC), pp. 1-6. IEEE, 2014.

[9]   Sdxcentral (2017) 'What is an OpenFlow Controller?' [online] available from   https://www.sdxcentral.com/sdn/definitions/sdn-controllers/openflow-controller/

[10]   Ryu (2017) Building SDN agilely [online] available from < https://osrg.github.io/ryu/>

[11]   Mininet (2017) Mininet: An Instant Virtual Network on your Laptop (or other PC) [online] available from < https://mininet.org/>

[12]   iPerf (n.d.) iPerf - The ultimate speed test tool for TCP, UDP and SCTP [online] available from https://iperf.fr/>

[13]   ETSI. 2012. "Throughput Measurement Guidelines." Etsi. European Telecommunications Standards Institute. Access online on 22 september 2022 at https://docslib.org/doc/9842978/throughput-measurement-guidelines

Towards adopting Virtual Computing Labs in Libyan Higher Education Institutions

Elmarash[2] Abubker Abdelsadiq[1*], Gharsa

[1] abubkr.abdelsadiq@elmergib.edu.ly, [2] gharsa.ali@elmergib.edu.ly

[1,2] Department of Computer Science, College of Science, Elmergib University, Libya

ABSTRACT

The majority of the IT infrastructure in Libyan universities is out-of-date and unable to support the demands of the present-day educational system. Computer laboratories constitute the corner stone of the practical sessions in IT colleges. In which students struggle to fulfil their practical lessons, and prepare course's assignments. Fortunately, Virtual Computing Labs (VCL) introduce a promising alternative supported by the big advances in cloud computing. In this research we found that the implementation of VCLs bring in flexible access, instant feedback, on the fly maintenance, top-notch equipment and lower costs which are considered as some of the great benefits wins the competition with physical computer labs. Based on Azure Lab Services as a virtual computer lab layer and Microsoft Teams as a collaboration layer, a collaborative VCL architecture that can replace the on-campus traditional labs is proposed.

Keywords: E-learning, Cloud computing, Virtual Computing Labs.

1   Introduction

Computer labs are a crucial component of the instructional environment in computer science departments and technology faculties in Libyan Higher Education Institutions (HEIs). Each lab contains up to 30 machines. Each machine has the necessary applications to conduct the practical sessions. The predominant operating system in use in college computer labs is Microsoft Windows. Equipment for computer labs that includes programs like C++ compilers, Java Virtual Machines, Eclipse, Netbeans, Visual Studio, Microsoft SQL Server, Microsoft Office, and other graphical design programs. Technical staff and IT departments' admins use the installed software to support the recognized curricula. However, missing or damaged apps, disconnections from the local server (if one existed), sluggishness, availability, a lack of internet connectivity, and out-of-date software are frequent complaints from students and faculty at Libyan HEIs. Fortunately, relying on Cloud Computing lab based VCLs is a quick and workable option to get beyond these issues. It is a service that enables numerous distant computers to connect to a single host

computer, where, users (students and teaching staff) can access files and other network resources, run programs on the host computer, and more by logging on to a terminal server. In computer labs in Libyan HEIs, the technology holds the promise of replacing the deteriorating infrastructure that is currently in existence. The term Cloud Computing refers to the on-demand, pay-as-you-go delivery of IT resources through the Internet. Through which technological services can be used from a cloud provider on an as-needed basis to access computing power, storage, and databases instead of purchasing, owning, and maintaining physical data centers and servers [1]. Great benefits of cloud computing include agility, elasticity, cost savings and fast deployment. There are three well-known technologies associated with Cloud Computing, specifically Software-as-a-Service (SaaS), Platform-as-a-Service (PaaS) and Infrastructure-as-a-Service (IaaS) [2]. A Lab-as-a-service (LaaS) is education platform called Virtual Computing Lab (VCL) is being suggested as well, and it offers a controlled environment for hands-on experiments using cloud-based lab technologies [3]. So, using VCLs students can remotely manage the virtual machines (VMs) and carry out the experimental activities without physically being in the lab by connecting over the internet by using their access credentials. In order to remedy the existing Lab infrastructure in Libyan HEIs the following models of cloud computing may be considered [4]:

1. IaaS (Infrastructure as a Service). A university's computational infrastructure is virtualized and shared for the purpose of solving internal tasks, including special software installation. This infrastructure may be used as a base for the creation and deployment of VCL.
2. PaaS (Platform as a Service). Virtualized resources with installed required packages are shared
3. SaaS (Software as a Service). The most common model of VCL representation is as a web-service, a successful example can be found in [2] and [3].
4. DaaS (Data as a Service). It is an additional model for providing data sources as a cloud services.
5. HaaS (Hardware as a Service). This model is used for sharing unique equipment, e.g., near-field scanning optical microscopes through an appropriate interface.

The next section presents the previous studies. Following that we present important two VCLs models, Apache VCL, and Azure Virtual Service, we show their important architecture aspects and discuss how they are provisioned as a LaaS to help HEIs in the teaching and learning process. In Section 4 we discuss the appropriate VCL architecture that we should adopt in HEIs Libya. Finally, we discuss our research and draw conclusion with future work, in Section 5 and 6 respectively.

2   Related work

Over the past few years, cloud implementations in higher education institutions have steadily grown [5], [6], with many academic institutions now utilizing one or more cloud services. With its promise to supply a variety of computer services in a way that has never been seen before, cloud computing represents a new paradigm in computing in HEIs [7]. It is likely to reduce expenditure and also reduce labor-related costs, as less people (e.g., technicians, admins) than before will be required to run a cloud-based IT infrastructure [8], [9]. The Virtual Computer Laboratory (VCL) was founded in the spring of 2004 [10] with the goal of giving students and researchers dedicated remote access to a variety of computing environments from any networked location, on or off campus, the VCL code base was approved as an incubator project by the Apache Software Foundation (ASF) in November 2008, VCL became an Apache top level project in June 2012. VCL became an Apache top level project in June 2012 [10]. In another study in Georgia State University the authors presented a collaborative virtual computer lab (CVCL) environment to support collaborative learning in cloud-based virtual computer labs, a setting that allows students to reserve virtual computers labs with multiple participants and support remote real-time collaboration among the participants during a lab. In this study we proposed different model of CVCL architecture based on Azure Lab services and Microsoft teams.

3   Virtual Computing Labs Technologies

Different cloud computing lab technologies that aim to provide LaaS are exist. For the purpose of this study in this section we present two main technologies that can help HEIs with limited budget to go for virtual labs instead of on-campus labs, Apache Virtual Computing Laboratory (VCL) and Azure Lab Services. The VCL is an open-source implementation of on-demand utility computing and services-oriented technology providing wide-area access to solutions based on virtualized resources, including compute, storage, and software resources. It is defined by University of North Carolina campuses [10]. While Microsoft's Azure Lab Services [11] is a service that makes it easier to manage the infrastructure for virtual computer labs on the Azure cloud. From setting up, starting, and terminating virtual machines to scaling infrastructure, it manages every aspect of computer lab infrastructure. Administrators can simply set up labs for classes, decide how many and what kind of VMs participants need, and add people to classes. Users of the lab only need to register in order to access the VM and complete activities in class.

3.1   Apache Virtual Computing Lab

Apache VCL platform depicted in Figure1 considered the most widely used virtual computer lab system, it is a free and open-source cloud computing platform with the primary goal of delivering dedicated, custom compute

environments to users [10], which was initiated at North Carolina State University (NCSU) for applying cloud computing to teaching and learning [12] . VCL supports provisioning several different types of compute resources including physical bare-metal machines, virtual machines hosted on several different hypervisors, and traditional computing lab computers you would normally find on a university campus [10]. When a user uses a program via VCL, the program runs on the server and VCL allows the user to control that program from his/her own computer. The VCL is equipped with user interface consists of a self-service web portal. Using the portal, students and faculty can access software and applications that were typically only available while on campus in a lab or via individual software purchase and installation [12].
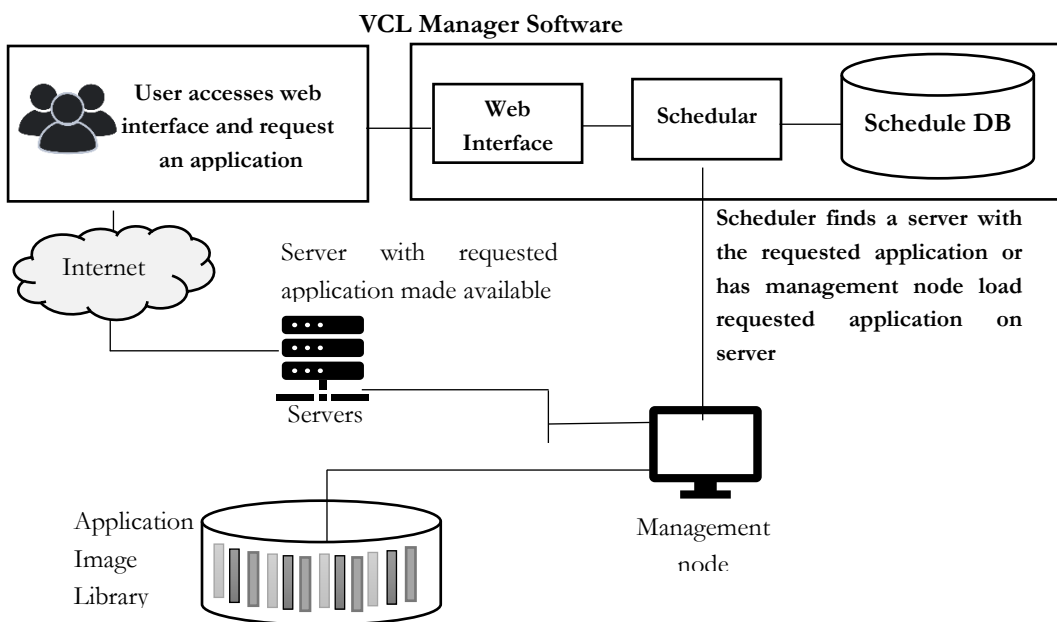
Figure 1 Apache VCL [10]

3.2   Azure Lab Services

Microsoft Azure Lab Services is a service that enables the virtual computer laboratory infrastructure administration and management in the Azure cloud. It manages all aspects of the infrastructure of a computer lab, including setting up, starting, and stopping virtual machines as well as expanding the infrastructure as needed. Administrators may easily set up laboratories for classes, decide how many and what kind of VMs participants need, and add users to classes. Users of the lab only need to register in order to access the VM and complete activities in class. Figure 2 shows an overview of Azure Lab Services [13]. The benefits of using Azure Lab Services include the following [7].

• Since Azure Lab Services manages VMs and lab access and provides supporting infrastructure like operating system images, laboratory setup can be completed more quickly and flexibly. This frees up laboratory administrators to concentrate on laboratory setup as needed.

• User-friendliness through the use of access protocols that can be used on a variety of operating systems and regular desktop and laptop computers as well as a straightforward registration process.

• Vlab consumption charges are only estimated when the VM is active to ensure accurate and efficient cost computation. The VM schedule policy can be configured by administrators to automatically turn on and off the VM when not in use.

Through VCL, users who previously had to visit to a computer lab or install hardware and software on their own machines may now access it remotely. Additionally, as it can frequently be difficult for various applications to coexist on the same machine, it reduces the workload that computer labs must bear in order to keep numerous applications on individual lab machines.
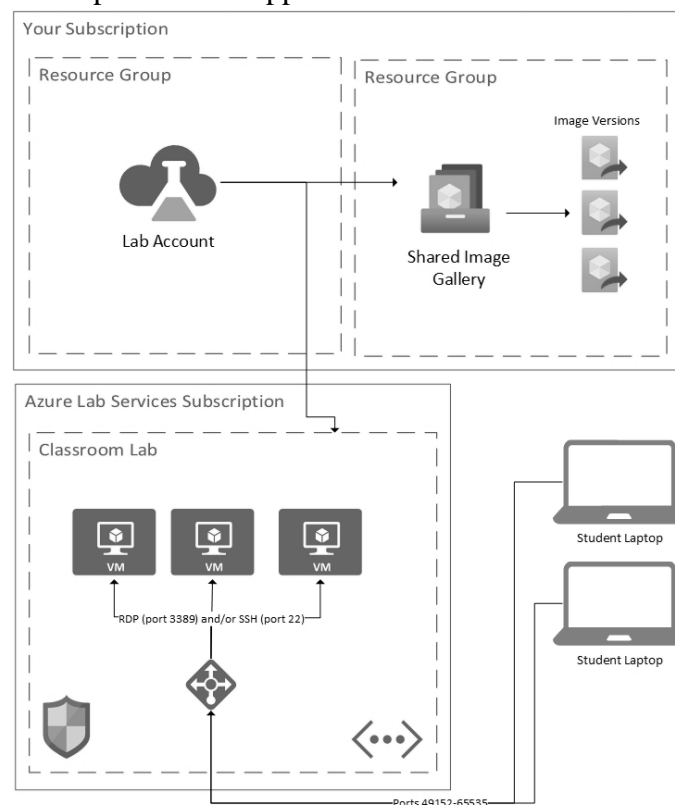
Figure 2 Overview of Azure Lab Services infrastructure [14]

For Lab administrators, a great management tool provisioned through VCL over Azure Lab Services is that it keeps operating system images with the

required apps and unique configurations and deploys them to a server as needed in response to user requests. This would significantly contribute in a better management in terms of quick installations and dynamic changes in course's requirements. Faculties, IT departments and students all share the benefits of such great technology. IT department, for example, Manage Azure Portal, create the University environment and set up access to on-premises resources if existed. Whereas, the faculty manages lab service portal, they can easily and flexibly implement virtual machine gallery for easy customization. Following that, students use Lab Service portal to access from any where using remote desktop connection that is available on every operating system or web client. Azure Lab Services offers new approach for service education institutions in general to help students learn computer programs. Just a few things are required to get it going. No matter how many students are registered or how complicated the virtual machine is, schools may easily configure and launch classes. Gratitude to Azure Labs, with a minimal management and supervision, no longer are students required to complete their coursework in a physical computer lab. The price structure Azure Labs also enables faculties to plan their budgets for the semester and maximize utilization of their budget with no loss. Finally, in this regard, Azure Labs clearly offers students a practical and cost-effective way to acquire the computer skills they will require during their educational journey.

4   Proposed VCL Architecture for Libyan HEIs

For Libyan HEIs we adopt a Collaborative Virtual Cloud Lab CVCL model presented in [12]. The CVCL environment uses a layered design to run on top of a virtual computer lab system that already exists, such as Azure. Two layers, a virtual computer lab layer and a collaboration layer make up the layered architecture, as depicted in Figure 3. The collaboration layer employs services from the virtual computer lab layer, it builds on top of Azure Lab Services, indicating a loose coupling between the two layers. Accordingly, the collaboration in the traditional lab might be accomplished utilizing our suggested design, ensuring that students do not lose out on the true benefits of cooperating in a virtual lab.
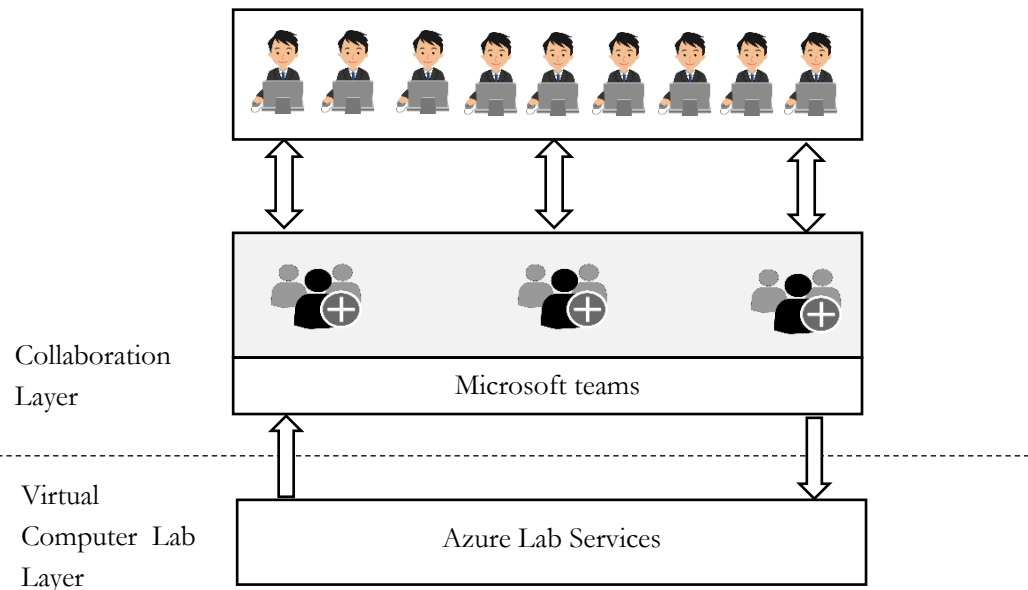
Figure 3 Collaborative Virtual Computer Lab on top of Azure Lab Services

For the purpose of bringing individuals together around tasks, interests, or other cooperation requirements, students groups established in Microsoft Teams [15] . Channels could be established within such teams to focus on a particular subject, area, or project. In Teams, meetings can be held in one of the channels where team discussions occur, files are saved, and files can be shared. Because of its flexibility, Microsoft Teams enables creating teams and channels that correspond to the needs and specific purposes.

5   Discussion

The tragedy of out-dated computer laboratories in Libyan HEIs never solved and would continue as long as there is no efficient alternative that is manageable and cost effective. As the cloud service in general follows a pay-as-you-go approach, the establishment of virtual Lab based on Azure Lab Services does not require capital expenditure investment, nor it needs extra labour requirements. So, the restrictions of high asset capital investment costs do not prevent the deployment of cloud-based such as Azure. The price of utilising cloud resources makes up the cost of developing a cloud-based Lab. Explicitly the configuration of the VMs, the applications needed, and any other features would determine the price of the laboratory. For instance, in a recent study [7], a virtual lab established on a university campus was contrasted with Azure based Lab with 50 VMs while taking the Total Cost of Ownership into account (TCO) [11], the later won the competition by 26% lower than his competitor. To this end, we stress that universities should think of the Cloud-based computer laboratories seriously. The advantages are countless, for instance:

- Increasing the accuracy and accessibility of data, software, and research materials.
- Increasing end users' mobility will make resources available wherever and whenever they are needed.
- Utilizing computational and application performance to its fullest.
- Offering a self-service portal and quick web access.
- Keep the budget to the Computer Labs' operational needs.

6   Conclusions

In this study, We discussed the difficulty with the HEIs' computer lab infrastructure in Libya. We presented two different cloud-based alternatives. On the basis of that, we proposed the cloud-based laboratories as a substitute solution, in order to transform the current scenario and provide educators and students with a better learning environment. Our proposed architecture considered the collaborations factor in practical studies as a main factor that should be included. Future study aims to implement virtual laboratory based on Azure Lab Services to teach a computer-programming course investigate its performance, usability and its real cost based on the available local resources and services.

References

[1] "Amazon Web Services," [Online]. Available: https://aws.amazon.com/what-is-cloud-computing/.

[2] Redhat, "Types of cloud computing," [Online]. Available: https://www.redhat.com/en/topics/cloud-computing/public-cloud-vs-private-cloud-and-hybrid-cloud.

[3] P. D. H. R. Pardeep Kumar, "Cloud Computing based Computer Science Lab : Laboratory-as-a-Service," *Journal of Network Communications and Emerging Technologies,* vol. 3, 2015.

[4] M. K. K. B. Alexey Dukhanov, "Design Virtual Learning Labs for Courses in Computational Science with use of Cloud Computing Technologies," in *14th International Conference on Computational Science*, 2014.

[5] M. R. Kritika Verma, "Impact of Cloud on E-Learning," in *5th International Conference on Computational Intelligence and Communication Networks*, 2013.

[6] B. D. M. M. M. P. P. S. S. S. A. D. waneesh Gupta, "Role of cloud

computing in management and education," *Elsevier ,* 2021.

[7] R. F. S. S. Dwi Susanto, "Cloud-Based Virtual Computer Laboratory Implementation – Object-Oriented Programming Classes," *Jurnal Nasional Teknik Elektro dan Teknologi Informasi,* vol. 11, no. 1, 2022.

[8] N. Sultan, "Cloud computing for education: A new dawn?," *International Journal of Information Management,* pp. 109-116, 2010.

[9] V. H. Pardeshi, "Cloud Computing for Higher Education Institutes: Architecture, Strategy and Recommendations for Effective Adaptation," in *Symbiosis Institute of Management Studies Annual Research Conference (SIMSARC13)*, 2014.

[10] A. VCL, "The Apachi Software Foundation," 20 June 2012. [Online]. Available: https://vcl.apache.org/.

[11] A. Microsoft, "Total Cost of Owner Ship Calculator," Microsoft, [Online]. Available: https://azure.microsoft.com/en-us/pricing/tco/calculator/. [Accessed 29 October 2022].

[12] H. L. A. G. B. Y. P. Xiaolin Hu, "Collabrative Learning in Cloud-Based Virtual Computer Labs," in *IEEE*, 2018.

[13] A. L. Services, "Azure Lab Services - Administrator Guide," Microsoft, 26 October 2022. [Online]. Available: https://learn.microsoft.com/en-us/azure/lab-services/administrator-guide. [Accessed 28 October 2022].

[14] A. L. Services, "Architecture Fundamentals in Azure Lab Services when using lab accounts," Microsoft, 31 05 2022. [Online]. Available: https://learn.microsoft.com/en-us/azure/lab-services/classroom-labs-fundamentals-1. [Accessed 29 10 2022].

[15] M. Teams, "Microsoft Teams help & learning," Microsoft , [Online]. Available: https://support.microsoft.com/en-us/teams. [Accessed 26 October 2022].

Enhancement of earth grid electrode performance by adding parallel-insulated conductor.

Asheraf Eldieb[1*], Salah Mousa[2],

[1] asheraf.eldieb@sabu.edu.ly, Salah.mousa@sabu.edu.ly[2],

[1,2] Department of Electrical and Electronic Engineering, College of Engineering, Sabratha University, Libya

1   ABSTRACT

The high-frequency performance of vertical earth rods is important for designing earthing systems and lightning protection systems, hence they have proved their advantages in order to protect electrical apparatus during severe lightning strikes, and an easy path for electrical current to ground was successfully achieved. The current distribution tests in the insulated and bare sections of the 88m horizontal electrode system were carried out at the Cardiff University outdoor earthing test facility at Llanrumney fields. Several test frequencies were used ranging from 52Hz to 100 kHz using the impedance measurement system (IMS) instrument, Impulse tests were carried out on the grid 5m×5m, 25 mesh with/without bonding to the 4.8m rod were measured with the Modular Impulse Generator (MIG) for a range of impulse rise times (~1.44-6μs). Examples of the transient voltage response (earth potential rise). It was concluded that the voltage distribution along the conductor at 52Hz is flat and the current flowing from the insulated conductor to the buried bare conductor. This paper would also illustrates experimental results of a grid with and without high frequency electrode enhanced with proposed insulated above ground conductor. The aim of this work is to improve impulse response performance by reducing the earth potential rise of the earth grid. This experimental work has proved that using insulated conductors in parallel with earth grid has significantly enhanced the impulse response; little reduction in voltage at slow rise time was noticed. However, the grid impedance effect has also been demonstrated at fast rise time.

Keywords: Current distribution, High frequency electrode, earth potential rise, impulse.

2   Introduction

One of the key indicators for evaluating the performance of earthing electrodes is their ability to dissipate ground fault current into the surrounding soil. In practice, this is usually translated into the requirement of achieving low earth resistance. Some standards [1, 2] provide guidelines for designing and evaluating

performance under power frequency, without much detail regarding high frequency and transient performance. Other standards [3, 4] recommend for high frequency performance either increasing grid mesh density in specific substation areas or adding vertical rods bonded to the main grid for earthing specific equipment. The benefits of adding vertical rods have been evaluated in [5], a study in which the high frequency and transient performance of substation earthing systems were assessed. In general, earthing electrodes and systems are commonly designed based on applying recommendations for meeting power frequency requirements, however, designing for transient and high frequency fault currents calls for consideration of other factors contributing to the electrode performance. Of practical significance, the current distribution between the conductors of the earthing system and the relative proportion of current dissipated by each of these conductors are factors worth considering since they may influence safety parameters such as earth potential rise and ground surface potential. To investigate the behaviour of the grid earth electrode under transient response, many different approaches have been adopted, and several different parameters have been proposed. The parameters used by many researchers include the dynamic impulse impedance $v(t)/i(t)$, the voltage peak to current peak ratio (V_p/I_p), and this is valid for characterizing concentrated earth electrodes having negligible inductance where the impulse current and voltage peaks occur at the same instant of time. In the case of high circuit inductance, which results in the instants of voltage and current peaks not to coincide, the ratio of voltage at peak current to peak current is used to avoid the inductive effect, this definition of the impulse resistance $(V@I_p /I_p)$ is commonly used [6]. In the PhD programme at Cardiff University [7], the current distribution tests in the insulated and bare sections of the 88m horizontal electrode system were carried out at the Cardiff University outdoor earthing test facility at Llanrumney fields. Several test frequencies were used ranging from 52Hz to 100 kHz using the impedance measurement system (IMS) instrument. It was concluded that the voltage distribution along the conductor at 52Hz is flat and the current flowing from the insulated conductor to the buried bare conductor. However, at higher frequency, both the voltage and current distributions in the insulated conductor show a fall in magnitude along the length of the conductor [8].

In another PhD programme [9], a new method has been proposed to increase the effective length of the 88m horizontal earth electrode by connecting an additional insulated parallel conductor bonded to the bare underground horizontal electrode at points along its length. The results were shown that the addition to such enhancement reduces inductance effects and helps dissipation of injected currents,

so that a greater length of buried earth conductor is utilised. Tests on an earth grid with and without enhancements were carried out at Llanrumney field site under low/high frequency and analysed in the deliverable HVE-PR-3. It was shown that the addition of a parallel insulated conductor has no major effect on the impedance of the earth grid at low frequency. However, at high frequencies, a reduction in impedance becomes apparent especially for the "enhanced two" then followed by the "enhanced one" and the "enhanced three" setups. In this paper, the transient impulse response of the earth grid electrode with and without above insulated conductor, buried in a non-uniform soil, was investigated experimentally at the Cardiff University outdoor earthing test facility at Llanrumney fields.

3   Experimental Setup

Figure 1 shows a schematic diagram of the purpose-built experimental setup of the 5×5m, 25 mesh earth grid at the Cardiff University earthing test facility at Llanrumney fields. The earth grid was bonded with a single copper rod with a 14 mm diameter and driven to 4.8m depth. Additionally, the grid was bonded with above-ground insulated conductors with cross-sectional area of 25mm2 in different configurations. Current was injected at the centre of the grid with a ring electrode used as the current return, as shown in Figure 1. A reference potential electrode was placed 150m away from the injection point and perpendicular to the return lead to minimise mutual coupling effects. Lilco current transformers of 0.1V/A sensitivity with a bandwidth of 20MHz were used for current measurements. Voltage measurement was achieved using a differential voltage transducer of 25MHz bandwidth and ratio of 1/20, 1/50 and 1/200 attenuation. To obtain the fast rise time, series resistances of 247Ω were used as shown in Figure 1. DC earth resistance tests were carried out using a composite earth tester (Megger DET2/2). Transient Impulse tests were carried out using Modular Impulse Generator (MIG2000-6). Figure 2 shows the setup of tests using Modular Impulse Generator (MIG2000-6). The charging voltage up to 6300 V, and the peak output voltage and current of the MIG are indicated on the front. The MIG0603-UL is a Hybrid or combination generator with a voltage wave shape 1.2/50 µs and a current wave shape 8/20 µs. The earth potential rise at the point of current injection in the test object was measured with respect to a remote reference electrode, fixed 100m away, and was connected by a lead placed orthogonal to the current return lead as shown in Figure 1. The test sources were supplied from an A.C. power supply via an isolation transformer.
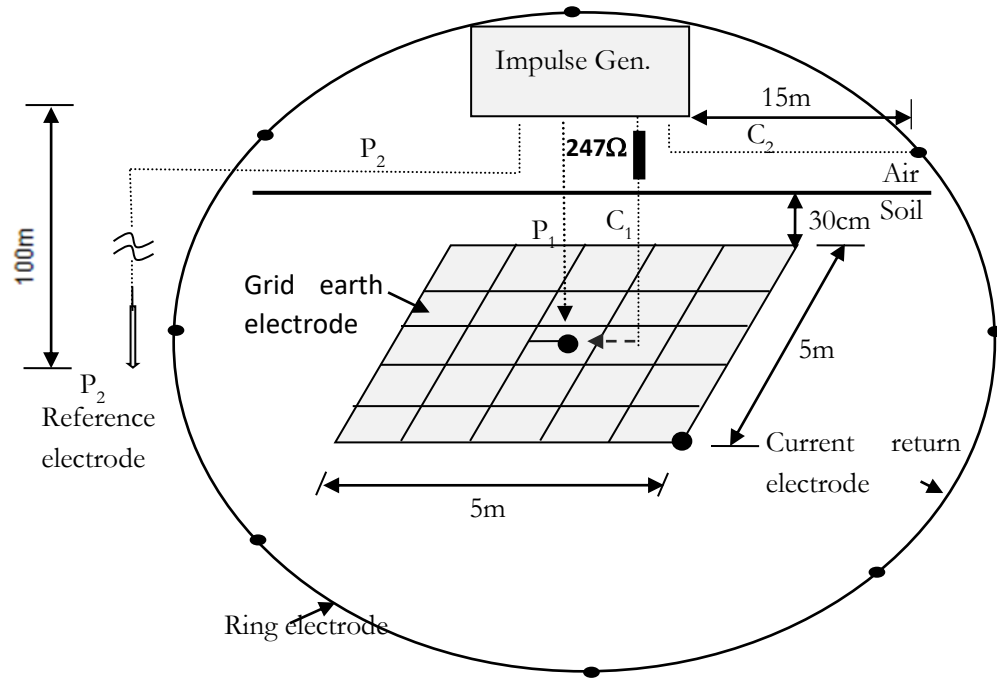
Figure 1: Test set-up for measurement of earth potential rise of grid 5m×5m, 25mesh
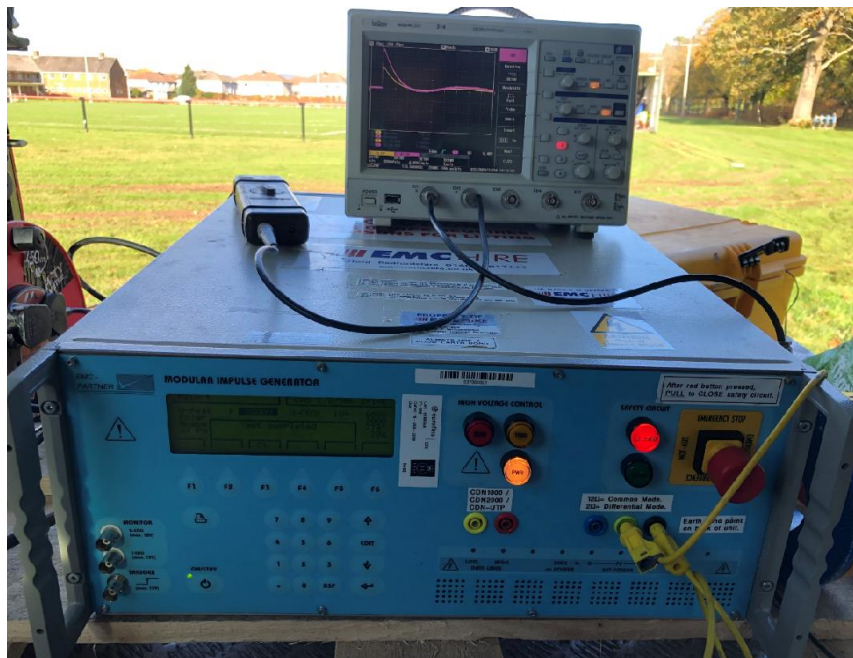
Figure2: Picture of MIG at field test site

4 Impulse Test Results and Discussions

Impulse tests were carried out on the grid 5m×5m, 25 mesh with/without bonding to the 4.8m rod were measured with the Modular Impulse Generator (MIG) for a range of impulse rise times (~1.44-6µs). Examples of the transient voltage response (earth potential rise) are shown in Figure 3. The grid with/without 4.8m rod, is subjected to 1.43/47 µsec impulse currents of 5.1 A amplitude. It can be seen from Figure 3 that the TEPR reaches its peak after the injected impulse current for the grid and rod only but much more quickly in the case of the grid with 4.8m rod. This highlights the effect of capacitive component which is greater for the bonded grid with the rod. Equation (1) is used where the instants of the impulse voltage peak and current peaks do not coincide, so as to eliminate any inductive effect in the test results. The equation of calculating the impulse resistance was used in this test. The comparison between measurement and simulation results for transient performance for these proposed enhancements will be investigated under fast impulse current injection using CDEGS 'FFT Module' in the future.

$$R_{imp} = \frac{V_{@I_P}}{I_P} \quad \ldots\ldots\ldots \text{ (1)}$$

Table 1 shows the peak TEPR voltages that occurred as a result of employing the various earthing systems. From Figure 3 and Table 1, it can be seen that bonding the 4.8m HF rod with the grid has the largest effect on reducing the peak TEPR.

Table 1: Effect of High Frequency Rod on Measured d Peak TEPR

Earth System Configuration	I_p (A)	Maximum (Peak) TEPR V_{pk}(V)	Percentage Decrease in TEPR with reference to rod Only%	Impulse Resistance R_{imp} (Ω)	DC Resistance (Ω)
Rod only	5.1	76.2	-	14.9	16.3
Grid only	5.1	51.8	32.1	9.9	8.6
Grid with HF Rod	5.1	39.3	48.4	7.7	6.9
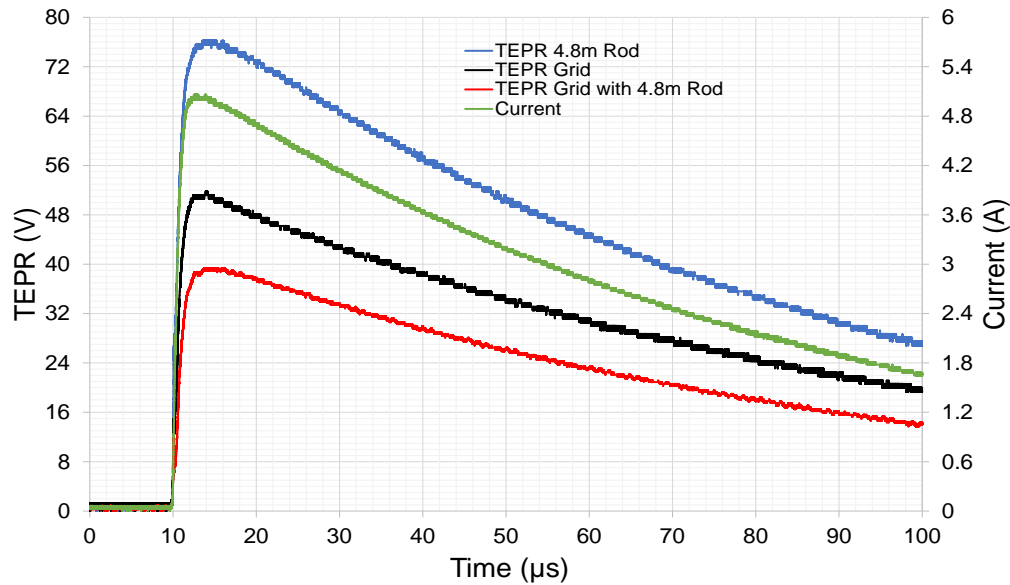
Figure 3: Voltage and current at injection point (grid 5m×5m, 25meshs)

In the previous deliverable, three proposals were selected to investigate the effect of bonding above insulated conductor with the bare grid under low/high frequency, all these proposals are shown in Figure 4. The current was injected at the centre of the grid. The horizontal enhancements and the down lead used to connect the current injection conductor to the grid are insulated. The tests were to investigate the benefit of bonding an insulated ground conductor to the 5m×5m, 25mesh grid. Figure 5 shows the effect of horizontal enhancements on the earth potential rise of the earth grid. The peak injected current was 5.1A with 1.43μs rise time at the injection point, and this is shown in Figure 1. Due to the fact that the cases where 'enhanced one', 'enhanced two' and 'enhanced three' configurations were employed, this produced the same TEPR curve, it is difficult to distinguish the separate curves from the figure. Therefore, the results were also tabulated. From the results presented in Table 2, it can be seen that the percentage reduction in the voltage of a grid with enhanced one, enhanced two and enhanced three scenarios are 22%, 24% and 24 % respectively compared to the grid only.

Table 2: Effect of Enhancements on Simulated Peak TEPR

Config	I_p	$V@I_p$	R_{imp}	V_p
Rod 4.8m	5.1	76.2	14.9	76.2
Grid	5.1	50.6	9.9	51.8
Grid with HF	5.1	38.7	7.7	39.3
Enhanced One	5.1	39.0	7.7	40.3
Enhanced Two	5.1	38.3	7.5	39.6
Enhanced Three	5.1	39.0	7.7	39.3

a)   Enhanced One

b) Enhanced Two
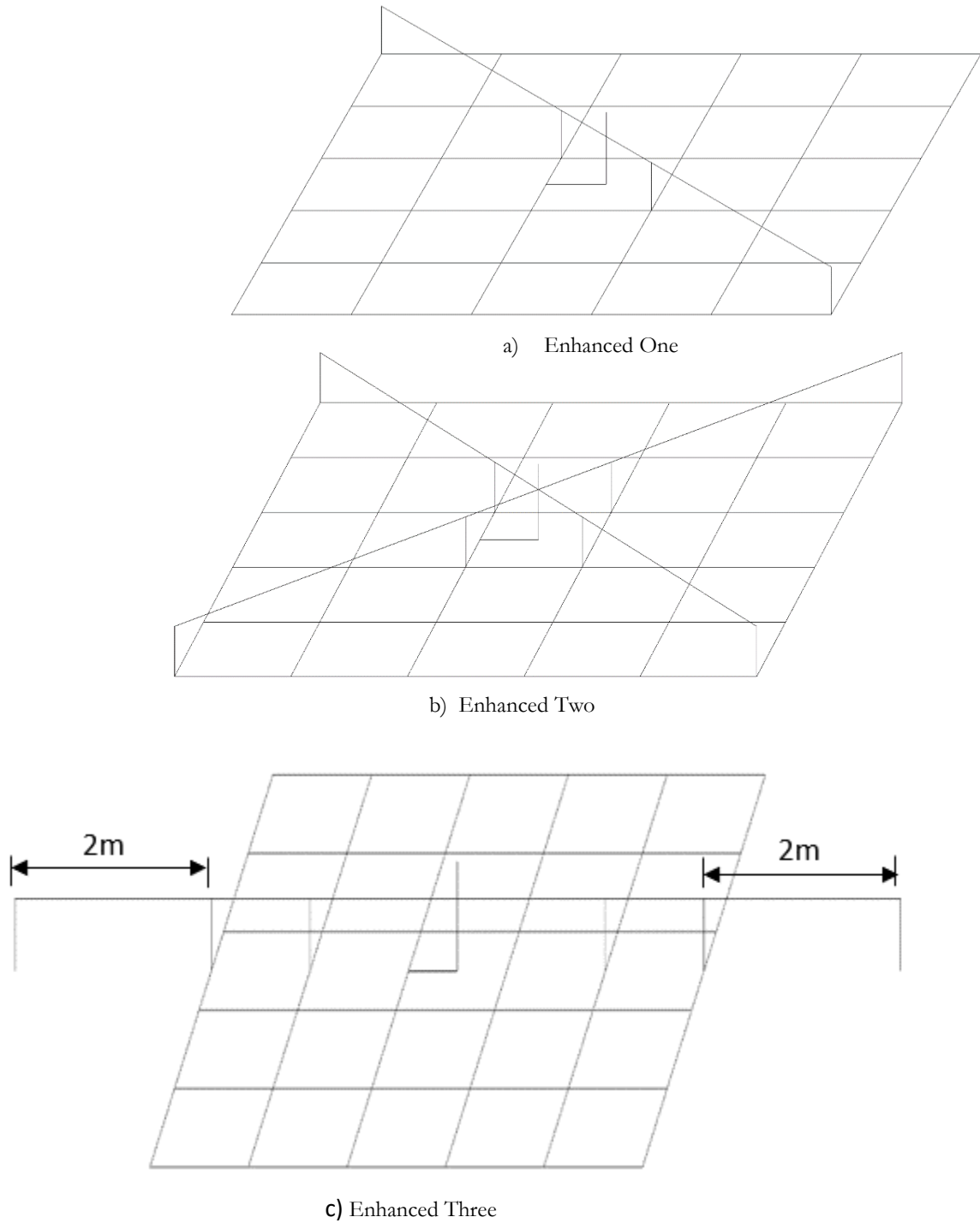
c) Enhanced Three

Figure 4: 5m x 5m Grid with above insulated conductor in enhanced configuration and Grid Centre Current Injection, a) Enhanced One, b) Enhanced Two, and c) Enhanced Three
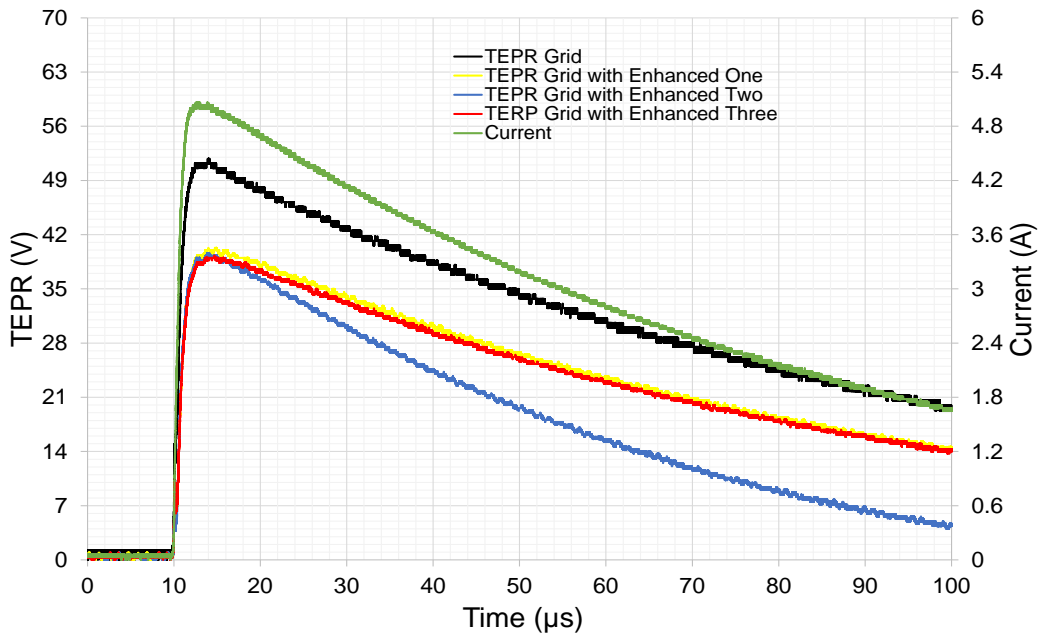
Figure 5: Voltages and current shapes at injection point for the grid 5m×5m, 25mehs with enhanced one, enhanced two and enhanced three

The grid EPR for an impulse current of 14.1A peak and 6μs rise time was measured in order to compare with the fast rise time, as shown in Figure 6. As can be seen from Figures 5 and 6, the voltage peak for the grid is close to the peak voltages of the grid with three proposed enhancements. However, a significant reduction obtained when the grid with enhancement was subjected to the fast rise time as shown in Figure 5, and this may be due to the faster rise time containing higher frequency components than slow rise time currents.
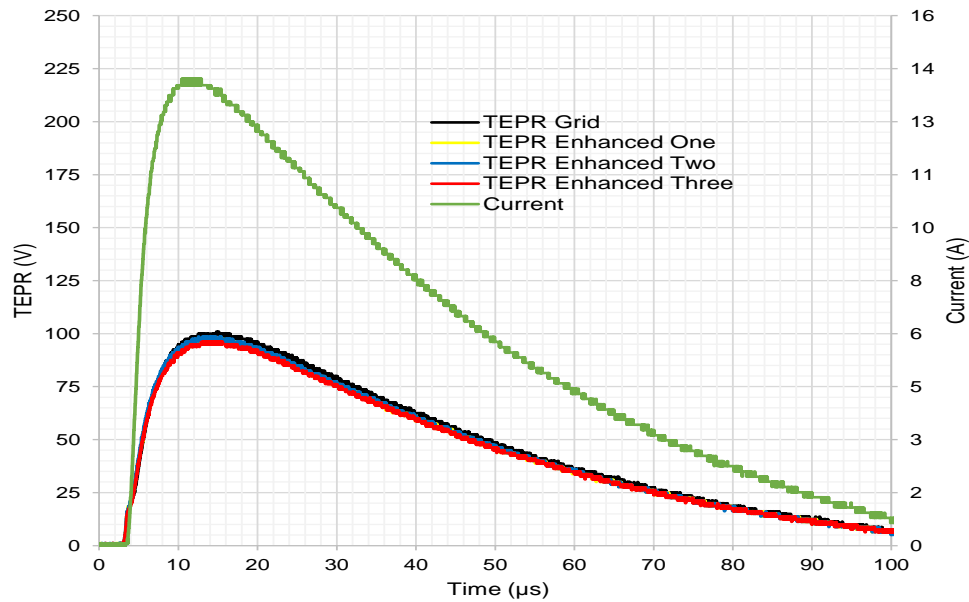
Figure 6: Transient response of the grid electrode with enhancements under slow rise time.

5 Conclusion

This paper investigates work including the experimental results of the grid with /without the high frequency electrode and the proposed insulated above conductor at the Llanrumney field test site. Experiments to assess the impact of the enhancement conductors on the impedance magnitude of the earth grid at transient response was carried out at the test site. Three proposed scenarios were selected. Improved impulse response performance by reducing the earth potential rise of the earth grid was determined experimentally by connecting above insulated conductors in parallel with the earth grid. Using these additional enhancements, little reduction in voltage at slow rise time. However, the grid impedance effect has been demonstrated at fast rise time.

6 References

1.   IEEE Std.80-2013, 'IEEE Guide for Safety in AC Substation Grounding', The Institute of Electrical and Electronics Engineers, New York, 2013.

2.   BS 7430:2011, 'Code of practice for protective earthing of electrical installations', British Standards Institution, London, 2011.Jones P., "Electrical measurement of large area substation earth gridsn", Cardiff University, PhD Thesis, 2001.

3.   ENA TS-41-24-1, 'Guidelines for the Design, Installation, Testing and Maintenance of Main Earthing Systems in Substations', Energy Networks Association, UK, 2009.

4.   EN50522:2010, 'Earthing of power installations exceeding 1 kV a.c.', CENELEC, 2010R.

5.   H. Griffiths, F. Van De Linde, N. Ullah, A. Haddad and N. Harid, 'High Frequency and Impulse Earthing of Surge Arresters', 2014 Int. Conference on Lightning Protection (ICLP), Shanghai, China, Sep 2014.

6.   N. Harid, H. Griffiths and A. Haddad, ''Effect of return path of on impulse characteristics of earth electrodes,'' Proceedings on 7th Asia-Pacific International Conference on Lightning, pp. 1-4, Chengdu, China, 2011.

7.   S. Mousa, "Experimental Investigation of Enhanced Earth Electrode Systems under High Frequency and Transient Conditions," *Cardiff University PhD Thesis,* 2014.

8.   S. Li et al., "An improved protection method of grounding electrode line for UHVDC based on injection method", *Autom. Elect. Power Syst.*, vol. 43, pp. 155-162, Aug. 2019.

9.   A. Mghairbi," Assessment of earthing systems and enhancements of their performance,'' Ph.D. dissertation, Cardiff University, 2012.

الهندسة النفطية

The Effect of Urine Matrix on Absorption Signal of Trace Elements in Flame Atomic Absorption Spectrometry

Abdelsalam Asweisi[(1)], Mohamed Elbakush[(2)], and A. S. A. Sammour[(3)]

1,2Departement of chemical engieneering, university of Tripoli, Tripoli-Libya

a.amhmed@uot.edu.ly

Abstract

Analysis of trace elements in highly interfering matrices such as urine usually accompanied with erroneous readings because of high concentration of some salts in this matrix. The optimization of the instrumental parameters of flame atomic absorption including effect of burner height, flame stoichiometry of fuel to oxidant were studied. To examine the effect of matrix concentration on the absorption signal and the reality of the absorbance values given by the instrument in presence of highly interfering matrix such as urine on of cadmium, chromium, and nickel were investigated, hence the sensitivity and reproducibility of the instrument readings and then sensitivity and reproducibility of the analysis were tested. Improvements of analysis in presence of highly interfering matrices using ethanol, citric acid and EDTA as a releasing agents were investigated.

Key words: atomic absorption spectrometry, interferences, sensitivity, trace element analysis

1. Introduction

The importance of trace metals in biological samples derives from their essentiality and toxicity effects on lining organisms. Determination of trace elements by flame atomic absorption spectrometry (FAAS) is one of the most important methods in analysis [1]. Due to low concentration and higher interfering effects of many biological sample such as urine, blood serum, and other related samples like seawater and soil background correction system to overcome the interference problems by matrix [2]. number of analytical steps is reduced and limits of detection are reduced [3],[4].The nebulization of a washing solution prior to and after each sample efficiently washes both the nebulizer and burner, which has a favorable effect on the analysis of samples of high salt content [5]. Analytical chemist uses many samples pretreatments methods such as separation, preconcentration and extraction. The classical extraction and separation methods are usually time consuming and labor intensive and require large volumes of light purity solvents and environmental problems, because of solvent disposal because of the former difficulties accompanied with the extraction and pre-concentration methods these step maybe avoided [6]. Direct analysis of highly interfering matrices by flame atomic absorption spectrometry (FAAS) limited by the matrix affection on the absorption signals of the analyte. Attenuating or increasing of this signal was common problem during the analysis. Direct determination of some trace elements in urine matrix investigated. The higher concentration of urine matrix attenuates the absorption signal of analyte into some extents [7-8].

2. Aim of study

The aim of this work is to study the effect an artificial urine matrix on the absorption signal of some trace elements with known concentration as compared with the determination of some trace elements in standard solution, also addition of some releasing agents to enhance the sensitivity and reduce the matrix effect on the signal. Optimization of some instrumental parameters such as burner height and fuel to oxidant flow rate.

3. Experimental

All glassware's were socked with deionized water and 0.2% purified nitric acid. The standard solutions were prepared from highly pure stock solutions specially made for analysis by flame atomic absorption spectrometer. A novAA350 double beam flame atomic absorption spectrometer equipped with deuterium lamp background correction was used , with computer control for the different components in the instrument like slit width fuel flow , intensity of light by controlling lamp currant applied ,burner height , wavelength , and Stoichiometry of fuel to oxidant , In all experiments an air/acetylene flame was used. An artificial urine solution was prepared according to the recipe provided by Brooks and Keevil.61 The artificial urine solution contained 0.1g lactic acid, 0.96g citric acid, 6.625g $NaHCO_3$, 25.525g urea, 0.9175g $CaCl_2$, 13.15g NaCl, 1.23g $MgSO_4$, 3.55g $NaSO_4$, 6.25g K_2HPO_4, and 3.35g NH_4Cl all mixed in 1 L deionized water.

3. **Results and discussion**

3.1 Optimization of cadmium analysis in presence of artificial urine solution:

Optimization of cadmium analysis in presence of artificial urine matrix is investigated using 0.5 ppm Cd in artificial urine solution, the results obtained for fuel-oxidant Stoichiometry and burner height are shown in figures (1 a and 1 b) respectively. Better absorption values are obtained at 40-fuel oxidant and 7 mm burner height of instead of 40 and 9 mm for standard solution.
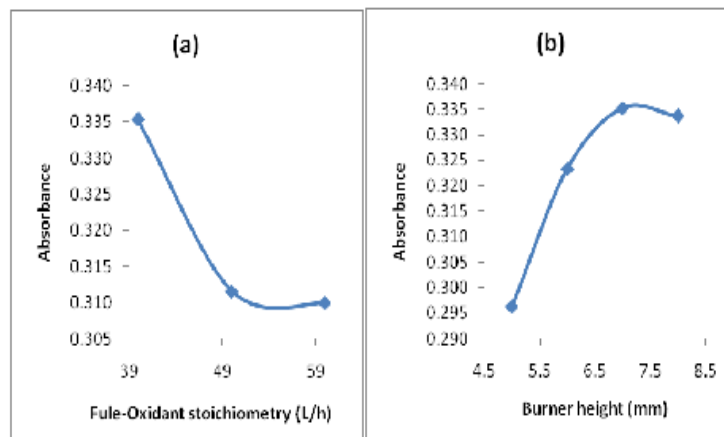
Figure 1: The effect of two parameters on absorbance signal of cadmium analysis presence in artificial urine solution (a): effect of fuel-oxidant stoichiometry at burner height 7 (b): effect of burner height at 40 fuel-oxidant stoichiometry.

3.1.1 Effect of some additives on absorption of Cadmium in artificial urine matrix:

The effects of additives such as releasing agents on the absorption signal of Cadmium in artificial urine matrix were investigated and then compared with that of standard solution at 800C.Figures (2) below show the effects of addition of some releasing agents to 0.5 ppm cadmium solution in presence of artificial urine matrix at 800C. From the figure below, better enhancement for absorption signals in all cases at higher temperatures obtained, with ethanol the signal becomes even better than that for the standard solution,   the same effects were obtained with sodium chloride matrix[9].
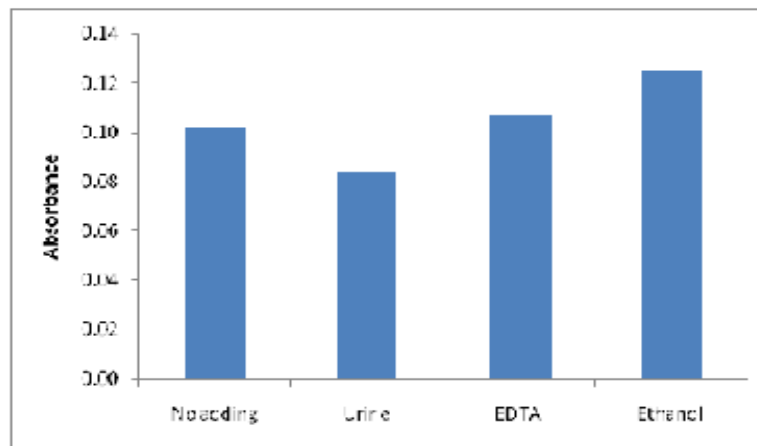
Fig. 2: The absorbance of 0.5 ppm Cd in artificial urine solution with different additives at 80^0 C.

3.2 Optimization of nickel analysis in presence of artificial urine solution:

Optimization of nickel analysis in presence of artificial urine matrix is investigated using of 1 ppm Ni in artificial urine solution , the results obtained for fuel-oxidant Stoichiometry and burner height are shown in figures (3 a and 3b) respectively. Better absorption values obtained at 50 fuel oxidant and 10 mm burner height instead of 50 and 9 mm for standard solution.
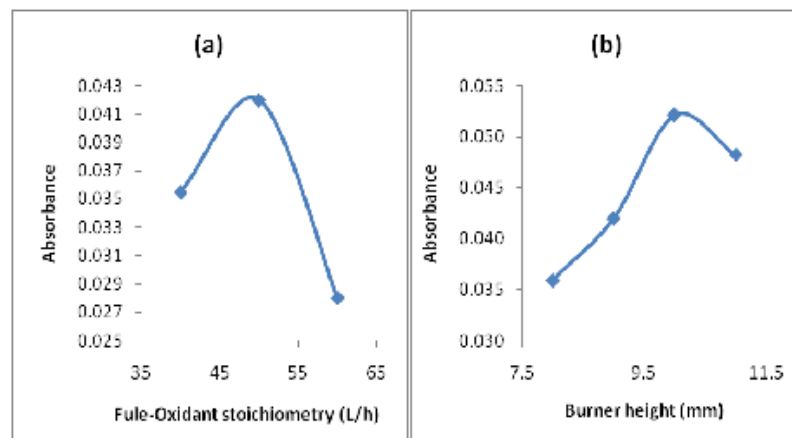
Figure 3: The effect of two parameters on absorbance signal of nickel analysis Presence in artificial urine solution (a): effect of fuel-oxidant stoichiometry at burner height 9 (b): effect of burner height at 50 fuel-oxidant stoichiometry.

3.2.1 Effect of some additives on absorption of nickel in artificial urine matrix:

The effects of some additives such as releasing agents on the absorption signal of nickel in artificial urine matrix investigated and compared with that of standard solution at 800C. Figure (4) below show the effect of addition of some releasing agents to 1 ppm nickel presence of artificial urine matrix at 800C. From the figure below, better enhancement for absorption signal in all cases at higher temperatures obtained.

.
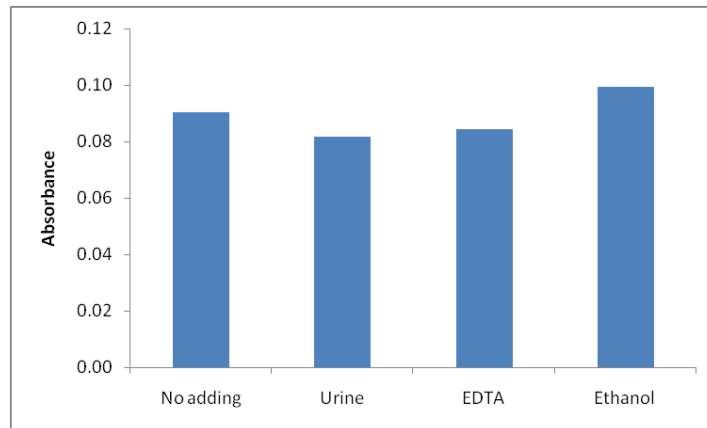
Figure 4: absorbance of 1 ppm Ni in artificial urine solution with different additives at 80^0C.

3.3 Optimization of chromium analysis in presence of artificial urine solution:

Optimization of chromium analysis in presence of artificial urine matrix is investigated using 1.5 ppm Cr in artificial urine solution , the results obtained for fuel-oxidant Stoichiometry and burner height are shown in figures (5a and 5b) respectively. Better absorption values are obtained at 90 fuel-oxidant stoichiometry and 11 mm burner height of instead of 100 and 10 mm for standard solution.
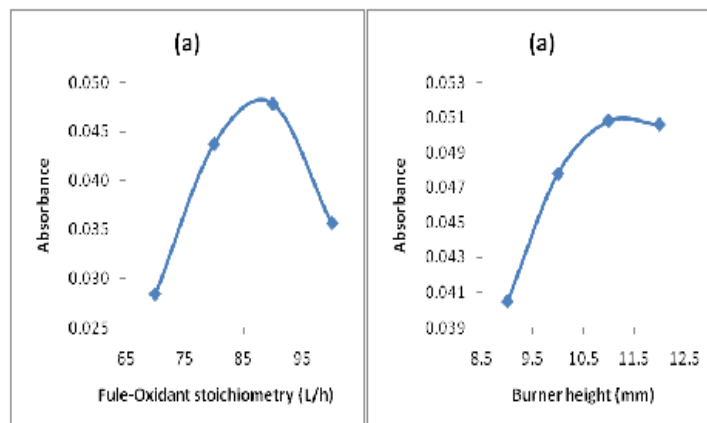
Figure 5: The effect of two parameters on absorbance signal of chromium analysis
In presence of artificial urine solution (a): effect of fuel-oxidant stoichiometry at burner height 10
(b): effect of burner height at 90 fuel-oxidant stoichiometry.

3.3.1 Effect of some additives on absorption of chromium in artificial urine matrix:

The effects of some additives such as releasing agents on the absorption signal of chromium in artificial urine matrix are investigated and compared with that value in case of standard solution at 800C.   Results obtained at 800C shown in figure (6). As can be seen from the figure below show the effect of addition of some releasing agents to 1.5 ppm chromium presence of artificial urine matrix at 800C. From the figure below, better enhancement for absorption signal in all cases at higher temperature. Generally EDTA works better with chromium in presence of urine matrix than ethanol.
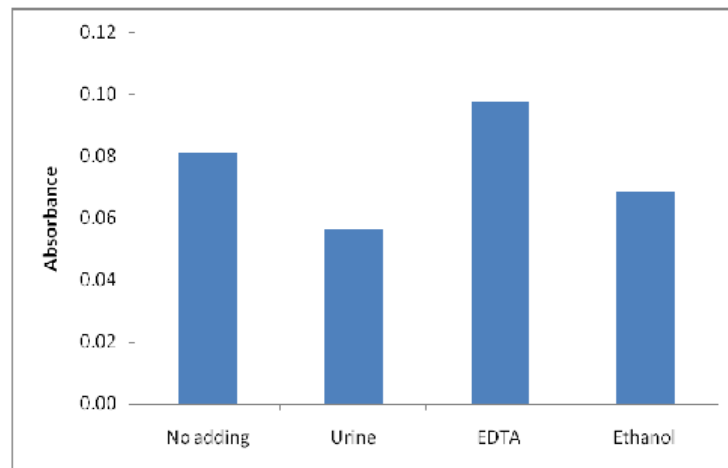
Figure 6: The absorbance of 1.5 ppm Cr in artificial urine solution with different additives at 80^0 C.

4. Conclusion

During the analysis of trace elements in presence of highly interfering matrices such as seawater, very high attention paid in order to get real absorbance values and then real concentration values. Dilution of the sample may done if the trace element high enough and can be detected, otherwise addition of releasing agents or more advanced techniques maybe used instead.

5. References:

[1] Bernhard Welz," Atomic Absorption spectrometry ", Weinheim - New York: Wiley, , 3rd edition (1999) 149- 208,477-572.

[2] John Edward Cantle, "Atomic Absorption spectrometry", Amsterdam - Oxford - New York: elsevier scientific publishing company, (1982), 95-200,1st edition.

[3] Richard D. Beaty and Jack D. Kerber, "Concepts, Instrumentation and Techniques in Atomic Absorption Spectrometry", Norwalk, CT, U.S.A: The Perkin-Elmer Corporation, (1990), 37-57, 2nd edition.

[4] The Perkin-Elmer Corporation, "Analytical Methods for Atomic Absorption Spectroscopy", Printed in the United States of America: The Perkin-Elmer Corporation, (1996), 3-51.

[5] Bekjarov, G.; Kmetov, V.; Futekov, L., Trace analysis in highly concentrated salt solutions of sodium chloride and ammonium fluoride using flame atomic absorption spectrometry. Z. Anal. Chem.8, (1989), 335, 971-974

[6] Diaz F.J. Determination of cyanocobalamin by atomic-absorption spectrophotometry with a pre-mix air-acetylene flame, Anal Chim Acta., Feb;58(2), (1972), 455-8.

[7] Cresser, M. S.; Armstrong, J.; Cook, J.; Dean, J. R.; Watkins, P.; Cave, M., Atomic Spectrometry UpdateEnvironmental Analysis. Journal of Analytical Atomic Spectrometry , 8, (1),(1993), 1R-44R.

[8] Yanagisawa, M.; Suzuki, M.; Takeuchi, T., Cationic interferences in the atomic absorption spectrophotometry of chromium. Analytica Chimica Acta, 52 (2), (1970), 386-389.

[9] A. Asweisi / Mor. J. Chem. 4N°4 (2016) 954-960.

An Investigation of Usage Eco-friendly Corrosion Inhibitor in Acidic Environment

Abdalbaset M. Algish[1],Fathi I Ashour [1] Salah.M.Algoul[2] Abdalhamed A. Musbah[3]

[1] Chemical and Petroleum Department, The Higher Institute for Science and Technology, Algaraboli, Libya

algishabdalbaset@gmail.com   **0926040434**

[2] Libyan Polymer Research Centre -Tripoli, Libya   [3] Chemical Engineering Department, Awlad Ali High Institute for Science and Technology, Tarhuna, Libya

Abstract

Corrosion is a major concern in the industrial application of ferrous alloys, this is as a result of the enormous cost involved in damages, maintenance and corrosion control. Stainless steels have high corrosion resistance capacity because of the existence of chromium, as a result of the high cost of traditional corrosion inhibitor, science turned to green corrosion inhibitor to try to compensate for it. In this regard we used a lot Cactus oil in acidic media (H_2So_4 –Hcl) for 4 sample, Variable rates and varying periods of time it was found that the corrosion rate decreases and the best result is a corrosion rate of 0.0001 iron within Hcl in 72 hr ,H_2So_4) within 72 hr.

Keywords: Corrosion inhibitor, Cactus oil, corrosion rate, Hcl, H_2So_4.

1. Introduction

Almost all metals and alloys are unstable in the Earth's atmosphere and therefore susceptible to corrosion. Corrosion deterioration of metallic alloys by chemical interaction with their environments is one of the major sources of industry overhead costs because of maintenance and repair of damaged and worn-out equipment and parts. In general, a good portion of the loss can be avoided by proper corrosion control and monitoring. One of the best methods to reduce the rate of metallic corrosion is by the addition of inhibitors in which even small concentrations can result in decrease of the corrosion rate of metallic surface [1- 6]. However, there are conditions aiding the selection of a suitable inhibitor substance. These include, the cost and amount of the inhibitor required, long term toxicological effects on the environment, the inhibitors' ability to treat the corroded surfaces, the inhibitor's availability and stability in the environments. In various industries, mild steel has been used extensively as a building material owing to its cost effectiveness, and high mechanical strength [1, 2]. Although, through electrochemical and chemical reactions it has been very reactive with the environmental constituents and hence, component metal loss arises as a result of corrosion. Corrosion occurs as a result of cross section losses, having lower ductility, ultimate strength and yield strength. It decreases the life span of structures resulting into structural vulnerability leading to structural failure [1]. Various efforts have been previously carried out to reduce unfavorable reactions mostly through frequently occurring industrial developments such as acid

pickling, acid descaling, and acid cleaning etc. of which the utilization of corrosion inhibitors is one of the best methods [3]. Globally, corrosion problems mostly occurs in industries as a result of service and environmental conditions. Corrosion might not have immediate negative effect on the material but it affect the physical appearance, mechanical behavior and strength resulting into significant operational complications [4]. In industries, acidic solutions are largely used for acidizing, de-scaling, chemical cleaning and acid pickling for steel, the most frequently used is hydrochloric acid. Naturally, these occur in corrosive environment resulting into intense corrosion complications experienced in industrial processes. Acid corrosion inhibitors was applied extensively to minimize or prevent loss of material associated with the acid [5]. Mild steel is frequently used as a raw material for construction of pipelines, buildings and bridges [6], its pre-mature failure and deterioration has resulted into a gross expenditure of several billions of dollars globally [7]. Since mild steel is an essential part of infrastructural facilities which includes pipelines, port facilities and bridges, these cost expenditure include replacement, maintenance and loss of productivity. The use of paint coatings has been applied to create a protective barrier. The use of pigments inhibiting corrosion is an essential constituent in paints. Over time, these pigments percolate from the coatings thereby inhibiting the concealed metal substrate, which breaks particularly in paint coating [8]. The most efficient pigment inhibiting corrosion used for different alloys and metals, e.g. mild steel, has compounds of metal chromates in its oxidation state (Cr^{+6}) [6] for example strontium chromate. Chromate compounds behaves in a method of either reducing or blocking both cathodic and anodic rate of reaction. In addition, (Cr^{+6}) has been reported as an occupational carcinogen related to sinus, naser and lung cancer [2]. In recent decades, various alternative inhibitors have been considered as substitutes for chromates, including metallic ions (rare earth metals and zinc), oxyanions (phosphates, molybdates and nitrates) and organic compounds (carboxylates). All have demonstrated some extent of inhibition effectiveness [8]. Mild steel corrosion by atmospheric conditions is a broad topic that have been researched by different authors. Various researchers have reviewed the corrosion process. A huge quantity of these information is obtainable on mild steel by atmospheric corrosion at mid and short term .Various studies have been conducted on the use of organic corrosion inhibitors, it has frequently been applied in various control measures such as its effectiveness to impede corrosion of mild steel in seawater .Usually, the use of inhibitors as a preventive mechanism against corrosion is principally attributed to inhibitor molecular adsorption which result to surface modification of the mild steel and formation of subsequent protective laye. Several kinds of inhibitors has been utilized as an effective means of inhibiting corrosion in various electrolytic media for mild steels. These media include sea water, hydrochloric and sulfuric acid concentrations. This manuscript reviews corrosion inhibitors as building evidence for Mild Steel [7].

2-Materials and Methods

2.1. Materials

At this stage, small square iron pieces of standard known dimensions are used as shown in the Figure (1.1). They are prepared before use so that they have equal polished faces for all samples to give close results that were placed in different corrosive environments.

They are placed on a sensitive scale to measure their weight as shown in Figure (1.2), and then placed in clean flasks containing acid solutions to measure their weight before and after corrosion over a period of three days, and then measure their weight after adding green oils to these solutions.

Figure (1.1) showing the samples

Preparation of solutions and samples 2.3

To carry out these experiments, we prepare a set of clean flasks of a known size, as well as an amount of Hcl - H_2so_4 known focus . We have selected about 8 fine and evenly polished iron parts samples. The length and width are approximately 2 cm. Then calculated the weight using a sensitive scale. The weights were as follows:

wg	NO
9	1
9	2
9	3
9	4
9	5
9	6
9	7
9	8

Put these samples in clean flasks and we also used 4Hcl -type acid flasks Samples (1-4) and . were placed Four more flasks containing H_2so_4 (5-8)

3.Experimental procedure

This experiment is simple, effective, and reliable to determine the desired value which represents the intensity of corrosion that is already occurred upon the corroded metal , it is as follows :-

The sample is polished and pre-weighed mild iron specimens were immersed in 1000ml Hcl with and without watercress as corrosion inhibitor corrosion inhibitor

was supplied from almadena company by different concentration 2 ml , 4 ml , 6 ml immersion time was varied from 24, 48, 72, h. The corrosion rate was measured by weight loss The samples are taken out at end of time, then cleaned with acetone and its weight is calculated by the sensitive balance.

Calculation corrosion rate(CR)

$$C.R = \Delta w / At$$

$\Delta w = w_f - w_i$

Effect of time

The effect time was studied for different times (24 , 48 , 72 hr) in presence and absence corrosion inhibition

Table.1. shows the C.R without corrosion inhibitor in Cl

Sample no	Time hr	C R g/cm$^{2.}$.h	Time hr	C R g/cm$^{2.}$.h	Time hr	C R g/cm$^{2.}$.h
1	24	0.004	48	0.0006	72	0.002
2	24	0.007	48	0.0005	72	0.001
3	24	0.006	48	0.0005	72	0.00007
4	24	0.004	48	0.0006	72	0.0002

Table.2. effect of 2 ml of *Cactus oil*

Sample no	Time hr	C R g/cm$^{2.}$.h	Time hr	C R g/cm$^{2.}$.h	Time hr	C R g/cm$^{2.}$.h
1	24	0.001	48	0.0001	72	0.00001
2	24	0.0002	48	0.0003	72	0.00003
3	24	0.001	48	0.0002	72	0.0003
4	24	0.001	48	0.001	72	0.0001

Table.3. effect of 4ml of *Cactus oil*

Sample no	Time hr	C R g/cm$^{2.}$.h	Time hr	C R g/cm$^{2.}$.h	Time hr	C R g/cm$^{2.}$.h
1	24	0.0006	48	0.0001	72	0.00002
2	24	0.0001	48	0.00004	72	0.0001
3	24	0.0002	48	0.0002	72	0.0001
4	24	0.001	48	0.0001	72	0.0002

Table.4.effect of 6ml of *Cactus oil*

Sample no	Time hr	C R g/cm$^{2.}$.h	Time hr	C R g/cm$^{2.}$.h	Time hr	C R g/cm$^{2.}$.h
1	24	0.0003	48	0.0002	72	0.0002
2	24	0.0004	48	0.0001	72	0.0001
3	24	0.001	48	0.0002	72	0.0001
4	24	0.0004	48	0.0003	72	0.0001

Table 5 shows the C.R without corrosion inhibitor in H$_2$SO$_4$

Sample no	Time hr	C R g/cm$^{2.}$.h	Time hr	C R g/cm$^{2.}$.h	Time hr	C R g/cm$^{2.}$.h
5	24	0.004	48	0.0005	72	0.001
6	24	0.008	48	0.0004	72	0.001
7	24	0.011	48	0.001	72	0.0002
8	24	0.001	48	0.001	72	0.004

Effect of concentration of *Cactus oil*
Table 6 . effect of 2 ml of *Cactus oil*

Sample no	Time hr	C R g/cm$^{2.}$.h	Time hr	C R g/cm$^{2.}$.h	Time hr	C R g/cm$^{2.}$.h
5	24	0.00077	48	0.00071	72	0.00163
6	24	0.00131	48	0.00091	72	0.00131
7	24	0.0010	48	0.0013	72	0.00196
8	24	0.00167	48	0.00054	72	0.00128

Table 7 . effect of 4 ml of *Cactus oil*

Sample no	Time hr	C R g/cm$^{2.}$.h	Time hr	C R g/cm$^{2.}$.h	Time hr	C R g/cm$^{2.}$.h
5	24	0.000656	48	0.00042	72	0.00196
6	24	0.000145	48	0.0021	72	0.00019
7	24	0.000968	48	0.00081	72	0.00127
8	24	0.00164	48	0.00053	72	0.00018

Table 8. effect of 6 ml of *Cactus oil*

Sample no	Time hr	C R g/cm$^{2.}$.h	Time hr	C R g/cm$^{2.}$.h	Time hr	C R g/cm$^{2.}$.h
5	24	0.000937	48	0.000937	72	0.000146
6	24	0.0021	48	0.00208	72	0.000114
7	24	0.00118	48	0.00118	72	0.00173
8	24	0.00145	48	0.00145	72	0.00041

Result &Discussion

By Looking at the previous results, we find that the corrosion rates in (HCL) without corrosion inhibitor are greater than after adding the inhibitor, so we find that the highest corrosion rate in 24 hours without corrosion was for the sample 3 0.007 gm/cm$^{2.}$.h and after adding 2ml inhibitor it was for the sample 1 0.001 gm/cm$^{2.}$.h .In 48 hr, the highest corrosion rate was 0.006 gm/cm$^{2.}$.h for sample 4 and after the inhibitor it became 0.001 gm/cm$^{2.}$.h for sample 4. After 72 hr it was 0.002 gm/cm$^{2.}$.h for sample 1 and after they added the inhibitor 0.0001 gm/cm$^{2.}$.h . In the same way when changing the concentration of corrosion inhibitor to 4ml and 6ml , we find that the highest corrosion value when adding 4 ml was 0.001 gm/cm$^{2.}$.h at 24 hours for sample 4 and 0.0001 gm/cm$^{2.}$.h for sample 4 at 48 hr 0.0001 gm/cm$^{2.}$.h for sample 2 at 72 hr and for 6ml was0.001 gm/cm$^{2.}$.h for sample3

In 24 hr and 0.0002 gm/cm$^{2.}$.h for sample 2 and 0.0001 gm/cm$^{2.}$.h in72 hr.

By Looking at the previous results, we find that the corrosion rates in (H$_2$SO$_4$) without corrosion inhibitor are greater than after adding the inhibitor, so we find that the highest corrosion rate in 24 hours without corrosion was for the sample 7 0.011 gm/cm$^{2.}$.h and after adding 2ml inhibitor it was for the sample 8 0.00117 gm/cm$^{2.}$.h .In 48 hr the highest corrosion rate was 0.001 gm/cm$^{2.}$.h for sample 7 and after the inhibitor it became 0.00013 gm/cm$^{2.}$.h for sample 7. After 72 hr it was 0.001 gm/cm$^{2.}$.h for sample 6 and after they added the inhibitor 0.00019 gm/cm$^{2.}$.h for sample 6 . In the same way when changing the concentration of corrosion inhibitor to 4ml and 6ml , we find that the highest corrosion value when adding 4 ml was 0.00104 gm/cm$^{2.}$.h at 24 hr for sample 8 and 0.00164 gm/cm$^{2.}$.h for sample 6 at 48 hr 0.00196 gm/cm$^{2.}$.h for sample 5 at 72 hr and for 6ml was 0.00108 gm/cm$^{2.}$.h for sample 6 in 24 hr and 0.00158 gm/cm$^{2.}$.h for sample 7 and 0.00173 gm/cm$^{2.}$.h in72 hr for sample 7.

Conclusions

— At the end of the study we find the following: -

— 1.*Cactus* oil can used as Corrosion Inhibitor in 10M(Hcl –H_2so_4) .

— 2- After using the corrosion inhibitor, we find that the corrosion rate decreases with the passage of time and the concentration of the corrosion inhibitor increases

— 3. The highest value for corrosion rate in Hcl was 0.001 gm/cm².h after adding 4ml from inhibitor obtained in absences of corrosion inhibitor in 24 hr.

— 4. The highest value for corrosion rate in H_2so_4 was 0.0117 gm/cm².h after adding 2ml from inhibitor obtained in absences of corrosion inhibitor in 24 hr.

— 5. The lowest value for corrosion rate in Hcl was 0.0002 gm/cm².h after adding 6ml from inhibitor obtained in absences of corrosion inhibitor in 72 hr.

— 5. The lowest value for corrosion rate in H_2so_4 was 0.000146 gm/cm².h after adding 6ml from inhibitor obtained in absences of corrosion inhibitor in 72 hr.

References

[1] Abdalbaset M. Algish[1],Fathi I Ashour [1] Salah.M.Algoul[2] Abdalhamed A. Musba

The Third Libyan Conference on Chemistry and its Applications (Lcca2019) Benghazi University, Benghazi, Libya Sep 7th – 9th, An Investigation Of Usage Eco-friendly Corrosion Inhibitor In HCl Environment.

[2] Javidan, F., Heidarpour, A., Zhao, X.L., & Minkkinen, J. (2016). Application of high
strength and ultra-high strength steel tubes in long hybrid compressive members: experimental and numerical investigation. Thin-Walled Structures, 102, 273–285.

[3] Verma, C., Ebenso, E. E., Bahadur, I., & Quraishi, M. A. (2018). An overview on plant
extracts as environmental sustainable and green corrosion inhibitors for metals and alloys
in aggressive corrosive media. Journal of Molecular Liquids, 266, 577–590. **https://doi.org/10.1016/j.molliq.2018.06.110**.

[4] Yilmaz, N., Fitoz, A., Ergun, Ü, & Emregül, K. C. (2016). A combined electrochemical
and theoretical study into the effect of 2- ((thiazole-2-ylimino) methyl) phenol as a corrosion inhibitor for mild steel in a highly acidic environment. Evaluation and Program
Planning, 111, 110–120. https://doi.org/10.1016/j.corsci.2016.05.002.

[5] Saji, V.S. (2010). A review on recent patents in corrosion inhibitors. Recent Patents on
Corrosion Science, 2, 6–12.

[6] Abdel Hameed, R.S. (2011). Ranitidine drugs as non-toxic corrosion inhibitors for mild
steel in hydrochloric acid medium, Portugaliae. Electrochim. Acta, 29, 273–285.

[7] Mattsson, E. (2001). Basic Corrosion Technology for Scientists and Engineers, 2nd ed.,
Institute of Materials, IOM Communications, London.

[8] Somers, A. E., Hinton, B. R. W., Bruin-dickason, C. De, Deacon, G. B., Junk, P. C., &
Forsyth, M. (2018). New, environmentally friendly, rare earth carboxylate corrosion inhibitors for mild steel. Corrosion Science, 139, 430–437. https://doi.org/10.1016/j.corsci.2018.05.017.

High-density polyethylene/date palm tree fiber composites: Effect of chemical treatment and fiber type

Anour Shebani[1*], Hussein Etmimi[2], Omaya Abujarir[3], Ebtesam Ahmed[4]

[1] anwar1701@yahoo.co.uk, [2] hmetmimi@gmail.com, [3] ebtesam413@gmail.com,

[4] omia_abujarir@icloud.com

[1, 2] Libyan Polymer Research Center, Tripoli-Libya
[3, 4] Higher Institute for Science and Technology, Al-Grabolli-Libya
* Corresponding author Email: anour@prc.ly or anwar1701@yahoo.co.uk

ABSTRACT

Date palm tree fiber (DPTF) at a loading of 20 wt% was incorporated as a natural filler in high-density polyethylene (HDPE) to fabricate various HDPE/DPTF composites. The effect of fiber type and its chemical treatment on the properties of the resultant composites was investigated. Two different parts of the date palm tree, namely: meshes and leaflets were used to obtain the DPTFs, which were chemically treated by polyethylene glycol (PEG). Mechanical, water resistance and morphological properties of the composites containing the treated and untreated DPTFs were studied. Generally, composites made with treated DPTFs had better mechanical properties, namely higher impact strength and Shore D hardness than that of neat HDPE and composites made with untreated DPTFs. The highest impact strength and hardness was measured for composites containing treated DPTFs obtained from the meshes. In addition, composites made with treated DPTFs had better water resistance properties (more hydrophobic nature and less water absorption) than that of composites with untreated DPTFs. Contrary, as shown by water vapour transmission rate measurements, the diffusion of water in its vapour state increased when treated DPTFs (obtained from both meshes and leaflets) was used. Microscopic observations indicated the formation of a homogenous fiber particle distribution in composites made with treated DPTFs in comparison to those made with untreated DPTFs. This indicates the presence of a good interfacial adhesion (thus compatibility) between the treated DPTFs and the HDPE matrix, which resulted in the formation of composites with improved mechanical as well as water resistance properties.

Keywords: Chemical treatment; date palm; high-density polyethylene; mechanical properties; water resistance

1 Introduction

In recent years, natural fibers (NFs) have received a great interest by many scientists and polymer engineers to be used as reinforcing materials in polymer composites instead of conventional fillers [1, 2]. This is due to many advantages that are associated with NFs, which include ease of decomposability, environmentally friendly, low cost, low weight and high mechanical properties. Nowadays, NFs-reinforced polymer composites are used in various industrial products and outdoor

applications. For example, NFs-reinforced polymer composites are used in transportation (automobiles, railway coaches, aerospace), military applications, building and construction industries (ceiling panels, partition boards), packaging, and many other consumer products [3-5]. NFs can be classified into three main categories, which are plant fibers, animal fibers, and mineral fibers. However, the most common NFs used to reinforce polymers are plant fibers. These include leaf-type fibers (pineapple, sisal, and abaca), core-type fibers (hemp, jute, and kenaf), grass/reed-type fibers (wheat, corn, and rice), seed-type fibers (cotton, kapok, and coir), bast-type fibers (flax, jute, hemp and ramie), and other types (wood and roots) [5, 6]. Generally speaking, NFs derived from plants are similar and mainly consist of cellulose, hemicellulose, lignin, and other substances. It has been reported that a large variety of NFs, which include wood, cotton, bagasse, rice straw, rice husk, wheat straw, flax, hemp, pineapple leaf, coir, oil palm, date palm, doum fruit, ramie, kenaf, bamboo, sisal and jute are used to reinforce polymers [7, 8]. Palm trees are widely grown in Libya and nearby countries (in North Africa and the Middle East), which can be considered as a good source of NFs. They would be a good reinforcing filler for polymers, which can be of a great interest in the area of polymer composites [9, 10]. In fact, palm tree fibers (PTFs) have been successfully utilized as fillers for the reinforcement of thermoplastics and thermoset composites in recent years [11]. PTFs could be extracted from different parts of the palm trees, namely: the midribs, spadix stems, leaflets, and meshes. These PTFs are hydrophilic lightweight fibers that are easy-to-obtain at low-cost and possess good durability that withstand well against deterioration [12]. In addition, it was found that composites containing fibers that obtained from palm trees have moderate tensile and flexural properties compared with composites containing other NFs such as grass reeds, kenaf, ramie, sisal, coir, banana fiber [9]. This might be attributed to the fact that PTFs have the highest cellulosic content (nearly 50%) as compared to other NFs [13]. This might be also due to the low bulk density of PTFs compared to other NFs [14]. Generally, polymer composites that are reinforced with PTFs have been successfully used for many applications including parts and components, which are used in the automotive industry [15, 16].

The main aim of this work is to fabricate and study the effect of different types of date palm tree fibers (DPTFs) and their chemical treatment on the properties of high-density polyethylene (HDPE) composites. These include: mechanical (impact strength and Shore D hardness), water resistance(water absorption (WA), hydrophobicity, water vapor transmission rate (WVTR)) and morphological properties of the resultant composites. In general, polyethylene is the most commonly used polymer matrix in polymer composites, which are reinforced with NFs because of its relatively low processing temperature and good processability [17]. Therefore, HDPE has been chosen as the matrix material in this study.

2 Experimental work

2.1 Materials

Date palm tree meshes and leaflets were obtained from Al-Grabolli city, Libya. HDPE obtained from Saudi Basic Industries Corporation (SABIC) (HDPE F00952, Melt flow index (MFI) = 0.05 g/10 min (ISO 1133, 190 °C, 2.16 Kg), density = 952 g/cm^3 (ISO 1183)). Polyethylene glycol (PEG) with weight average molecular weight of 400 g/mole (PEG400) in liquid form was purchased from Alfa Aesar, UK.

2.2 Preparation and treatment of DPTFs

Date palm tree meshes and leaflets were first washed with tap water to remove any contaminants, adhering dirt and dust. They were air-dried at room temperature for 48 h and then grinded and sieved to obtain DPTFs with sizes ranging from 38 to 150 μm. PEG was used as a treatment agent for the DPTFs obtained from both meshes and leaflets. The dry DPTFs were stirred in PEG solution (30 vol%) at 100 °C for 2h in a reflux system. They were then removed from the solution, washed with deionized water to remove the excess PEG, and then dried in an oven at 80 °C for 24 h.

2.3 Preparation of composites

The treated and untreated DPTFs that obtained from both meshes and leaflets were dried in an oven at 80 °C for about 4 h, after which they were mixed with HDPE using twin screw extruder (Brabender, Germany) (L/D ratio of 48) with screw speed of 70 r.p.m. at 180°C. The obtained composites were subsequently cooled in air for 24 h and then cut to small pieces by scissors. Details of the composites and their codes are reported in Table 1.

Table 1: *Composition of composites and their codes*

Composite code	HDPE (wt%)	DPTFs from untreated meshes (wt%)	DPTFs from treated meshes (wt%)	DPTFs from untreated leaflets (wt%)	DPTFs from treated leaflets (wt%)
HDPE	100	0.0	0.0	0.0	0.0
Comp.1	80	20	0.0	0.0	0.0
Comp.2	80	0.0	20	0.0	0.0
Comp.3	80	0.0	0.0	20	0.0
Comp.4	80	0.0	0.0	0.0	20

2.4 Characterization of DPTFs

2.4.1 Fourier transform infrared spectroscopy (FTIR)

FTIR was employed to monitor the changes in chemical structure of DPTFs obtained from both meshes and leaflets caused by PEG treatment. FTIR analysis was carried out using Tensor II machine (Bruker, Germany) with a wavenumber resolution of 4 cm^{-1}. The samples were mixed with KBr powder, pressed into pellets and scanned in a range of 500 to 4000 cm^{-1} with an average of 32 scans.

2.4.2 Characterization of composites

2.4.2.1 Impact strength and hardness

Specimens for impact strength test were prepared using injection molding machine (Xplore 12ml, Netherlands). Charpy impact test was carried out using (CEAST Resil-Impactor tester) at room temperature with impact energy of 15 J. The specimens for impact test were prepared and notched according to ASTM (D256-10). A minimum of five specimens were tested and an average value was taken. Hardness was investigated by a Durometer in Shore D scale at room temperature according to ASTM (D2240) (a minimum of 10 measurements were taken for each composite and an average value was recorded).

2.4.2.2 Water absorption (WA)

Water uptake measurements were used to determine the WA behavior of the composites. Composites were pressed at 5 MPa using a small press at 180 °C to obtain thin films (~ 1mm). Films with an area of 2 cm^2 were cut and used in this test. Before testing, all films have been dried at 80 °C in an air-circulated oven overnight, then placed in a desiccator. Subsequently, films were weighed with a OHAUS analytical digital balance (with a resolution of 0.1 mg). The films were immersed in water and weighed over time for three weeks at room temperature. The excess water on the surface of each film was removed with blotting paper before weighing. This test has been conducted in accordance with the procedure recommended by ASTM D570 [18]. Five specimens from each sample were weighed before and after immersion (over time) and the water uptake (WU) was calculated as follows:

$$WU(\%) = \frac{m_1 - m_0}{m_0} x\ 100 \tag{1}$$

Where, m_1 is the mass of the sample after immersion (g) and m_0 is the mass of the sample before immersion (g).

2.4.2.3 Contact angle measurements

The contact angle measurements were carried out to determine the hydrphilicity/hydrophobicity of the neat HDPE and the obtained composites' surface. The measurements were carried out using Ramè-Hart instrument (model 200-F4) at room temperature. Drops of water (3 μL) were deposited on the surface of the HDPE and all the composites with a micro-syringe. Images of the water drops were acquired through a digital camera positioned on a static contact angle analyzer. The contact angle (θ) was measured automatically from the image setup. The contact angle measurements were repeated five times for each sample and the average value was recorded.

2.4.2.4 Water vapor transmission rate (WVTR) test

The WVTR test was used to determine the amount of water vapor that passes through the composite under 70% relative humidity (RH) at room temperature for 24 h. This specific RH was achieved using saturated NaCl solution following the work of Timusk [19] and Kuishan [20]. Zeolite (~2g) was placed in glass containers, which

were sealed with films made from HDPE and the HDPE/DPTF composites. Films were prepared by pressing samples at 5 MPa using a small press machine at 180 ℃, which gave thin films of ~1 mm thickness. Films with diameters of 3 cm were cut and used. The containers were then placed in a dissector filled with the saturated salt solution to maintain a constant RH at room temperature for 24 hours. All WVTR measurements were repeated three times and an average value was recorded. The WVTR was calculated as follows [20]:

$$WVTR = \frac{w_1 - w_0}{A} \qquad (2)$$

Where, w_0 is the weight of sample before exposure to water (g), w_1 is weight of sample after exposure to water (g) and A is the exposed area of the film in m^2.

2.4.2.5 Morphological properties

Microscopic observations of HDPE and its composites were carried out by an optical microscope (XP-501 transmission polarizing microscope, Turkey), equipped with a color digital camera (Moticam 2) and Motic Images Plus 2 software at different magnifications.

3 Results and discussion

3.1 Characterization of DPTFs

3.1.2 FTIR analysis

FTIR was used to identify the functional groups present in the DPTFs obtained from meshes and leaflets and to monitor the changes in their chemical structures caused by PEG treatment. It has been reported that these plant fibers contain a variety of functional groups such as alkenes, phenolic hydroxyl group, aromatic groups, b-glucose linkages and other oxygen-containing groups (ester, ketone and alcohol) [21]. In general, the characteristic bands of these functional groups correspond to the absorption bands of lignin, hemicellulose and cellulose [22]. Figure 1 presents the FTIR spectra of DPTFs obtained from the meshes before and after PEG treatment. Figure 2 shows the FTIR spectra of DPTFs obtained from the leaflets before and after PEG treatment.
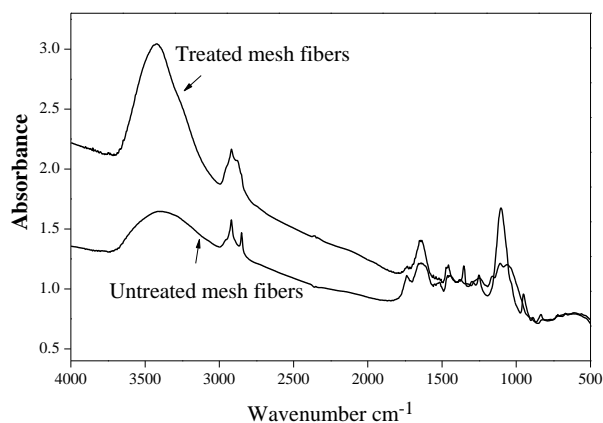
Figure 1: *FTIR spectra of DPTFs obtained from treated and untreated meshes.*

The broad band at 3750-3200 cm^{-1} shown in Figure 1 is typical of hydroxyl (-OH) groups (stretching and flexing vibration frequencies of the intra- and intermolecular hydrogen bonds of cellulose) [23-25]. From Figure 1, one can see that the broad absorption band for DPTFs obtained from meshes at 3750-3200 cm^{-1} of -OH groups was intensified (became narrower and more defined) after PEG treatment, suggesting the occurrence of hydrogen bonding between PEG and the functional groups in the fibers. This could lead to reduce the number of -OH groups from the fiber surface, which results in meshes with a hydrophobic nature [21]. The absorption band at 2990-2905 cm^{-1} is due to the stretching vibrations of CH_2. The small absorption band at 2890-2805 cm-1 are due to the C–H symmetric stretching of the methylene (CH_2 and CH_3) groups [26]. The latter two bands are generally overlapped after PEG treatment. This means that the proportions of CH_2 and CH_3 were higher in the treated DPTFs than in the untreated one. This is rather expected because PEG contains a greater proportion of these groups, which can be recorded in the FTIR spectra [27]. A small band was observed at 1780-1714 cm^{-1} due to the carbonyl (C=O) stretching from the ester linkage of hemicellulose and lignin. An increase in the intensity of this band was observed after the treatment with PEG. This could indicate a slight change in hemicellulose and lignin has occurred due to the treatment with PEG. Furthermore, the peak representing the ether groups in treated mesh at 1253 cm^{-1} had changed noticeably; it became wider compared to the same peak in the untreated mesh fiber water spectrum. This may indicate the removal of some materials during PEG treatment [28]. Overall, it appears that treatment of the DPTFs obtained from meshes with PEG resulted in a significant interaction between the PEG and the mesh fibers via hydrogen bonding.
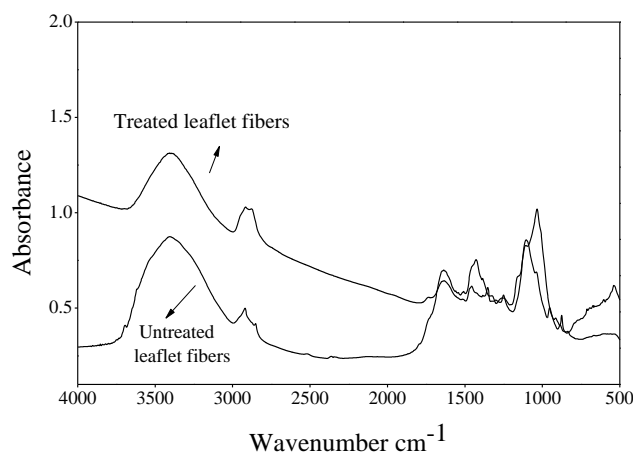
Figure 2: *FTIR spectra of DPTFs obtained from treated and untreated leaflets.*

From Figure 2, it can be seen that contrary to the DPTFs obtained from the meshes, the absorption band for -OH groups at 3750-3200 cm^{-1} in the DPTFs obtained from leaflets were similar before and after PEG treatment (no significant change in beak broadening was noticed). Furthermore, treatment of leaflets with PEG did not cause any other significant changes in the FTIR spectra of the DPTFs obtained from the

leaflets. From Figure 1 and 2, one can clearly see that the influence of PEG treatment was much more distinct in the case of DPTFs obtained from the meshes than those obtained from the leaflets.

3.2 Characterization of composites

3.2.1 Impact strength and hardness

It has been shown that NFs can improve the fracture toughness, crack resistance, tension performance, flexural properties, impact strength, and fatigue behavior of composites [29]. The impact strength and Shore D hardness of neat HDPE and composites made with DPTFs obtained from meshes and leaflets are shown in Table 2. Composites with untreated DPTFs (obtained from both meshes and leaflets) had higher impact and lower Shore D hardness than that of pure HDPE. However, composites with treated DPTFs (obtained from both meshes and leaflets) appeared to have higher impact strength and Shore D hardness than that of pure HDPE and composites with untreated ones. This probably indicates that PEG treatment improved the interfacial adhesion between the fibers and the HDPE matrix (better compatibility). This resulted in better fiber particle distribution, which led to the formation of composites with improved mechanical properties [10]. Moreover, as seen in Table 2 the highest impact strength and hardness was obtained by composite made with treated DPTFs obtained from the meshes. This is in agreement with the FTIR results, which indicated better interfacial adhesion between DPTFs obtained from PEG-treated meshes and HDPE. This resulted in even better fiber-matrix adhesion and therefore much better fiber distribution occurred in comparison to the composites made with the DPTFs obtained from the leaflets. Consequently, higher impact strength and hardness were observed for composites made with treated DPTFs obtained from the meshes.

Table 2: *The impact strength and Shore D hardness of HDPE and HDPE/DPTF composites*

Composite code	Impact strength (KJ/m^2)	Shore D hardness
HDPE	8.19 (0.10)*	57.5 (0.32)*
Comp.1	10.04 (0.76)*	57.3 (1.24)*
Comp.2	11.06 (0.52)*	63.8 (1.42)*
Comp.3	9.53 (0.42)*	57.4 (0.92)*
Comp.4	10.31 (0.36)*	59.3 (1.42)*

* Standard deviation between brackets

3.2.2 Water uptake test

Composites based on plant fibers are sensitive to water. Therefore, it is of great significance to study the water absorption (WA) characteristics of these composites. This is because WA could affect the properties of these composites, resulting in changes of bulk properties such as dimensional stability, as well as mechanical and physical properties [30]. Figure 3 shows the WA behavior for the HDPE/DPTF composites.
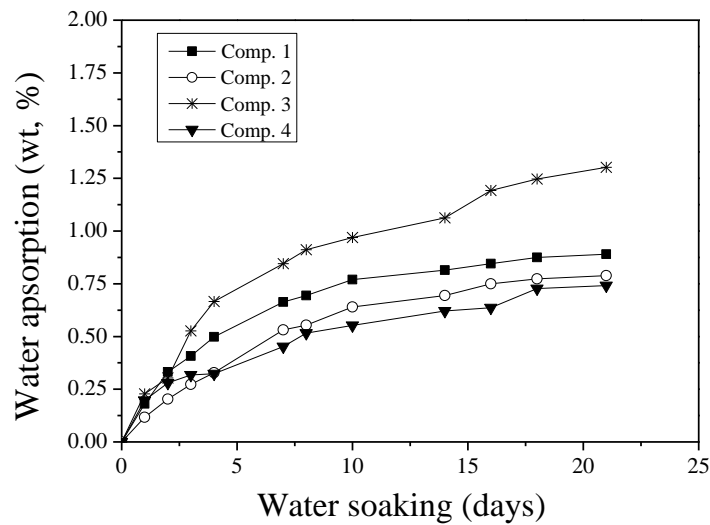
Figure 3: *WA behavior for the prepared composites.*

From Figure 3, one can see that in general water uptake of the composites increased with soaking time and thereafter it became relatively constant after 16 days except for the composite made with untreated DPTFs obtained from leaflets. It has been shown that cellulose and hemicellulose components in plant fibers are mostly responsible for the WA of NFs, since they contain many easily accessible -OH groups which offer a level of hydrophilic character to these fibres [31, 32]. As illustrated in Figure 3, the incorporation of treated and untreated DPTFs obtained from meshes and leaflets had no significant effect on the water uptake of HDPE. All HDPE/DPTF composites generally showed a relatively very low water uptake, ranging from 0.75-1.25 wt%. From Figure 3, one can also see that treatment of DPTFs with PEG slightly reduced the WA of the composites containing them in comparison to composites with untreated fibers. According to Shu-pin *et. al.* [33], the improvement of water-related properties can enhance the interfacial bonding between wood fibers and polypropylene matrix by heat treatment with PEG. Also, heat treatment with PEG could result in improvement in the dimensional stability of these composites. Russly and Luqman [34] claim that treatment with PEG could result in a decrease in void volume, which enhance the adhesion between fibers and polymer, which restrict water penetration and storage at the interface. However, it is known that WA of such composites can be affected by the existence of lumens, holes, voids, flaws, poor interfacial adhesion, and microcracks at the interface between the filler and the polymer matrix [35].

3.2.3 Contact angle measurements

The value of the contact angle can vary from 0-180°, 0° representing fully wetted surfaces (very hydrophilic) and 180° representing totally non-wettable surfaces (very hydrophobic). In other words, wettability and hydrophilicity/hydrophobicity are closely related phenomena. It should be mentioned here that hydrophobic surfaces are characterized by a contact angle of 90° or more and hydrophilic surfaces are

characterized by a contact angle of less than 90º. Table 4 shows the effect of PEG treatment on the contact angle of HDPE/DPTF composites made with DPTFs obtained from both mesh and leaflet. Contact angle of neat HDPE is also shown for compassion.

Table 4: *Contact angle of HDPE and HDPE/DPTF composites*

Composite code	Contact angle (θ^o)
HDPE	81.10 (3.1)*
Comp.1	77.82 (1.0)*
Comp.2	78.78 (0.9)*
Comp.3	74.67 (2.8)*
Comp.4	78.46 (2.6)*

* Standard deviations between brackets

As shown in Table 4, the contact angle of neat HDPE and composites were <90°, which indicates that they all had surfaces with a hydrophilic nature. However, the contact angle of composites was lower than that of neat HDPE. This indicates that the presence of treated and untreated fibers resulted in composites with more hydrophilic nature. This is properly due to the presence of excess of polar groups on the surface of the composites, which caused by the addition of mesh and leaflet fibers (treated and untreated). This is because these fibers, which are derived from plants mainly consist of cellulose, hemicellulose, lignin, and extractives, as mentioned previously. It should be mentioned here that the decrease in contact angle can be probably due to increased roughness of the film surface caused by the fibers [36, 37]. Also, contact angle measurements may depend on other factors, such as surface energy, surface chemical structure, viscosity of the liquid and surface cleanliness [38-39]. From Table 4, one can also see that in both cases (composites with mesh and leaflets), lower contact angle was observed when untreated fiber was used. This indicates that using treated fibers resulted in composite surfaces with less hydrophilic nature than that of composites made with untreated fibers. This is probably due formation of hydrogen bonding between -OH groups of PEG and -OH groups of cellulosic materials of mesh and leaflet fibers. Therefore, less polar groups are available in the composite surface which led to the formation of surfaces with less hydrophilic character. This in in good agreement with the WA measurements, which showed that composites made with treated DPTFs had lower WU values (see Figure 3).

3.2.4 Water vapor transmission rate (WVTR)

WVTR is the standard measurement by which polymer films are compared for their ability to resist water vapor transmission through them. Lower WVTR values indicate better water resistance of a polymer material. Table 3 shows the WVTR for the HDPE and its composite films which contain treated and untreated DPTFs obtained from meshes and leaflets.

Table 3: *WVTR of neat HDPE and HDPE/DPTF composites*

Composite code	WVTR (g/m^2/24h)
HDPE	0.007 (0.001)*
Comp.1	0.019 (0.006)*
Comp.2	0.032 (0.299)*
Comp.3	0.020 (0.003)*
Comp.4	0.031 (0.001)*

* Standard deviation between brackets

Table 3 illustrates that neat HDPE films displayed very low WVTR, which is 0.007 g/m^2/24h. However, all composites exhibited higher WVTR than that of neat HDPE. The highest increase (from 0.007 to 0.031-0.032 g/m^2/24h) was obtained by the composites, which contain treated DPTFs obtained from meshes and leaflets. Whereas a lower increase (from 0.007 to 0.019-0.020 g/m^2/24h) was obtained by the composites containing untreated DPTFs obtained from meshes and leaflets. This is contrary to the results obtained from the WA test, which indicated that composites made with treated DPTFs had less WA. This can be explained by the fact that the WVTR test depends on diffusion of water vapour through the composite film in addition to the solubility.

3.2.5 Morphological properties

The optical microscopy images in Figure 4 clearly show the agglomeration of fiber particles in the composites made with untreated meshes and leaflets (Figure 4a and 4c) in comparison to composites made with treated meshes and leaflets (Figure 4b and 4d). This heterogeneous particle distribution led to lower interfacial adhesion between the untreated fibersand HDPE matrix. Contrary, composites made with treated fibers exhibited better compatibility between the fiber and HDPE, which was apparent from the absence of fiber aggregation (relatively better fiber distribution). Moreover, no sign of voids and filler pull-outs (retreats) from the HDPE matrices were observed in all composites made with treated fibers.
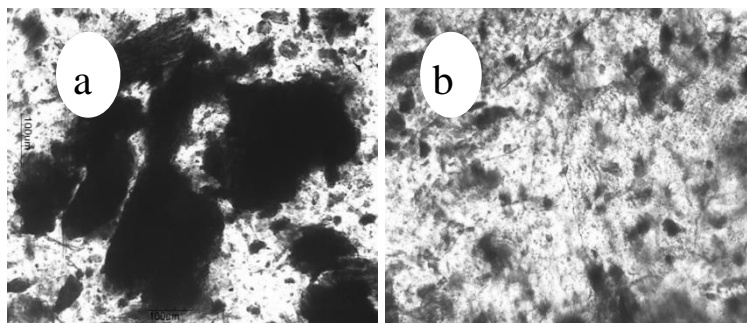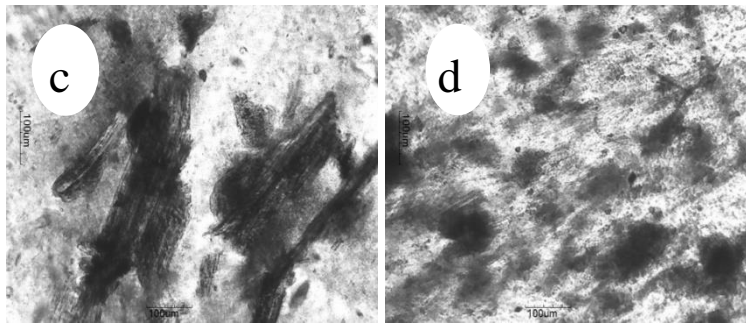
Figure 4: *Optical microscopy images of composites made with: a) untreated meshes, b) treated meshes, c) untreated leaflets and d) treated leaflets.*

4 Conclusion

The effect of adding different types of date palm tree fibers (DPTFs) and their chemical treatment on the properties of HDPE was investigated. DPTFs were obtained from two different parts in the date palm tree (i.e., meshes and leaflets), which were treated by polyethylene glycol (PEG). Mechanical, water resistance and morphological properties of the obtained composites were investigated. Overall, treating the DPTFs with PEG appeared to have a considerable effect in reinforcing HDPE. Results revealed that the treatment of DPTFs improved the impact strength and Shore D hardness compared to neat HDPE, significantly. Moreover, composites made with DPTFs obtained from treated meshes had better mechanical properties than that made with treated leaflets. In addition, ccomposites made with treated DPTFs (obtained from both meshes and leaflets) had better water resistance properties (less hydrophilic nature and less water absorption) than that of composites made with untreated DPTFs. Contrary, the water vapour transmission rate measurements indicated that the diffusion of water in its vapour state increased when treated DPTF (both mesh and leaflets) was used. Optical microscopy images clearly showed the formation of significantly less fiber aggregation in composites made with treated DPTFs (both meshes and leaflets). Moreover, no sign of voids and filler pull-outs (retreats) from the HDPE matrix were observed in composites made with treated DPTFs. This resulted in better fiber particle distribution, thus composites with improved mechanical as well as water resistance properties were formed.

5 References

[1]   M. Y. Khalid, A. Al Rashid, Z. U. Arif, W. Ahmed, H. Arshad and A. A. Zaid, "Natural fiber reinforced composites: Sustainable materials for emerging applications", *Results in Engineering*, vol. 11, no. x, pp. 1-12, 2021, Available online: 31 July 2021. https://doi.org/10.1016/j.rineng.

[2]   P. Jagadeesh, Y. G. Girijappa, M. Puttegowda, S. M. Rangappa, and S. Siengchin, "Effect of natural filler materials on fiber reinforced hybrid polymer

composites: An Overview", Journal of Natural Fibers, vol. 19, no. 11, pp. 4132-4147, Published online: 21 Dec 2020. https://doi.org/10.1080/15440478.2020.1854145.

[3]   S. Afridhi, M. J. Thomas, B. V. Ravish, N. Hugar, I. Hariprasad, "Fabrication of Jute fibre reinforced PMC and evaluation of its mechanical Properties", *International Journal of Research in Advent Technology*, Special Issue, pp. 70-74, May 2018. Available online at www.ijrat.org.

[4]   M. Biron, "Material selection for thermoplastic parts: Practical and advanced information for plastics engineers", Elsevier Ltd., USA, 2016.

[5]   A. H. Lotfi, H. Li, D. V. Dao1 and G. B. Prusty, "Natural fiber–reinforced composites: A review on material, manufacturing, and machinability", *Journal of Thermoplastic Composite Materials,* vol. 34, no. 2, pp. 1-47, 2019, Published online: 28 April 2019. https://doi.org/10.1177/0892705719844546.

[6]   N. S. Sadeq, Z. G. Mohammadsalih, D. Ali, "Natural fibers and their applications: A review", *Journal of Al-Farabi For Engineering Sciences*, vol. 1, no. 2, pp. 51-63, Published online: January 2022.

[7]   F. Yao, Q. Wu, H. Liu,Y. Lei and D. Zhou, "Rice straw fiber reinforced high density polyethylene composite: Effect of coupled compatibilizating and toughening treatment", *Journal of Applied Polymer Science,* vol. 19, no. 4, pp. 2214-2222, Access online on 15 February 2011 at https://doi.org/10.1002/app.32946.

[8]   F. Yao, Q. Wu, Y. Lei and Y. Xu, "Rice straw fiber-reinforced high-density polyethylene composite: Effect of fiber type and loading", *Industrial crops and products,* vol. 28, pp. 63-73, 2008, Accepted 20 January 2008, https://doi.org/10.1016/j.indcrop.2008.01.007.

[9]   B. Neher, Md. R. Bhuiyan, H. Kabir, Md. Qadir, Md. Abdul Gafur and F. Ahmed, "Study of mechanical and physical properties of palm fiber reinforced acrylonitrile Butadiene Styrene Composite", *Materials Sciences and Applications*, vol. 5, no. 1, pp. 39-45, 2014, Access online on January 2008 at http://dx.doi.org/10.4236/msa.2014.51006.

[10]   B. Aldousiri, M. Alajmi and A. Shalwan, "Mechanical Properties of Palm Fibre Reinforced Recycled HDPE", *Advances in Materials Science and Engineering*, vol. 2013, pp,   1-7,   January   2013, http://dx.doi.org/10.1155/2013/508179.

[11]   M. R. Asyraf, M. R. Ishak, A. Syamsir, N. M. Nurazzi, F. A. Sabaruddin, S. S. Shazleen, M. F. Norrrahim, M. Rafidah, R. A. Ilyas, M. Z. Abd Rashid and M. R.

Razman, "Mechanical properties of oil palm fibre-reinforced polymer composites: A review", *Journal of Materials Research and Technology,* vol. 17, pp. 33-65, 2022, Available online on 31 December 2021 at https://doi.org/10.1016/j.jmrt.2021.12.122.

[12]   A. Mohajerani, S. Hui, M. Mirzababaei, A. Arulrajah, S. Horpibulsuk, A. Abdul Kadir , M. Rahman and F. Maghool, "Amazing types, properties, and applications of fibres in construction materials", *Materials,* vol. no. 16, pp. 2-45, 2019, Published on 7 August 2019. https://doi.org/10.3390/ma12162513.

[13]   W. Ghori, N. Saba, M. Jawaid and M. Asim, "A review on date palm (phoenix dactylifera) fibers and its polymer composites", *Materials Science and Engineering*, vol. 368, 2018, doi:10.1088/1757-899X/368/1/012009.

[14]   K. Almi, S. Lakel, A. Benchabane and A. Kriker, "Characterization of date palm wood used as composites reinforcement", *Acta Physica Polonica A*, vol. 127, no. 4, pp. 1072-1074, 2015.

[15]   B. Agoudjil, A. Benchabane, A. Boudenne, L. Ibos, and M. Fois, "Renewable materials to reduce building heat loss: Characterization of date palm wood", *Energy and Buildings.* vol. 43, no. 2-3, pp. 491-497, 2011. Available online 13 October 2010, https://doi.org/10.1016/j.enbuild.2010.10.014.

[16]   M. R. Asyraf, A. Syamsir, A. Supian, F. Usman, R. A. Ilyas, N. Nurazzi, M. Norrrahim, M. R. Razman, S. Z. Zakaria, S. Sharma, Z. Itam and M. Z. Rashid, "Sugar palm fibre-reinforced polymer composites: Influence of chemical treatments on its mechanical properties", *Materials,* vol. 15, no. 3852, pp. 1-22, Published on 27 May 2022. https://doi.org/10.3390/ma15113852.

[17]   A. M. Badji, E. Ly, D. Ndiaye, A. Diallo, N. Kebe and V. Verney, "The Effect of Poly-Ethylene-co-Glycidyl Methacrylate Efficiency and Clay Platelets on Thermal and Rheological Properties of Wood Polyethylene Composites", *Advances in Chemical Engineering and Science*, vol. 6, pp. 436-455, 2016. doi: 10.4236/aces.2016.64040.

[18]   ASTM D570 – 98, Standard Test Method for Water Absorption of Plastics, 2010.

[19]   P. C. Timusk, K. D. Pressnail, and V. F. Striesky, "Moisture-related properties of oriented strand board." *10DBMC International Conference on Durability of Building Materials and Components*, Lyon. 2005.

[20]   L. Kuishan, Z. Xu, and G. Jun, "Experimental investigation of hygrothermal parameters of building materials under isothermal conditions." *Journal of Building Physics,* vol. 32, no. 4, pp. 355-370, 2009, First published online on 1 April, 2009 https://doi.org/10.1177/1744259108102832.

[21]   B. Jyoti1, D. Singh, S. Kaushik, V. Bhalla, S. Wadhwa and D. K. Pandey, "Ultrasonic attenuation in yttrium monochalcogenides, *Journal of Pure and Applied Ultrasonics,* vol. 40, no. 4, pp. 93-99, 2018, Published on 1 December 2018.

[22]   M. Antunes and J. I. Velasco, "Vegetable fibres from agricultural residues as thermo-mechanical reinforcement in recycled polypropylene-based green foams", *Waste Management*, vol. 32, no. 2, pp. 256-263. Available online 15 October 2011. https://doi.org/10.1016/j.wasman.2011.09.022.

[23]   M. Polettoa, V. Pistor, R. Marlene, C. Santana and A. Zattera, "Materials Produced From Plant Biomass: Evaluation of crystallinity and Degradation Kinetics of Cellulose", *Materials Research*, vol. 15, no. 3, pp. 421-427, 2012, Access online on June 2012 https://doi.org/10.1590/S1516-14392012005000048.

[24]   M. C. Popescu, C. M. Popescu, G. Lisa and Y. Sakata, "Evaluation of morphological and chemical aspects of different wood species by spectroscopy and thermal methods, *Journal of Molecular Structure*, vol. 988, no. 1-3, pp. 65-72, 2011, Available online 5 January 2011. https://doi.org/10.1016/j.molstruc.2010.12.004.

[25]   E. Sargunam and A. T. Raja, "An analytical study and characterization of therma; and FTIR studies of urinary calculi", *International Journal of Current Science Research*, vol. 2, no. 4, pp. 591-602, April 2016.

[26]   T. P. Sathishkumar, P. Navaneethakrishnan, S. Shankar and R. Rajasekar, "Investigation of chemically treated randomly oriented sansevieria ehrenbergii fiber reinforced isophthallic polyester composites", *Journal of Composite Materials*, vol. 48, no. 24, pp. 1-15, 2013, First published online on 24 September 2013, https://doi.org/10.1177/0021998313503589.

[27]   M. Sánchez, F. J. Alvarado, A. Martínez-Chávez, L. Hernández-Montelongo, R. F. Escamilla, V. V. and C. Escamilla, "The effects of henequen cellulose treated with polyethylene glycol on properties of polylactic acid composites", *Bioresources*, vol. 14, no. 2, pp. 2707-2726, 2019.

[28]   X. Zhang, F. Wang, and L. M. Keer, "Influence of surface modification on the microstructure and thermo-mechanical properties of bamboo fibers", *Materials*, vol. 8, pp. 6597-6608, 2015, Published on 24 September 2015. https://doi:10.3390/ma8105327.

[29]   A. Nourbakhsh, and A. Ashori, "Fundamental studies on wood-plastic composites: effects of fiber concentration and mixing temperature on the mechanical properties of poplar/PP composite", *Polymer Composites*, vol. 29, no. 5, pp. 569-573, 2008, Published on 24 March 2008. https://doi.org/10.1002/pc.20578.

[30]   C. K. Abdullah, M. Jawaid, H. P. Abdul Khalil, A. Zaidon, and A. Hadiyane, "Oil palm trunk polymer composite: Morphology, water absorption, and thickness swelling behaviors", *Bioresources*, vol. 7, no. 3, pp. 2948-2959, 2012.

[31]   M. Ichazo, C. Albano, J. González, R. Perera, M. Candal, "Effect of Natural Fiber Reinforced Polypropylene Composite Using Resin Impregnation", *Composite Structures*, vol. 54, pp. 207-214, 2001. http://dx.doi.org/10.1016/S0263-8223(01)00089-7.

[32]   M. Beg and K. Pickering, "Reprocessing of wood fibre reinforced polypropylene composites: Hygrothermal ageing and its effects", *Composites: Part A*, vol. 39, no. 9, pp. 1565-1571, 2008. Available online 20 June 2008. https://doi.org/10.1016/j.compositesa.2008.06.002.

[33]   L. Shu-pin, C. A. Jin-zhen and W. Xing, "Properties of PEG/thermally modified wood flour/polypropylene (PP) composites", *Forestry Studies in China*, vol. 14, no. 4, pp. 307-317, 2012, 2012. https://doi.org/10.1007/s11632-012-0405-x.

[34]   A. Russly, C. A. Luqman, "Polyethylene glycol on the characteristics of kenafcellulose/low-density polyethylene biocomposites", *International Journal of Biological Macromolecules,* vol. 47, no. 2, pp. 292-297, 2010, Available online 24 April 2010. https://doi.org/10.1016/j.ijbiomac.2010.04.004.

[35]   B. A. Alshammari, N. Saba, M. D. Alotaibi, F. M. Alotibi, M. Jawaid and Y. O. Alothman, "Evaluation of mechanical, physical, and morphological properties of epoxy composites reinforced with different date palm fillers", *Materials*, vol. 12, no. 13, pp. 1-17, 2019, Published: 3 July 2019. https://doi.org/10.3390/ma12132145.

[36]   R. Bernard and P. Kristin, "Roughness effects on contact angle measurements", *American Journal of Physics*, vol. 76, no. 11, pp. 1044-1074, accepted 6 June 2008, https://doi.org/10.1119/1.2952446.

[37]   C. Lazrak, B. Kabouchi, M. Hammi, A. Famiri, M. Ziani, "Structural study of maritime pine wood and recycled high-density polyethylene (HDPEr) plastic composite using Infrared-ATR spectroscopy, X-ray diffraction, SEM and contact angle measurements", *Case Studies in Construction Materials,* vol. 10, pp. 1-8. https://doi.org/10.1016/j.cscm.2019.e00227.

[38]   A. W. Adamson, and A. P. Gast, "Physical chemistry of surfaces", John Wiley & Sons, Inc., USA, 1990.

[39]   J. N. Israelachvili, "Intermolecular and surface forces", 2ed, Academic Press, UK, 1992.

Physiochemical and Mechanical Analysis of Local Gypsum Deposits, East Benghazi, Libya

Ibrahim M. Abou El Leil[1], *Ahmed Mohammed[2], Farag Adam[3]

[1] ibrahim.aboueleil@gmail.com, [2] ahmed.mohammed@tu.edu.ly, [3] faragabam1991@gmail.com

[1] Petroleum Engineering Department, Faculty of Engineering, Tobruk University

[2, 3] Geology Department, Faculty of Science, Tobruk University

*Corresponding author email: ahmed.mohammed@tu.edu.ly

ABSTRACT

The local gypsum deposits were investigated in order to determine their physical and chemical properties. General properties such as physical and chemical properties are tested using standard laboratory procedure. The raw gypsum has been produced by open pit mining technique. The study was conducted to evaluate the characteristics of gypsum from Al Mabrouk mining sites; one is a huge reserve with great thickness and two others with less thickness. Samples of gypsum from the studied sites were obtained and their physical and chemical properties were determined. They were calcined into plaster of Paris (P.O.P) in an oven between 105°C (221°F) and 200°C (392°F). The raw gypsum samples were analyzed to determine their chemical constituents using XRF technique. The major significant constituents such as Sulphur Trioxide (SO_3); Calcium Oxide (CaO); Magnesium Oxide (MgO); Sodium Oxide (Na_2O); Potassium Oxide (K_2O); Manganese Oxid (MnO); Titanium Oxide (TiO_2); Ferric Oxide (Fe_2O_3) and combined matter (Loss-on-ignition) were determined. Based on the previous tests the results confirmed that the investigated gypsum is suitable for several purposes e. g. cement manufacture, source sulphates, construction and production P.O.P for use in plasterboards.

Keywords: Gypsum, deposit, physiochemical, properties, plaster of Paris, changes chemical composition.

1 Introduction

The mineral gypsum precipitated some 100 to 200 million years ago when sea water evaporated. From a chemical point of view it is calcium sulphate Dihydrate ($CaSO_4.2H_2O$) deposited in sedimentary layers on the sea bed. Under high pressure and temperature gypsum turns into anhydrite ($CaSO_4$). In nature, gypsum and anyhdrite occur as beds or nodular masses up to a few meters thick. Gypsum is formed by the hydration of anhydrite. The depth of hydration can range from the surface of the deposit down to three hundred meters, depending on temperature and pressure, topography and the structure of the deposit. Anhydrite is often mined in conjunction with gypsum, but is comparatively limited in its technical applications. The content of gypsum in sedimentary rock varies from 75% to 95%, the rest being clay and chalk [1]. Gypsum is a common sulphate mineral of great commercial importance, it composes of hydrated calcium sulphate ($CaSO_4. 2H_2O$). It is a white mineral of calcium sulphate found in deposits in the earth crust. Gypsum is a less reflective, glass-like soft stone; which is of great importance for the manufacture of many

industrial products. Gypsum is formed through geological processes, hence it occurs in nature in various forms. These forms can basically be grouped into two broad categories of rock gypsum and sand gypsum. Rock gypsum is described as having different colours ranging from transparent or white; sometimes grey, yellowish to red. Gypsite is gypsum mixed with sand and dirt [2]. Commonly used in many industries, gypsum ($CaSO_4 \cdot 2H_2O$) is a monomineral sulphate sedimentary rock, built almost exclusively from the mineral of the same name, with anhydrite, calcite and halite admixtures [3,4]. The crystal structure of gypsum depends mainly on the conditions in which the raw material transformations took place and a specific phase (temperature and pressure) was created [5-8]. Gypsum/anhydrite are produced from open-cast mines, or underground mines using pillar and stall mining methods, that give extraction rates of up to 75%. Gypsum is normally only screened to remove 'fines' (mainly mudstones), then crushed and finely ground. Gypsum/anhydrite for cement manufacture is supplied in crushed form for further fine grinding with cement clinker [6]. When Gypsum ($CaSO_4,2H_2O$) is ground to a powder and heated at 150° to 165° C, three-quarters of its combined water is removed producing hemi-hydrate plaster ($CaSO_4,1/2H_2O$), commonly known as the 'Plaster of Paris'. When this powder is mixed with water the resulting paste sets hard as the water recombines to produce Gypsum again. This process can be repeated almost indefinitely, with important implications for recycling [7]. Gypsum is one of the oldest known minerals used in basic and construction materials. As far back as 7000 BC, gypsum was already used as a base for frescoes in the town of Catal Huyuk in Asia Minor [9]. Gypsum was also used in its natural form for sculptures and building blocks, as plaster and in the mortar of world-famous buildings such as the towers of Jericho, the Great Pyramid of Cheops or the Palace of Knossos [9]. The Romans knew about the advantageous properties of gypsum and spread the knowledge about its preparation to the area north of the Alps. Much of this knowledge during the Migration Period (400–700 AD). It was not until the architectural style of Romanticism that gypsum returned to the scene as a building material. Gypsum technology was further developed during the period of industrialization in the 19th century, which provided a clear distinction between gypsum dihydrate, hemihydrate and completely dehydrated anhydrite and the importance of different firing temperatures [9]. The world production of gypsum is in range of 140–160 million tons [10].

2   World Mine Production and Reserves

Gypsum and anhydrite occur all over the world and are usually easy to exploit. In global terms, around 50 % of the gypsum is used for the production of cement, 39 % for the production of plaster and stucco (which also includes wallboards) and around 10 % in agriculture. Due to its low price gypsum and gypsum products are not usually transported over long distances, which in the past prevented the recycling of gypsum waste. During the past few years better technologies were developed for the increased recycling of gypsum [9]. Table 1 presents the world production of gypsum by countries.

Table 1 *World production of gypsum by countries [10]*

Countries	Mine production (MT*)		Reserves (MT*)
	2018	2019	
United States	21,100	20,000	700,000
Algeria	2,500	2,500	NA*
Brazil	3,200	3,200	340,000
Canada	3,000	3,000	450,000
China	15,500	16,000	NA
France	3,000	3,000	NA
Germany	3,200	3,200	NA
India	2,700	2,700	37,000
Iran	16,000	16,000	NA
Japan	4,700	4,700	NA
Mexico	5,400	5,400	NA
Oman	7,000	7,000	NA
Pakistan	2,200	2,200	4,900
Russia	3,800	3,800	NA
Saudi Arabia	3,310	3,300	NA
Spain	7,000	7,000	NA
Thailand	9,300	9,300	1,700
Turkey	10,000	10,000	200,000
Other countries	20,000	21,000	NA
World total (rounded)	143,000	140,000	Large

* NA = Not available   *MT = million tons

3 Significance of Study and Problem Statement

The importance of this study can be summarized as Libya has a great quantities of raw materials estimated as millions of tons the raw materials characterized by the lower contents of impurities the most locations of these materials located on or nearby the highways the easy of transportation by trucks or belt conveyor to achieve the sustainable development and support the national income. These rocks haven't subjected in details studies and evaluation the study spotlight on the importance of these rock materials as a natural resource there is no available concerning data can be used as reference.

4   Objectives of Study

The main aim of this study is to focus on the assessment of the raw materials of local gypsum deposits required as a raw material for various industrial purposes particularly cement manufactures in the investigated locations throughout:

1.   Study the chemical composition of raw materials.
2.   Determination their characterizations and the potentiality as construction raw material.

Fifth Conference on Engineering Sciences and Technology (CEST-2022) 20-22 December 2022/ Libya

Physiochemical and Mechanical Analysis of Local Gypsum Deposits, East Benghazi, Libya

3. Correlation between these raw materials and the standard ones to distinguish their quality.
4. Highlight on the raw materials as natural resources in Libya.
5. The study regards as preliminary one for more detail study later.

Figure 1 *Sidi Al Mabrouk (Site 1)*
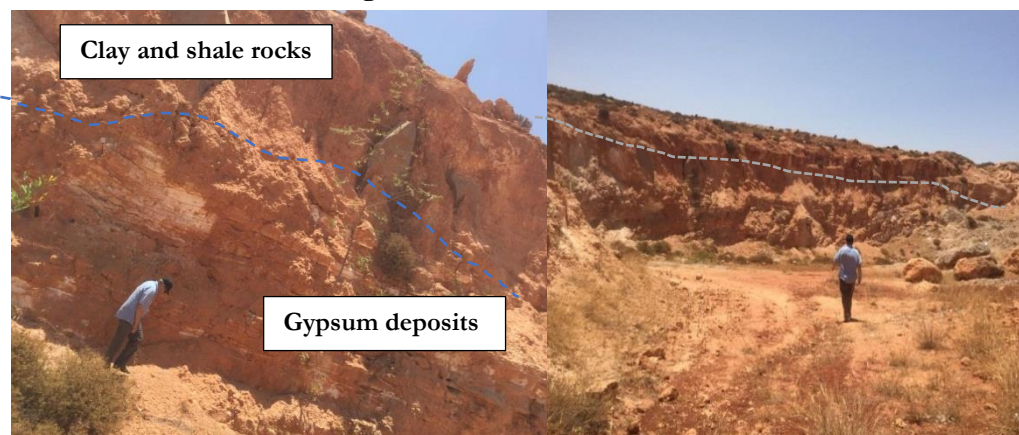
Figure 2 *Sidi Al Mabrouk (Site 2)*   **Figure 3** *Sidi Al Mabrouk (Site 3)*

5   Materials and Methods

5.1   Location of Studied Sites

Gypsum deposits occur in different locations all over Libya with different amounts and reserves. This study has been carried out on the area including a high reserve of gypsum deposits namely Mabrouk quarry lies in the east Benghazi city e. g. Al Rajma and Sidi Mabrouk. Figure 2 a map illustrates the different location deposits of vaporits rocks such as gypsum and salts.
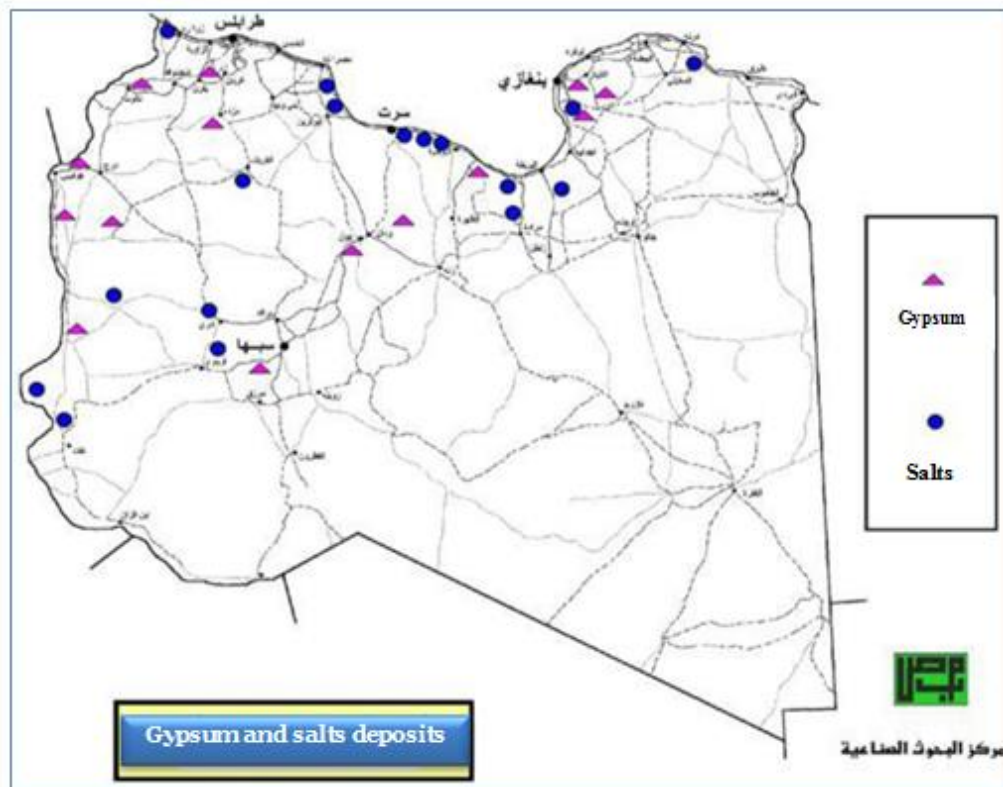
Figure 4 *Location map of gypsum and salts deposits [11]*

Figures 5 & 6 a satellite images show the location of the studied area and their investigated sites at Al Mabrouk quarry.

Figure 5 *Satellite image for the location of study are (Mabrouk quarry)*
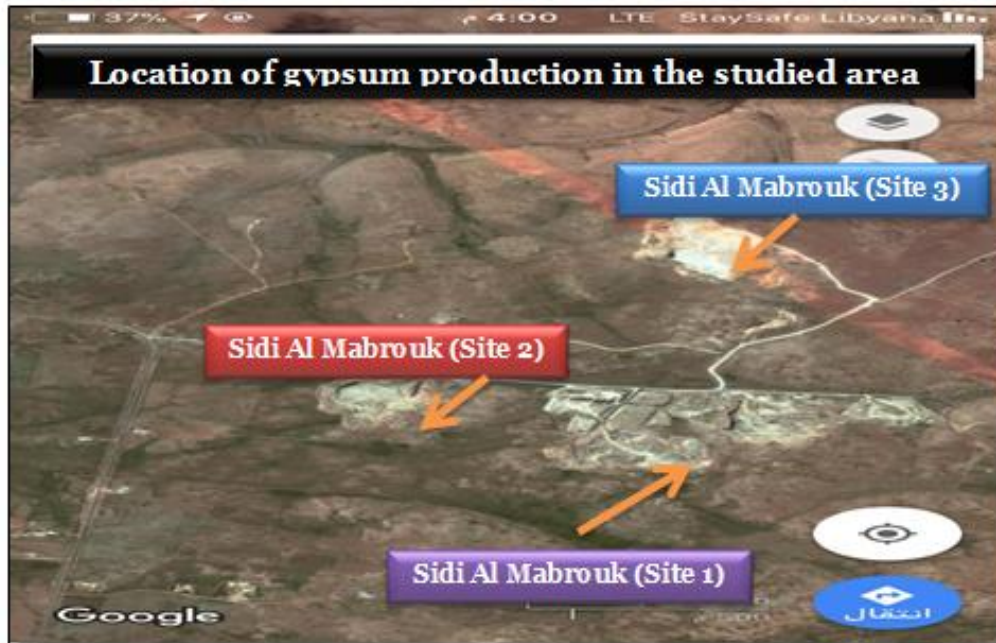
Figure 6 *Satellite image for the study sites at Al Mabrouk quarry*

On the other hand, Figures 5 through 7 photos show the gypsum face cuts at the investigated three sites of Al Mabrouk quarry.

5.2   SAMPLES COLLECTION

The extraction and exploitation of gypsum in the studied area is mainly carried out by open pit methods (Figure 7).

Figure 7 *Open cast mining process in the investigated locations*

To assessment the quality of the gypsum as raw material for the different applications, the raw gypsum samples were brought from the locations of studied sites represented by the three sites, three samples of each site (Figure 6). These samples were subjected to the chemical analysis and physical tests to determine their characterizations. All tests have been carried out in Libyan National Cement Company at Al Fataih area to determine the different constituents using XRF technique.

Figure 8 *The collected samples from Al Mabrouk quarry*

Sample of gypsum from the sites were crushed to fine particles in stages. The final crushing resulted in flour like texture. The powder was loaded into kettles and calcined at about 105°C (221°F), a temperature reasonably above the minimum temperature necessary for calcinations as reported by Coburn [12]. The result obtained from each sample was added and an average result obtained.

5.3 Formation of the Plasterboards

The Plasterboard panel consists of a layer of gypsum plaster sandwiched between two layers of paper. The raw gypsum, $CaSO_4.2H_2O$, was heated to drive off the water then slightly re-hydrated to produce the hemihydrate of calcium sulphate ($CaSO_4. 1/2H_2O$).

5.4 Sample Analysis

The gypsum samples were dried under naturally conditions and later soaked in tap water for 24 hours to reduce impurities such as clay within the gypsum. The gypsum minerals were placed on wire mesh on three steps in an oven in order to allow free circulation of heat in the oven. The temperature of the oven was regulated at 105°C as a preliminary test for 24 hours.

5.5 Mechanical Properties Measurements
5.5.1 Compressive Strength

Compressive Strength test have been carried out on three samples that representing the three studied sites for the investigated P.O.P specimens. After calcination process and grinding the samples were moulded with a dimensions $200 \times 100 \times 20$ mm. The compressive results revealed a relative variation between the investigated sits as shown in Table 2.

Table 2 *Compressive strength of board samples*

Location	Sample average volume (mm)	Failure load (KN)	Compressive strength (KN/ mm^2)
Site (1)	$200 \times 100 \times 20$	11.75	0.588
Site (2)	$200 \times 100 \times 20$	12.14	0.607
Site (3)	$200 \times 100 \times 20$	12.89	0.645

5.5.2 Modulus of Rupture

Munai [13] presented an explanatory study gives a mathematical formula could be used to estimate the modulus of rupture as following:

$M = 3WL/2bd^2$

where, Lbd sample dimensions and the failure load by KN.

Three samples represented the three studied locations were subjected to examination and the results were presented in Table 3.

Table 3 *Compressive strength of board samples*

Location	Sample average volume (mm)	Failure load (KN)
Site (1)	$200 \times 100 \times 20$	0.40
Site (2)	$200 \times 100 \times 20$	0.43
Site (3)	$200 \times 100 \times 20$	0.46
Failure load average (KN)		0.43

$M = 3WL/2bd^2$

L = 80 mm,   b = 100 mm,   d = 10 mm

W = 0.43 KN

Modulus of rupture $= 3 \times 0.43 \times 10^3 \times 80/2 \times 100 \times 10^2 = 5.16$ N/mm^2

ASTM – C-59, (1990) recommended that the minimum value of bearing strength for Plaster Of Paris is 267 N, and 455 N for flexural strength. Accordingly, the obtained result of the investigated samples is 516 N which greater the recommended value of ASTM – C-59, (1990).

6   Results and Discussion

The gypsum ore deposits occur in a huge amounts and high reserves. The thickness varies from site to another ranging from a few meters to more than 20 meters of the outcrops beds (Figure 9). Generally overlain by clay rocks or sometimes calcareous ones. The area

have irregular land morphology depending on the lithology and tectonics of the region. The rock outcrops are common on the upper slopes. Weathering products cover the lower slopes. Peaks around the region are generally W-E and sometimes NW-SE trending. The climate is an east Mediterranean one. In the region, the summer is mild and humid and the winter is mild and wet. Precipitation occurs mostly in the form of rainfall, intensifying winter.
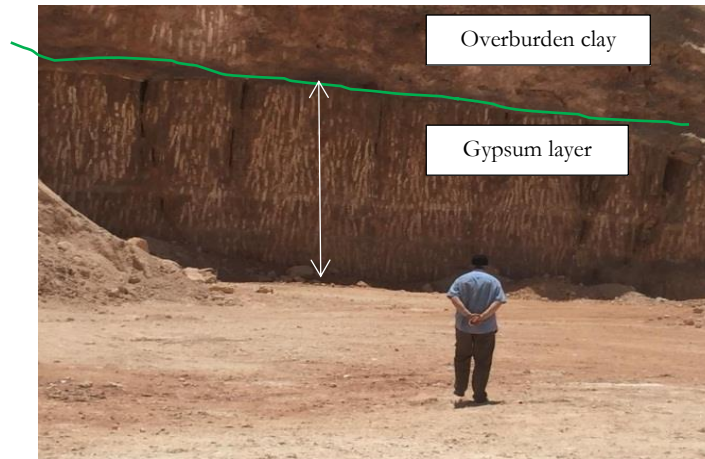
Figure 9 *Thickness variation of gypsum depsites*

Generally, in the point of view of the previous geological studies, Libya has beendivided into four main regions as following:

1.   Northwestern region: include Tripoli area, Al Jofra coastal plain, Nafossa mountain, Hamada basin and northern Gargaf elevations.

2.   Northcentral region: include Sirte basin and Al Jofra area.

3.   Northeastern region: made up of Cyrinica area, Al Jabal Al Akhadar, Al Sarir and Al Jaghboub.

4.   Southwestern region: represented by Fazan area and Merzq basin.

This study has been performed on the local gypsum deposits in north east Benghazi city which belonging to the Northeastern region which covered by a succession of clay and limestone rocks which go back to the Tertiary of Cenozoic Era, representing by Al Faidiyah formation.

6.1 Chemical Analysis

Three samples from different from each quarries were ground to fine powder using mortar and pestle to prepare for chemical analysis. Tables 5 through 7 provide the results of chemical analysis for the studied locations.

Table 5 *Chemical composition of three gypsum samples for site (1)*

Chemical compound	Chemical composition (Wt. %)			Average ($\bar{x}$)
	Sample (1)	Sample (2)	Sample (3)	
SO_3	43.40	44.19	42.99	43.52
CaO	23.06	23.90	22.96	23.30
MgO	1.45	1.49	1.50	1.48
K_2O	0.33	0.30	0.29	0.31
Na_2O	0.21	0.25	0.26	0.24
MnO	0.033	0.32	0.30	0.217
TiO_2	0.050	0.045	0.052	0.049
Fe_2O_3	0.25	0.20	0.21	0.22
Cl	0.0050	0.0042	0.0056	0.0049
L.O.I.*	33.40	29.20	30.53	31.043
$\sum$	99.19	99.70	99.10	99.33

L.O.I.* = loss on ignition

Table 6 *Chemical composition of three gypsum samples for site (2)*

Chemical compound	Chemical composition (Wt. %)			Average ($\bar{x}$)
	Sample (1)	Sample (2)	Sample (3)	
SO_3	43.43	43.16	42.40	42.99
CaO	22.82	21.96	20.99	21.92
MgO	1.07	1.02	1.15	1.08
K_2O	0.25	0.22	0.19	0.22
Na_2O	0.21	0.19	0.24	0.213
MnO	0.024	0.030	0.032	0.028
TiO_2	0.0037	0.0031	0.002	0.0029
Fe_2O_3	0.22	0.26	0.31	0.26
Cl	0.0040	0.0039	0.0044	0.0041
L.O.I.	30.93	32.19	33.80	32.31
$\sum$	98.96	99.02	99.12	99.03

Table 7 *Chemical composition of three gypsum samples for site (3)*

Chemical compound	Chemical composition (Wt. %)			Average ($\bar{x}$)
	Sample (1)	Sample (2)	Sample (3)	
SO$_3$	42.70	41.15	40.12	41.32
CaO	22.66	24.16	25.01	23.94
MgO	1.12	1.19	1.21	1.17
K$_2$O	0.33	0.35	0.41	0.36
Na$_2$O	0.19	0.28	0.30	0.26
MnO	0.026	0.032	0.031	0.029
TiO$_2$	0.040	0.044	0.046	0.043
Fe$_2$O$_3$	0.22	0.290	0.310	0.273
Cl	0.004	0.0091	0.0062	0.0064
L.O.I.	31.80	31.37	31.58	31.58
$\sum$	99.09	98.88	99.02	98.99

The gypsum samples were dried under naturally conditions and later soaked in tap water for 24 hours to reduce impurities such as clay within the gypsum. The gypsum minerals were placed on wire mesh on three steps in an oven in order to allow free circulation of heat in the oven. The temperature of the oven was regulated at 105°C as a preliminary test for 24 hours. Only partial transformation to hemihydrates was observed. To achieve the required calcination of gypsum, the temperature was raised to about 200°C (392°F) for another 24hours. The calcined gypsum was brought out and the mineral was observed to become completely whitish in physical presentation. The same process was carried out for the second batch of calcination. In order to achieve smooth and homogenous finish to the board surface, the calcined mineral was ground and 200µm sieve was used to obtain fine powder. The powder was then placed into clean polythene bag to avoid moisture absorption. The average chemical composition of the investigate gypsum is shown in Tables 8, while Table 9 gives the chemical composition of the plaster in percentage by weight. Tables 10 and 11 give comparison of the chemical composition of the studied gypsum and its plaster with those of pure gypsum respectively.

Table 8 *Chemical composition of plaster of site (1)*

Chemical compound	Chemical composition (Wt. %)			Average ($\bar{x}$)
	Sample (1)	Sample (2)	Sample (3)	
SO$_3$	54.12	55.16	53.77	54.35
CaO	26.90	27.02	25.97	26.63

H_2O	16.10	15.02	19.33	16.82
$\sum$	97.12	97.2	99.07	97.80

Table 9 *Chemical composition of plaster of site (2)*

Chemical compound	Chemical composition (Wt. %)			Average ($\bar{x}$)
	Sample (1)	Sample (2)	Sample (3)	
SO_3	53.41	54.16	53.62	53.73
CaO	25.66	26.14	24.88	25.56
L.O.I.	19.87	18.88	20.22	19.66
$\sum$	98.94	99.18	98.72	98.95

Table 10 *Chemical composition of plaster of site (3)*

Chemical compound	Chemical composition (Wt. %)			Average ($\bar{x}$)
	Sample (1)	Sample (2)	Sample (3)	
SO_3	53.10	52.19	52.77	52.69
CaO	24.19	25.84	25.98	25.34
L.O.I.	21.74	20.12	21.40	21.09
$\sum$	99.03	98.15	100.15	99.11

Table 11 *Comparing average gypsum and plaster chemical composition with pure gypsum*

Chemical compound	Pure gypsum (wt. %)	Gypsum (wt. %)			Pure gypsum plaster (wt. %)	Gypsum plaster (wt. %)		
		Site (1)	Site (2)	Site (3)		Site (1)	Site (2)	Site (3)
$CaSO_4$	79.20	72.24	71.16	69.67	93.50	90.12	88.66	87.54
$2H_2O$	20.95	26.57	27.95	29.33	6.50	9.05	10.14	10.98
$\sum$	100.15	98.80	99.11	98.99	100.00	99.17	98.80	98.52

Figure 10 gives a comparison between the local investigated gypsum samples and the standard pure one; while Figure 11 depicts the comparison between the studied gypsum plaster samples and the pure gypsum plaster. Both of them display no much difference which indicate that the local gypsum has good characterizations. It was recommended by Singer [13] that pure gypsum should have about 93. 8% $CaSO_4$ and 6.2% H_2O while the American Standard of Testing Materials (ASTM) – C-59 (1990) recommends 85% minimum of dehydrated purity. Thus, sites 1, 2 and 3 are 90.12%, 88.66% and 87.54% respectively have met the ASTM – C – 59 [14] requirements.
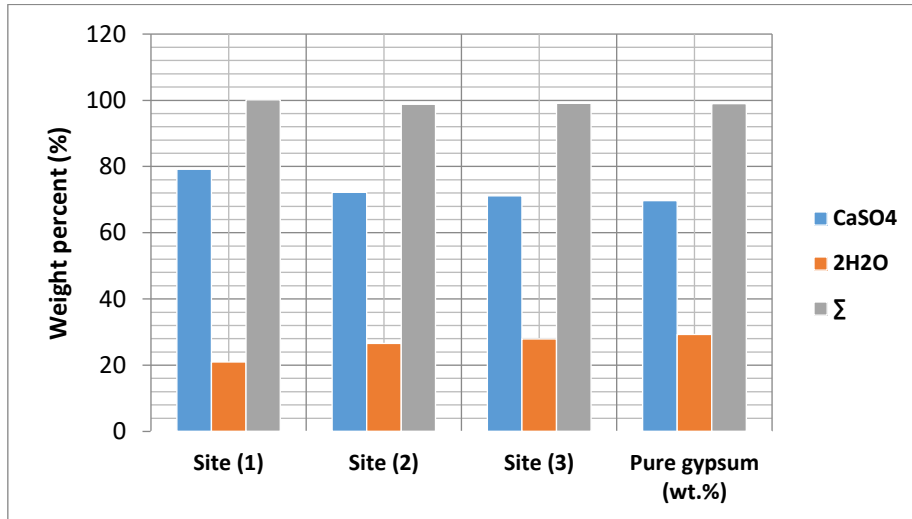
Figure 10 *A comparison between local gypsums and standard one*
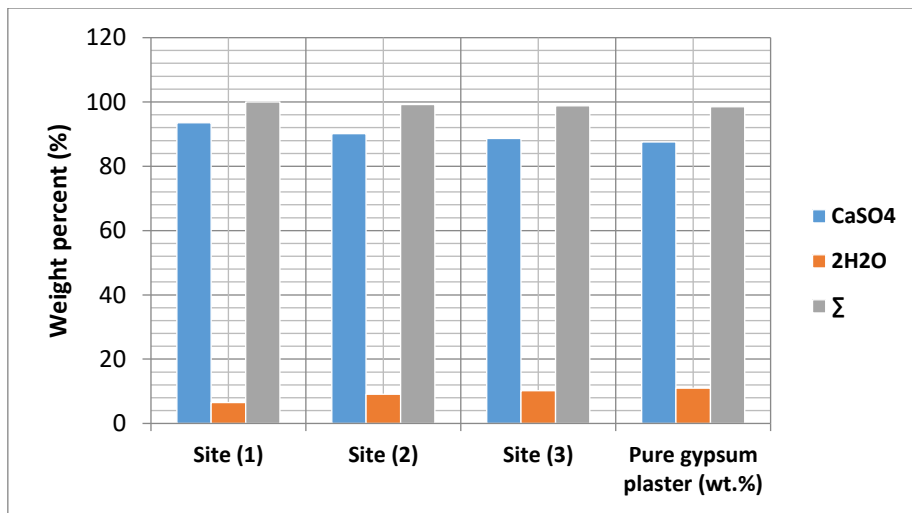
Figure 11 *A comparison between local gypsum plaster and the pure gypsum plaster*

6.2   Setting Time

The plaster of Paris has a very short setting time which sometimes limits its usefulness, in some conditions like in buildings; however, the short setting time is a useful property. The optimum setting time is usually determined by the user's needs and convenience which can also be controlled through the use of additives. Table 12 shows the setting time of various mixes.

Table 12 *Setting time of calcined plaster with different water ratios*

S/N	Water ratio (ml)/dry plaster (g)	Pouring time (sec)	Setting time (sec)
1	150/350	19.0	370
2	160/350	24.0	485

3	170/350	29.0	498
4	180/350	34.0	530
5	190/350	38.0	565
6	200/350	41.0	610

The findings were obtained in Table 10 reveal that, as the quantity of water increased so did the setting time. Although 200 ml of water was poured in 41.0 seconds, 3 seconds less than the pouring time of 190ml, a longer time of 610 seconds was recorded as the setting time for the 200ml as against that of the 190 ml (565 seconds). This shows that the setting time is dependent upon the water content rather than the pouring time as illustrated in Figure 12.
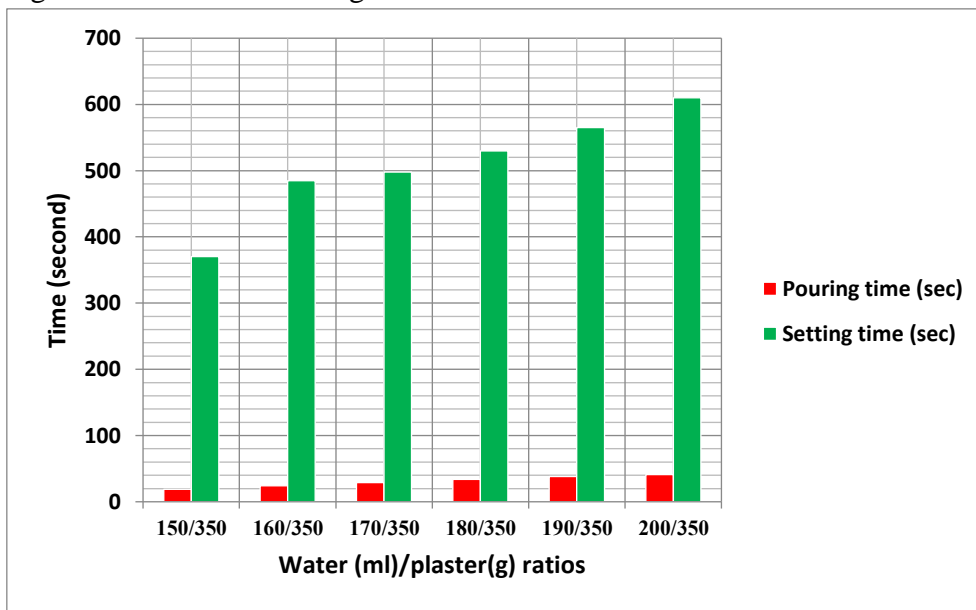
Figure 12 *Relationship between water/plaster ratios and time*

7 Conclusions

The varieties of gypsum minerals investigated in this study that based on the results of the physical and chemical analyses, it can be concluded that studied local gypsum has satisfied the requirement of good gypsum. The tests carried on the gypsum and plaster produced revealed that the gypsum is suitable for the production of quality calcium sulphate, hemihydrate ($CaSO_4.1/2H_2O$) which is termed Plaster Of Paris (P.O.P). The ability to control the time of rehydration by addition of retarders or accelerators offers the huge and diverse nature of industrial applications in medicine, art, ceramics, building and construction among others. On the other hand, the mechanical testing of Plaster Of Paris samples revealed an acceptable characterization for construction purposes according to the recommended value of ASTM – C-59, (1990).

References

[1]   Euro gypsum organization (2010), Living with gypsum, euro gypsum magazine, p4 16.

[2]   Corburn, A., Dudley, D., & Spence, C. (1989). Gypsum Plaster, its manufacture, Uses and Immediate technology. London. pp. 5 – 29.

[3]   Borkowska, M., & Smulikowski, K. (1973). Rock forming minerals. Warszawa: Wydawnictwa Geologiczne.

[4]   Akerman, K. (1964). Gypsum and anhydrite. Warszawa: PWN.

[5]   Pinheiro, S. M., & Camarini, G. (2015). "Characteristics of gypsum recycling in different cycles," International Journal of Engineering and Technology, 7(3), 215.

[6]   Luk, W. K., & Darvell, B. W. (2003). Effect of burnout temperature on strength of gypsum-bonded investments.Dental materials, 19(6), 552-557.

[7]   W. Lou., B. Guan and Z. Wu, "Dehydration behavior of FGD gypsum by simultaneous TG and DSC analysis,"Journal of thermal analysis and calorimetry, vol. 104, no.2, pp. 661-669, May 2011 DOI: 10.1007/s10973-010-1100-6.

[8]   T. Fukami, S. Tahara, K. Nakasone and C. Yasuda, "Synthesis crystal structure, and thermal properties of $CaSO_4\ 2H_2O$ single crystals, "International journal of chemistry, vol. 7, no.2, pp.12-20, July 2015 DOI:10.5539/ijc.v7n2p12.

[9]   K. Regulska and A. Repelewicz, "Properties of gypsum composites with sawdust, "E3S Web of Conferences," 97(02037), 1-5 DOI:10,1051/e3sconf/20199702037.

[10] U.S. Geological Survey (2020) Mineral Commodity Summaries, January 2020.

[11] Industrial Research Center (2004) Department of Geological Researches and Mining, Tripoli, Libya.

[12] A. Corburn, D. Dudley and C. Spence, Gypsum Plaster, its manufacture, Uses and Immediate technology. London. pp 5– 29, 1989.

[13]   F. Singer, S. S. Singer, Industrial Ceramics. Chapman and Hall Limited, London.1455pp, 1971.

[14]   American Standard of Testing Materials (ASTM) – C-59 (1990).

[15]   D. M. Munai, The Viability of Nafada Gypsum as Material for the Production of Plaster of Paris Suitable for Slip Casting Mould. Unpublished M.Tech. Thesis, Abubakar Tafawa Balewa, University, Bauchi, Nigeria, 2000.

Fifth Conference on Engineering Sciences and Technology (CEST-2022) 20-22 December 2022/ Libya

Phytoremediation Treatment of drilling cuts contaminated with petroleum hydrocarbons using Bermuda grass (Cynodon dactylon)

Phytoremediation Treatment of drilling cuts contaminated with petroleum hydrocarbons using Bermuda grass (Cynodon dactylon)

Adel E. Elallam, adel.alallam@yahoo.com

College of Engineering Technology - Janzour

Chemical and Environmental Engineering Department

Abstract

Phytoremediation of drilling waste contaminated soils was tested using a native Bermuda grass species. A glasshouse experiment evaluated the ability of grass to survive, degradation of petroleum hydrocarbons in contaminated soils. In this study, Bermuda grass was planted in soil comprising different ratios of soil: waste to examine the effect of petroleum hydrocarbons concentrations. Biomass measurements including shoot biomass, grass height, leaf area, roots height and density were made, in addition to testing for any TPHs contamination, and the role of microorganisms and enzymes in the dissipation of petroleum hydrocarbons. This research suggested that Bermuda grass is a useful species for phytoremediation of soils contaminated by drilling waste. Bermuda grass also is shown to have the potential to remediate soils contaminated by petroleum hydrocarbons when the contamination level below 7350 mg kg-1 TOC. The grass offers an environmentally-friendly, cost-effective waste management option for some sites despite requiring a longer time. Results from this study are helpful for further field phytoremediation studies.

Keywords: Phytoremediation, Bermuda grass, TPHs contamination Biomass.

1.   Introduction

The process of drilling oil and gas wells for exploration and production generate massive quantities of drilling waste contains cutting and spent drilling fluids. This type of waste classified as 'toxic waste' cause environmental problems and considered one of the main problems facing the oil and gas industry in Libya due to the significant negative ecological impacts to the surrounding environment. Up to now, in most of drilling operations in Libya, drilling waste temporarily stored in earthen pits close to drilling operations before disposal to the land or buried in theses pits. This waste management option provides a simple and low cost disposal method, but its unsuitable solution for wastes that contain high concentrations of organic materials and heavy metals and other harmful components that could migrate from the pit to cause pollution of surrounding water bodies, soil and air (Biltayib .2006). Engineering techniques used in treatment of soil contamination based on physical, chemical and thermal processes are very expensive and not always effective. Biological treatment techniques are perhaps the most suitable in Libya due to their low-inputs and low- cost. Further work is required to specifically assess the efficiency of these approaches for the remediation of drilling waste in the context of the Libyan environment. The biological treatment solutions such as bioremediation has become a valuable alternative to chemical and physical (traditional) methods.

Fifth Conference on Engineering Sciences and Technology (CEST-2022) 20-22 December 2022/ Libya

Phytoremediation Treatment of drilling cuts contaminated with petroleum hydrocarbons using Bermuda grass (Cynodon dactylon)

Bioremediation has low operation cost (costs 10-20% of other mechanical treatments) (El-Dars et al. 2016), and can be used efficiently in removing of organic and heavy metals from contaminated water and soils. Bioremediation treatment techniques divided into two broad categories in-situ and ex-situ media. In-situ treatment processes involve treatment of contaminated soils and water in the place of generation, without removal to different site for treatments which reduce the cost of treatment, where in Ex-situ treatment processes, the contaminated media transferred to a treatment area (US EPA. (2018)), among the bioremediation techniques, Phytoremediation has emerged as good choice to detoxify polluted sites (Soils, water and sediments) in-situ. Phytoremediation is the use of vegetation to minimise the contamination volume, mobility of contaminants, or toxicity of contaminants in soil, groundwater, or other contaminated media (USEPA, 2000; Etim 2012). It is defined as a biological technology use plants for in situ removal, degradation, or clean-up of different types of pollution including metals, pesticides, explosives, and oi contaminants in different contaminated media (soils, sludge, sediments, surface water and groundwater), the used plants also help stabilise contaminates and reduce its mobility from sites by wind, rain, and groundwater to other areas. The most important factors affecting the successful phytoremediation are plant type and addition of soil amendments and bulking agents (ElDars et al. 2016). Phytoremediation is best implemented at sites with lower contamination by organic materials or heavy metals and usually applied through one of these mechanisms: Phytotransformation, Rhizosphere Bioremediation, Phytostabalisation, Phytoextraction, Phytovolotalisation or Rhizofiltration. Among the various mechanisms involved in phytoremediation of contaminated soils, Rhizodegredation is of major significance for the enhanced removal of hydrocarbons from soil (Lijuan Cheng et al. 2019). The performance of Rhizodegredation mechanism enhanced by root exudates such as enzymes and flavonoids, organic acids, sugars and amino acids which play the major role to induce bacteria and fungi growth in rhizosphere soil and consequently leading to degradation and mineralization of hydrocarbons pollutants (Dadrasnia, and Ismail, (2015)). Several plants already identified and trailed to be used in the rizoremidation of organic compounds and heavy metals (Anyasi and Atagana. (2018)), among of them wild grass species such as Bermuda grass (Cynodon dactylon) and Tall fescue (Festuca arundinacea Schreb) and stargrass (Ponterderiaceae). The selection of Bermuda grass because it is grows well on a variety of soil from heavy clay to deep sands, it tolerates both acid and alkaline soil conductions and is highly tolerant to salt, drought, anoxia (flooding), cold and soil compaction (Buble 2009). Moreover, it has extensive, fibrous, widely branched and deep root systems which can provide significantly larger root surface area for colonization by microorganism in its rhizosphere (Turgeon 1980) are mainly restricted by hydrophobic and toxicological nature of the contaminants, as well as the synergy existing between plant roots and soil microorganisms (Wang et al. 2011). In most of previous studies, the phytoremediation of hydrocarbons using Bermuda grass was conducted in natural soil or synthetic soil, there is no available studies

Fifth Conference on Engineering Sciences and Technology (CEST-2022) 20-22 December 2022/ Libya

Phytoremediation Treatment of drilling cuts contaminated with petroleum hydrocarbons using Bermuda grass (Cynodon dactylon)

conducted in drilling waste cutting or soils with calcareous nature which may affect the growth of the grass and effect all of biodegradation process. According to the principles of phytoremediation treatment of hydrocarbons through Rhizodegredation mechanism, the main objective of this research is to test the tolerance levels of Bermuda grass species to grow in drilling waste contain high concentration of petroleum hydrocarbons and have a calcareous nature and the adoption of this species to the desert climate in Libya, and providing a preliminary evaluation of the effectiveness of Bermuda grass as potential phytoremediater species to clean up and/ or reduce the contamination in drilling waste .

2.   Material and Methods

2.1   Site and Soil samples collection

Two different drilling waste samples and uncontaminated native soil sample for experiment were collected during the drilling operations in Jalu area in Libyan Desert. The physical properties, chemical composition and texture of soil samples shown in table 1. All samples were dried in air for 2 weeks, sieved through 2 mm mesh to eliminate coarse rock and plant material, and thoroughly mixed to ensure uniformity.

Table 1. Physical properties, chemical composition and texture of soil samples

Test	Unit	WBMW	OBMW	N. Soil
pH	-	8.4	8.8	8.7
EC	ms/cm	4.06	4.2	0.08
T.D.S	mg/Kg	2035	1995	38
Moisture	Wt. %	12.4	55.2	3.79
L.O.I	Wt. %	21.3	59.5	4.35
TPH	Wt. %	1.47	8.56	0.15
Cr	mg/Kg	28.4	34.3	10.8
Mn	mg/Kg	43.3	33.7	80.1
Cu	mg/Kg	9.3	34.5	16.4
Zn	mg/Kg	50.9	74.8	19.3
As	mg/Kg	2.0	6.17	1.37
Cd	mg/Kg	0.44	0.72	0.0
Ba	mg/Kg	1066	3832	242
Pb	mg/Kg	10.3	61.0	7.07
Na	mg/Kg	2089	2217	1328
Ca	mg/Kg	280972	253821	5978
Mg	mg/Kg	2211	19523	1843
K	mg/Kg	1279	11306	7218
Cl	mg/Kg	8400	6590	112
NO3-N	mg/Kg	0	0	0
PO4-P	mg/Kg	0	0	0
SO4-2-S	mg/Kg	303	2152	120
Mean Particle Size	☐m	314	193	124

Fifth Conference on Engineering Sciences and Technology (CEST-2022) 20-22 December 2022/ Libya

Phytoremediation Treatment of drilling cuts contaminated with petroleum hydrocarbons using Bermuda grass (Cynodon dactylon)

Specific Surface Area	cm^2/g	2043	3173	795
Soil Texture	-	Loamy Sand	Loamy Sand	Sand
Minarology by XRD		Calcite CaCO$_3$ Quartz SiO$_2$ Ankirite Ca(Fe^{+2},Mg)(CO$_3$)$_2$	Calcite CaCO$_3$ Quartz SiO$_2$ Bairite BaSO$_4$	Quartz

WBMW= Water based mud waste   **OBMW= Oil Based mud waste**   **N. Soil= Native Soil**

• Bermuda Grass

Commercially Bermuda grass (Cynodon dactylon) was selected in these experiments due to it is availability in Libya and the gained experience in adapting of this plant to the harsh conditions, such as heat, extensive light, and drought.

2.2   Green House Experiments

Pot experiments were conducted during the summer period (June, July and August) in order to grow the candidate grass for 2 months (60 days) in contaminated soil at greenhouse condition similar as possible to Libyan Desert climate. The drilling waste and native soil samples was supplied with a compound fertilizer (N : P$_2$O$_5$: K$_2$O = 10: 8: 9) to compensate the shortage of essential nutrients (N & P) in drilling waste and native soil samples and kept for equilibration for 1 week in air then sieved through a 2 mm mesh sieve.

2.2.1 Pot experiment set-up

The experimental design contains three different treatments (Control, WBMW and OBMW). In control treatment only native soil was used where in WBMW and OBMW treatments, different TPH and HMs contamination levels was prepared by dilution of contaminants in drilling waste samples using native soil. Table 2 illustrate the treatments and approximation concentration of TOC in each treatment.

Table 2. Description of pot experiment design

Code	Treatment	Dilution Factor	TOC Level Wt. %	Approx. TOC concentration mg/Kg
C	Control (Native Soil)	1	-	-
25W	25WBMW:75Native Soil	4	0.37	3675
50W	50WBMW:50Native Soil	2	0.74	7350
100W	100 WBMW	1	1.47	14700
25O	25OBMW:75Native Soil	4	2.14	21400
50O	50OBMW:50Native Soil	2	4.28	42800
100O	100 OBMW	1	8.56	85600

Each treatment was replicated 4 times, making at total of 28 pots. About 300 g of soil samples (Control or contaminated soil) were added to a plastic pot with a radius of 7.0 cm and a height of 15 cm. According to the results obtained from germination tests of Bermuda grass in native soil, seeding of 50 g /m^2 selected, and similar seeds

Fifth Conference on Engineering Sciences and Technology (CEST-2022) 20-22 December 2022/ Libya

Phytoremediation Treatment of drilling cuts contaminated with petroleum hydrocarbons using Bermuda grass (Cynodon dactylon)

weight sow in each replicate. All pots arranged randomly and exposed to greenhouse condition for 60 days at temperature controlled between 25 to 35 °C and humidity between 40- 60%.

The watering for all pots were adjusted to 30% of water holding capacity of each treatment (0.1 ml/g) to avoid leaching of hydrocarbons and heavy metals from soil. In addition, a 10/1000 strength liquid fertilizer (N: P_2O_5: K_2O = 10: 8: 9) was applied weekly. After 60 days, the plants extracted carefully from each pot then divided into roots and shoots by cutting the aboveground parts of the plants at the soil surface. Both parts sealed in plastic envelopes **Analysis :**For measurement of biomass, the root parts of grass were washed thoroughly with tap water then by deionised water to remove soil particles, then placed in paper bags and dried in oven at 45 °C for 72 hours, the average of roots length and dry weight was measured. The physical analysis of the soil samples that was firmly attached to the roots conducted using conventional methods. The chemical analysis was conducted using Gas Chromatography equipped with flame ionisation detector (GC-FID) type Agilent model 7890 for measurement of total petroleum hydrocarbon (TPH) concentration. The microbial activity in rhizosphere soil was evaluated using Biolog plate and the microbial enzymes activity was evaluated by measuring the (DHA)

3. Results and dissection

Drilling waste samples analysis: The physical, chemical and texture analysis of the drilling waste samples prior to grass planting as given in Table 1 shows that both samples have sandy loam texture, classified as alkaline soil and considered as calcareous soil have high content calcium carbonate. The concentration of calcium in both drilling waste cuts (WBMW & OBMW) very high 280972 and 253821 mg/kg respectively which detrimental to turf grass, causing damage to grass leaves and blades and affect growth of candidate grass. The analysis results indicate that both drilling waste cuts classified as heavy petroleum-contaminated soils containing high concentration of petroleum hydrocarbons, low levels of toxic heavy metals such as copper, manganese and chromium, and very poor nutrients (Phosphors & Nitrogen) which expected to have negative impact in grass growth.

Grass Growth and Biomass measurements

Bermuda grass showed a promising behaviour and high potential of adaptation to soils contaminated by low levels of petroleum hydrocarbons (after dulition of raw WBMW&OBMW using native soil) as shown by the growth and biomass production in control, 25W and 50W treatment during a period of 60 days in greenhouse condition. There are no visible adverse symptoms such as wilting, lodging or defoliation observed before harvest during the study period. The response of Bermuda grass to TPH and HMs contamination level was ranging from reasonable growth in control and 25W treatment to moderate effect in 50W treatment. The grass growth in treatments 100**W**, 25**O**, 50**O** and 100**O** were severely stunted, thus this treatment will not be considered in the further discussion in plant development or phytoremediation of petroleum hydrocarbons. The results showed that no grass growth in all treatments contains more than 7350 mg/kg TPH which may attribute to the high levels of petroleum hydrocarbons and the oily nature of this treatments.

Fifth Conference on Engineering Sciences and Technology (CEST-2022) 20-22 December 2022/ Libya

Phytoremediation Treatment of drilling cuts contaminated with petroleum hydrocarbons using Bermuda grass (Cynodon dactylon)

Figure 1. Reduction in plant parts length in different amended WBMW treatments

As shown in figure 1, Bermuda grass exhibited good growth rates in native soil (control

0.0 % wt. %. Approx. 0 mg/Kg TOC) and in WBMW diluted treatments, 25W (0.37 % wt. Approx. 3675 mg/Kg TOC) and 50W (0.74 % wt. % 7350 mg/Kg TOC). The rate and extent of grass growth in control and 25W was almost the same where it is reduced by approx. 16 % in 50W treatment. The plant height decreased significantly with increasing in the contamination level (p <0.001). No difference in average grass length between control and 25W, in both treatment was almost similar (approx. 29 cm) after 60 days. However, plant Lenght reduced by approx. 16% with increasing of the contamination level in treatment 50W and by approx. 86 % in treatment 100W when compared with the control as shown in figure 2.
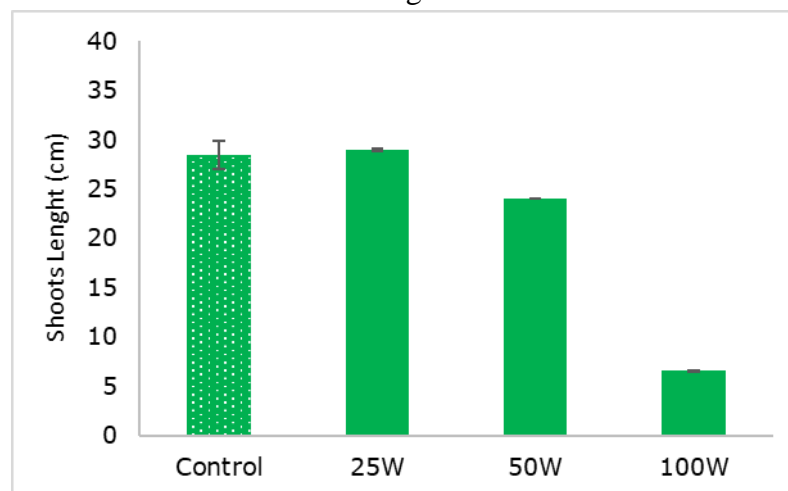
Figure 2. Plant height of Bermuda grass in different WBMW treatment

The results showed that roots density and length different qualitatively and quantatively between the treatments. The roots length in successful treatments decreased significantly (P=0.001) as the contamination level by HMs and TPH increased. The root of plant in

Fifth Conference on Engineering Sciences and Technology (CEST-2022) 20-22 December 2022/ Libya

Phytoremediation Treatment of drilling cuts contaminated with petroleum hydrocarbons using Bermuda grass (Cynodon dactylon)

control and 25W treatment were distinctly larger and more fibrous than the root system in 50W treatment. The root length reached the highest level in treatment 25W, and then declined. Besides, no significant (p > 0.1) decrease was found in root length and root weight between control and 25W treatments as shown in table 3 and figure 1 .

Table 3. The changes in plant parts length under different contamination levels

Treatment	Control	25W	50W	100 W
Length of plant parts				
Shoots (cm)	28.5	28.9	24.0	4.1
Reduction (%)		+ 1.4	-16	-86
Roots (cm)	7.8	8.0	5.7	0.5
Reduction (%)		+ 2.5	-22	-93

Biomass and leaf area Measurements

Based on the results illustrated in figure 3 of biomass measurements (Dry weight), it was found that the total biomass yield per pot decreased significantly as the contamination level increased. The biomass measurements of treatment 25W did not reduced significantly when compared with the control, but contrary to the expectations showed reasonable outgrowth (approx. + 40%) in dry shoot weight, whereas that a significant (p < 0.001) reduction was observed in treatment 50W and 100W (-48 % and -97%) respectively as shown in figure 4.

Figure 3. Total biomass (dry weight) of Bermuda grass in different WBMW treatment. .

Fifth Conference on Engineering Sciences and Technology (CEST-2022) 20-22 December 2022/ Libya

Phytoremediation Treatment of drilling cuts contaminated with petroleum hydrocarbons using Bermuda grass (Cynodon dactylon)
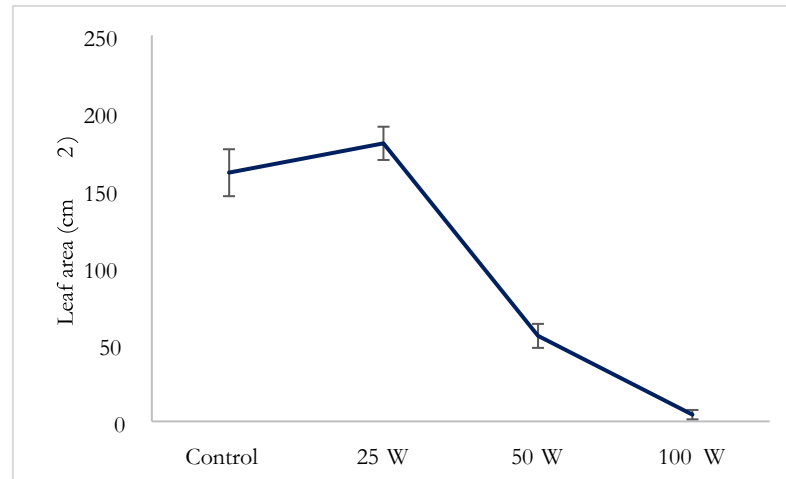
Figure 4. Leaf area of Bermuda grass in different WBMW treatment.

The obtained results support the finding of many researchers whom concluded the destructive effect of high levels of petroleum hydrocarbons and heavy metals in grass growth (Basumatary et al. 2012 ; Htwe et al. 2016). Overall, petroleum hydrocarbons found to have an inhibiting plant growth and effect the general p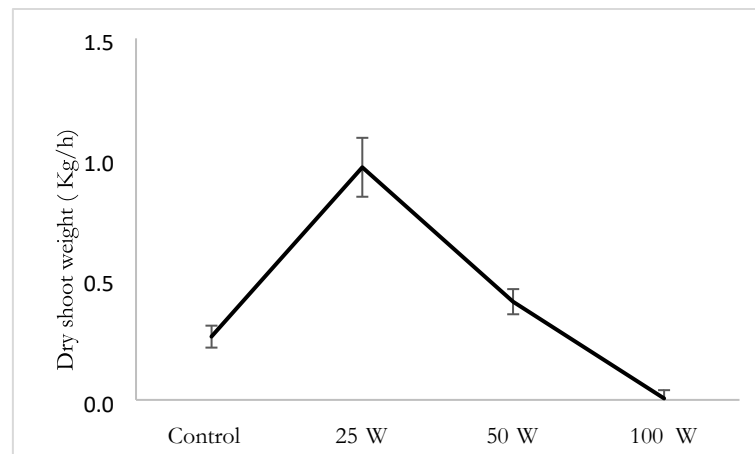lant health (especially root system), duo to the toxicity nature of these types of compounds. This finding broadly supports the work of other studies in this area linking the survival of different grass species in soils contaminated by petroleum hydrocarbons. Different authors observed similar adverse effect on plant growth in soils contaminated by hydrocarbon. (Razmjoo et al. , 2012; Saraeian et al. 2016) was reported reduction in shoot and roots growth of Bermuda grass planted in soil contain 6 wt. % petroleum hydrocarbon contaminates. Bermuda grass shoot fresh and dry weight decreased significantly with increasing in the level of contamination.

Effect of Soil texture and changes in soil properties .

During the watering procedure for the plants in the greenhouse experiments, it noticed that the treatments 100**W**, 25**O**, 50**O** and 100**O** have very low water holding capacity and showed low permeability and low infiltration for irrigation water and looked as flooded soil. Contrary, the other treatments such as control, 25W and 50W exhibited good water holding capacity and reasonable grass growth. Also, it noticed that the treatments which amended by addition of native soil for the purpose of dilution of contamination level gave better grass growth comparing with the un-amended treatments which may attributed to different reasons as mentioned in literature:

i)   Native soil played the role of bulking agent and increased the soil porosity and the aeration in 25W and 50W treatment, thus, increased the oxygen diffusion and the microbial activity needed for grass growth (El-Dars et al. 2016)

ii)   The hydrophobic nature of treatments 25O, 50O 100W and 100O as a result of high TPH content led to low permeability and low infiltration of water in these treatments causing artificial drought in the subsurface layer of soil in those treatment which affected negatively on grass growth (Edama et al. 2011).

Fifth Conference on Engineering Sciences and Technology (CEST-2022) 20-22 December 2022/ Libya

Phytoremediation Treatment of drilling cuts contaminated with petroleum hydrocarbons using Bermuda grass (Cynodon dactylon)

iii)   The higher clay content in the unsuccessful treatments leads to binding of the soil particles by the effect of irrigation water which governing water, air, bioavailability of nutrients and temperature in soil, which in turn, govern plant growth.

The changes in pH value of soil After 60 day greenhouse experiment illustrated in table 4. The obtained results shows that pH value of the control, 25W and 50W treatments exhibited good grass growth was in the range of 7.3, which is close to the optimum pH value recommended by Pawar, R. (2015) to enhance the bioavailability of essential nutrient needed for grass growth (pH 6.0 -6.5), and very close to the pH value needed for Phytoextraction of heavy metals as recommended by Htwe et al. (2016).

Table 4. Changes of pH-value after planting of Bermuda grass in different treatments

Treatment	control	25W	50W	100W	25O	50O	100O
Before Planting	8.7	8.4	8.4	8.4	8.4	8.8	8.8
After planting	7.2	7.3	7.3	10.8	11.1	11.3	11.6

In the unsuccessful treatment such as   100W, 25O, 50O and 100O, it is apparent that the high pH values result from the high calcium carbonate content in these treatments which lead to less vigorous growth and nutrient deficiencies and inhibiting the Bermuda grass growing in these treatments.

Effect of TPH on phytoremediation by Bermuda grass

The biomass measurements illustrated in Figures (1,2,3 and 4) in this research showed that the shoot growth of Bermuda grass reduced scientifically (p-value <0.001) as the petroleum contamination levels in the soil increased. The same effect (p-value < 0.001) was recorded in roots density and leaf area as petroleum contamination levels increased up to 0.74 wt.% TOC (approx. 7350 mg kg-1).

Despite the fact that hydrocarbon pollution depressed plant growth to some extent as the petroleum hydrocarbon concentration increase, the results indicate that the Bermuda grass can survive and tolerate petroleum hydrocarbons concentration below (0.74 wt. % approx. 7350 mg kg-1 TOC), and it is can efficiently dissipate the petroleum hydrocarbon from amended drilling waste, indicating that phytoremediation, using this species is useful technique for remediation of soils contaminated by drilling waste polluted with petroleum hydrocarbons in level < 0.74 wt.% TOC. Similar results were obtained by Yateem et al., (2000) using alfalfa and perennial ryegrass as phytoremediater plant in soil contaminated by the presence of 1% TPHs. The chemical analysis of the rhizosphere soil for treatments 25-W and 50-W demonstrated 99.0 and 98.0 % reduction in TPH content respectively (table 6), compared with 32% reduction in the nonplanted controls after the bioremediation treatment for 60 days. The results indicate that the higher reduction in TPH content was in the rhizosphere region (almost 67 % in both treatments). The reduction of

Fifth Conference on Engineering Sciences and Technology (CEST-2022) 20-22 December 2022/ Libya

Phytoremediation Treatment of drilling cuts contaminated with petroleum hydrocarbons using Bermuda grass (Cynodon dactylon)

TPH in unplanted control may be attributed to the evaporation by the action of glasshouse temperature changes (25-35ºC) during the glasshouse experiment period, or to the microorganism activity in this samples.

Table 5: TPH concentration in leachate of planted soil contaminated by drilling waste in treatments (25-W and 50-W) after glasshouse experiment for 60 days

TPH Fraction	TPH (mg kg^{-1}) in leachate of planted treatments	
	25-W	50-W
n-C10	0	0
n-C11	0.00	0.00
n-C12	0.00	0.00
n-C13	0.00	0.00
n-C14	0.00	0.00
n-C15	0.00	0.00
n-C16	0.00	0.00
n-C17	0.66	1.32
n-C18	0.00	0.00
n-C19	0.00	0.00
n-C20	0.43	0.87
n-C21	0.69	1.37
n-C22	0.00	0.00
n-C23	1.40	2.81
n-C24	0.06	0.11
n-C25	0.00	0.00
n-C26	0.00	0.00
n-C27	0.00	0.00
n-C28	0.00	0.00
n-C29	0.00	0.00
n-C30	0.00	0.00
n-C31	0.00	0.00
n-C32	0.00	0.00
n-C33	0.00	0.00
n-C34	0.00	0.00
Total TPH conc.	3.24	6.48

The efficiency of Bermuda grass in removal of petroleum hydrocarbons from amended drilling waste samples was expected when compared to previous studies using Bermuda grass in remediation of petroleum hydrocarbons contaminated soil. In accordance with the present results, Kaimi et al., (2007) obtain similar results, by comparing the efficiency of Bermuda grass with another twelve-plant species in

Fifth Conference on Engineering Sciences and Technology (CEST-2022) 20-22 December 2022/ Libya

Phytoremediation Treatment of drilling cuts contaminated with petroleum hydrocarbons using Bermuda grass (Cynodon dactylon)

removal of TPH from soil contaminated by (1.5 wt.% TOC) and they found more than 65 % reduction in TPH caused by the plant and almost 37% reduction was lose by evaporation. The results also in line with Saraeian et al., (2016) who found that Bermuda grass reduce the petroleum hydrocarbon content to approx. 40% from soil contaminated by 2 % wt. TOC, and with Razmjoo et al., (2012) where degradation was reported to be 41 % from soils contaminated by 6 % wt. TOC. This study also confirmed these findings and furthermore showed that Bermuda grass tolerate contamination by petroleum hydrocarbons levels below (0.74 wt. % TOC) and can maintain its growth when faced different stress applied in this experiment such as waste texture, calcareous nature of the waste, contamination by TPH and HMs and Desert climate changes.

Effect of plants on soil microbiology

The obtained Biolog Plate results used as a qualitative marker to evaluate the diversity and population of microorganisms able to survive in in drilling waste and metabolize the petroleum hydrocarbons. Soil microbiology activity were investigated using BIOLOG-GN2 plates in order to obtain an idea about the variation of microbial diversity in the planted drilling waste samples. The obtained results also used to know how this variation is influenced by the different environmental stresses such as the high TPH concentration, the calcareous nature of drilling waste and the desert climate changes. The results at the end glasshouse study showed that the bacterial enumeration were higher by orders of magnitude in the amended drilling waste planted treatments. The obtained data also confirmed that the growth of the Bermuda grass in amended drilling waste significantly augmented the number of biodegradative bacteria in the root zone for treatments 25W and 50W as well as the activity and diversity of the microbial communities. The general trend was an increase of the proportion of biodegrading bacteria in the microbial community during the treatment in the rhizosphere soil in all planted soil samples. The obtained data corresponds with findings made in similar studies that have assessed microbial counts in contaminated soils (Mcintosh et al. 2015; Varjani and Upasani, 2017).

These experiments confirm that the addition of plants and soil amendments increases bacterial counts compared to unplanted soils and also confirms that Bermuda grass could tolerate the contamination levels in amended drilling waste, and that the rhizosphere soil in planted samples contains survived organisms can tolerate the stress such as TPH contamination, heat and the calcareous nature of drilling waste, and that Bermuda grass will be effective in terms of bioremediation of petroleum hydrocarbons through a rhizosphere effect.

Soil enzymes activity assays

In order to assure the correct sequence of biochemical reactions in the planted treatments, the soil dehydrogenase enzymes activity DHA was measured after 60 days

Fifth Conference on Engineering Sciences and Technology (CEST-2022) 20-22 December 2022/ Libya

Phytoremediation Treatment of drilling cuts contaminated with petroleum hydrocarbons using Bermuda grass (Cynodon dactylon)

glasshouse experiment, and used as indicator of soil quality changes resulting from phytoremediation management practices using Bermuda grass. The dehydrogenases enzymes representing the most important enzymes in rhizosphere soil and belonging to the 'oxidoreductases' class and being used as indicator in the soils microbial activity during the phytoremediation of contaminated soils (Quilchano and Marañón, 2002) (Salazar et al., 2011). The results in figure show the dramatically increase in DHA activity in treatments 25W and 50W after cultivated by Bermuda grass for 60days and a little change in the control samples.
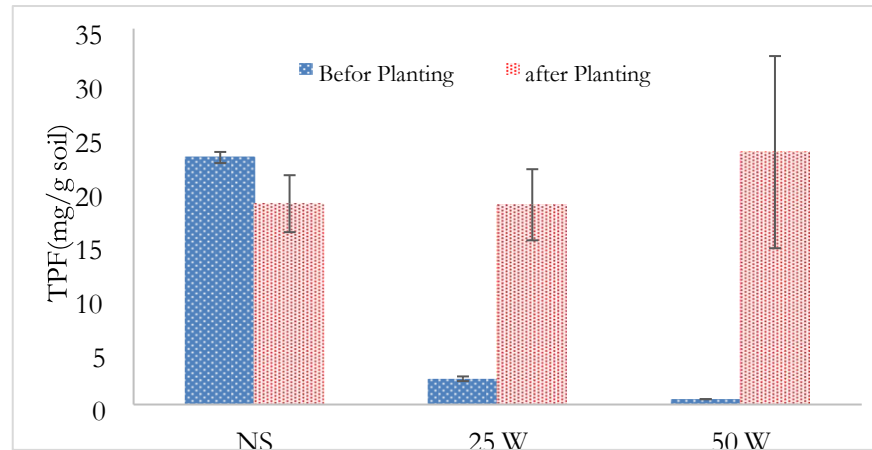
Figure 5. Activity levels of soil dehydrogenases enzymes in remediated soil

The obtained results showed enhancement of DHA values in planted treatments, indicating that the metabolism of soil microbes was promoted, thus resulting in the enhanced microbial which indicate that the general activities of microbes in planted soil were enhanced (Teng et al. 2015; Alrumman et al. 2015). Treatment 50W showed the highest increase in DHA value where treatment 25W and the control shows similar DHA values. From the DHA activity data, the stimulation of petroleum hydrocarbon degrading microbes expected in all successful treatments and that the enzymatic dehydrogenation effect of plants on organic compounds was greatly enhanced under low-level hydrocarbon contamination stress; thereby expected to be effectively promoting and improving degradation of TPHs in rhizosphere soil.

Conclusion

Throughout this study, several evidence was presented that Bermuda grass is an important plant species that can be effectively applied as phytoremediater for clean-up of heavy metals and petroleum hydrocarbon from drilling waste and can efficiently survive and tolerate petroleum hydrocarbons concentration below (0.74 wt. % □ 7350 mg/Kg)

Fifth Conference on Engineering Sciences and Technology (CEST-2022) 20-22 December 2022/ Libya

Phytoremediation Treatment of drilling cuts contaminated with petroleum hydrocarbons using Bermuda grass (Cynodon dactylon)

- Phytoremediation of petroleum hydrocarbons using Bermuda grass has proven to be a feasible method for remediation of drilling waste contains heavy metals and petroleum hydrocarbons less than 0.74 wt.% in the Libyan desert climate.
- It was concluded that the degradation of petroleum hydrocarbons was enhanced through a rhizosphere effect by the effect microorganisms, which through its diversity, density and activity degrade hydrocarbons and facilitate the mobility of heavy metals in the polluted soil.
- The presence of high concentrations of petroleum hydrocarbons reduce the biomass and relative growth rate as the concentration increase.
- Amendment of drilling waste by addition of native soil have larger particle size increase the soil porosity, aeration, oxygen diffusion and water holding capacity in contaminated soil, thus enhance the microbial activity which reflects positively on the phytoremediation efficiency of candidate grass.

References

Anyasi, R. and Atagana, H. (2018). Profiling of plants at petroleum contaminated site for phytoremediation. International Journal of Phytoremediation, 20(4), pp.352-361.

Basumatary, B., Bordoloi, S. and Sarma, H. (2012). Crude Oil-Contaminated Soil Approach. International Journal of Environmental Science and Development, pp.252-257.

Biltayib. M.2006, Oil production in Libya using an ISO 14001 environmental management.

Dadrasnia, A. and Ismail, S. (2015). Bio-Enrichment of Waste Crude Oil Polluted Soil: Amended with Bacillus 139SI and Organic Waste. International Journal of Environmental Science and Development, 6(4), pp.241-245.

Ehmiada M. (2008). Developing an environmental management approach to Libya's upstream petroleum industry. PhD Thesis, Sheffield Hallam University (United Kingdom).

El-Dars, Farida & El-Tohamy, Sayed & Abdelhfeez, Islam. (2016). Removal of total petroleum hydrocarbons from contaminated soil via phytoremediation and amended with sugarcane. Etim E. E. Phytoremediation and Its Mechanisms: A Review. International Journal of Environment and Bioenergy, 2012, 2(3): 120-136

Htwe, W., Kyawt, Y., Thaikua, S., Imai, Y., Mizumachi, S. and Kawamoto, Y. (2016). Effects of lead contamination in soils on dry biomass, concentration and amounts of lead accumulated in three tropical pasture grasses. Grassland Science, 62(3), pp.167-173.

Fifth Conference on Engineering Sciences and Technology (CEST-2022) 20-22 December 2022/ Libya

Phytoremediation Treatment of drilling cuts contaminated with petroleum hydrocarbons using Bermuda grass (Cynodon dactylon)

Kandziora-Ciupa, M., Nadgórska-Socha, A., Barczyk, G. and Ciepał, R. (2017). Bioaccumulation of heavy metals and ecophysiological responses to heavy metal stress in selected populations of Vaccinium myrtillus L. and Vaccinium vitis-idaea L. Ecotoxicology, 26(7), pp.966-980.

Mingorance, M., Valdés, B. and Oliva, S. (2007). Strategies of heavy metal uptake by plants growing under industrial emissions. Environment International, 33(4), pp.514-520.

Onwukwe, S. and Nwakaudu, M. (2012). Drilling Wastes Generation and Management
Pawar, R. (2015). The Effect of Soil pH on Bioremediation of Polycyclic Aromatic Hydrocarbons (PAHS). Journal of Bioremediation & Biodegradation, 06(03).

Phytoremediation by Using Cyperus brevifolius (Rottb.) Hassk. Water, Air, & Soil Pollution, 223(6), pp.3373-3383.

Quilchano, C. and Marañón, T. (2002). Dehydrogenase activity in Mediterranean forest soils. Biology and Fertility of Soils, 35(2), pp.102-107.

Reichenauer, T. and Germida, J. (2008). Phytoremediation of Organic Contaminants in Soil and Groundwater. ChemSusChem, 1(8-9), pp.708-717.

Salazar, S., Sánchez, L., Alvarez, J., Valverde, A., Galindo, P., Igual, J., Peix, A. and Santa-Regina, I. (2011). Correlation among soil enzyme activities under different forest system management practices. *Ecological Engineering*, 37(8), pp.1123-1131.

Truong, P.N. and Baker, D. (1998). Vetiver Grass System for Environmental Protection.
US EPA. (2018). Phytoremediation of Contaminated Soil and Ground Water at Hazardous Waste Sites | US EPA.

Upgrading OF Tajura Seawater Reverse Osmosis Desalination Plant By Integrated Membrane Systems

Abdulghader Elarbi [1*], Mukhtar Ashur [2] , Melaed Musbah [3]
[1] aaelarbi@elmergib.edu.ly, [2] ashour60@academy.edu.ly

[1] Department of Chemical Engineering, El-Mergib University, Al-Garaboli, Libya
[2] School of Engineering, Libyan Academy, Tripoli, Libya
[3] Water Desalination Department, Tajura Nuclear Research Center (TNRC)
*Corresponding author email: aaelarbi@elmergib.edu.ly

ABSTRACT

The Tajura seawater reverse osmosis desalination plant commenced operation in 1984 with only 50% of its production capacity (10,000 m^3/d). Feed water is supplied from an open intake located at Tajura on the Mediterranean coast and treated prior to RO using a conventional pre-treatment system. As time passed, numerous obstacles brought down the plant's production capacity to its lowest level. The operation problems with the coagulation-flocculation pre-treatment system led to an increase in the silt density index (SDI_{15}) and fouling of the RO membrane. In addition, a non-continuous plant operation increased differential pressure, salt passage, and decreased water production through the membranes. This paper describes the problems encountered in the existing conventional pre-treatment system and the conceptual Integrated Membrane System (IMS) design as a part of the plant rehabilitation process of the Tajura RO plant in Libya. The proposed design of the pre-treatment system for the Tajura RO plant utilizes Hydranautics IMS technology. The IMS design is based on long experience from the operation of the two separate RO pilots with different pre-treatment systems for a period of four months on the Mediterranean coast at Tajura city. The previously published data from those pilot plants confirmed the prior assumption that UF pre-treatment produced stable feed water quality, measured by reduced turbidity and by the SDI15. The upgrading of the Tajura RO plant by IMS was designed for full product capacity (10,000 m³/day). The plant will employ dissolved air flotation pre-treatment followed by Hydranautics IMS membrane technology consisting of four UF racks with Hydranautics HydraCap80, the overall UF plant is designed for a continuous UF to permeate flow of 670 m³/h. The nominal flux rate is 72.1 L/m²/h with all UF blocks in operation and downstream two seawater RO trains with SWC5 membranes working at 35% recovery.

Keywords: Conventional pre-treatment; Membrane pre-treatment; Desalination Reverse Osmosis; Integrated Membrane System.

1 Introduction

Pre-treatment is critical in RO applications because it directly impacts the fouling of the RO membranes. Fouling of the RO membranes results in increased operating costs from increased cleaning demands, increased feed pressures, and reduced membrane life. Additionally, fouling can result in reduced permeate water quality and permeate quantity, thereby impacting production from the RO facility.

The conventional pre-treatment system was applied to seawater RO plant from its early

days and continues to be used today. Recently, UF has been recognized as competitive pre-treatment for RO systems [1,2]. A system designed with a UF as pre-treatment prior to a RO system has been referred to as an Integrated Membrane System (IMS). However, there are several of markets and regions where the use of IMS for brackish and seawater applications is growing [3]. Figure 1 shows the cumulative capacity of seawater RO plants with UF pre-treatment vs. time, which gives a clear indication of the overall fast adoption speed of IMS pre-treatment technology.
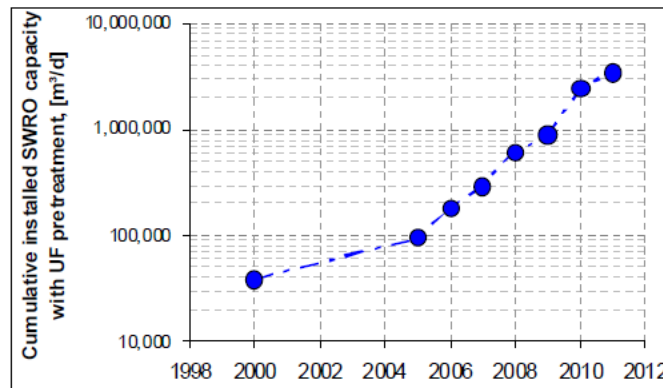

Figure 1 *Cumulative capacity of SWRO plants with UF pre-treatment [3]*

Examples of large seawater RO plants where the concepts of IMS have been implemented Table 1. The better-known plants with membrane pre-treatment are Addur, Bahrain Fukuoka, Japan, Kindasa, Saudi Arabia, and YuHan, China [4,5].

Table 1: *Summary Examples of large seawater plants with membrane pre-treatment are RO plants*

Location	Addur, Bahrain	Fukuoka, Japan	Kindasa, Saudi Arabia	YuHan, China
Membrane filtration capacity,m^3/day	140,000	96,000	90,0000	70,000
Operational status	Operational since May 2000	Operational since May 2005	Startup Mid 2006	Startup Early 2006
Membrane technology	Pressure- driven UF back washable Spiral wound	Pressure-driven UF back washable Spiral wound	Pressure-driven UF capillary	Submersible UF capillary
Pre-treatment Membrane Module manufacturer	Nitto Denko	Nitto Denko	Hydranautics	Zenon

The Tajura Nuclear Research Center (TNRC) operates an RO system with conventional pre-treatment at Tajura city in Libya on the Mediterranean shore. It was commissioned in 1984 with only 50% of its production capacity (10,000 m^3/d). The plant used the two-stage process of desalination in the period between 1984 and 1999. Since 1999 to date the utilized membranes have directly converted seawater to potable water with a conductivity of 500 micro Siemens. The second pass was kept to be utilized in cases when high-purity water was needed. The process design of the plant was influenced by long-term experiences of the deteriorating quality of seawater. This deterioration was particularly experienced with high levels of suspended solids and silt density index. In addition, problems with the facility's pre-treatment system, coupled with some operational difficulties have significantly reduced the plant's performance. The existing conventional pre-treatment system was considered unfit to deal with these seawater conditions throughout the seasons [6]. Following the recent experience in large RO plants and the continued cost reduction, on account of the technological improvements and worldwide competition by several membrane manufacturers, UF is now seriously considered for application in seawater systems [7,8].

Design hydranautics IMS technology has been employed, which incorporates Hydranautics HydraCap60™ ultra filtration modules and Hydranautics high rejection and energy saving SWC5 seawater RO membranes. The design is based on the previously published data from the operation of two different types of pilot plants with a period of four months, each pilot plant has different pre-treatment technologies for RO systems. These included: conventional pre-treatment and UF were installed at Tajura city in Libya on the Mediterranean Sea . The results from these pilots indicated that the UF membrane pre-treatment provided superior water quality for the RO plant, measured by reduce turbidity and SDI$_{15}$. The results have shown that the UF membrane system was able to consistently reduce SDI$_{15}$ values to less than 3 and had turbidity values to less than 0.2 NTU, while over 70% of the conventional media filtration unit SDI$_{15}$ values were over 3 and an average turbidity of 0.33 NTU [9].

The Tajura RO plant IMS designed for a production capacity of 10,000 m³/day. The plant employ dissolved air flotation pre-treatment followed by Hydranautics IMS membrane technology consisting of eight UF racks equipped with Hydranautics

HYDRAcap80®elements and downstream two seawater RO trains with SWC5 membranes working at 35% recovery.

This paper describes the problems encountered in the existing conventional pre-treatment system and the conceptual proposed IMS design as a part of the plant rehabilitation process of the Tajura RO plant in Libya.

2   Pre-treatment for SWRO Desalination

RO seawater systems operating on surface feed water, originating from an open intake source, require an extensive pre-treatment process to control membrane fouling. Therefore, the main factor for the successful operation of SWRO is maintaining a constant high feed water quality. Two kinds of pre-treated seawater have fed the RO membrane: pretreated seawater by the conventional system and pretreated by the UF system.

2.1   Conventional Pre-treatment

Conventional RO pre-treatment has been widely applied in the past for seawater RO plants to lower the SDI_{15} and to remove suspended solids and excessive turbidity. Conventional pre-treatment includes coagulation, sedimentation, filtration using sand and/or multimedia filters, lime softening and activated-carbon adsorption, and cartridge filter. Whilst conventional pre-treatment technology can be effective, it needs to be carefully designed, and diligently operated. Up-sets, due to feeding variability or contamination, will be transferred to the RO. Most examples of RO system failure are down to pre-treatment failings, either in design or operation. Several major disadvantages of conventional pre-treatment treating surface seawater contribute to higher rates of RO membrane fouling and shorter RO membrane life expectancy including:

- Significant fluctuations in the quality of RO feed are caused by changing raw water conditions.
- Difficult to achieve a constant $SDI_{15} < 3.0$, especially during high turbidity feed water conditions.
- The low removal efficiency of particles smaller than 10–15 microns.
- Possibility of breakthrough during filter backwash.
- Carryover of high concentrations of colloidal particles immediately following the backwash filter.
- Coagulant impact on RO membranes.

In addition to the above, slow filtration velocities also result in large land footprint requirements for a conventional pre-treatment system [10-12].

2.2   Advantages of membrane pre-treatment

As mentioned before, membrane processes are gaining importance for water applications as a result of the advances in membrane technology and increasing requirements on water quality. Pilots data are just recently available, documenting the benefits of membrane filtration to RO applications. For seawater applications, papers include[10-

12]; the benefits as described in these papers for membrane filtration as pre-treatment for RO are described below:

- Improved pretreated water quality, in terms of lower suspended solids and less biological content, resulting in improved RO operation
- Fewer RO membrane cleanings with resulting cost savings in cleaning chemicals
- Lower RO pressure drops from fouling, resulting in lower energy costs
- Longer RO membrane life associated with long-term improved pretreated water quality
- Increased flux rates in the RO system due to higher quality pre-treatment, resulting in a reduction in the size of the RO system with subsequent reduction in capital cost.
- Smaller plant footprint size (typically~ 30-60% of conventional) resulting in reduced capital investment
- Lower overall chemical and sludge handling costs if conventional technologies include coagulation, clarifiers, filtration, or other chemically intensive conventional pre-treatments
- Lower operator requirements due to complete automation
- Greater plant availability due to decreased downtime related to chemical cleanings
- Reduced environmental impact due to reduced chemical disposal requirements
- Membrane Integrity Testing provides a means to verify the removal of Giardia and Cryptosporidium-sized particles that are not available with granular media filtration.

2.3 Conventional vs. membrane pre-treatment

The comparison of conventional media filtration and low-pressure membrane (MF/UF) SWRO pre-treatment is presented in Table 2.

Table 2: *Comparison of conventional and MF/UF pre-treatment [10-12]*

Parameters	Conventional pre-treatment	MF/UF pre-treatment
Track record	Established	Rapidly developing
Feed water quality and removal efficiency	Lower removals possible	Better removals of organics, DBP's fine colloids, silt, and pathogens
Treated Water SDI$_{15}$	<4, 90% of the time	<2.5, 100% of the time, usually <1.5
Turbidity	<1.0 NTU	<0.1 NTU
Variable feed quality	Susceptible	Less sensitive
Post-treatment	Cartridge filters used	Optional ~ not usual
Filter replacement	Mean life ~20 years	Membrane life ~ 6 years
Energy usage	Less than MF/UF as it could be gravity flow	More energy for membrane TMP and backwash
Capital Costs	Cost competitive with MF/UF	Slightly higher than conventional pre-treatment. Costs continue to decline as developments are made
RO capital cost	Higher than MF/UF since RO operates at a lower flux	Higher flux is logically possible resulting in lower capital cost
RO operating costs	Higher costs as the fouling potential of RO feed water is high resulting in higher operating pressure. One experiences frequent cleaning of RO membranes	Lower RO operating costs are expected due to less fouling potential and longer membrane life

Chemical costs	High due to coagulant and process chemicals needed for optimization	Chemical use is low, dependent on raw water quality
Footprint	Larger, particularly if two-stage required	Significantly smaller footprint - Typically~ 30-60% (of conventional)

3 Brief Description of Tajura Seawater RO Plant

Tajura reverse osmosis desalination plant was designed to produce 10,000 m^3/d based on the Mediterranean seawater feed and was commissioned in 1984 with only 50% of its production capacity. Raw Water quality data for the Tajura seawater RO facility are shown in Table 3.

Table 3: *Raw water characteristics for the Mediterranean sea at Tajura coast [13]*

Component	Seawater Composition
Calcium Ca^{++}	455 mg/L
Magnesium Mg^{++}	1427 mg/L
Sodium Na^{++}	11600 mg/L
Potassium K^+	419 mg/L
Silica Si^{+1}	2 mg/L
Chloride Cl^{-1}	20987 mg/L
Biocarbonae HCO^3	163 mg/L
Sulphate SO^{4-}	2915 mg/L
Nitrate NO^{4-}	0 mg/L
TDS	38,000 mg/L
Conductivity	55 μS/cm
PH	8.3 standard units
Temperature	15-35 C°
Total Fe	0.55 mg/L

3.1   The process

Seawater is drawn through a 1.3 km long pipeline into a seawater basin with a capacity of 1920 m^3. The seawater is then pumped to mechanically filtered and then pumped into the pre-treatment section. Figure 2 illustrates the schematic process flow diagram of the Tajura plant. The pre-treatment consists of online coagulation-flocculation, 8- dual media filters (DMF), and 5-micron cartridge filters. The chemicals that can be injected into the seawater are copper sulfate solution ($CuSO^4$) for disinfection, sulfuric acid to reduce the pH, Ferric chloride sulfate solution ($FeClSO^4$) for destabilization, and agglomeration of the colloidal particles and a coagulant aid. The coagulated flocks are filtered off in the dual media filter (DMF) beds followed by filtration through 5-micron cartridge filters and de-chlorination by sodium bisulfate solution injection complete the pre-treatment of feed water. From the pre-treatment section, water is fed to the RO section. The RO system consists of two stages. The first RO stage consists of four parallel RO racks with 99 pressure vessels each. The system can be operated with either

two racks 50% or four racks 100% of the total capacity with 30% recovery of product water. The product water of the first stage is collected in the buffer tank. Water from the buffer tanks is fed to two racks of the second stage using of two high-pressure pumps (for 50% operation one rack is operated). 85% of the first stage desalted water is recovered by the second stage. The product water is partially de-carbonated and post-treated with chlorine; stored in storage tanks. The major design parameters of RO membrane systems are presented in Table 4. The plant used the two-stage process of desalination in the period between 1984 and 1999. From 1999 up to date the membranes utilized were directly converting seawater to potable water with conductivity in the range of 500-micro. The second pass was kept to be utilized in cases when high-purity water was needed.

Table 4: *SWRO Plant main design parameter*

Parameters	Value
Product TDS	<500 mg/l
Recovery rate	30%
Feedwater TDS	38,000 mg/l
Feed temperature	15–35 °C
Membrane type	TFC spiral wound membrane

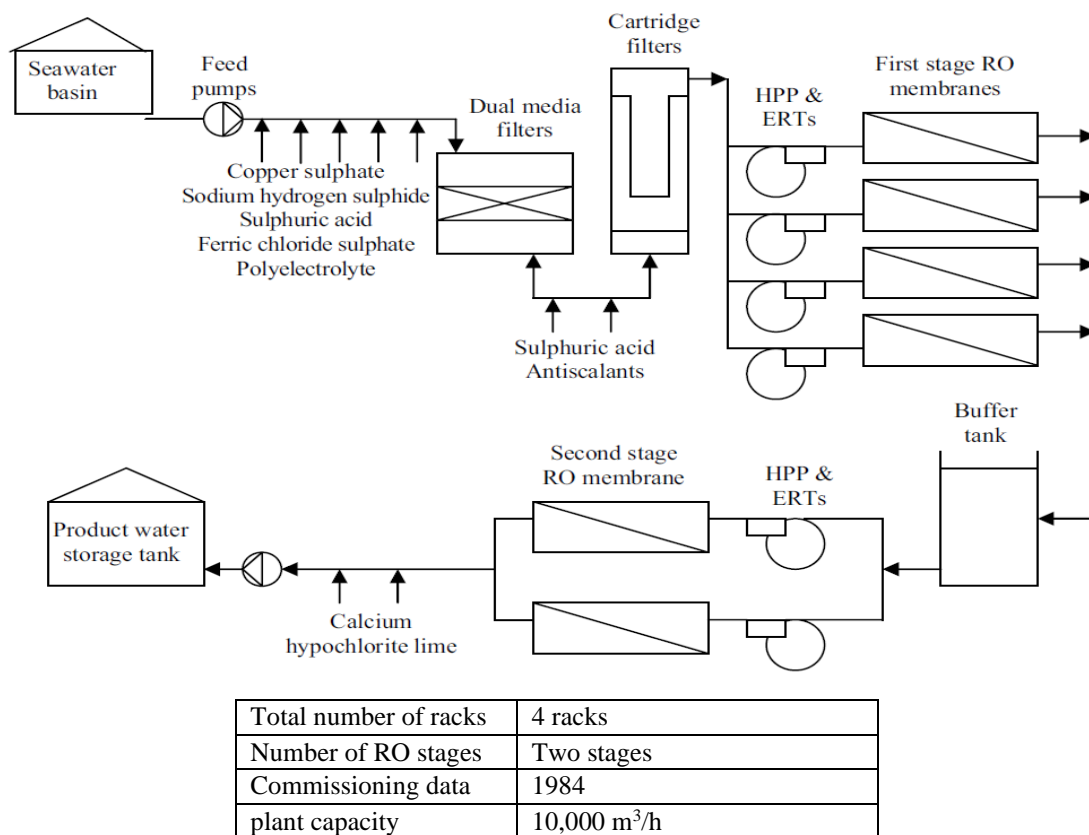| Total number of racks	4 racks
Number of RO stages	Two stages
Commissioning data	1984
plant capacity	10,000 m³/h

Figure 2 illustrates the schematic process flow diagram of the Tajura RO plant [13].

3.2 Operational experience with a conventional pre-treatment system at the Tajura plant

As it has been mentioned earlier that the Tajura plant is producing drinking water at a rate of less than 50% of its design capacity. Problems with the facility's pre-treatment system, coupled with some operational difficulties have significantly reduced the plant's performance [6].

3.2.1 Coagulation-flocculation unit

The coagulation-flocculation unit is out of operation, the tanks are corroded and leakage is noticed as in Figure 3. The mixers in the tanks are heavily corroded and destroyed, the condition of this unit is terrible and it can't be repaired. The nonexistence of this unit prevents the plant from working when the SDI_{15} of seawater is high.

Figure 3. Coagulation-flocculation tanks [6]

3.2.2 Multi-Media Filters

There are eight media filters, each having six automatically operated valves. Despite all the media filter vessels being in good condition but the problems with their valves have been experienced, Some of the valves failed shortly after the start-up under an actual pressure above the design value. These valves contribute largely to the complexity of the plant and increase the need for maintenance and repairs. Also, there is no yearly makeup for anthracite in the media filters. It is speculated that the quantity decreased due to the loss during the backwash process.

3.2.3 Silt Density Index (SDI_{15})

As a result, the existing pre-treatment system of the Tajura RO plant could not achieve1 an SDI_{15} value of less than 4.0 most of the time as shown in Figure 4, this was not meet with the SDI_{15} recommended by the manufacturer for the RO membrane which (< 4), this prevents keeping the plant in continuous operation. Non-continuous plant operation increased differential pressure, salt-passage and decreased the plant performance.
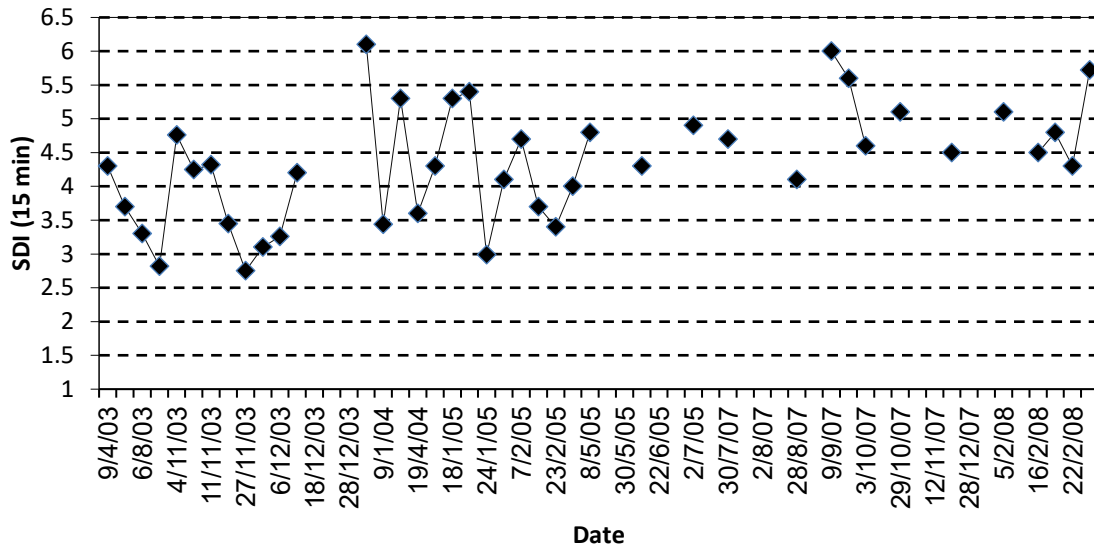
Figure 4. *SDI levels were obtained in the period between 2003– 2008.*

3.3 The UF system process conceptual design for the Tajura plant

Integrated Membrane System will be considered as an alternative option to conventional pre-treatment system for the Tajura RO plant. The proposed design of the pre-treatment system will utilize Hydranautics IMS technology. The IMS design is based on long experience from the operation of the two separate RO pilots with different pre-treatment units started in January 2013 for a period of four months on the Mediterranean coast at Tajura city. The results from those pilot plants confirmed the prior assumption that membrane pre-treatment will produce stable feed water quality, measured by reduced turbidity and by the SDI_{15}. The results have shown that the membrane filtration units were able to consistently produced SDI_{15} values less than 3 and turbidity values less than 0.2 NTU, while over 70 % of the conventional media unit SDI_{15} values were over 3 and produced an average turbidity of 0.33 NTU [9]. The membrane modules that have been selected for the pre-treatment unit of the Tajura RO plant are HYDRAcap80® UF modules made by Hydranautics. Each UF block consists of 44 UF elements of single-bore hollow fibre membranes with a bore size of 0.8 mm and a molecular weight cut-off (MWCO) of 150,000 Dalton. The overall UF plant is designed for a continuous UF to permeate flow of 670 m³/h. The nominal flux rate is 72.1 L/m²/h with all UF blocks in operation. The UF system design parameters are presented in Table 5.

Table 5: *The main design parameters of HYDRAcap80 UF membrane for the Tajura plant*

Parameter	Value
Number of racks	4
Total number of modules	176

| Nominal Membrane Area	670 ft^2 (62.2 m^2)
Module type	HYDRACAP 80
Material	Hydrophilic Polyethersulfone
Fiber Dimensions	ID 0.8 mm, OD1.4mm
Maximum Applied Pressure	73 psig (5 bar)
Maximum Operating Temperature	104 °F (40 °C)
Feed water PH Range	4-10
Feed water Chlorine Concentration	100 ppm
Volume to be treated	17473 m^3/day
Volume to produce	16086 m^3/day
Waste water volume	1387 m3/day
Recovery	92.1%
Average rack flux	72.1 LMH
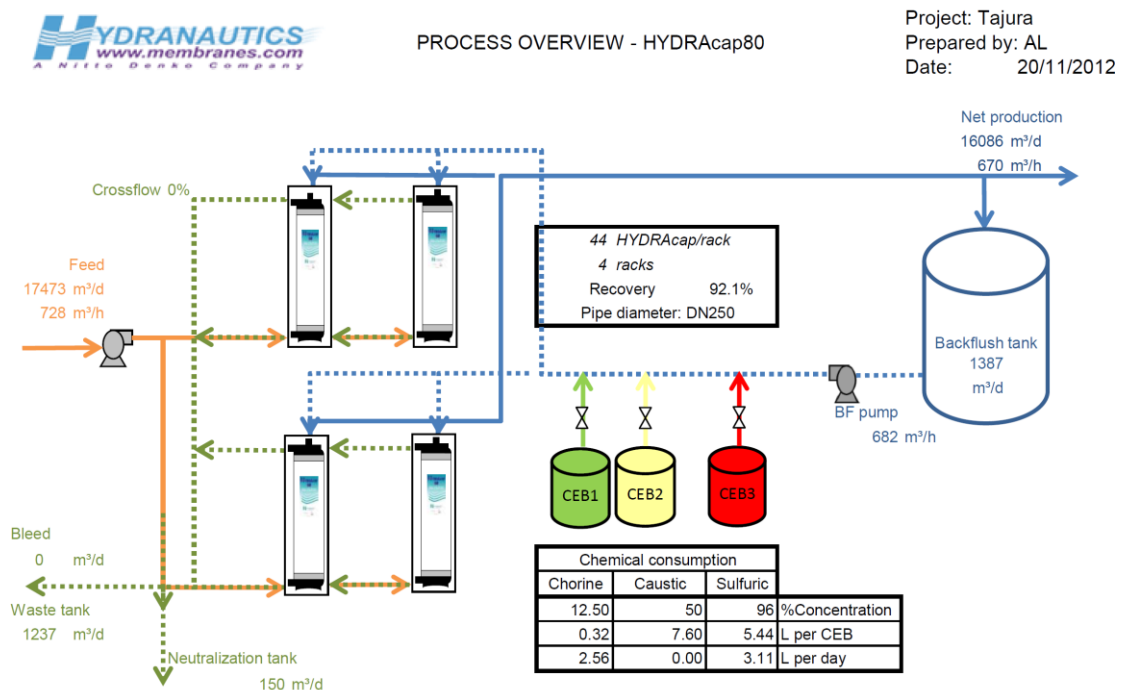
Figure 6 *UF Membrane Pre-treatment Process Flow Schematic.*.

4 CONCLUSIONS

Seawater reverse osmosis desalination is a rather complex process when associated with fouling and scaling problems. It requires careful study to selected the proper pre-treatment systems for control membrane fouling and successful long-term performance of RO membrane. From the experiences it can be seen the RO plant at Tajura has an enormous problems encountered in the existing conventional coagulation-flocculation pre-treatment. UF membrane pre-treatment prove to be effective to provide superior water quality, and were able to handle wide swings in incoming water quality. The Integrated Membrane System had suggested as part of plant rehabilitation process of Tajura RO plant. The membrane modules that have been selected for pre-treatment unit

are HYDRAcap80® UF modules made by Hydranautics company. The overall UF plant is designed for a continuous UF to permeate flow of 670 m³/h. The nominal flux rate is 72.1 L/m²/h with all UF blocks in operation and downstream two seawater RO trains with SWC5 membranes working at 35% recovery.

5 Reference

[1]   J. G. Jacangelo, K. Schwab, and H. Huang, "Pre-treatment for low pressure membranes in water treatment: A review," *Environmental Science and Technology*, vol. 43, no. 9, pp. 3011-3019, Abbrev. April, 2009. https://doi.org/10.1021/es802473.

[2]   A. Brehant, V. Bonnelye, and M. Perez, "Comparison of MF/UF pre-treatment with conventional filtration prior to RO membranes for surface seawater desalination ," *Desalination*, vol. 144, no. 1, pp. 353-360, Abbrev. September, 2002. http://dx.doi.org/10.1016/S0011-9164(02)00343-0.

[3]   M. S. Bosch, S. Rosenberg and R. Chu, "Novel Trends in Dual Membrane Systems for Seawater Desalination: Minimum Primary Pre-treatment and Low Environmental Impact Treatment Schemes" *International Desalination Association*, vol. 2, no. 1-3 , pp. 56-71, 18 Jul 2013. https://doi.org/10.1179/ida.2010.2.1.56.

[4]   K. Barushid, A. Hashim, T. Kannari, T. Tada, and H. Iwahori, "UF Membrane Performance at Addur: expectation, reality and prospects," *International Desalination Association*, World Congress on Desalination and Water Reuse, September11-16, 2005,Singapore.
https://conferencealerts.com/show-event?id=ca1hmm6m.

[5]   Gr. K. Pearce, S. Talo, K. Chida, A. Basha, A. Gulamhusein, "Pre-treatment options for large scale SWRO plants: case studies of UF trials at Kindasa, Saudi Arabia, and conventional pre-treatment in Spain," *Desalination*, vol. 167, no. 1-3, pp. 175-189 Abbrev. 15 August 2004. https://doi.org/10.1016/j.desal.2004.06.1271 .

[6]   M. Ababoud and S. Elmasallati, "Potable water production from seawater by the reverse osmosis technique in Libya," *Desalination* , vol. 203, no. 1-3, pp. 119-133, Abbrev. February, 2007. https://doi.org/10.1016/j.desal.2006.04.007.

[7]   P. Glueckstern, M. Priel and M. Wilf, "Field evaluation of capillary UF technology as a pre-treatment for large seawater RO systems" *Desalination*, vol. 147, no.1-3, pp. 55-65 Abbrev. 10 September 2002. https://doi.org/10.1016/S0011-9164(02)00576-3.

[8]   O. Lorain, B. Hersant, F. Persin, A. Grasmick, N. Brunard and J. M. Espenan, "Ultrafiltration membrane pre-treatment benefits for reverse osmosis process in seawater desalting. Quantification in terms of capital investment cost and operating cost reduction" *Desalination*, vol. 203, no.1-3, pp. 277-285 Abbrev. 5 February 2007. https://doi.org/10.1016/j.desal.2006.02.022.

[9]   A.A. Elarbi,   M.M. Ashour, , M.A. Musbah, A.A. Abozirida,"Comparative Performance of UF vs. Conventional Pre-treatment for SWRO: pilot studies" The 1st International Conference on Chemical, Petroleum, and Gas Engineering (ICCPGE 2016) 20–22 December 2016,Alkhoms-Libya. https://elmergib.edu.ly/iccpge/iccpgePapers/163.pdf.

[10]   A. Brehant, , V. Bonnelye and M. Perez, "Comparison of MF/UF pre-treatment with conventional filtration prior to RO membranes for surface seawater desalination," *Desalination*, vol. 144,no. 1-3, pp. 353-360, Abbrev. 10 September, 2002. https://doi.org/10.1016/S0011-9164(02)00343-0.

[11]   F. Knopsa, S. Hoof, H. Futselaarb, and L. Broensb, "Economic evaluation of a new ultrafiltration membrane for pre-treatment of seawater reverse osmosis," *Desalination*, vol. 203,   no.   1-3,   pp.   300-306,   Abbrev.5   February,   2007. https://doi.org/10.1016/j.desal.2006.04.013 .

[12]   L. Henthorne, "Evaluation of Membrane Pre-treatment for Seawater RO Desalination," *United states Bureau of Reclamation Desalination and Water*, 2007. Access online on 5 April 2022 at https://www.usbr.gov/research/dwpr/reportpdfs/Report106.pdf

[13]   I. M. El-Azizi, A. M. Omran, "Design criteria of 10,000 m³/d SWRO desalination plant of Tajura Libya," *Desalination*, vol. 153, no. 1-3, pp. 273-279, Abbrev. 10 February 2003. https://doi.org/10.1016/S0011-9164(02)01146-3.

The effect of middle components purity in quaternary mixture separation using distillation system

Jamal Ahmed Enghita

Department of Chemical Engineering, Faculty of Engineering (Algaraboli), Elmergib University

Corresponding Author Email: enghitaj@gmail.com

Abstract

Separation processes play critical roles in industry, including the removal of impurities from raw materials and the overall separation processes accounts for 40-70% of both capital and operating costs in industry. The main objective of this study was exploration of design and economic features of conventional distillation schemes for separation of quaternary mixture (Propane, i-Butane, n-Butane, i- Pentane) with high products separation of 95%, 90%, 90%, and 95%, respectively for the equimolar feed composition. The studied distillation schemes are: the effect of middle components purity (i-C4 and n- C4) is also on energy and capital investments, conventional distillation scheme, The middle components purity was changed from 90% to85%and 80 %.The results of economic study show conventional Distillation cases studied at different composition of middle components purity at (0.9, 0.85and 0.8) and we get highest saving on the case of 80% side stream composition with 19 %saving in energy and 17%saving in TAC, and the saving on case of 85% side stream composition with 12% saving in energy and 11 % saving in TAC, compared with case of 90%middle component purity.

Keywords: Separation processes, Conventional distillation column, Process optimization, Quaternary mixture, Separation.

Introduction

There are many separation technologies such as distillation, extraction, adsorption, crystallization, and membrane-based technologies. However, many considered the distillation technique is a mature technology and represents 70% of all separation systems [1]. In addition, distillation is the largest single energy consumer in the chemical process industries but distillation does not consume energy but degrades the heat input to the reboilers that is subsequently rejected in the condenser. The most effective way to reduce the energy consumption of distillation is by effective heat integration. Design and operation of the distillation are to be considered simultaneously with its heat integration. For single distillation columns, it is straightforward to identify appropriate heat integration opportunities. For complex distillation systems, the most appropriate combination of distillation system design, operation, and heat integration are far from straightforward. The whole separation system together with its heat integration and utility system must be considered simultaneously. The rapid increase of energy prices in the past decades has given motivation to many efforts to conserve energy. To conserve energy, the ideas of component purity and heat integration have received more attention.

Introducing thermal couplings to eliminate intermediate reboilers and condensers to save energy and capital cost, improving operability of thermally coupled columns, enabling double and multi-effect distillation of thermally coupled configurations, performing simultaneous heat and mass integration, and conducting any thermally coupled distillation in n-product streams are very important issues in separation processes. Many workers have studied distillation configurations for multi-component distillation systems [2]. Thermal couplings configurations have been known for a while, but it was not used until the 1980s particularly when configurations started to receive more attention due to their potential for large heat duty savings and cost effectiveness. Improving energy efficiency in refineries and Gas plant has been studied extensively in the realm of production management due to the potential of large energy savings and gas emission reduction. Sittig has reported energy saving for petroleum refinery industry and suggested the use of intermediate reboilers in crude towers can reduce the heat load on the furnace in order to increase the energy efficiency of the system [3]. Similar work is conducted to study and concluded that the installation of preflash units or prefractionator columns to existing crude oil distillation installations could save energy and allow the furnace to reduce its utility consumptions [3] In 1994, Dhole and Buckingham have published a methodology based on pinch analysis for saving energy in distillation units [4]. Many approaches have been applied to optimize CDUs with the consideration of economic efficiency and environmental impact They are mainly divided into two categories. One is based on the heat integration analysis to reduce energy consumption by retrofitting heat exchanger networks [4] . They reported results showed an increase in heat recovery of the heat exchanger network to reduce the utility consumption in the process furnaces. Most of the work dealed with simple configuration(sequences of conventional one-feed, two product columns).The main objective of the present study was exploration of design and economic features of conventional distillation schemes for separation of quaternary mixture of Propane, i-Butane, n-Butane, and i- Pentane with high products separation of 95% propane and 95% of i-pentane. The present work is based on studying and rigorous modeling (design and simulation) of some conventional schemes for the separation of quaternary mixture of light hydrocarbons(C3, i-C4, n-C4 and i-C5). Economic evaluation of the distillation schemes is also studied.

Design of Distillation Systems

Different types of distillation systems are studied and compared to the conventional direct scheme. The Conventional Direct Sequence given by Elaahi and Luyben [12] is designed, simulated, and economically evaluated in term of energy saving and TAC. In case of quaternary mixture separation, the designed distillation systems consisted of three distillation columns and direct separation sequence is analyzed. Each column has feed stream, top product (distillate), and bottom product, in addition to total condenser and reboiler for each one. The studied distillation systems are selected from different types of middle component purity (90%, 85%,% and 80%). The sequence is

direct in which the lightest component is taken overhead in each column, the bottom of the first column is fed to the second column, and the bottom of the second is fed to the third column. Figure 1 shows the designed conventional direct distillation sequence with total condensers. The conventional scheme is considered as the base case scheme for all the investigated schemes to compare the percentage of savings in both energy and total annual cost (TAC).
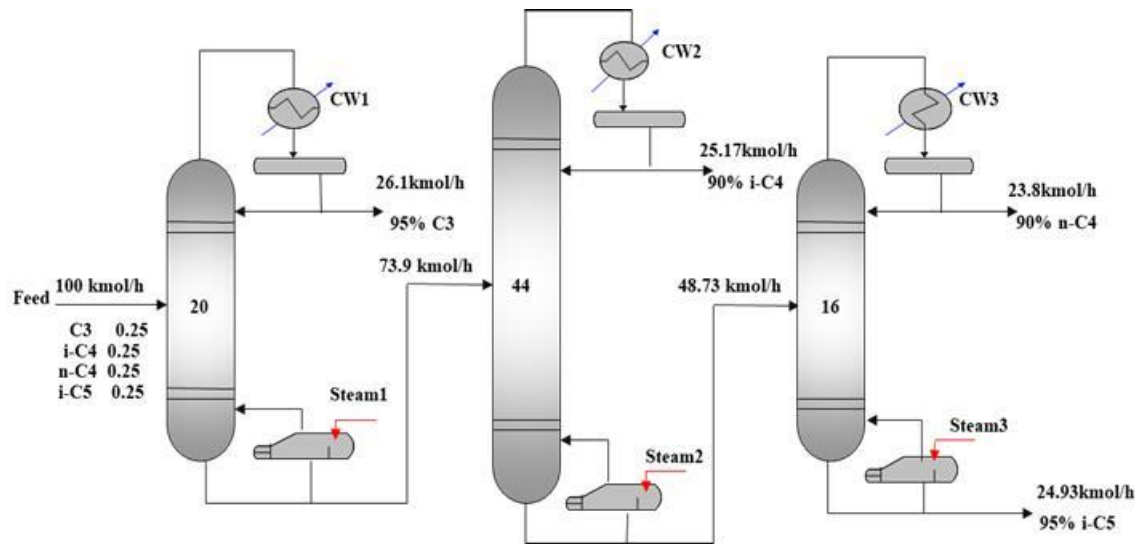
Figure 1: Conventional direct distillation sequence with total condensers.

Cases Study

The separation of quaternary mixture consisted of Propane, i-Butane, n-Butane, and i-Pentane by several distillation schemes for 95 mol% product purity for both of Propane and i-Pentane in addition, of 90% for i-Butane and n-Butane. The feed composition consisted of same mole percentage of the studied hydrocarbons (25%) for case 1. The feed composition was saturated liquid hydrocarbons at 50 °C with flow rate of 100 kmol/h. The feed and product specifications of the studied rigorous schemes are given in Table 1.

Table 1: Feed and product specifications for the case study

Components	Feed stream	Product streams			
		A	B	C	D
	fraction	fraction	fraction	fraction	fraction
Propane	0.25	0.95	0.09	0.00	0.00

i-Butane	0.25	0.04	0.90	0.09	0.00
n-Butane	0.25	0.01	0.01	0.90	0.05
i-Pentane)	0.25	0.00	0.00	0.01	0.95
Total	1.00	1.00	1.00	1.00	1.00

For a certain number of trays, the reflux ratio is calculated by the HYSYS. The feed location to each column is adjusted by changing the location up and down until the lowest value of the reflux ratio is achieved at the specified product purities.

Estimation of trays Number, Reflux Ratios and Feed Location

1- Fenske equation: For multi component systems, an approximate value of the minimum number of equilibrium stages (at total reflux) may be obtained from the Fenske equation. In the Fenske equation, given below as Equation 1, relative volatility is based on the light key relative to the heavy key[9].

$$N_{\min} = \frac{\ln\left[\left(\dfrac{x_{LK}}{x_{HK}}\right)_D \left(\dfrac{x_{HK}}{x_{LK}}\right)_B\right]}{\ln(\alpha_{LK/HK})_{av}}$$

[1]

Where $N_{\min}$ = minimum number of equilibrium stages

    x_{LK} = mole fraction of light key

    x_{HK} = mole fraction of heavy key

    D   = when used as subscript, denotes distillate product

    B = when used as subscript, denotes bottom product

$(\alpha_{LK/HK})$= average value of relative volatility of light key relative to heavy key

The average value of relative volatility is calculated from the mean value of relative volatility at the top of the column $(\alpha_{LK/HK})_D$ and at the bottom of the column $(\alpha_{LK/HK})_B$. $(\alpha_{LK/HK})_D$ is based on the dew point temperature of the overhead vapor whereas $(\alpha_{LK/HK})_B$ is based on the bubble point temperature of the bottom liquid.

$$(\alpha_{LK/HK})_{av} = \sqrt{(\alpha_{LK/HK})_D (\alpha_{LK/HK})_B}$$

[2]

Since the distributions of the non-key components in the distillate and bottoms are not known, determinations of the dew and bubble points are partially trial and error.

2- Minimum reflux by Underwood method: For multi-component mixtures, the Underwood method may be used for estimating minimum reflux ratio. Underwood proposed Equations (3) and (4) for calculation of minimum reflux ratio[9]:

$$\sum_{i=1}^{n} \frac{\alpha_i x_{f_i}}{\alpha_i - \theta} = 1 - q$$

[3]

Where n = number of components

α_i = average relative volatility based on component i relative to heavy key

x_{f_i} = mole fraction of component i in feed

q   = number of moles of saturated liquid produced on the feed tray per mole of feed

θ = unknown parameter to be determined by trial and error

The correct value of θ will be between relative volatility of the two key components. After the value of θ is determined, Equation (4)
 may be used to determine minimum reflux ratio.

$$R_{\min} + 1 = \sum_{i=1}^{n} \frac{\alpha_i x_{D_i}}{\alpha_i - \theta}$$

[4]

 Where $R_{\min}$ = minimum reflux ratio ,

x_{D_i} = mole fraction of component i in distillate (D)

3- Number of equilibrium stages by Gilliland correlation: Once minimum stages and reflux ratio are known, the number of equilibrium stages may be determined as a function of selected values of operating reflux ratio. Several methods have been proposed including the correlation of Gilliland to determine the number of equilibrium stages as a function of reflux ratio.

 The Gilliland correlation was first developed as a plot of $\dfrac{N - N_{\min}}{N + 1}$ versus , but

latter was transformed by (Eduljee, 1975) into Equation [9]

$$\frac{N - N_{\min}}{N + 1} = 0.75 \left(1 - \left[\frac{R - R_{\min}}{R + 1} \right]^{0.566} \right)$$

[5]

Where N = number of equilibrium stages , $N_{\min}$ = minimum number of equilibrium stages

R   = operating reflux ratio   , $R_{\min}$ = minimum reflux ratio

Results of the Shortcut Analysis

For a given feed and product specifications (Table 2) and after material balance around the studied sequence, the unknown composition of each component is determined, and then the light and heavy keys can be specified. After that, the minimum number of trays (Fenske equation), minimum reflux ratios (Underwood equation), and the feed stage locations (Kirkbride equation) are estimated. The results of shortcut method for case 1 are summarized and given in Table 2 .

Table 2: Shortcut method results of case 1

Parameter	Column 1	Column 2	Column 3
N_{min}	10	22	8
R_{min}	3.72	6.31	2.25
$R = 1.1\,R_{min}$	4.09	6.941	2.475
$N = 2\,N_{min}$	20	44	16
M	10	22	8
P	10	22	8

Results of Rigorous Simulation Schemes
According to the TAC calculation in the present case study, the plant life operating time was selected to be 10 years with 8000 operating hours per year.

Case 1: The results of Base case (Conventional direct distillation sequence with 90% middle component purity) are given in Table 3. In this separation process, It notice a relative volatility (αav) of the columns αav3 > αav1 > αav2. This means that the trays of column 2 to separate the products (B,C, and D) need more than other columns and also the column 2 consume high energy compared to the other columns. The column 2 consumed high energy and increase the highest cost in both, capital and operating cost with respect to the other two columns.

Table 3: The base case

	Column 1	Column 2	Column 3
Column pressure (kpa)	*1455*	652.4	456.9
Column diameter (m)	0.84	0.884	0.5455
Aave	1.781915	1.292199	2.088117
Reflux ratio	6.69	8.3	2.52
Condenser duty (KJ/hr)	3.79E+06	4.40E+06	1.68E+06
Reboiler duty (KJ/hr)	2.53E+06	3.91E+06	1.58E+06
Theoretical number of stages	*20*	40	14
Overall column efficiency	82	76	70

Actual number of stages	*26*	60	24
Annual capital cost ($/yr)	2.98E+04	4.11E+04	1.70E+04
Total annual capital cost ($/yr)		8.79E+04	
Cooling water cost ($/yr)	1.28E+04	1.48E+04	5.64E+03
steam cost ($/yr)	1.73E+05	2.68E+05	1.08E+05
Operating cost ($/yr)	1.86E+05	2.82E+05	1.14E+05
Total operating cost ($/yr)		5.82E+05	
TAC ($/yr)	2.16E+05	3.23E+05	1.31E+05
TAC of the whole sequence ($/yr)		6.70E+05	
Total annual cost saving %		0	
Total operating cost saving %		0	
Total QR (KJ/hr)		8.02E+06	
Total QR saving %		0	
TAC saving %		0	

Case 2: From Table 5 shows the effects of middle component purity (MCP), i-C4 and n-C4, of the composition of 0.85 for the previous scheme on energy consumption. , Distillation Sequence with 85% MCP where the reboiler duty of the second and third column shows the reduction in energy consumption from 3.91E+06 kJ/h to 2.98+06kJ/h and from 1.58E+06 kJ/h to 1.51E+6 kJ/h, respectively. These effects are translated into energy saving of 12.4 % and TAC saving of 11.45 % as shown in Table 4.

Table 4: Middle component purity for Case 2 (0.85).

	Column 1	Column 2	Column 3
Column pressure (kpa)	*1455*	654.9	456.9
Column diameter (m)	0.84	0.8	0.542
αave	1.960013	1.355843	2.385092
Reflux ratio	6.3	7.20	2.1
Condenser duty (KJ/hr)	3.80E+06	3.47E+06	1.61E+06
Reboiler duty (KJ/hr)	2.53E+06	2.98E+06	1.51E+06
Theoretical number of stages	*20*	40	14
Overall column efficiency	82	75	72
Actual number of stages	*26*	60	24
Annual capital cost ($/yr)	2.98E+04	3.62E+04	1.65E+04
Total annual capital cost ($/yr)		8.26E+04	
Cooling water cost ($/yr)	1.28E+04	1.17E+04	5.42E+03

steam cost ($/yr)	1.73E+05	2.04E+05	1.03E+05
Operating cost ($/yr)	1.86E+05	2.16E+05	1.09E+05
Total operating cost ($/yr)	5.10E+05		
TAC ($/yr)	2.16E+05	2.52E+05	1.25E+05
TAC of the whole sequence ($/yr)	5.93E+05		
Total annual cost saving %	6.056285485		
Total operating cost saving %	12.2753769		
Total QR (KJ/hr)	*7.02E+06*		
Total QR saving %	12.40803093		
TAC saving %	11.45905826		

Case 3: Case 3: From Table (5) below, we can notice the effects of middle component purity (0.8) for the previous scheme, Distillation Sequence with 80% midle component purity), where the reboiler duty of the second column is reduced from 3.91E+06 kJ/h to 2.45E+06 kJ/h. And 1.58E+06 to 1.48E+6 kJ/h For third column with respect with base case. These effects are translated into energy saving of 19.1 % and TAC saving of 17.74 % as shown next table

Table 5: Case 3, Middle component purity (80%)

	Column 1	Column 2	Column 3
Column pressure (kpa)	*1455*	654.9	456.9
Column diameter (m)	0.85	0.74	0.55
αave	1.960026	1.2907	2.089
Reflux ratio	4.3	5.6	1.85
Condenser duty (KJ/hr)	3.81E+06	2.93E+06	1.59E+06
Reboiler duty (KJ/hr)	2.54E+06	2.45E+06	1.48E+06
Theoretical number of stages	*20*	40	14
Overall column efficiency	82	76	72
Actual number of stages	*26*	60	24
Annual capital cost ($/yr)	3.00E+04	3.22E+04	1.68E+04
Total annual capital cost ($/yr)	7.90E+04		
Cooling water cost ($/yr)	1.28E+04	9.88E+03	5.37E+03
steam cost ($/yr)	1.74E+05	1.67E+05	1.02E+05
Operating cost ($/yr)	1.87E+05	1.77E+05	1.08E+05

Total operating cost ($/yr)		4.72E+05	
TAC ($/yr)	2.17E+05	2.09E+05	1.25E+05
TAC of the whole sequence ($/yr)		5.51E+05	
Total annual cost saving %		10.104524	
Total operating cost saving %		18.90037931	
Total QR (KJ/hr)		6.49E+06	
Total QR saving %		19.10462651	
TAC saving %		17.74583435	

Results of energy consumption TAC saving in addition to capital and operating cost saving for all the studied cases are summarized in Tables 6 and 7. The energy saving for the case 2 is reached to 12.4% while for case 3 erased to about 19.1% as shown in table 7. For there more the TAC saving for case 2 and case 3 were 12.4% and 17.74%. there are signification differences in both energy and take saving between case 2 and case 3. The saving in case 3 increased to 6.70% and 6.34% for energy and TAC saving when respectively. The results proved the importance of using middle component purity in distillation processes for high yield separation of hydrocarbons.

Table 6: TAC and total Q_R saving percentage for all the studied schemes

Studied Scheme	TAC saving (%)	Energy saving (%)
Case 1: Conventional direct distillation (base case)	0	0
Case 2: Conventional direct distillation sequence with 85% middle component purity	11.40	0 12.4
Case 3: Conventional direct distillation sequence with 80% middle component purity	17.74	19.104

The comparison of operating cost and capital cost for the studied cases are performed and the results is presented in Table 7. the operating cost of case 2 drops to 12.27% for case 3.where only drops for the capital cost of case 2 and 10.10% drops e for case 3. The decrease in the capital cost of the direct distillation processes is considered to be high ,which will affect the cost of products.

Table 7: Capital and total operating cost saving percentage for all the studied cases

Studied Scheme	Capital cost saving %	Operating cost saving %
Case 1: Direct distillation (base case)	0	0
Case 2: Direct distillation with85% middle component purity)	6.05	12.27
Case 3: Direct distillation with 80% middle component purity	10.10	18.90

Discussion

During this process, it was noticed that the largest increase in the cost of the second column is due to the largest size because of its stages which reached to 44 stages, while the other two columns reached the first 20 stages and the third 16 stages. It lead to the second column was the most energy consumption and costly in capital. This is due also to the separation of iC4 and nC4 more difficulty and knead due to the convergence of their physical and chemical properties (close to zoetrope system) and while this was not noticed in columns 1 and 3. The component C3 was separated from the mixture in the first column and nC4 was separated from iC5 in the 3th column resulted from the wide differences in their physical properties, particular boiling points which is the main factor in the distillation processes. Likewise, it was noted that the volume of coolers and boilers in the second column is larger than in the other two columns, which increased the cost of construction and operation process in terms of providing steam and pure water for the coolers.

Conclusions

The following points can be deduced from the present study
1. In distillation operations when separating a quaternary mixture, the purity of intermediate vehicles plays a significant role in cost and energy saving.

2. In the design process, we observed that the second column is always more expensive in energy and cost of capital because ISO-Butane and N-Butane . These compounds are close to physical and chemical properties.

3. Distillation process is a continuous separation process It is very important to reduce the cost of high quality products, otherwise the process will not be economically viable.

4. By reducing of the energy consumed, it means a decrease in the waste gases as a result of the combustion of light fuel or natural gas, which means environmental protection.

References

1- Perry and Chilton "Chemical engineering hand book", McGraw Hill company, 1973, 5th edition.

2- ZheyuJiang and Rakesh Agrawal, Process intensification in multi-component distillation: A review of recent advancements, Chemical Engineering Research and Design, V 147, 2019, 122-145.].

3- M. Sittig, 1978, Petrolum Refinary Industry Energy saving and Environmental Control, Noyes Data Corporation, New Jersey.]

4-Dhole, V.; Buckingham, (1994). *P. Refinery column integration for debottlenecking and energy saving, ESCAPEIV Conference, Dublin, March*.

5- Doherty, M. F. and Malone, M. F. J., Eds., (2001). Conceptual Design of Distillation Systems. McGraw-Hill Inc., New York.

6- Peter M. S., and Timmerhaus K. D., (1988). "Plant Design and Economics for Chemical Engineers".3d ed., McGraw-Hill Inc., New York.

7- Emtir M., Mizsey P., and Fonyo Z., (2003) " Economic and controllability investigation and comparison of energy-integrated distillation schemes", BudapestUniversity of Technology and Economics. Budapest, Hungary. Chem. Biochem. Eng.

8- Smith, R. (2005). Chemical Process design and integration, John Wiley and Sons Ltd, England.

9- King C .J., Separation processes 2nd Ed., McGraw-Hill Inc., (1980) New York.

10 - [Rohm and Wenzel, 2003] Wenzel, S. and Rohm, HJ (2003). Thermally coupled distillation columns using total cost optimization. Chemical Engineering & Technology.

11- Stichlmair J. G., and Fair J.R., (1998). Distillation Principles and Practices, Wiley-VCH, Canada.

12- Abolgasem Elaahi and William L. Luyben (1983). *Alternative Distillation Configurations for Energy Conservation in Four- Component Separations,* Ind.Eng.Chem. Process Des.Dev.,vol 22, No.1

13- Suphanit B., Bischert A., and Narataruksa P., Exergy loss analysis of heat transfer across the wall of the dividing-wall distillation column. Energy 2007, 32, (11), 2121- 2134.

15- Chemical Engineering magazine, (April, 2015) Chemical Engineering Plant Cost Index. Economic indicators,(www.che.com/pci)

Appendixes

Appendix A: Sizing and costing of Equipments

The sizing of distillation columns and heat transfer equipment requires the determination of flow rates, temperatures, pressures, and heat duties from the flow sheet of mass and energy balance, and these quantities can then be used to determine the capacities needed for the cost correlation .

A1; Sizing and Costing of distillation columns

1- The light and heavy key is determined, and then the relative volatility is calculated using Equation

$$\alpha_{LK/HK} = \frac{K_{LK}}{K_{HK}} \qquad [A1.1]$$

Where $\alpha_{LK/HK}$ = Relative volatility of the light key relative to the heavy key

K_{LK} = Equilibrium constant of the light key

K_{HK} = Equilibrium constant of the heavy key

Where K_{LK}, K_{HK} are taken from HYSYS simulator results.

2- The average viscosity μ_{av} between the top and bottom of the column is estimated.

3- For a given number of theoretical stages HYSYS simulator calculates column diameter after converging for selected valve tray distillation column and for flooding rate ranging from 70-80%.

4- In order to estimate the actual number of trays (N_{actual}), overall column efficiency (E_o) is estimated from Doherty & Malone correlation (2001)[5]:

$$E_o = 0.24 + 0.76 \exp\left(-(\mu\alpha)^{0.5}\right) \qquad [A1.2]$$

Then the actual number of trays N_{actual} can be estimated by dividing the theoretical number of trays N in the column section by the efficiency, E_0:

$$N_{actual} = \frac{N_{theoritical}}{E_0} \qquad [A1.3]$$

5- The tray stack height is then calculated using Equation [3-4], assuming 0.6m (24 in) tray spacing (Doherty, and Malone, 2001)[5]:

$$h = (N-1)(0.6) \qquad [A1.4]$$

Where h = tray stack height in meters

6 - By adding three meters as disengagement space (1.2m for the top, and 1.8m for the bottom of the column), the total height can be estimated:

$$H = h + 3.00 \qquad\qquad [A1.5]$$

Where $H =$ the total height of the column in meters

Capital cost of distillation columns

The capital cost of the column consists of the installation cost of the column shell and the installation cost of the tray stack.

For carbon steel construction distillation column with valve tray internals the updated bare module cost (installation cost) for each of the column shell and tray stack can be calculated by using the following cost equations that are updated with the Marshall & Swift index. For comparison a single value of M&S=1490.2 is selected, (Chemical Engineering magazine April, 2015)[14].

Installed cost of column shell,

$$\$ = (\frac{M\&S}{280}) * (2982) * d^{1.066} * H^{0.802} \qquad\qquad [A1.6]$$

If the design pressure (P) is more than 345 kpa, a correction factor [1+1.45*10^(-4)(P345)] is applied.

Installed cost of the column trays,

$$\$ = (\frac{M\&S}{280}) * (136.14) * d^{1.55} * h \qquad\qquad [A1.7]$$

Where ; d is the column diameter, H is the column height and h is tray stack height

The total column cost is the sum of the installed cost of column shell and the installed cost of column trays.

Column cost = (Installed cost of shell) + (Installed cost of trays)   [A8]

A2; Sizing and Costing heat transfer equipments

The heat transfer area , of the condensers, reboilers and heat exchangers are calculated assuming the overall heat transfer coefficients, U, given in Table A1. and are calculated according to the following equation:

$$A = \frac{Q}{U \cdot LMTD} \qquad\qquad [A2.1]$$

where Q is the heat duty, and $LMTD$ is the logarithmic mean temperature difference:

$$LMTD = \frac{\Delta T_2 - \Delta T_1}{\ln \frac{\Delta T_2}{\Delta T_1}} \qquad\qquad [A2.2]$$

ΔT_2 is the temperature difference between the inlet streams, and ΔT_1 is the temperature difference between the outlet streams of the heat transfer equipment.

Table A1: Overall heat transfer coefficients: (Peters &Timmerhaus 1988)[6]

Heat transfer equipment	Overall heat transfer coefficient, U, [kJ / m^2 h °C]
Condenser	2800
Reboiler	3400
Heat exchanger	2100

Capital cost of heat transfer equipment

The cost of heat transfer equipment can be correlated as a function of surface area. Assuming shell and tube, floating head, and carbon steel construction, can be calculated by using the following cost equations that are updated with the Marshall & Swift index.

Installed cost of the heat equipment, (ICH) ,

$$\$ = (\frac{M \& S}{280})*(1562)*A^{0.65} \qquad \text{[A2.3]}$$

where: A = area m2, 18.6 < A < 464.5 and design pressure up to 1034.2 kpa.

Appendix B ;Estimation of operating costs

The operating cost includes the utility costs which is calculated per year as a function of the operating hours.

The operating costs are assumed only steam and cooling water costs. So we take the operating hours per year is set to be 8000 (hr).

The flow rate of cooling water, $\overset{\bullet}{m}_{CW}$, is calculated using the following equation (Turton et.al, 1998):[17]

$$\overset{\bullet}{m}_{CW} = \frac{Q}{C_P.\Delta T} \qquad \text{[B.1]}$$

Where the specific heat capacity of water, C_P, equals 4.181 J/K·g and ΔT is temperature difference.

Cooling water cost = $\overset{\bullet}{m}_{CW} \times$ cooling water price $\times$ operating hours $\times 10^{-3}$ $\qquad$ [B2]

The flow rate of steam, $\overset{\bullet}{m}_{STM}$, is calculated using the following Equation:

$$\overset{\bullet}{m}_{STM} = \frac{Q}{\lambda} \qquad \text{[B3]}$$

Where λ is the latent heat of steam, equal to 2070 kJ/kg for low-pressure steam and 2000 kJ/kg for medium-pressure steam, (Emtir, et.al 2004).[7]

Steam cost = $\overset{\bullet}{m}_{STM} \times$ LP-steam price $\times$ operating hours $\times 10^{-3}$ $\qquad$ [B4]

The utility prices used to calculate operating costs are given in Table 3.5:

Table B1: Utilities cost data(Emtir, et.al 2004)[7]

	utility prices Based on European prices	
Utility	Temperature (°C)	Price ($/ton)
LP-steam	160	17.7
MP-steam	184	21.8
Cooling water	23-40	0.0272

Appendix C: Estimation of Total Annual Cost (TAC)

The capital and operating costs are annualized over a period referred to as the plant lifetime, and assumed to be 10 years (8000 hrs / year) and Operating costs were assumed just only the utility cost (steam and cooling water).

Annual Capital Cost =Capital cost /Plant life   [C1]

the TAC (includes capital and utility costs) can be calculated according to the following equation:

TAC = Annual operating cost + Annual capital cost [C2]

The economic study provides the TAC as indicator that characterizes the different distillation design alternatives.